

Novel Design and Integration of Air Conditioning/Thermal Energy Storage with Phase
Change Material

BY

AHMED AL JEHANI

B.S., University of Alabama, 2002

M.S., Illinois Institute of Technology, Chicago, 2014

PhD Dissertation

Submitted as partial fulfillment of the requirements
for the degree of Doctor of Philosophy in Chemical Engineering
in the Graduate College of the
University of Illinois at Chicago, 2020

Chicago, Illinois

Defense Committee:

G. Ali Mansoori, Chair
Said Al-Hallaj, Advisor
Christos G. Takoudis, Chemical Engineering
Sangil Kim, Chemical Engineering
Yayue Pan, Mechanical Engineering

This dissertation is dedicated to everyone I love; their genuine words and absolute support were my supplements on this exciting journey. This thesis is especially dedicated to my amazing parents, my beautiful wife, my wonderful kids, and to the rest of my beautiful family and friends. Without their support and compassion this would never have been accomplished.

ACKNOWLEDGMENTS

Sincere acknowledgments to my academic advisor, Professor Said Al-Hallaj for his continuous support, academic guidance and supervision of publications since I started the program about five years ago. I also would like to express my deep appreciation to Professor Ludwig Nitsche for his supervision of publications, academic guidance and support on the past two years. I also would like to kindly express my gratitude to the PhD defense and advising committee: Professor G. Ali Mansoori (Chairman of the committee), Professor Christos G. Takoudis, Professor Sangil Kim, and Professor Yayue Pan. I also would like to acknowledge AllCell Technologies company for allowing me to use their R&D's lab and instruments which allows me to publish the work with special thanks to Mr. Siddique Khateeb for the lab technical support and the lab activity supervision, feedback and review of some of the publications.

CONTRIBUTION OF AUTHORS

Chapters 1-5 represent published manuscripts ((Ahmed Aljehani, Nitsche, and Al-Hallaj 2020; Ahmed Aljehani et al. 2018; S. Al-Hallaj et al. 2018)) which were written and published during the time of my PhD research work. For the publications ((Ahmed Aljehani, Nitsche, and Al-Hallaj 2020; Ahmed Aljehani et al. 2018)) I was the main author and a major contributor of the work and the publications. Professor Said Al-Hallaj provided the academic guidance and supervision of the research work/publications since I started the program about five years and a half ago. Professor Ludwig Nitsche provided the academic guidance and supervision of the research work/publications over the last two years and half. Mr. Siddique Khateeb provided the technical support of some of the lab activities, experimental work and the material characterizations in addition to the review and proofread of some of the publications. In the conference paper publication (S. Al-Hallaj et al. 2018), I contributed as a co-author in writing the manuscript for that conference paper based on the literature review and the knowledge I acquired working on my PhD research work.

TABLE OF CONTENTS

<u>CHAPTER</u>		<u>PAGE</u>
1.	INTRODUCTION	1
1.1	Background.....	1
1.2	Problem Statement.....	4
1.3	Significance of the Problem.....	5
1.4	Purpose of the Study.....	7
1.5	Significance of the Study.....	8
1.6	Thesis chapters at a glance.....	9
2.	CONCEPTUAL FRAMEWORK AND LITERATURE REVIEW.....	12
2.1	Thermal Energy Storages (TES) in principle.....	12
2.2	Types of Thermal Energy Storage systems.....	16
2.3	Potential Phase Change Materials for TES.....	22
2.4	Proposed Phase Change Composite (PCC).....	29
2.5	Theoretical foundations.....	32
2.6	Research goals with respect to conceptual framework.....	40
3.	PCC MATERIAL CHARACTERIZATION.....	41
3.1	Materials and preparations.....	41
3.2	Matrix of experiments	43
3.2.1	Latent heat, melting temperature, impregnation & evaporation rate.....	45
3.2.2	Thermal conductivity and diffusivity measurements.....	63
3.2.3	SEM (Scanning Electron Microscope) imaging.....	68
3.2.4	XRD (X-ray diffraction) analysis.....	84
3.2.5	Material mechanical compression testing.....	92
3.3	Summary of observation from PCC material characterization chapter.....	97
4.	PCC-TES EXPERIMENTAL TESTING.....	100
4.1	PCC-TES structural overview.....	100
4.2	Materials and initial preparations of the PCC-TES structure.....	102
4.3	Experimental testing: Design.....	105
4.4	Experimental testing: testing activity.....	107
4.4	Experimental testing: Results and discussion.....	108

TABLE OF CONTENTS (continued)

<u>CHAPTER</u>		<u>PAGE</u>
5.	SYSTEM-LEVEL EVALUATION OF THE INTEGRATION CONCEPT.....	111
5.1	Proposed system.....	111
5.2	The Aspen Plus® model.....	116
5.2.1	1 st flowsheet –conventional AC.....	118
5.2.2	2 nd flowsheet – discharging mode of the PCC-TES.....	121
5.2.3	3 rd flowsheet- charging mode of the PCC-TES.....	124
5.3	Theoretical background and foundations.....	125
5.4	The analytical model.....	129
5.4.1	Characterization of melting and solidification behaviors.....	130
5.5	Material evaluations.....	140
5.6	Model validation.....	141
5.7	Case studies.....	151
5.7.1	Case study-1: [AC + PCC-TES] vs. conventional AC.....	152
5.7.1.1	Case study 1: Comparison criteria.....	152
5.7.1.2	Case study 1: Testing basis.....	152
5.7.1.3	Case study 1: Results and discussion.....	153
5.7.1.4	Case study 1: Conclusion.....	158
5.7.2	Case study-2: PCC-based TES vs. PCC-based ICE.....	159
5.7.2.1	Case study 2: Introduction	159
5.7.2.2	Case study 2: Comparison criteria.....	161
5.7.2.3	Case study 2: Testing basis.....	161
5.7.2.4	Case study 2: Results and discussion.....	162
5.7.2.5	Case study 2: Conclusion.....	164
6.	NUMERICAL MODELING OF TRANSITET HEAT TRANSFER.....	165
6.1	Introduction, motivation and hypothesis.....	165
6.2	PDE model with one space dimension.....	172
6.3	Numerical model equations.....	173
6.4	ODE model based on lumped capacitance.....	181
6.5	Results and discussion.....	182
6.6	Summary.....	195

<u>CHAPTER</u>	TABLE OF CONTENTS (continued)	<u>PAGE</u>
7.	TECHNO ECONOMIC EVALUATION (CASE STUDY)	196
7.1	Backgrounds and introduction.....	196
7.2	Geographic location and climate.....	201
7.3	Data collection and evaluation.....	202
7.4	Case study approach (Can PCC-TES help?).....	207
7.5	Case study discussion/results.....	208
7.6	Summary.....	210
8.	CONCLUSIONS.....	211
8.1	Summary of Contributions.....	211
8.2	Recommendations for future work.....	212
	APPENDIX.....	213
	CITED LITERATURE	214
	VITA	227

LIST OF TABLES

<u>TABLE</u>	<u>PAGE</u>
1. Table 3.1: Matrix of experiments for PCC material characterization.....	44
2. Table 3.2: n-Tetradecane suppliers' information and pricing in (\$/kg)	46
3. Table 3.3: Latent heat (kJ/kg) measurement (averaged for each group).....	47
4. Table 3.4: Phase change material's melting temperature (oC) measured at heating rate of 1 °C/min.....	48
5. Table 3.5: Summary of observations.....	58
6. Table 3.6: Phase change material's melting temperature (°C) measurement.....	59
7. Table 3.7: PCM weight % of impregnated graphite blocks.....	61
8. Table 3.8: PCM evaporation rate from impregnated graphite blocks.....	62
9. Table 3.9: Experimental figures of n-Tetradecane evaporation rate in ($\mu\text{g} / \text{m}^2 \cdot \text{s}$)....	63
10. Table 3.10: Latent heat (kJ/kg) of impregnated graphite with PCM.....	65
11. Table 3.11: Measured Thermal diffusivity & calculated thermal conductivity.....	68
12. Table 3.12: Mechanical compression testing for all four densities of compressed expanded graphite impregnated with paraffin evaluated for this study.....	94
13. Table 3.13: Summary of observations from characterization experiments of proposed PCC, effects of varying density by compression on properties of interest.....	98
14. Table 4.1: detailed information about the PCC-TES structure and copper tubes for the experimental testing	104
15. Table 4.2: Heat released by EG vs. PCC-TES designed heat storage.....	110
16. Table 5.1: Phase change composite (PCC) material.....	140
17. Tabel 5.2: AC refrigerant loop data & Ethylene Glycol (EG) data.....	140
18. Table 5.3: Copper-tubes dimensions for the PCC-TES system.....	141

LIST OF TABLES (continued)

<u>TABLE</u>	<u>PAGE</u>
19. Table 5.4: Simulation model validation: (model input vs. real experiment input) for the actual 4 kWh PCC-TES benchtop.....	144
20. Table 5.5: Simulation model validation: (model output vs. experimental results) for the actual 4 kWh PCC-TES benchtop.....	147
21. Table 5.6: Cooling load demand required to be met by both systems.....	153
22. Table 5.7: Modeling Comparison: Conventional AC vs. an integrated unit (AC+ PCC-TES).....	155
23. Table 5.8: Breakdown of electricity consumed by each refrigeration compressor and associated reduction in CO ₂ emissions.....	155
24. Table 5.9: Breakdown of electricity's cost per compressor consumption.....	157
25. Table 5.10: Cooling load demand required to be met by both systems + systems attributes.....	161
26. Table 5.11: Comparing the discharging rates of PCC-TES vs. PCC-ice in addition to comparison of most important system attributes effecting discharging rates.....	162
27. Table 6.1: Major parameters of the mathematical model.....	180
28. Table 6.2: Averaged error between experimental & simulation curves (Fig 6.10)...	186
29. Table 6.3: Averaged error between experimental & simulation curves (Fig 6.11)...	188
30. Table 7.1: Oil consumers of the 25% local share (source: (Lahn and Stevens 2011; Organization of Petroleum Exporting Countries 2016; Yamani 2012)).....	189

LIST OF TABLES (continued)

<u>TABLE</u>	<u>PAGE</u>
31. Table 7.2: Distribution of the total installed capacity by region.....	204
32. Table 7.3: Electricity consumption by category.....	204
33. Table 7.4: Saudi Arabia electricity production matrix.....	205
34. Table 7.5: Saudi Arabia upcoming projects to expand electricity production.....	206
35. Table 7.6: Case Study 7.1: PCC-TES installed to offset 50% of peak demand in Saudi Arabia.....	208
36. Table 7.7: Case Study 7.2: PCC-TES installed to offset 25% of peak demand in Saudi Arabia.....	209

LIST OF FIGURES

<u>FIGURE</u>	<u>PAGE</u>
1. Figure 1.1: Energy use by US residential home.....	2
2. Figure 1.2: Energy use by commercial buildings.	3
3. Figure 1.3: Southern California Edison 2018 residential rate plan TOU-D-A designed for high-energy users.....	6
4. Figure 1.4: Southern California Edison 2018 residential rate plan TOU-D-B designed for low/medium-energy users.....	6
5. Figure 2.1: Full load/demand shift with full cooling storage.....	14
6. Figure 2.2: Peak shaving (Partial load during Peak-hours)	15
7. Figure 2.3: Demand/load limiting.....	16
8. Figure 2.4: Classifications of thermal energy storages evaluated in the literature.....	17
9. Figure 2.5: Classifications of latent storages with a focus on solid-liquid transition..	19
10. Figure 2.6: Latent heat of fusion is much larger than sensible heat.....	21
11. Figure 2.7: Classifications of phase change materials evaluated.....	24
12. Figure 2.8: Classical Stefan problem Concept in association with freezing of seawater material.....	33
13. Figure 3.1: Actual picture of DSC device at AllCell Facility Lab.....	46
14. Figure 3.2: DSC exotherm curves of samples (Group A).....	50
15. Figure 3.3: DSC exotherm curves of Group A after 50 cycles of heating/cooling.....	51
16. Figure 3.4: DSC exotherm curves of samples (Group B)	52

LIST OF FIGURES (continued)

<u>FIGURE</u>	<u>PAGE</u>
17. Figure 3.5: DSC exotherm curves of Group B after 50 cycles of heating/cooling...	53
18. Figure 3.6: DSC exotherm curves of samples (Group C)	54
19. Figure 3.7: DSC exotherm curves of Group C after 50 cycles of heating/cooling...	55
20. Figure 3.8: DSC exotherm curves of samples (Group D)	56
21. Figure 3.9: DSC exotherm curves of Group D after 50 cycles of heating/cooling...	57
22. Figure 3.10: Nearly identical PCM weight % of impregnated graphite blocks along the duration of graphite impregnation experiment	60
23. Figure 3.11: Schematic of in-plane and through-plane samples with respect to compact direction.....	64
24. Figure 3.12: DXF-200 laser flash instrument at AllCell Facility lab	65
25. Figure 3.13: SEM images of graphite matrix (unfilled with paraffin) showing (a) at x200 magnification and (b) at x5000 magnification (Mills et al. 2006).....	69
26. Figure 3.14: SEM images of graphite matrix (filled with paraffin) showing (a) at x200 magnification and (b) at x5000 magnification (Mills et al. 2006).....	69
27. Figure 3.15: SEM device at Argonne Lab Facility.....	72
28. Figure 3.16: SEM images at (x50 magnification) of graphite samples-- CEG-Sample 1, CEG-Sample 2, CEG-Sample 3 and CEG-Sample 4—(no paraffin impregnation) at four various densities of (670 g/l), (490 g/l), (380 g/l) and (150 g/l.).....	73
29. Figure 3.17: SEM images at (x100 magnification) of graphite samples-- CEG-Sample 1, CEG-Sample 2, CEG-Sample 3 and CEG-Sample 4—(no paraffin impregnation) at four various densities (a) 670 g/l, (b) 490 g/l, (c) 380 g/l (d) 150 g/l.....	74

LIST OF FIGURES (continued)

<u>FIGURE</u>	<u>PAGE</u>
30. Figure 3.18: SEM images at (x300 magnification) of graphite samples-- CEG-Sample 1, CEG-Sample 2, CEG-Sample 3 and CEG-Sample 4—(no paraffin impregnation) at four various densities (a) 670 g/l , (b) 490 g/l , (c) 380 g/l (d) 150 g/l.....	75
31. Figure 3.19: SEM images of graphite matrix (paraffin impregnated) showing at x30, x150, x300 and x 500 magnifications for PCC-sample 1.....	76
32. Figure 3.20: SEM images of graphite matrix (paraffin impregnated) showing at x2.50k, x5.0K and x5.01k magnifications for PCC-sample 1.....	77
33. Figure 3.21: SEM images of graphite matrix (paraffin impregnated) showing at x30, x150, x300 and x 500 magnifications for PCC-sample 2.....	78
34. Figure 3.22: SEM images of graphite matrix (paraffin impregnated) showing at x2.50k, x5.0K and x5.01k magnifications for PCC-sample 2.....	79
35. Figure 3.23: SEM images of graphite matrix (paraffin impregnated) showing at x30, x150, x300 and x 500 magnifications for PCC-sample 3.....	80
Figure 3.24: SEM images of graphite matrix (paraffin impregnated) showing at x2.50k, x5.0K and x5.01k magnifications for PCC-sample 3.....	81
36. Figure 3.25: SEM images of graphite matrix (paraffin impregnated) showing at x30, x150, x300 and x 500 magnifications for PCC-sample 4.....	82
37. Figure 3.26: SEM images of graphite matrix (paraffin impregnated) showing at x2.50k, x5.0K and x5.01k magnifications for PCC-sample 4.....	83
38. Figure 3.27: XRD device at Argonne Lab Facility.....	84
39. Figure 3.28: XRD patterns for (4) samples of the same compressed expanded graphite at various densities.....	86
40. Figure 3.29: XRD patterns for (4) samples of PCC at various densities.	87
41. Figure 3.30: XRD patterns for Sample 1 of CEG and PCC.....	88
42. Figure 3.31: XRD patterns for CEG and PCC of sample 2.....	89
43. Figure 3.32: XRD patterns for CEG and PCC of sample 3.....	90

LIST OF FIGURES (continued)

<u>FIGURE</u>	<u>PAGE</u>
44. Figure 3.33: XRD patterns of CEG and PCC for Sample 4.....	91
45. Figure 3.34: Mechanical testing device at AllCell Technologies Lab Facility.....	93
46. Figure 3.35: Mechanical compression test for PCC-Sample 1.....	95
47. Figure 3.36: Mechanical compression test for PCC-Sample 2.....	95
48. Figure 3.37: Mechanical compression test for PCC-Sample 3.....	96
49. Figure 3.38: Mechanical compression test for PCC-Sample 4.....	96
50. Figure 3.39: Mechanical compression test for PCC-Samples 1/2/3/4.....	97
51. Figure 4.1: PCC-TES conceptual design; PCC-TES exchanging heat with EG.....	101
52. Figure 4.2: Actual representation of the proposed PCC-TES system.....	101
53. Figure 4.3: Inside view of the actual 4kWh PCC-TES structure.....	102
54. Figure 4.4: Discharging experiment of the actual 4 kWh PCC-TES.....	105
55. Figure 4.5: Actual 4kWh PCC-TES system's main components.....	106
56. Figure 4.6: Schematic of the PCC-TES system's main components.....	109
57. Figure 5.1: AC's conventional refrigeration cycle.....	112
58. Figure 5.2: Complete system. EG Loop #1 mediates heat exchange between incoming hot air and the (thawing) PCC during discharging mode. EG Loop #2 mediates heat exchange between the refrigerant and the (freezing) PCC during charging mode.....	112
59. Figure 5.3: Discharging mode operates with valves 1 and 2 closed and valves 3 and 4 open. During peak day hours cooling of hot air is divided between the refrigerant loop and the melting PCC.....	113
60. Figure 5.4: Charging mode operates with valves 1 and 2 open and valves 3 and 4 closed. During night hours the AC refrigerant loop cools and freezes the PCC.....	114

LIST OF FIGURES (continued)

<u>FIGURE</u>	<u>PAGE</u>
61. Figure 5.5: PCC-TES conceptual design; exchanging heat with EG stream.....	115
62. Figure 5.6: Actual representation of the proposed PCC-TES system.....	116
63. Figure 5.7: First flow sheet simulating major components of vapor compression refrigeration loop meeting the entire cooling demand (base case) of 16 kW.....	120
64. Figure 5.8: First flowsheet, this time simulating major components of vapor compression refrigeration loop meeting 50% of the cooling demand (reduce load case) of 8 kW.....	120
65. Figure 5.9: Second flowsheet simulates the discharging process and addresses phase change behavior and associated valuable information.....	123
66. Figure 5.10: The third flowsheet simulates the charging process and addresses phase change behavior and associated valuable information.....	125
67. Figure 5.11: A conceptual temperature profile of a layer of finite thickness with upper and lower external energy sources illustrated by left and right heat sources.....	127
68. Figure 5.12: Space-time continuum theory approach to solve present heat transfer problem.....	128
69. Figure 5.13: A conceptual approach to discretize PCC-TES and calculate time duration with respect to position (s) for melting progression of overall structure.....	135
70. Figure 5.14: Schematic of the PCC-TES system's main components.....	142
71. Figure 5.15: Actual 4kWh PCC-TES system's main components.....	142
72. Figure 5.16: Representation of discharging experiment temperature profiles with respect to time.....	148

LIST OF FIGURES (continued)

<u>FIGURE</u>	<u>PAGE</u>
73. Figure 5.17: Temperature w/ respect to position during the melting progression.....	150
74. Figure 5.18: Timing of melting profiles with respect to position in PCC-TES.....	150
75. Figure 5.19: high number of copper tubes is required for ice-TES to compensate for the low thermal conductivity of ice.....	163
76. Figure 6.1: AC's conventional refrigeration cycle.....	166
77. Figure 6.2: Complete system. EG Loop #1 mediates heat exchange between incoming hot air and the (thawing) PCC during discharging mode. EG Loop #2 mediates heat exchange between the refrigerant and the (freezing) PCC during charging mode.....	167
78. Figure 6.3: Charging mode operates with valves 1 and 2 open and valves 3 and 4 closed. During night hours the AC refrigerant loop cools and freezes the PCC.....	168
79. Figure 6.4: Discharging mode operates with valves 1 and 2 closed and valves 3 and 4 open. During peak day hours cooling of hot air is divided between the refrigerant loop and the melting PCC.....	169
80. Figure 6.5: Schematic of the PCC-TES system.....	170
81. Figure 6.6: Actual experimental set up of the PCC-TES system.....	171
82. Figure 6.7: PCC-TES concept design; PCC-TES exchanging heat with EG stream..	172
83. Figure 6.8: Internal details/Dimensions of one slab of the PCC-TES.....	173
84. Figure 6.9: Three-dimensional representation of the change in dimensionless temperature of the PCC structure with respect to dimensionless time and position, as calculated numerically.....	182
85. Figure 6.10: Experimental time traces of temperature measured with prefixed thermocouples plotted against numerical counterpart. The PCC temperature traces (θ_1) for various positions ζ that correspond to the placement of thermocouples. Slabs (6, 9, 12, 18, and 21) correspond to ζ positions (0.21, 0.32, 0.42, 0.64 and 0.74)	184

LIST OF FIGURES (continued)

<u>FIGURE</u>	<u>PAGE</u>
86. Figure 6.11: The PCC temperature traces (θ_1) for various positions (ζ) as time elapsed plotted against numerical counterpart for comparison.....	187
87. Figure 6.12: Experimental results: EG inflow and outflow temperature profiles.....	189
88. Figure-6.13: Three-dimensional representation of the change in dimensionless temperature of EG fluid with respect to dimensionless time and position.....	190
89. Figure 6.14: 2-dimensional representation of the change in dimensionless temperature of PCC- θ_1 with respect to position (ζ) at early stages of the experiment.....	191
90. Figure 6.15: 2-dimensional representation of the change in dimensionless temperature of EG fluid θ_2 with respect to position ζ at early stages of the experiment.....	192
91. Figure 6.16: Lumped capacitance model.....	194
92. Figure 6.17: Enthalpy intake comparison (PDE vs. ODE)	194
93. Figure 7.1: Saudi Arabia's energy consumption/production/export forecast.....	198
94. Figure 7.2: Weather in Riyadh, Saudi Arabia.....	202
95. Figure-7.3: Rapid increase in peak demand in Saudi Arabia between 2005-2014.....	205

NOMENCLATURE

ABBREVIATIONS

AC	Air Conditioner
CEG	Compressed Expanded Graphite
COP	Coefficient of Performance
EG	Ethylene Glycol
MWh	Megawatt-hour
NTU	Number of Transfer units (Dimensionless)- it is used to simplify heat exchanger analysis in the event that outlet temperatures are not readily available
ODE	Ordinary Differential Equation
PCC	Phase Change Composite
PCM	Phase Change Materials
PDE	Partial Differential Equation
TES	Thermal Energy Storage

NOMENCLATURE (continued)

Greek letters

α_1	Thermal diffusivity in the solid phase (m^2/s)
$\gamma(\theta_1)$	Dimensionless temperature-dependent effective heat capacity
ϕ	Volume fraction of the tubes passing through the PCC stack of slabs
ψ	Dimensionless factor to represent ratio of thermal capacities between the PCC and EG
ϱ_1	Density of PCC's materials (kg/m^3)
ϱ_2	Density of EG (kg/m^3)
τ	Dimensionless time
θ_1	Dimensionless PCC's Temperature
θ_2	Dimensionless EG's Temperature
ζ	Dimensionless position coordinate

NOMENCLATURE (continued)

Other symbols (mostly appeared in Chapters 4 & 5)

$A_{(eff-tube)}$	Effective area of heat transfer fluid (HTF)'s tubes, (m^2)
A_{PCM}	Surface area of the Phase Change Material (PCM), (m^2)
C_p	Specific heat of the Phase Change Material (PCM), (kJ/kg. K)
Cp_{eff}	Effective specific heat of the phase change material, (kJ/kg. K)
d_i	Inside diameter of the HTF tube, (m)
d_o	Outside diameter of the HTF tube, (m)
h_{fluid}	Heat transfer coefficient of the heat transfer fluid (HTF), (kJ/s.m ² . K)
ΔH	Latent heat or Energy content of the PCM per mass of PCM, (kJ/kg)
Δh	Energy content per volume of the PCM, (kJ/ m ³)
m	Mass of the PCM, (kg)
Δm	Fraction melted (or solidified) of the PCM during phase change
Q	Cumulative heat or thermal energy, (kJ)
s	Depth or (location) of moving phase boundary, (m)
t	Melting duration of the PCM, (s)
T_f	Final temperature of the PCM, (°C)
T_i	Initial temperature of the PCM, (°C)
T_m	Melting temperature of the PCM, (°C)
λ_{PCM}	Thermal conductivity of the PCM, (kJ/s.m.K)
λ_{wall}	Thermal conductivity of the HTF tube wall, (kJ/s.m.K)

NOMENCLATURE (continued)

Other symbols- (mostly appeared in Chapter 6)

\mathcal{A}	Dimensionless constant \mathcal{A} describes interphase heat transfer, given in terms of the Biot Number (Bi) and the volume fraction (ϕ) of the tubes passing through the PCC
B	Dimensionless coefficient to represent Peclet number involving flow velocity (U) in the EG and thermal diffusivity (α_1) within the PCC
\mathcal{C}	Dimensionless constant to represent interphase heat transfer
\mathfrak{D}	Dimensionless constant to represent the dimensionless thermal conductivity
\mathcal{F}	Tortuosity factor
A_c	Cross-sectional area of the PCC slab in the xy-plane (m^2)
Bi	Dimensionless Biot Number
k_l	Thermal conductivity of the PCC material (kJ/s.m. K)
L_{eff}	Effective length of the tubes factoring in total perimeter of the tubes and the al area of the PCC slab in the xy-plane A_c (m)
T_1	PCC material's Temperature ($^{\circ}\text{C}$)
T_2	Ethylene Glycol's Temperature ($^{\circ}\text{C}$)
U	Ethylene Glycol's velocity (m/s)
z	Position coordinate (m)

SUMMARY

This study evaluates the use of phase change composite (PCC) material, consisting of paraffin (namely, n-Tetradecane) and expanded graphite, as a potential storage medium for cold thermal energy storage (TES) systems to support air conditioning (AC) applications. The PCC-TES system is to be integrated with the vapor compression refrigeration cycle of an AC system. The use of this proposed solid PCC material is novel. The PCC has excellent material and thermal characteristics as compared to ice or chilled water that are predominantly used in commercial TES systems for air cooling applications. This study proposed and tested a hypothesis, which suggests that integrating a conventional AC with a PCC-TES would result in significant benefits concerning compressor size, compressor efficiency, electricity consumed and CO₂ emissions. A multi-layer study was thoroughly conducted involving: (1) literature review (2) material characterization (3) experimental work (4) proof of concept simulation (5) numerical modeling (6) real-life implementation evaluation. The study examined several key thermo-physical properties of PCC material. Actual experimental benchtop system has been built and tested. A simulation model using Aspen Plus® was successfully generated to perform overall system-level assessment and proof of concept. The simulation model also compared the use of PCC materials as the energy storage medium versus the use of ice. A detailed numerical model was also successfully built to describe in detail the transient heat transfer problem of a PCC-TES systems exchanging heat with a heat transfer fluid (namely Ethylene Glycol). The actual experimental benchtop validated the analytical/numerical simulation models. The study was wrapped up by addressing real-life implementation of proposed integration between the AC and PCC-TES for hot and humid climate region with high electricity demand.

CHAPTER 1: INTRODUCTION

The work illustrated in this chapter of the dissertation is partially published in the Journal of energy and conversion management and the Journal of Applied Thermal engineering:

- A. Aljehani, S. A. K. Razack, L. Nitsche, S. Al-Hallaj, *Design and optimization of a hybrid air conditioning system with thermal energy storage using phase change composite*, Energy Convers. Manage. 169 (2018) 404–418. doi: 10.1016/j.enconman.2018.05.040.
- B. Ahmed Aljehani, Ludwig C. Nitsche, Said Al-Hallaj, *Numerical Modeling of Transient Heat Transfer in a Phase Change Composite Thermal Energy Storage (PCC-TES) System for Air Conditioning Applications*, Applied Thermal Engineering, 2019, <https://doi.org/10.1016/j.applthermaleng.2019.114522>.

1.1 Background

World population is rapidly growing, and energy demand is unquestionably increasing in accordance. The future is even more challenging when the world population double or triple and when the earth resources continue to become more and more scarce. Energy ever-increasing demand is a common concern around the world. A large portion of the electricity consumed in the US and all over the world is associated with air conditioners especially in warm-climate regions and especially during summer seasons. According to the US Department of Energy, air conditioners annually cost homeowners around 29 billion dollars and release 117 million tons of CO₂ to the air (Ubay 2009). A recent study (Rhodes, Stephens, and Webber 2011) revealed that approximately one-fifth of the electricity consumption in Austin Texas during peak-hours is attributed to air conditioners p0-operated in single-family residential homes. A similar study conducted in Spain revealed that air conditioners are responsible of more than one-third of the electricity consumption during peak-hours in Madrid (Izquierdo et al. 2011). Likewise, a study of Saudi Arabia's

electricity consumption (Lahn and Stevens 2011) revealed that air conditioners account for 50% of the increase in electricity peak demand.

The air conditioner (AC) units in the US and around the world are mostly oversized to meet peak cooling load during hot summer days. The underutilized capacity of oversized AC units wastes significant amounts of electricity during cooler hours/days of the year and leads to more carbon emissions.

Moreover, high demand of electricity during peak-hours drives up the transient price of electricity. (Figures 1.1 and 1.2) with reference to (National Academy of Sciences, National Academy of Engineering 2010) highlight the energy use by residential homes and commercial buildings respectively. (Figures 1.1 and 1.2) highlight that HVAC (Heating, Ventilation and Air Conditioning) is the major electricity consumer in both residential and commercial buildings.

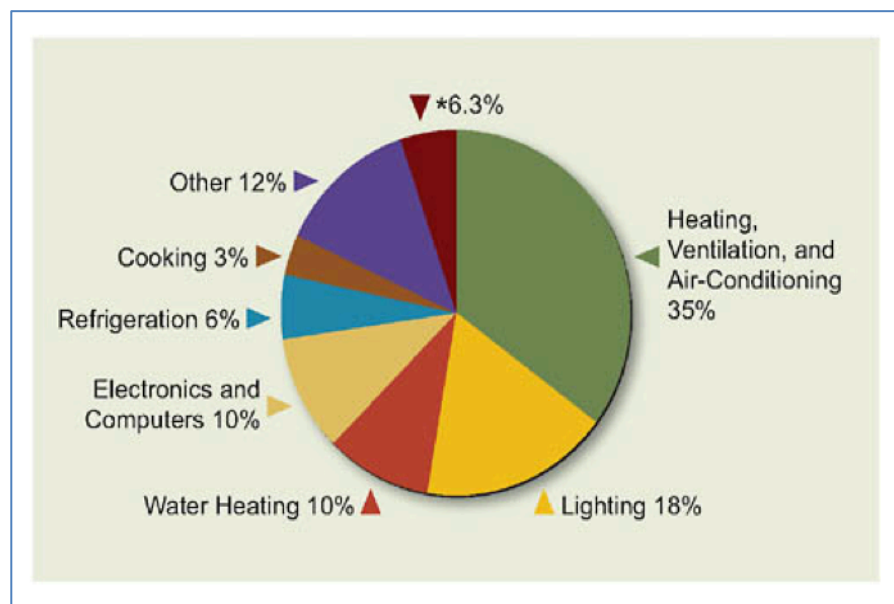


Figure 1.1: Energy use by US residential homes (source: (National Academy of Sciences, National Academy of Engineering 2010))

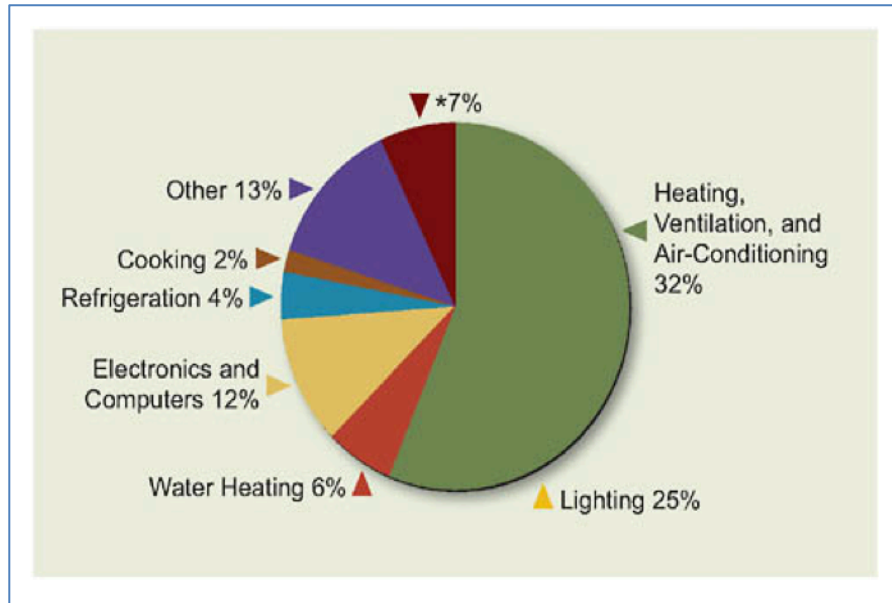


Figure 1.2: Energy use by commercial buildings (source: (National Academy of Sciences, National Academy of Engineering 2010))

On the production side, utility companies are adopting various energy efficiency programs and energy storage technologies to offset carbon emissions and avoid building new additional power plants and distribution lines to meet the peak in electricity demands.

On the demand-side, residential and commercial customers are motivated to avoid “Time of Usage (ToU)” electricity charges and demand charges by opting for alternative technologies that are available or emerging in or to the market.

A TES system is a good alternative solution for demand-side management to shift the AC electricity usage from peak-hours to off-peak-hours, thereby also reducing the overall carbon footprint compared to a conventional air conditioning system. Consequently, TES can result in reducing the size of the AC compressor and lead to great reductions in electricity consumption, electricity bills, and carbon emissions. Therefore, the TES system

will be integrated with an AC unit such that the TES system can provide additional cooling to the building.

A typical TES system cools the building during peak-hours (when electricity prices are high) by absorbing heat from the incoming hot air for the spaces that need to be cooled. At night (when electricity prices are low), the TES then rejects the stored heat by exchange with the refrigeration loop of a conventional AC.

1.2 Problem statement

Public utility companies, around the world, struggle to meet ever-increasing electricity demand and aim to avoid building tremendously expensive new power plants and distribution lines. In some parts of the world, high demand all at once causes frequent unpleasant power outages (remember senior citizens and people with special needs in their home who need to keep their medications refrigerated or keep their medical devices in operations). Availability of electricity is not a luxury; it is a necessity. As a consequence, high demand of electricity during peak-hours drives up the price of electricity consumed during peak-hours. Moreover, AC units are designed large enough to meet the high cooling demand during hot afternoon summer hours, yet they are oversized for cooler hours of the day and cooler seasons of the year. That is an inefficient use of electricity and unnecessary CO₂ emissions during cooler hours/seasons.

1.3 Significance of the problem

As briefly discussed in previous sections, air conditioners are heavily responsible for a large portion of the electricity demand all around the world. High electricity demand during peak-hours not only drives up the price of electricity consumed at those hours, but also high electricity demand all at once may even lead to power outages.

Additional power plants to serve the purpose of meeting high-peak demand come at an expense and lead to even more harmful emissions. Therefore, public utility companies in many parts of the world introduced the “Time of Usage (ToU) fare” concept and added the “demand charge” fees. “Time of Usage (ToU)” fare suggests different price for electricity consumed depending on the hour of the day at which it was consumed. The “demand charge” fees are added to a consumer’s electricity bill, once a month, if the kilowatt (kW) consumed by the consumer exceeded a certain upper limit over any given period during peak-hours. In the US, for example, Southern California Edison Electric utility company applies time of usage (ToU) electricity charges during peak-hours which is 0.235 \$/kWh from 12 pm to 6 pm plus a demand charge of \$9.5/MAX kW for each billing cycle (Southern California Edison 2016). The company applies \$0.191/kWh and \$0.064/kWh electricity ToU charges for mid-peak and off-peak-hours respectively. The rates in 2018 are even higher as illustrated by (Figures 1.3 and 1.4). Higher rates prove the fact those additional power plants to meet the ever-increasing peak demand come at an expense. Nearly the same for the year 2019 as well.

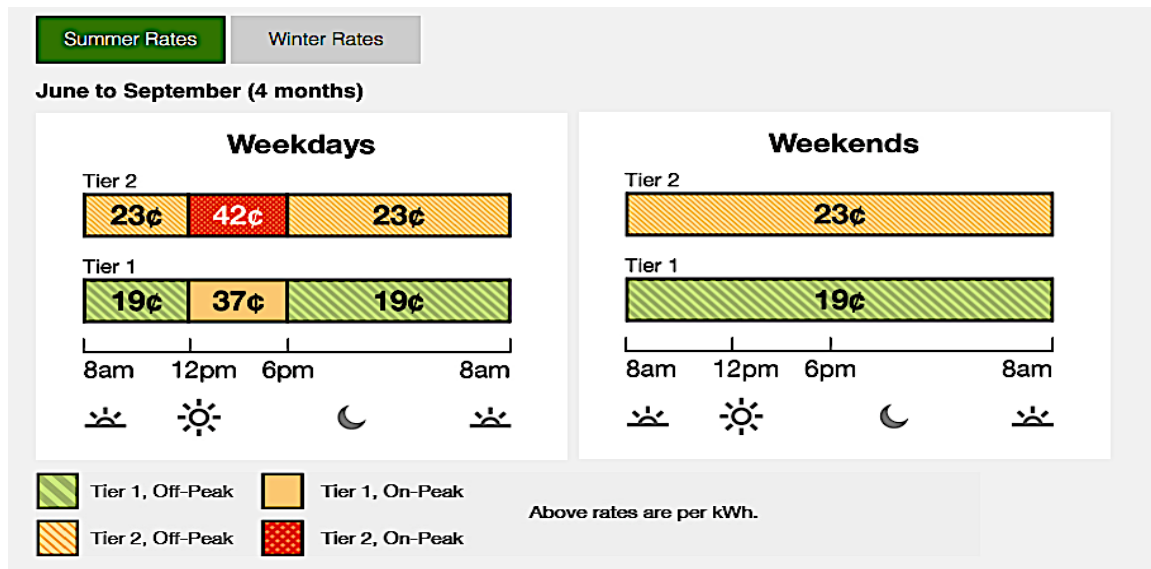


Figure 1.3: Southern California Edison 2018 residential rate plan TOU-D-A (Southern California Edison Time-of-use Residential Rate Plans 2018).

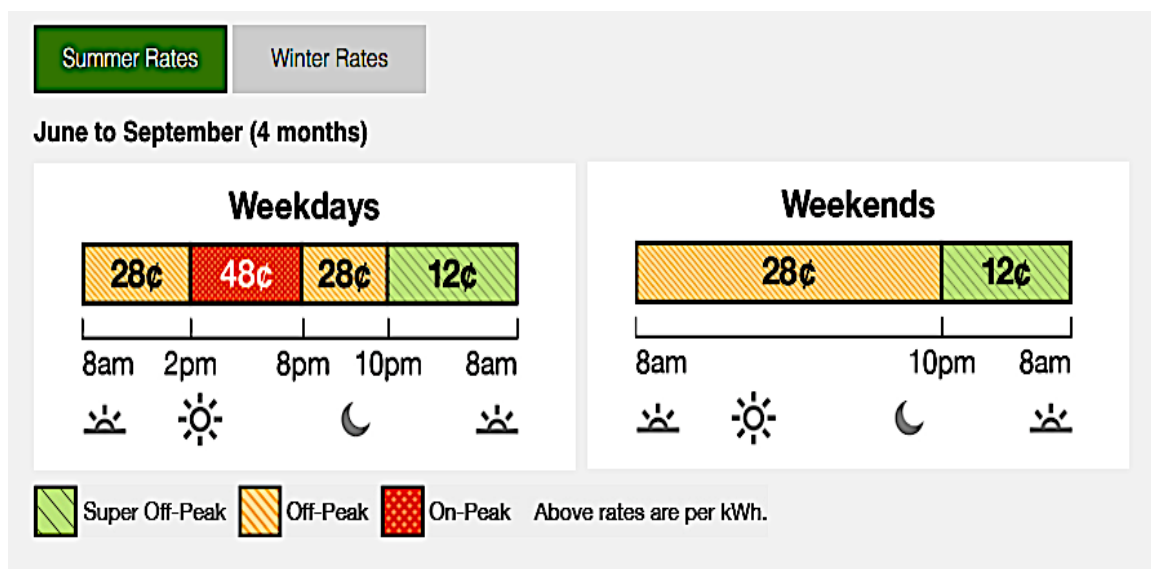


Figure 1.4: Southern California Edison 2018 residential rate plan TOU-D-B (Southern California Edison Time-of-use Residential Rate Plans 2018).

Utility companies are also encouraging and adopting various high-energy efficiency equipment, energy efficiency awareness programs and energy storage technologies to offset wasteful energy consumptions and carbon emissions.

1.4 Purpose of the study

This study evaluates the use of a phase change composite (PCC) material consisting of paraffin wax (n-Tetradecane) and expanded graphite as a potential storage medium for cold thermal energy storage (TES) systems to support air conditioning applications. The PCC-TES system is to be integrated with the vapor compression refrigeration cycle of an air conditioning (AC) system. This study evaluates the utilization of a PCC material (consisting of n-Tetradecane “paraffin” and expanded graphite) as the storage medium for a TES system integrated into AC as a demand-side management solution. The following hypothesis is proposed and tested:

Hypothesis. Integrating the vapor compression refrigeration cycle of a conventional AC with a PCC-TES as a demand-side management solution would provide significant benefits for electrical consumption and demand management. The proposed [AC + PCC-TES] integration would (1) reduce the refrigeration compressor size requirement (and thereby attendant power consumption, CO₂ emissions, and capital costs), and (2) enhance efficiency in all modes of operation: off-peak, mid-peak and peak. The aggregate effect of these advantages could ultimately reduce necessity to build more expensive power plants and distribution lines and reduce carbon emission.

1.5 Significance of the Study

First, the use of this potential phase change composite material is novel and has not been reported in the literature. The PCC has excellent material and thermal characteristics as compared to ice or chilled water that are predominantly used in commercial TES systems for air cooling applications.

Second, this study is the first detailed study to thoroughly address the hybrid integration between PCC-TES and air conditioning systems. Such a multi-layer study has not yet been addressed in the literature.

The study branches into few main levels:

- I. Literature review and theoretical foundations are presented in Chapter 2.
- II. Lab analysis and material testing & characterization are discussed in Chapter 3.
- III. The experimental work is presented in Chapter 4.
- IV. A system-level modeling and Simulation, by Aspen Plus® simulation software enhanced with suitable mathematical equations written as Fortran code within the Calculator Block of Aspen Plus ® to guide the simulation, is discussed in Chapter 5.
- V. A detailed numerical approach to adequately describe the transient heat transfer using Fortran, discussed in Chapter 6.
- VI. A brief assessment on real-life implementation is illustrated in Chapter 7.

The following section goes over the thesis chapters at a glance.

1.6 Thesis chapters at a Glance

Chapter 2 is the literature review chapter. Chapter 2 will shed some light on the principles of thermal energy storage (TES), types of TES, current and potential materials to serve as the energy storage medium in TES systems, and the proposed phase change composite material (presented in this study). Chapter 2 will also discuss theoretical foundation of this study and the pioneer mathematical modeling of melting and freezing processes that involve dealing with the moving interphase boundary by early mathematical treatment of such processes; which is exemplified by the work of Josef Stefan published between the years of 1889 to 1891. Chapter 2 will briefly discuss the historical development of the classical Stefan Problem and the work introduced later on (2003) by Kostenko et al (Kostenko, Pribis, and Puzynin 2003). Unlike the Stefan problem, the work by (Kostenko et al) discussed a special case of the classical Stefan problem at which the heat source is distributed within the phase change medium not only exposed to the outside surface (as the Stefan problem was set up). Both mathematical formulations by Stefan and Kostenko et al accounted for the phase change at a single temperature. The heat source in the heat transfer problem discussed in this thesis is distributed within the phase change composite (PCC) material; similar in a way to the work by (Kostenko et al. 2003). However, the present thesis study accounts for phase change over a range of temperatures in light of the physical characteristics of the proposed PCC materials; unlike the heat transfer presented by Stefan and (Kostenko et al. 2003) that accounted for the phase change at a single temperature. Therefore, this thesis incorporated the effective specific heat method, with reference to (Khateeb et al. 2005), into the equation developed by (Kostenko et al) and adequately accounted for a phase change material that transforms over a melting range.

Chapter 3 illustrates the matrix of experiments outlined to conduct the lab analysis and characterizations of the proposed phase change composite (PCC) material consisting of about 78% low-temperature paraffin (namely, n-Tetradecane, $C_{14}H_{30}$) and 22% compressed expanded graphite. Compacted expanded graphite and n-Tetradecane were analyzed and certain properties of interest were examined. The PCC characterization involves measurements and analysis of latent heat, melting point, graphite impregnation, evaporation rate, thermal diffusivity, thermal conductivity, surface morphology and mechanical strength testing.

Chapter 4 discusses the experimental work done as part of this thesis. 4 kWh-PCC-TES benchtop system has been put together for experimental testing and real-world proof of concept purposes. The PCC-TES is made of 28 slabs of PCC stacked on top of each other. The whole PCC-TES stack is thermally insulated from outside boundaries. Copper tubes carrying the heat transfer fluid (HTF), namely Ethylene Glycol (EG), are sandwiched between each two neighboring slabs. The tubes run through the PCC-TES structure from top to bottom, carry the HTF which exchange heat with the PCC materials. The experiment is conducted to examine and analyze the heat exchange characteristics between the PCC-TES and the EG.

Chapter 5 presents a simulation model using Aspen Plus® which was developed to perform overall system-level assessment and proof of concept evaluation. Chapters 5 and 6, formulated analytical and numerical mathematical representations of the heat transfer problem respectively; which were prepared as branches of the overall multi-layer of the present thesis.

The analytical model presented in Chapter 5 was written as a Fortran code within the calculation block of Aspen Plus® to accurately estimate the time duration of the melting/solidification of the PCC-TES while exchanging heat with a stream of Ethylene Glycol. Chapter 6 illustrates a detailed numerical approach to describe the transient heat transfer in a Phase Change Composite-Thermal energy storage (PCC-TES) exchanging heat with a heat transfer fluid (namely Ethylene Glycol) in space and time domains. Both, analytical and numerical models were crosschecked and validated with experimental work.

To help addressing the new challenging situation of the ever-increasing local energy's demand at many major oil-exporting countries, Chapter 7 came to light. Due to the hot Saudi Arabian's climate, air conditioners are the largest consumers of electricity produced in Saudi Arabia. Electricity production in Saudi is primarily driven by oil and gas. Chapter 7 studied how PCC-TES can have a positive impact on the electricity consumed by air conditioning and consequently increase the oil share that Saudi Arabia can offer to the international market. The work presented by thesis has been also published:

- A. A. Aljehani, S. A. K. Razack, L. Nitsche, S. Al-Hallaj, *Design and optimization of a hybrid air conditioning system with thermal energy storage using phase change composite*, Energy Convers. Manage. 169 (2018) 404–418. doi:10.1016/j.enconman.2018.05.040. **[Presented by Chapters 2, 4 & 5]**
- B. Ahmed Aljehani, Ludwig C. Nitsche, Said Al-Hallaj, *Numerical Modeling of Transient Heat Transfer in a Phase Change Composite Thermal Energy Storage (PCC-TES) System for Air Conditioning Applications*, Applied Thermal Engineering, 2019, <https://doi.org/10.1016/j.applthermaleng.2019.114522>. **[Presented by Chapter 6].**
- C. Al-Hallaj S, Khateeb S, Aljehani A, Pintar M. *Thermal energy storage for smart grid applications*. In: AIP conference on proceedings, vol. 1924; 2018. p. 20007 [AIP Publishing, 2018]. **[Partially presented in Chapter 2]**
- D. Ahmed Aljehani and Said Al-Hallaj “Material Characterization of Potential Phase Change Composite (PCC) for Thermal Energy Storage (TES)” submitted for publication at the journal of Energy Conversion and Management to **summarize Chapter 3** of the dissertation.

CHAPTER 2: CONCEPTUAL FRAMEWORK AND RELATED LITERATURE

The work illustrated in this chapter of the dissertation is partially published in the Journal of energy and conversion management, the Journal of Applied Thermal engineering and AIP conference:

- A. Aljehani, S. A. K. Razack, L. Nitsche, S. Al-Hallaj, *Design and optimization of a hybrid air conditioning system with thermal energy storage using phase change composite*, Energy Convers. Manage. 169 (2018) 404–418. doi: 10.1016/j.enconman.2018.05.040.
- B. Ahmed Aljehani, Ludwig C. Nitsche, Said Al-Hallaj, *Numerical Modeling of Transient Heat Transfer in a Phase Change Composite Thermal Energy Storage (PCC-TES) System for Air Conditioning Applications*, Applied Thermal Engineering, 2019, <https://doi.org/10.1016/j.applthermaleng.2019.114522>.
- C. Al-Hallaj S, Khateeb S, Aljehani A, Pintar M. *Thermal energy storage for smart grid applications*. In: AIP conference on proceedings, vol. 1924; 2018. p. 20007 [AIP Publishing, 2018].

2.1 Thermal Energy Storage (TES) in principle

The concept of integrating cold thermal energy storage (TES) into an air conditioning (AC) system has been widely evaluated in the literature aiming to partially or completely shift electricity demand from peak-hours to off-peak-hours (Mohammed M. Farid et al. 2004; Bo, Gustafsson, and Setterwall 1999; Arteconi, Hewitt, and Polonara 2012; MacPhee and Dincer 2009; Henze et al. 2008; Yau and Rismanchi 2012; S.M. Hasnain 1998; USDOE Office of Energy Efficiency & Renewable Energy and Office of Federal Energy Management Programs 2000; Syed Mahmood Hasnain and Alabbadi 2000; Caliskan, Dincer, and Hepbasli 2012). The TES system is to be integrated with an AC unit such that the TES system can provide additional cooling to the building during peak-hours by completely or partially shifting the cooling load to off-peak-hours. A typical TES system cools the building during peak-hours (when electricity prices are high) by absorbing heat from the incoming hot air for the spaces that need to be cooled. At night (when electricity

prices are low), the TES rejects the stored heat by exchange with the refrigeration loop of a conventional AC.

With reference to (Said Al-Hallaj et al. 2018; Dincer and Rosen 2001; Pacific Gas and Electric Company 1997; USDOE Office of Energy Efficiency & Renewable Energy and Office of Federal Energy Management Programs 2000; COMMISSION CALIFORNIA ENERGY and Systems 1996; Iten and Liu 2014; Mehling et al. 2012) the following concepts/terms are often stated when cold thermal energy storages are discussed:

- Cooling load or cooling demand is the heat required to be removed from a space to maintain a certain room temperature. Cooling load varies during the day in association with ambient temperature.
- Peak-hours: hours of the highest electricity usage. Usually, summer is the peak season for electricity consumption and noon hours are the peak-hours of the day.
- Off-peak-hours: hours of the lowest electricity usage as compared to hours of the day or seasons of the year.
- Mid-peak-hours: hours at which consumption falls in between the consumption during peak-hours and the consumption during off-peak-hours.
- TES Charging: this is the mode of operation at which the TES rejects the stored heat and consequently solidifies. This mode of operation is usually conducted during off-peak-hours when electricity is abundant and cheap.

- **TES Discharging:** this is the mode of operation at which the TES absorbs the heat and consequently melts. This mode of operation is usually conducted during peak-hours when electricity is expensive and limited. Based on the design and size of the system, the discharging mode can be utilized to satisfy one of the three main strategies of operations (load/demand shifting, peak shaving or demand limiting).
- **Load/Demand shifting (full load during peak-hours):** is the operation strategy at which the TES will be designed to meet the entire cooling load during peak-hours as illustrated by (Figure 2.1). This operation strategy and design is very attractive when the price for electricity usage during peak is very high compared to Mid-peak and off-peak-hours.

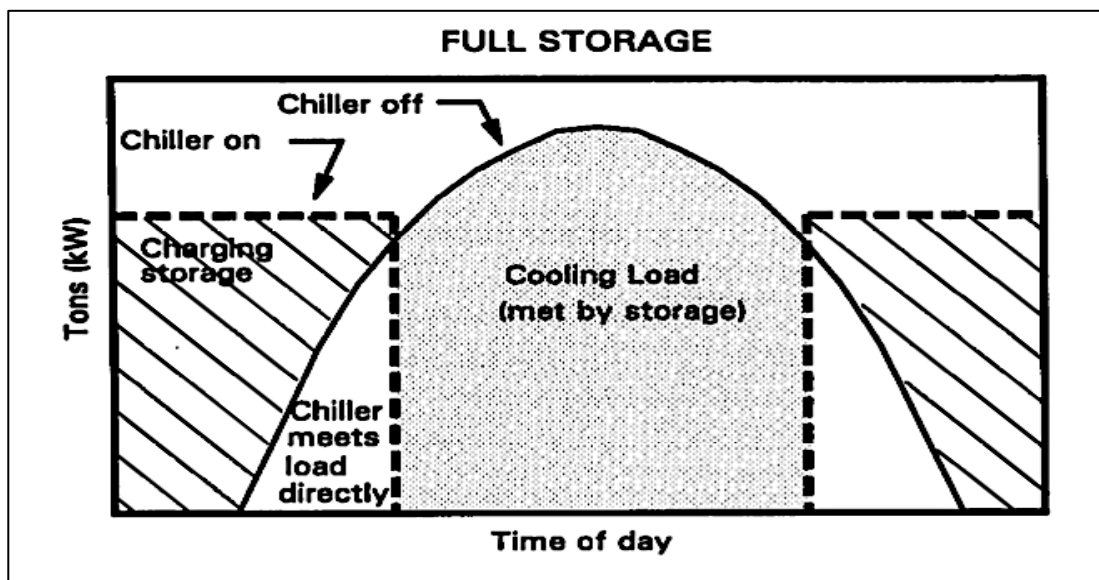


Figure 2.1: Full load/demand shift with full cooling storage, source: (USDOE Office of Energy Efficiency & Renewable Energy and Office of Federal Energy Management Programs 2000)

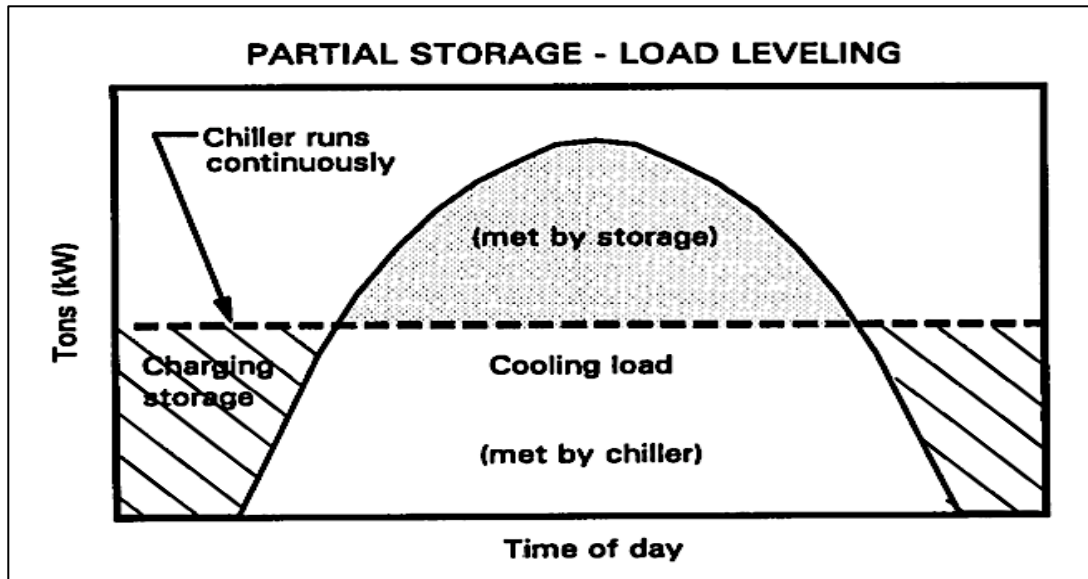


Figure 2.2: Peak shaving (Partial load during Peak-hours), source: (USDOE Office of Energy Efficiency & Renewable Energy and Office of Federal Energy Management Programs 2000)

- Peak shaving (partial storage- load limiting): is the operation strategy at which the AC is running at full capacity during the entire day while the TES meets the additional load during peak-hours as illustrated by (Figure 2.2). This operation strategy is attractive when there is a high fee for exceeding a certain maximum consumption limit during peak-hours.
- Demand limiting is the operation strategy at which the AC will be running at reduced capacity during peak-hours while the majority of the cooling load during peak-hours is met by the TES as illustrated by (Figure 2.3). This operation strategy is attractive when trying to limit electricity consumption specifically during peak-hours.

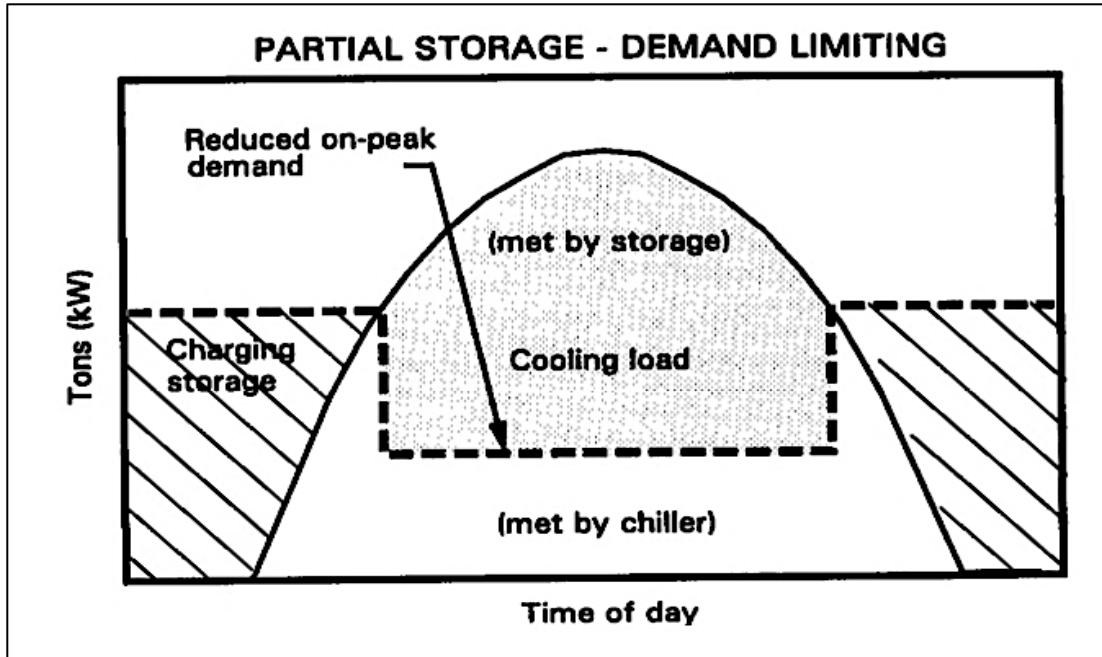


Figure 2.3: Demand/load limiting, source: (USDOE Office of Energy Efficiency & Renewable Energy and Office of Federal Energy Management Programs 2000)

2.2 Types of Thermal Energy Storage (TES) systems

Thermal energy storages employ the phenomena that materials can have a change of internal energy of and store (or reject) heat in the form of sensible heat, latent heat, thermochemical heat or a combination. (Figure 2.4) illustrates the classifications of thermal energy storages that been evaluated in the literature; with reference to (Shamseldin A. Mohamed et al. 2017).

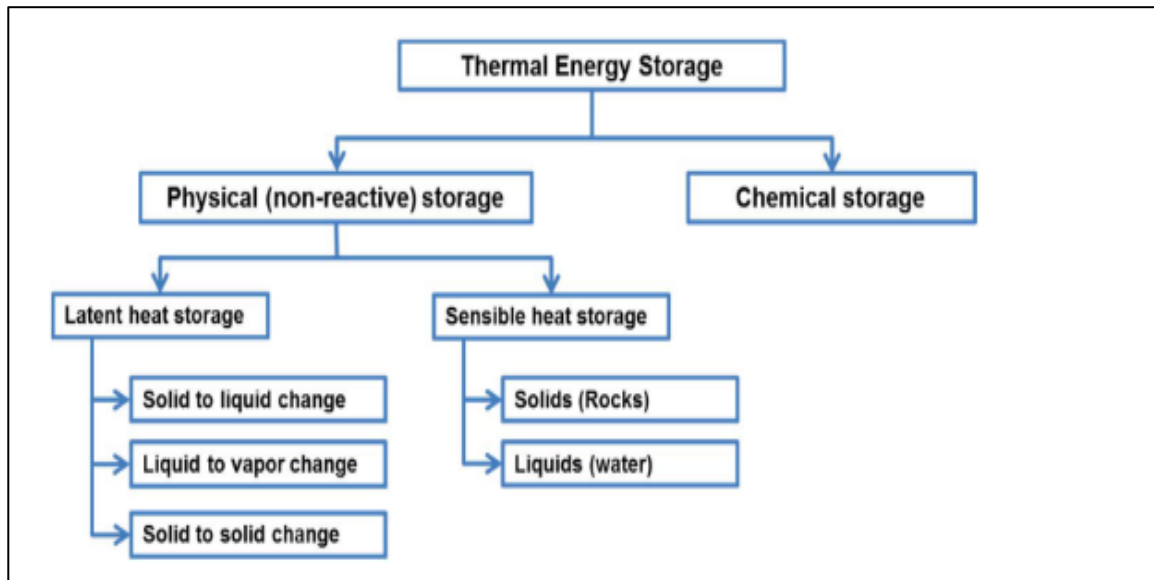


Figure 2.4: Classifications of thermal energy storages in the literature (source: (Shamseldin A. Mohamed et al. 2017))

The following bulleted list briefly describe the definition of each of the form at which TES material can have a change of internal energy while storing heat (Shamseldin A. Mohamed et al. 2017; Sharma et al. 2009; Pielichowska and Pielichowski 2014; Su, Darkwa, and Kokogiannakis 2015; Oró et al. 2012) :

- Sensible heat TES: at which TES systems store heat by raising the temperature of the material as described by equation (2.1):

$$Q = m C_p \Delta T \quad (2.1)$$

- Latent heat TES: at which storage medium material undergoes a phase change and stores heat. In this study, the focus is on solid-liquid phase change materials.

Amount of latent heat stored depend on the mass of the material and the latent heat of fusion of the material as illustrated by equation (2.2):

$$Q = \Delta m * \Delta h \quad (2.2)$$

Here, Δm is the fraction of mass melted/solidified and Δh is the latent heat of fusion of the phase change material (energy per unit mass).

- Thermochemical TES: at which the energy absorbed or released is governed by the extent of the reversible reaction that is leading to break or reform chemical bonds of the materials as illustrated by equation (2.3):

$$Q = \Delta m_{reacted} * \Delta h_{reaction} \quad (2.3)$$

Here, $\Delta m_{reacted}$ is the fraction of mass reacted and $\Delta h_{reaction}$ represents the endothermic/exothermic heat of the reversible reaction.

Latent heat storage is the category that will be discussed and evaluated in-depth in this study. Therefore, upcoming section will shed some light on some of the potential phase change materials intended for air conditioning applications.

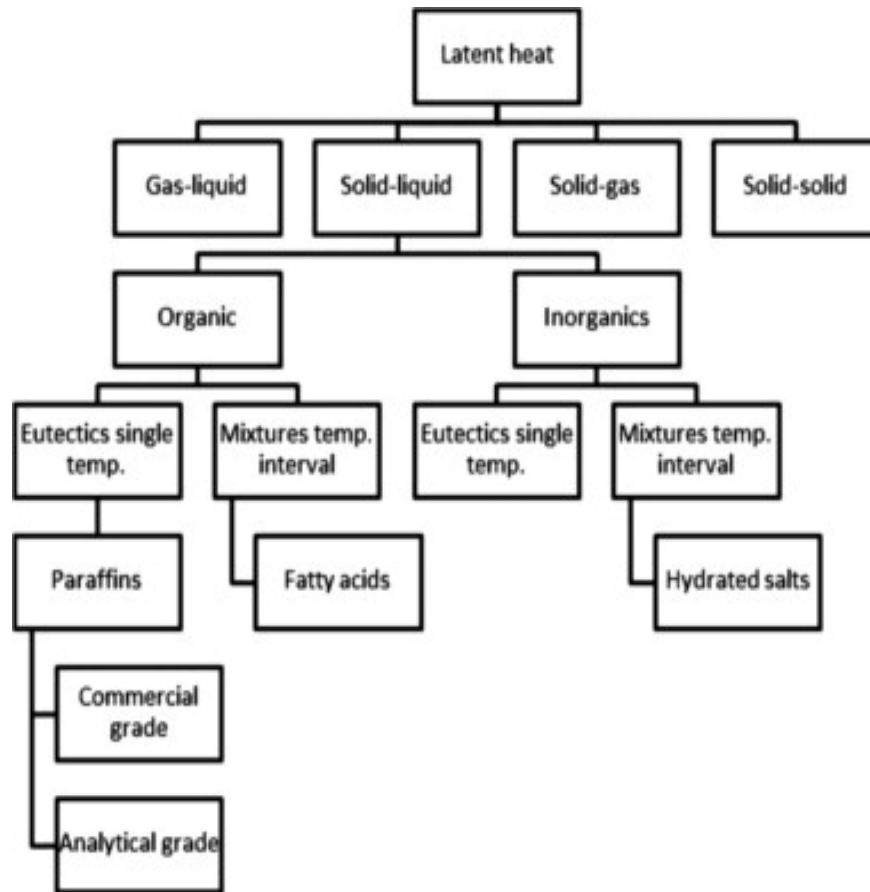


Figure 2.5: Classifications of latent storages with a focus on solid-liquid transition (source: (Iten and Liu 2014)).

With respect to storage medium, TES systems integrated with AC can be generally classified into two groups; sensible heat TES and latent heat TES.

A sensible heat TES system utilizes liquid or solids to store energy on the basis of heat capacity over a range of temperatures. A latent heat TES system, on the other hand, stores energy at the temperature of (or within a narrow band of temperatures covering) a phase transition of (solid-liquid, solid-solid, gas-liquid or solid-gas) as illustrated by (Figure 2.5). All cases of phase transition have been described by phase change materials (PCM), although in this study the focus is on solid-liquid.

Solid-liquid transitions has a wider range of materials and applications as compared to limited to variety in solid-solid phase change materials discussed by (Sarı, Biçer, and Alkan 2017; F. Wang et al. 2017; Elsayed 2015; Y. Zhou et al. 2017; Hu et al. 2014; Guldentops et al. 2018; Ababneh, Hijazin, and Jawarneh 2018; Chen et al. 2015). Moreover, solid-solid phase change's latent heat is usually smaller than solid-liquid phase change's latent heat as discussed by (Syukri, Aryadi, and Mansoori 1994).

Solid-gas phase change materials also studied (Pan and Zhao 2017; Flegkas et al. 2018; Bayon et al. 2018). However, solid-gas phase change materials necessities special vessels and mechanical equipment which lead to higher capital costs.

Liquid-gas phase change materials widely utilized for cooling process streams in oil refineries and gas plants in famous processes such as cascades refrigeration ((Yan, Chen, and Yu 2015; Sun et al. 2016; Ghorbani et al. 2018; Boyaghchi and Asgari 2017; Mohammadi and Ameri 2016; Bai, Yan, and Yu 2018; Salhi, Korichi, and Ramadan 2018; J. Wu et al. 2018; Y. Xu et al. 2015; J. Zhang and Xu 2011; Giannetti et al. 2017; Cabello et al. 2017; Jiang et al. 2017; Eini et al. 2016; Lizarte, Palacios-Lorenzo, and Marcos 2017; L. Wang et al. 2011; Megdouli et al. 2016; Cimsit, Ozturk, and Kincay 2015)) however obligates special vessels and equipment leading to higher capital costs as well.

Latent heat is much larger than sensible heat as illustrated by (Figure 2.6), so latent heat systems are typically more compact.

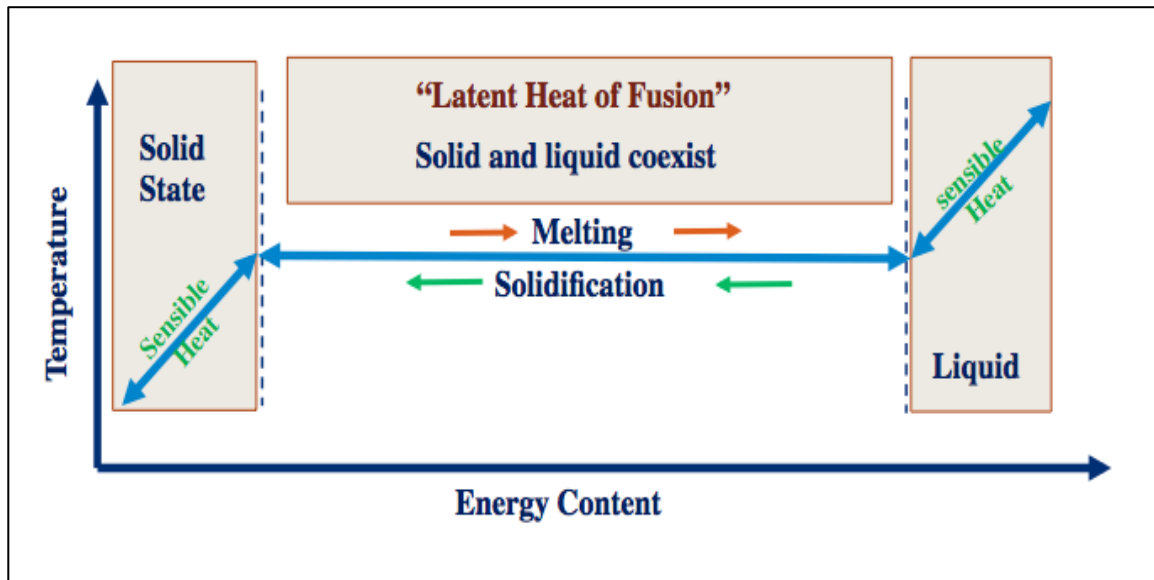


Figure 2.6: Latent heat of fusion is much larger than sensible heat.

Ice and chilled water, as examples of latent heat TES versus sensible heat TES storage mediums respectively, have been popularly used for commercial cold (TES) applications integrated into a conventional air conditioning system (Mohammed M. Farid et al. 2004; Bo, Gustafsson, and Setterwall 1999; Arteconi, Hewitt, and Polonara 2012; MacPhee and Dincer 2009; Henze et al. 2008; Yau and Rismanchi 2012; S.M. Hasnain 1998; USDOE Office of Energy Efficiency & Renewable Energy and Office of Federal Energy Management Programs 2000; Syed Mahmood Hasnain and Alabbadi 2000; Beghi et al. 2014; Habeebullah 2006).

Ice has some disadvantages such as supercooling issues, low thermal conductivity and low melting temperature (Zhai et al. 2013). Thus, need to be oversized to accommodate more of the (highly conductive) tubes to speed up the thermal response. Alternately, the vapor

compression refrigeration loop can be upsized to speed up solidification within the limited night hours. But this partially negates the purpose of integrating TES and reduces the overall operating efficiency of the ice-TES by 30% - 40% (Zhai et al. 2013). Clearly, neither oversizing refrigeration loop that cools the ice-TES system nor using extremely large number of highly conductive tubes is a cost-effective solution.

Chilled water TES, on the other hand, is a very mature system to divert electricity consumption from day to night (Yau and Rismanchi 2012). Given the relatively low thermal capacity of sensible heat (compared to latent heat), chilled water systems need very large equipment sizing to operate efficiently (Yau and Rismanchi 2012). They are only economical for very large loads – typically 7000 kWh or higher (S.M. Hasnain 1998).

2.3 Potential Phase Change Materials for cold TES systems

In light of the aforementioned deficiencies with ice and chilled water TES systems (as discussed in section 2.2), a wide variety of phase change materials (PCMs) evaluated in the literature (Himran, Aryadi, and Mansoori 1994; He and Setterwall 2002; Bo, Gustafsson, and Setterwall 1999; Mohammed M. Farid et al. 2004; Akif et al. 2010; Al-abidi et al. 2012; Rutberg et al. 2013; Akgu and Kaygusuz 2008; Kahwaji et al. 2016; Su, Darkwa, and Kokogiannakis 2015; Ukrainczyk, Kurajica, and Š 2010; Syukri, Aryadi, and Mansoori 1994; Pomianowski, Heiselberg, and Zhang 2013; Beghi et al. 2014) possess certain strengths and weaknesses depending on the intended application. However, only a few of the PCMs are feasible candidates for cold latent heat TES storages. For air conditioning applications the optimum melting temperature of a PCM should be in the

range of 5-10 °C and the latent heat and thermal conductivities should be large. PCMs need to be chemically stable, uniform during melting/solidification (i.e., producing no phase segregation), non-toxic, non-corrosive, and readily available at low cost (Himran, Aryadi, and Mansoori 1994; He and Setterwall 2002; Bo, Gustafsson, and Setterwall 1999; Mohammed M. Farid et al. 2004; Oró et al. 2012; Mehling and Cabeza 2008; Sharma et al. 2009; Shamseldin A. Mohamed et al. 2017).

As illustrated by (Figure 2.7), phase change materials can be classified into three main families (organic, inorganic and eutectic).

Among the organic materials- paraffin family, n-Tetradecane ($C_{14}H_{30}$) and n-Hexadecane ($C_{16}H_{34}$) are the most appropriate paraffin waxes for cold storage applications (Himran, Aryadi, and Mansoori 1994; Kousksou et al. 2010; He, Martin, and Setterwall 2003; Choi, Cho, and Lorsch 1992). $C_{14}H_{30}$ has a melting temperature of 5.8 °C and a theoretical latent heat value of 227 kJ/kg, while n-hexadecane has a higher latent heat value (236 kJ/kg) and a higher melting point of 18.1 °C (Syukri, Aryadi, and Mansoori 1994; Bo, Gustafsson, and Setterwall 1999). The melting point of n-Tetradecane ($C_{14}H_{30}$) lies within the advantageous range of 5-10 °C, making it the more suitable choice for a cold TES application.

Among the organic materials- non-paraffin family, fatty acids are widely evaluated. Fatty acids expose good material properties such as (no supercooling issues, good latent heat, chemical stability and self-nucleating) as discussed by (Fang et al. 2010; Silakhori et al. 2014; Roxas-dimaano and Watanabe 2002; Sari 2003). However, the melting points of most fatty acids are higher than the suitable range for air cooling applications while the latent heat of the material is not very high (<150 kJ/kg) when compared to other PCMs

(Roxas-dimaano and Watanabe 2002). Another major drawback for fatty acids is the high cost of preparations of fatty acids that is 2-3 times the cost preparations of commercial paraffin materials (Sharma et al. 2009). Fatty acids are also being evaluated as shape stabilizers phase change materials and not as the main phase change material, as discussed by (Fang et al. 2010; Silakhori et al. 2014).

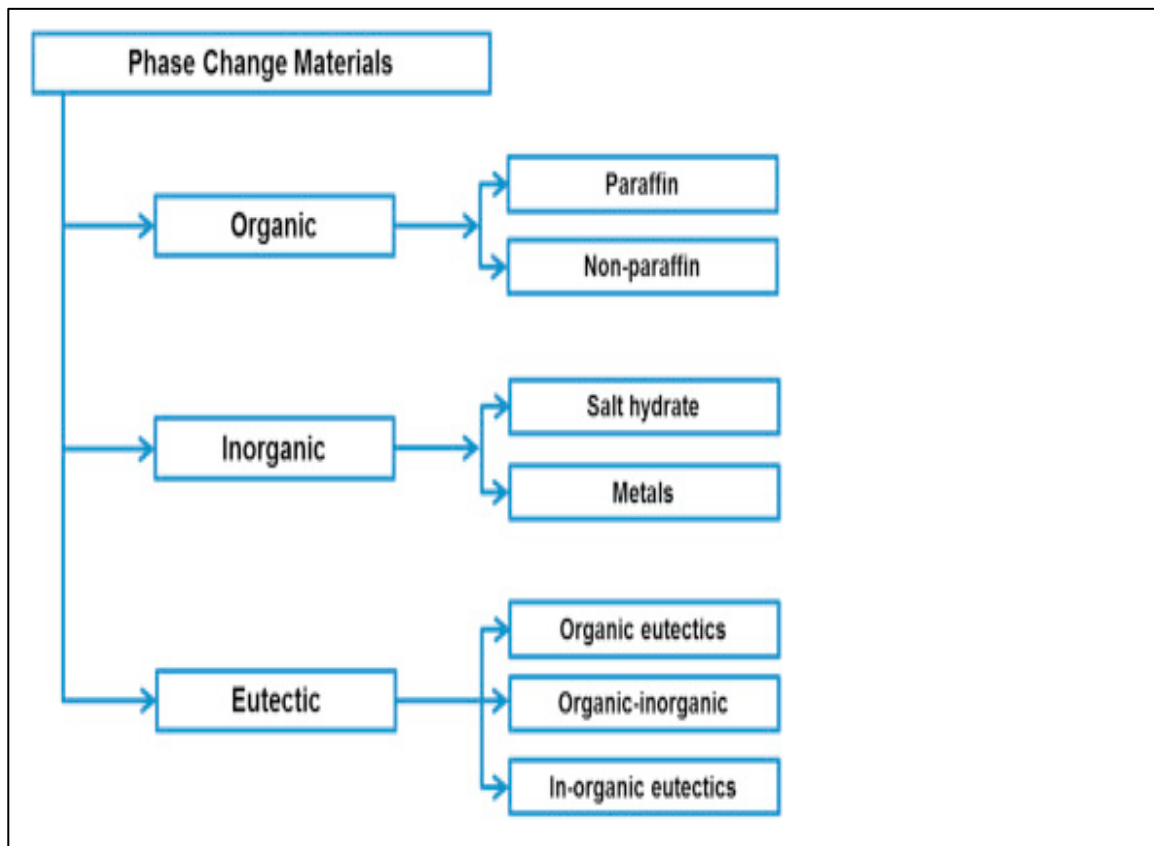


Figure 2.7: Classifications of phase change materials evaluated in the literature, source: with reference to (Shamseldin A. Mohamed et al. 2017)

Among the variety of inorganic materials, hydrated salts were assessed as highly potential storage medium material for thermal energy storage because of its abundance availability, good energy density (>200 kJ/kg) and cheap cost (Vasu et al. 2017; Chiu 2011; Solé et al.

2015; Shamseldin A. Mohamed et al. 2017; Kenisarin and Mahkamov 2016; Arai et al. 2018; Y. Wu and Wang 2015; Y. Liu and Yang 2018; Ye et al. 2017; Donkers et al. 2017; Trausel, De Jong, and Cuypers 2014). But most hydrated salts addressed in the literature are for heat storages, not cold storages. The hydrates salts with properties that fit cold storage criteria (a melting temperature between 5-10 deg C) are very limited as discussed by (Kenisarin and Mahkamov 2016). However, there some disadvantages with the limited list of available hydrated salts that are still pending major breakthroughs, such as low thermal conductivity, phase segregation, sub-cooling issues and corrosion (Guillot et al. 2012; Vasu et al. 2017; Shamseldin A. Mohamed et al. 2017; Solé et al. 2015; Chiu 2011; Mohammed M. Farid et al. 2004; S.A. Mohamed et al. 2017; García-Romero et al. 2012). Thicking agents were proposed to reduce phase segregation issues, however it is proved to reduce thermal conductivity (Mohammed M. Farid et al. 2004; García-Romero et al. 2012). Furthermore, the use nucleating agent could help to minimize supercooling issues with the help of thickening agent while negatively impacting energy density (Luisa F Cabeza et al. 2003). With reference to (Solé et al. 2015) “*Also, another big drawback is corrosion due to that a big part of TCM under research for building applications is solid salt hydrates reacting with water vapor*”.

The other family group that is being widely addressed in the literature is eutectic phase change material family (Efimova et al. 2014a; Kenisarin and Mahkamov 2016; Y. Liu and Yang 2017; Tang et al. 2016; Shamseldin A. Mohamed et al. 2017). Eutectic materials melt/freeze at a single temperature. Therefore, they do not segregate during phase change. That is a major advantage of eutectic materials. In addition to that, they have acceptable latent heat and thermal stability. Major drawback is nearly all of the eutectic materials are

suitable for high/medium temperature thermal energy storages and not for air conditioning applications (Shamseldin A. Mohamed et al. 2017). The lowest melting temperature of eutectics materials in recently published articles is around 18-21 °C as discussed by (Efimova et al. 2014b), which does not provide adequate driving force for heat exchange in air conditioning applications.

To characterize thermal behaviors of phase change materials, researches use special lab analysis devices such as Differential Scanning Calorimetry (DSC). Using a DSC, the phase transformation can be studied and vital information regarding melting temperature or melting range and associated latent heat quantities can be experimentally measured (Kousksou et al. 2010; He, Martin, and Setterwall 2003; Choi, Cho, and Lorsch 1992). This vital information is important to quantify how much the phase change material (PCM) can store energy in a certain mass of the PCM. It is also equally important to confirm that PCM material is melting at the specific range of temperatures that meets the intended purpose of the application. As it is well known, the phase change can occur at a single temperature or a range of temperatures depending on the nature of the materials. For example, research groups such as (Kousksou et al. 2010; He, Martin, and Setterwall 2003; Choi, Cho, and Lorsch 1992; Z. Zhang et al. 2012) studied the latent heat and melting temperature of organic- paraffin phase change materials (such as n-Tetradecane (C₁₄H₃₀) and n-Hexadecane (C₁₆H₃₄)). As discussed by (Aljehani et al. 2018), n-Tetradecane (C₁₄H₃₀) is the most appropriate paraffin for cold storage applications. C₁₄H₃₀ has a melting temperature range of 4-6 °C and a theoretical latent heat value of approximately 220 kJ/kg.

The research by (Kousksou et al. 2010) studied the melting temperature range of binary system of Tetradecane-Hexadecane using experimental and numerical technics. Different mixtures were studied and analyzed using various concentration ratios of Tetradecane and Hexadecane paraffin. The research work by (Kousksou et al. 2010) concluded that such mixtures will always have a melting range. They also found that the experimentally measured melting range depends on the mixture composition and the DSC heating rate. Likewise, the authors of (He, Martin, and Setterwall 2003) performed several phase equilibrium studies on the binary mixture of Tetradecane and Hexadecane paraffin for comfort cooling applications. They also found such paraffin has a melting and freezing range depending on the mixture concentration and the heating or freezing ramping rate settings of the DSC.

Moreover, the research work by (Choi, Cho, and Lorsch 1992) performed several analysis to characterize the thermal behavior of commercial and laboratory grades of Tetradecane and Hexadecane paraffin versus literature data. The analysis revealed that melting temperature range and fusion energy of laboratory grade is in good agreement with data in the literature. The commercial grade temperature range and fusion energy were 10% lower than data in the literature.

The work by (Z. Zhang et al. 2012) indicated the melting temperature range of a microstructure composite (containing paraffin and expanded graphite), measured by a DSC, is very close to the melting temperature range of the paraffin alone.

Other groups have analyzed many various samples from the inorganic PCM family- commonly known as hydrated salts. Accordingly, the analysis by (Y. Wu and Wang 2015;

Kenisarin and Mahkamov 2016) revealed phase segregation and sub-cooling issues in the hydrated salts/expanded graphite composite as shown by the DSC measurement.

It is worth mentioning that, the widely available paraffin samples are petroleum-based phase change materials (driven from petroleum products). On the other hand, bio-based phase change materials are available and driven from agricultural sources. Bio-based PCMs have similar characteristics to petroleum-based PCMs, measured and analyzed using the DSC device (Yu et al. 2014; Basturk and Kahraman 2016; Jeong et al. 2013, 2014; Kang et al. 2015). Apart from thermo-physical properties, availability and cost would be key factors that govern the selection between PCM driven from petroleum and the PCMs driven from agricultural sources.

Another important aspect is the ability of PCM to rapidly transfer heat is equally important to the capability of the PCM material to store a large amount of heat within a small volume. Therefore, the measurement of thermal conductivity and thermal diffusivity is fundamental.

It is worth mentioning, most of the PCMs alone have low thermal conductivity. Therefore, many researchers investigated and enhanced thermal conductivity and heat transfer rate of paraffin waxes with various additives/insertions (L. Liu et al. 2016; Ibrahim et al. 2017) such as alumina (Al_2O_3) (Arasu, Sasmito, and Mujumdar 2013), metallic matrix (Zalba et al. 2003; Khateeb et al. 2004), carbon fibers in random or in specific orientations (Fukai et al. 2002, 2000) graphite flakes (Lachheb et al. 2014) or graphite powders (Pincemin et al. 2008). Other groups proposed using a porous graphite matrix (Zalba et al. 2004; L.F. Cabeza et al. 2002; Z. Zhang et al. 2012). Others, investigated various geometries and

multiple PCMs to enhance heat transfer rate (Kurnia et al. 2013). These additives and insertions provided a considerable improvement for thermal conductivity and heat transfer rate, but some do not provide the required mechanical strength. Also, the paraffin leaked during and after the phase change from solid to liquid state. Leakage problem is being addressed by encapsulation as discussed by (Zalba et al. 2003; Mohammed M. Farid et al. 2004; Zalba et al. 2004), however most of these encapsulation techniques are not cheap. Thermal conductivity enhancement concepts and designs were not only limited to paraffin, it was also extended to hydrated salts (Y. Wu and Wang 2015; J. Liu et al. 2018; X. Zhang et al. 2018) and bio-based (Jeong et al. 2013; Basturk and Kahraman 2016; Yu et al. 2014) phase change materials.

2.4 Proposed Phase Change Composite (PCC)

As stated above, traditional thermal energy storage systems for building cooling, such as ice and chilled water are limited by low efficiency, slow response time (due to its low thermal conductivity) and necessity of large equipment sizing. Composite microstructure can significantly enhance the properties of thermal conductivity and/or uniformity. Such materials are called phase change composite (PCC) materials or composite phase change (CPC) materials; the former term will be employed in this study.

This present study utilizes a PCC material consisting of about 78% low-temperature paraffin (n-Tetradecane, $C_{14}H_{30}$) and 22% expanded graphite. The paraffin is described by (He and Setterwall 2002) as “*saturated hydrocarbon mixtures and normally consist of a mixture of mostly straight chain n-alkanes, $CH_3-(CH_2)_n-CH_3$* ”. The paraffin has several

advantages: chemical stability, tunable melting point/range based upon composition, uniform melting/solidification (producing no phase segregation), and also absence of toxicity, corrosivity and supercooling issues (Razack et al. 2016; He and Setterwall 2002; Bo, Gustafsson, and Setterwall 1999; Mohammed M. Farid et al. 2004; D. Zhou, Zhao, and Tian 2012).

As mentioned earlier, the paraffin ‘alone’ has low thermal conductivity. Therefore, the proposed PCC material in this present work utilizes the procedure of impregnating paraffin into a graphite porous structure. The graphite porous structure boosts thermal conductivity, prevents the paraffin leak; since paraffin molecules are actually entrapped within the graphite matrix porous and attracted by capillary while conforming to mechanical strength requirement (Mills et al. 2006; Razack et al. 2016; L.F. Cabeza et al. 2002; D. Zhou, Zhao, and Tian 2012). Capillary forces between the paraffin and graphite are still strong even after the PCM melts and changes phase to liquid state (Mills et al. 2006; Py, Olives, and Mauran 2001).

The proposed PCC material described in this study can achieve a thermal conductivity of approximately 22 W/m-K (approximately ten times the thermal conductivity of ice) due to the presence of expanded graphite three-dimensional structure (Mills et al. 2006; Razack et al. 2016; L.F. Cabeza et al. 2002; D. Zhou, Zhao, and Tian 2012). The three-dimensional structure of expanded graphite in previous studies was impregnated with a (high) melting point temperature paraffin to present a passive thermal management system for a Lithium-ion battery pack. On the other hand, in this present study a different type of paraffin with a (low) melting temperature (namely n-Tetradecane, $C_{14}H_{30}$) is impregnated into the three-

dimensional structure of compressed expanded graphite to serve as a different purpose being a thermal energy storage medium for air conditioning applications.

The use of this proposed PCC material in air conditioning applications is an important aspect of this investigation because it has many added advantages compared to ice or chilled water (i.e. faster heat transfer rate across the material, faster heat exchange rate with the heat transfer fluid, very low thermal gradients and uniform melting/solidification rates). The proposed PCC materials adequately coincide to the cold storage requirement of having a melting temperature that falls within the 5-10 degrees Celsius that matches the chiller operating temperature of an air conditioning system.

To our knowledge, the applications of this proposed phase change composite material for air conditioning has not been reported in the literature. In addition, the high phase transition temperature of the proposed PCC (compared to ice) increases efficiency and optimizes control strategies, which could enable a more flexible and resilient electric grid. The proposed system in the current study, an air conditioner with an integrated high-conductivity, phase change composite (PCC), can serve as a flexible resource to shave/shift on-peak air conditioning load, reduce compressor size and cycling, improve efficiency, and dynamically charge or discharge in response to expected grid operating levels.

2.5 Theoretical foundations

Characterization of the heat transfer processes during melting or freezing of phase change materials is significant to the design of the system. Mathematical modeling of melting and freezing processes involves dealing with the moving interphase boundary.

The mathematical formulation describing the melting and freezing processes is scientifically known as the “classical Stefan problem” and named after the Slovene physicist Josef Stefan. The classical Stefan problem is a well-recognized scientific research work concerning the solid-liquid phase changes performed by Josef Stefan and published between the years of 1889 to 1891 (Sarler 1995; Vuik 1984; Font 2014).

The history of the classical Stefan problem is described by (Vuik 1984) *“In 1889 Stefan had written four papers on free boundary problems. The paper on ice formation in the polar seas was reprinted in 1891 and has drawn the most attention of the scientific community”*.

As described by (Sarler 1995; Vuik 1984) the classical Stefan problem studied the freezing behavior of a seawater quantity, a material that may exist in either solid or liquid phase. A moving boundary surface during the solid to liquid phase transition (or vice versa) is generated between the two states of the matter. The seawater is initially at liquid state. The temperature of the air adjacent to the surface of the seawater is dropped to a temperature below the freezing temperature of the seawater. Accordingly, a solid layer of seawater is formed at the interface between air and seawater. The solid layer formed grows with time as illustrated by (Figure 2.8).

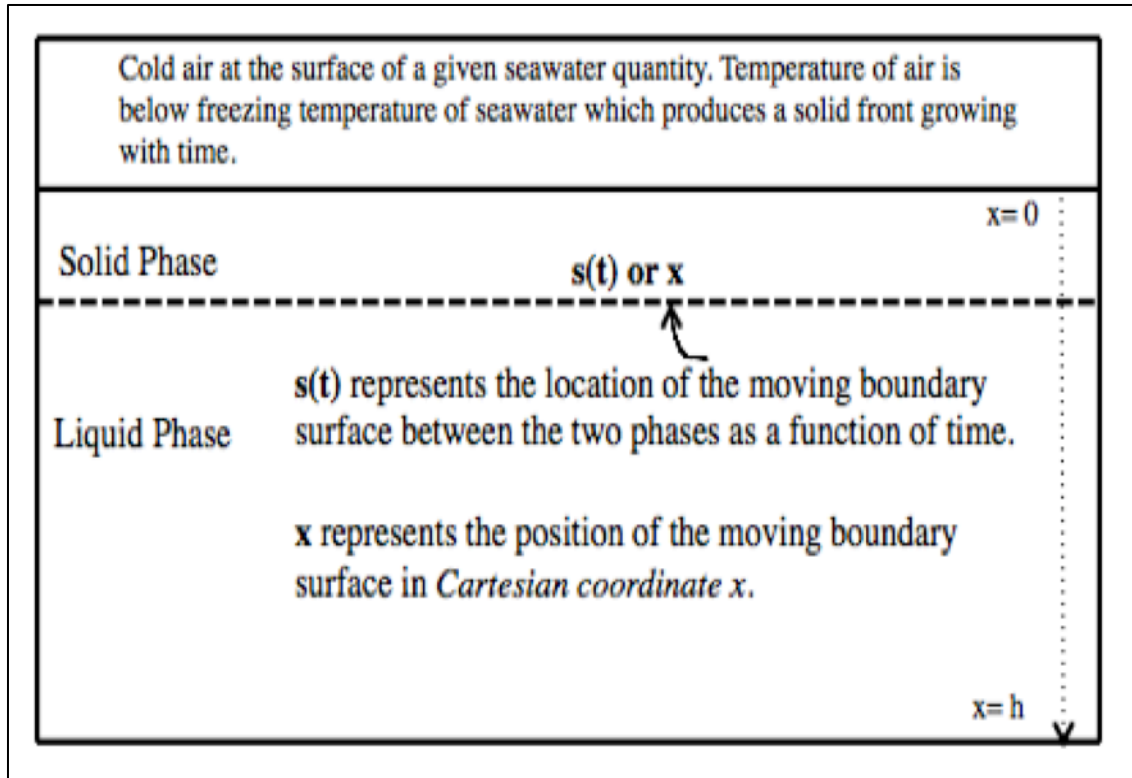


Figure 2.8: Classical Stefan problem Concept in association with freezing of seawater material

Stefan calculated the thickness (h) of the solid layer within time (t). Stefan found out that the ice layer is progressing in proportion with the square root of time (Sarler 1995; Vuik 1984). In honor of his work, the dimensionless number describing the ratio of sensible to latent heat is known as the Stefan number.

According to (Sarler 1995), preceding Stefan the solid-liquid phase change concept was demystified by pioneers such as Joseph Blake, Joseph Fourier, Lamé and Clapeyron, and Neumann. Between 1758 and 1762, Joseph Blake was the first to introduce the concept of latent heat. In 1822, Joseph Fourier provided the necessary physics and mathematics to address heat conduction. In 1831, Lamé and Clapeyron presented work classified as an extension to Joseph Fourier's work on heat conduction. They were the first to analytically

incorporate latent heat into heat conduction equation. They studied phase change transformation of the Earth's crust cooling down from an initially molten state. They found that the relation between the growing crust and time. In an unpublished series of lectures during the early 1860, Neumann provided a detailed solution for the problem addressed by Lamé and Clapeyron with the initial temperature being higher than the melting temperature.

The work by the early pioneers paved the way for the current understanding of the solid-liquid phase change concept. In recognition of the exact solution by Neumann to the problem posed by Lamé and Clapeyron, this solution of the classical Stefan problem is commonly known as the Neumann solution. Mathematical modeling, both analytical and numerical, of the melting and solidification behaviors of phase change materials is widely addressed in the literature.

However, the heat transfer problem addressed by this thesis work is not quite similar to the classical Stefan problem. In particular, in the heat transfer problem presented in this thesis, external energy source is actually distributed within the phase change material volume; not only introduced to the outside surface of the material like what is been discussed by the classical Stefan problem.

In 2003, the article by (Kostenko, Pribis, and Puzynin 2003) was introduced. The work by (Kostenko et al) discussed a special case of the classical Stefan problem at which the heat source is distributed within the phase change medium not only exposed to the outside surface (as the Stefan problem was set up).

Both mathematical formulations by Stefan and Kostenko et al. accounted for the phase change at a single temperature. On the other hand, the heat source in the heat transfer problem discussed in this present thesis is distributed within the phase change composite (PCC) material; similar in a way to the work by (Kostenko et al. 2003).

Moreover, this present thesis study accounts for phase change over a range of temperatures in light of the physical characteristics of the proposed PCC materials; unlike the heat transfer presented by Stefan and (Kostenko et al. 2003) that accounted for the phase change at a single temperature.

Therefore, this present thesis incorporated the effective specific heat method, with reference to (Khateeb et al. 2005), into the equation developed by (Kostenko et al) and adequately accounted for a phase change material that transforms over a melting range. The effective heat capacity method takes into account the latent heat of a phase change material (PCM) as introduced by academically distinguished research work by (Mohammed Mehdi Farid, Hamad, and Abu-Arabi 1998) which studied using dimethyl-sulfoxide as a phase change material (PCM) in a rectangular enclosure.

The work introduced by Kostenko et al (Kostenko, Pribis, and Puzynin 2003) stated “*we claim that the celebrated Stefan condition on the moving interphase, accepted in mathematical physics, cannot be imposed if energy sources are spatially distributed in the volume. A method based on Tikhonov and Samarskii ideas for numerical solution of the problem is developed*”. The final equation by Kostenko et al (Kostenko, Pribis, and Puzynin 2003) is equating the heat absorbed with the heat rejected from the heat source.

As introduced by Kostenko et al (Kostenko, Pribis, and Puzynin 2003), the classical Stefan problem had the two conditions (1) & (2), represented by equations (2.4) and (2.5) respectively as follow:

Condition (1):

$$K_{sol} \frac{\partial T (xs + 0, t)}{\partial x} - K_{liq} \frac{\partial T (xs - 0, t)}{\partial x} = L \rho_{sol} V_s ; \quad (2.4)$$

Reference (Kostenko, Pribis, and Puzynin 2003)

Condition (2):

$$T|_s = T^* ; \quad (2.5)$$

Reference (Kostenko, Pribis, and Puzynin 2003)

In condition (1)- represented by equation (2.4), as discussed by Kostenko et al (Kostenko, Pribis, and Puzynin 2003), left-hand side of the equation describes the heat flux per unit area over time in accordance with Fourier law. Heat flux is proportional to temperature gradient and material thermal conductivity. Right side of condition (1)- represented by equation (2.4), as discussed Kostenko et al (Kostenko, Pribis, and Puzynin 2003), takes into account latent heat (L) and density (ρ_{sol}) of phase change material in addition to velocity (V_s) of moving boundary. Condition (2)- represented by equation (2.5), as discussed by Kostenko et al (Kostenko, Pribis, and Puzynin 2003), illustrates temperature continuity where temperature at the surface, between the two phases of solid and liquid, equals the temperature of the phase transition. Kostenko et al (Kostenko, Pribis, and Puzynin 2003) discussed that the external heat source is not distributed within the volume

while $q(x,t)$ is eliminated in the conservation of energy equation presented by the classical Stefan problem.

Furthermore, as illustrated by Kostenko et al (Kostenko, Pribis, and Puzynin 2003), the method by [Tikhonov and Samarskii] formulated the conservation of energy equation illustrated by equation (2.6). Where, $L \delta(T - T^*) \partial T / \partial t$ and $\rho C \partial T / \partial t$ represent the heat added because of the phase transformation (latent heat of fusion) and the sensible heat stored respectively. Here, L is the latent heat of fusion, C is the specific heat and ρ is the density. On the other hand, $v \text{ grad } T$ represents the heat transported due to convection of molten material.

$$(\rho C + L \delta(T - T^*)) \left(\frac{\partial T}{\partial t} + v \text{ grad } T \right) = \text{div} (K \text{ grad } T) + q(x, t) \quad (2.6);$$

reference (Kostenko, Pribis, and Puzynin 2003)

The work by Kostenko et al (Kostenko, Pribis, and Puzynin 2003) proved that equation (2.6) may provide a better description of the case where the external heat is distributed within the phase change material's volume at which conditions (1) and (2) -- represented by equation (2.4) and (2.5) respectively-- are not applicable. Furthermore, the heat transported due to convection of molten material (illustrated by $v \text{ grad } T$) was ignored by (Kostenko, Pribis, and Puzynin 2003) to simplify the problem. Moreover, Kostenko et al (Kostenko, Pribis, and Puzynin 2003) assumed flux uniformity in the x-direction. Therefore, the term $q(x, t)$ became $q(t)$. So equation (3) becomes equation (2.7) in the method formulated by Kostenko et al:

$$(\rho C + L \delta (T - T^*)) \left(\frac{\partial T}{\partial t} \right) = q(t) \quad (2.7);$$

reference (Kostenko, Pribis, and Puzynin 2003)

Equation (2.7) in simple words is equating the heat absorbed, because of the phase transformation (latent heat of fusion) and the sensible heat stored, with the heat rejected from the heat source.

Another way to describe equation (2.7) will be equation (2.8) and employing the effective specific heat method, to adequately account for a phase change material that transforms over a melting range:

$$[\rho V C_{p_{eff}}] \frac{\partial T}{\partial t} = q(t) \quad (2.8)$$

Here, ρ is the density and V is the volume of the phase change material. $C_{p_{eff}}$ is the effective specific heat of the phase change material; which can be defined along the temperature profile with the equations (2.9-2.12) with reference to (Khateeb et al. 2005):

$$C_{p_{eff}} = C_{p_s}, \quad \text{if } T < T_s \quad (2.9);$$

reference (Khateeb et al. 2005)

$$C_{p_{eff}} = C_{p_s} + \frac{\Delta H (T - T_s)}{(T_m - T_s)^2}, \quad \text{if } T_s \leq T \leq T_m \quad (2.10);$$

reference, (Khateeb et al. 2005)

$$Cp_{eff} = Cp_s + \frac{\Delta H (2T_m - T - T_s)}{(T_m - T_s)^2}, \quad \text{if } T_m < T \leq T_l \quad (2.11);$$

reference, (Khateeb et al. 2005)

$$Cp_{eff} = Cp_l, \quad \text{if } T > T_l \quad (2.12);$$

reference, (Khateeb et al. 2005)

Here, (Cp_s) is the specific heat for the phase change material at solid phase, (Cp_l) is the specific heat for the phase change material at liquid phase, (ΔH) is the latent heat of the phase change material or in other words the energy content per mass of the phase change material, (T_s) is the temperature at which (and below which) the PCC material is completely solid. (T_l) is the temperature at which (and above which) the PCC material is completely liquid. (T_m) is a middle temperature between (T_s) and (T_l) during the phase change.

To obtain an analytical solution of the Stefan problem, the equation needs to be simplified. One common simplification is to evaluate the temperature gradient in one phase only and assume the other phase to be at the phase change temperature. This is called one-phase Stefan problem. A similarity solution of the Stefan problem is described by (Cengel and Ghajar 2011; Martinez 2014). In the approach by (Cengel and Ghajar 2011; Martinez 2014), space and time variables are combined into one variable (for example, a variable describing the relationship between the time and growing thickness as found by (Stefan, Lamé, Clapeyron and Neumann) to reduce the PDE to an ODE. Simplifications can

typically be applied only to specific cases, which idealize or approximate the physical situation. For the general case, involving complicated geometries or thermophysical properties that depend on temperature or time, numerical methods are required: finite differences, finite elements, boundary elements or the control volume method. Numerical formulations can be implemented using programming languages such as Fortran and Matlab. In numerical methods the goal is to approximate the true solution with some discretization of the continuous domain.

2.6 Research goals with respect to conceptual framework

In light of aforementioned, the ultimate goal of this study is to propose a hybrid [AC + (PCC-TES)] system design with strong potential for: leveling cooling demand between day and night, reducing AC compressor size and consequently electricity consumed, reducing demand, off-loading power plants, reduce obligation for peaker plants during peak-hours, reducing CO₂ emission as a result of reducing electricity consumed, savings in cost of electricity for electricity consumers, improving AC's coefficient of performance (COP). While, the proposed PCC material shall expose great materials strengths such as: high thermal conductivity, high latent heat, high thermal stability, acceptable mechanical strength, and low evaporation rate.

This dissertation thoroughly addresses proof of concept evaluation, material characterizations, process simulation and validation, numerical modeling of transient heat transfer and validation, and finally a case study of real-life implementation.

CHAPTER 3: PCC MATERIAL CHARACTERIZATION

The work illustrated in this chapter of the dissertation will be soon submitted for peer review publication in the Journal of energy and conversion management.

3.1 Materials and preparations

As introduced, the phase change composite (PCC) material presented in this study precisely consists of 78% low-temperature paraffin (alkane), namely n-Tetradecane, and 22% of compressed expanded graphite. To our knowledge, the applications of this specific PCC as a cold thermal energy storage (TES) for air conditioning has not been reported in the literature.

Both components of the proposed PCC are commercially available from local US and international suppliers. The first component of the PCC is n-Tetradecane (C₁₄H₃₀) which is a phase change material and a member of the organic paraffin family. It has been extensively explored in the literature as a potential storage medium for thermal management and cold thermal energy storage (TES) applications. In light of particular interest in passive comfort cooling applications, a predetermined list of properties of interest of various samples of n-Tetradecane (C₁₄H₃₀), were examined, benchmarked and analyzed. It is worth mentioning that, n-Tetradecane is a petroleum by-product and has very suitable properties for cooling applications. The melting temperature range of n-Tetradecane precisely falls within the optimum melting temperature range for air conditioning applications. It has a large theoretical latent heat of approximately 227 kJ/kg suitable for thermal storage applications and it is chemically stable with uniform melting and solidification behaviors. Also, n-Tetradecane has the capability to store and release a

large amount of thermal heat when changing phase between solid and liquid states. In parallel to organic paraffin, bio-based PCMs are also introduced, which have similar characteristics to petroleum driven n-Tetradecane while driven from natural plant oils and animal fat.

The second component of the PCC is the compressed expanded graphite which serves as the porous structure that holds the paraffin, boosts the thermal conductivity and provides required mechanical strength. The expanded graphite is commercially available. The preparation of expanded graphite from graphite flake is described by (Mills et al. 2006) as follows: “Expanded graphite is easily produced from flake graphite. Flake graphite is characterized by stacked sheets of carbon, where the carbon making up the sheet is held together by strong covalent bonds and the stacked sheets are held together by weak van der Waals bonds. In reactions with various acids, the weak bonds are overcome, and molecules of the reactant are incorporated between the layers of the graphite. The graphite structure has to expand to accommodate the reactant molecules, but the sheet structure remains intact”. Then, expanded graphite is compacted to required density (150-200 g/l) to prepare the compressed expanded graphite porous matrix structure using a piston machine and specially designed molds. Approximately 40-50 psi pressure is applied to compact the expanded graphite to the required density. It is worth mentioning that as the density of the graphite structure increases the graphite porosity decreases while thermal conductivity increases. On the other hand, as the density of the graphite structure decreases the porosity increases while thermal conductivity decreases. As the porosity increases the possibility to accommodate more phase change material increases and hence the latent heat capacity of the structure increases and vice versa. The compressed expanded graphite structure is then

soaked into a liquid bath of phase change material or namely n-Tetradecane, for at least 24 hours, until the graphite structure is impregnated (saturated) with n-Tetradecane forming the proposed phase change composite material (PCC). Therefore, compressed expanded graphite acts as the structure that holds the low-temperature paraffin within its porous structure, boosts the thermal conductivity of the overall phase change composite material (PCC) and further prevents the low-temperature paraffin from leaking. Due to capillary forces and surface tension, n-Tetradecane molecules are actually stay entrapped within the compressed expanded graphite porous matrix and do not leak. Capillary forces between the paraffin and graphite are still strong even after the PCM melts and changes phase to the liquid state (Mills et al. 2006; Py, Olives, and Mauran 2001).

3.2 Matrix of experiments

Table 3.1 illustrates the PCC material characterization's matrix of experiments. Compressed expanded graphite and n-Tetradecane were analyzed and certain properties of interest were examined. The PCC characterization was conducted in five stages as illustrated by Table 1. On stage one, identical testing procedures were performed on multiple PCM samples obtained from multiple local and international suppliers. All petroleum (n-Tetradecane)/bio-PCM samples were analyzed with respect to a set of properties of interest such as latent heat (kJ/kg), melting temperature (degree Celsius), graphite impregnation ratio (%) and finally evaporation rates from impregnated graphite samples in (microgram/m².s) at ambient conditions as illustrated in stage one of Table 1.

On stages two through five, samples of compressed expanded graphite impregnated with n-Tetradecane (C₁₄H₃₀), were examined and analyzed using DSC (Differential Scanning

Calorimetry) for latent heat and melting temperature analysis, DXF-200 laser flash analyzer for thermal diffusivity and thermal conductivity analysis, SEM (Scanning Electron Microscope) for surface morphologies analysis, XRD (X-ray diffraction) for crystal structure analysis and UTM (Universal Testing Machine) for mechanical strength testing as illustrated in stages two through five of the matrix of experiments summarized by Table 3.1

Table 3.1: Matrix of experiments for PCC material characterization

Stage	Characterization type	Testing Device
One	Latent heat, melting range, graphite impregnation, and evaporation rate	<p>DSC- Differential Scanning Calorimetry The device provided (latent heat and melting range) measurements for the phase change material (PCM) only and for the overall phase change composite (PCC)</p> <p>Soaking bath and benchtop evaporation Provided graphite impregnation and evaporation rate measurements for the PCC</p>
Two	Thermal conductivity & Thermal diffusivity	<p>Laser flash analyzer The device measures thermal diffusivity. Thermal conductivity was calculated based on measured thermal diffusivity.</p>
Three	Surface morphology	<p>SEM (Scanning Electron Microscope) The device provided surface morphologies images for compressed expanded graphite (CEG) only and for the PCC</p>
Four	Crystalline structure	<p>XRD (X-ray diffraction) The device provides insight about the crystalline structure of compressed expanded graphite only and overall PCC</p>
Five	Material mechanical compression testing	<p>Universal Testing Machine (UTM) The device provides stress-strain analysis and mechanical strength testing of the PCC</p>

3.2.1 Stage one of characterization: latent heat and melting temperature of the PCM, graphite impregnation with low-temperature paraffin and evaporation rate

On stage one of PCC characterization, suitable petroleum driven, namely n-Tetradecane($C_{14}H_{30}$), and bio-based PCM were ordered from various local and international suppliers. The bio-based PCM is carefully selected from a variety of bio-based PCMs to serve as the potential bio-based counterpart of the petroleum driven n-Tetradecane.

Table 3.2 below illustrates some logistic information about the phase change material (PCM) suppliers. The PCMs purchased vary with respect to supplier location, origin classification (petroleum driven vs. bio-based), availability, and cost in \$/kg (includes delivery cost). The tags (A, B, C, and D) were assigned to the 4 groups of purchased PCMs to keep suppliers anonymously. Identical testing procedures were performed on samples from groups (A, B, C and D). All petroleum/bio-based PCMs samples were analyzed with respect to a set of properties of interest such as latent heat in (kJ/kg), melting temperature in (degree Celsius), impregnation of compressed expanded graphite samples with PCM (percentage (%)) of original weight of graphite) and finally evaporation rates from impregnated compressed expanded graphite samples in (microgram/ $m^2.s$) at ambient conditions.

Table 3.2: n-Tetradecane suppliers' information and pricing in (\$/kg)

	Supplier Location	PCM Basis	Cost (\$/Kg)
Group A	USA	Petroleum-based (Driven from petroleum products)	9.5
Group B	USA	Bio-based (Driven from fat and vegetable oil)	4.5
Group C	International	Petroleum-based (Driven from petroleum products)	1.66
Group D	International	Petroleum-based (Driven from petroleum products)	2.15

Thermal properties were analyzed using a Differential Scanning Calorimetry (DSC) – namely, Mettler-Toledo Model No-DSC823e/700 -- (actual picture of the device is illustrated by Figure 3.1). Using a DSC, the phase transformation can be studied and vital information regarding melting temperature and associated latent heat quantities can be experimentally measured (Kousksou et al. 2010; He, Martin, and Setterwall 2003; Choi, Cho, and Lorsch 1992). It is essential to quantify how much the phase change material (PCM) can store energy in a certain mass of the PCM.



Figure 3.1: Actual picture of DSC device at AllCell Facility Lab

3.2.1.1 Latent heat in (kJ/kg)

Approximately 10 experiments were performed on each of the four groups of samples to determine averaged latent heat in (kJ/kg) for each group using a Differential Scanning Calorimetry (DSC), Mettler-Toledo Model No-DSC823e/700. Hence, ten specimens (8-12 mg each) were placed in 40 μL (microliters) aluminum pans, which were then hermetically sealed. The experiments were performed at a scan rate of 1 $^{\circ}\text{C}/\text{min}$ and the latent heat results for the heating cycle are shown in Table 3.3. The latent heat is calculated as the area under the large peak for the DSC curves that are showing on (Figures 3.2 to 3.9).

Table 3.3: Latent heat (kJ/kg) measurement (averaged for each group)

Supplier	Property Measured at a heating rate of 1 $^{\circ}\text{C}/\text{min}$ Averaged Latent heat (kJ/kg)
Group A	222.01 ± 1.11
Group B	202.24 ± 1.01
Group C	215.19 ± 1.08
Group D	227.51 ± 1.14

As expected, although from different local and international suppliers, all n-Tetradecane samples have shown generally uniform behaviors and very similar test results. Moreover, bio-based samples have also behaved in a similar manner to petroleum-driven samples to a very large extent with a couple of exceptions. DSC exotherm curves of each group are illustrated on (Figures 3.2 to 3.9). As shown in Table 3.3, latent heat values which were obtained from all samples from the various four groups are within acceptable 202-220 kJ/kg range. Samples from groups A, C and D exposed almost identical behaviors in DSC measurements in terms of latent heat values, melting temperature and exotherm curves as

represented by Table 3.3, Table 3.4 and Figures 3.2 through 3.9 respectively. As shown in Table 3.4, group B samples had a slightly higher melting temperature than the melting temperatures of groups A, C and D, however, all within the targeted melting temperature range.

Table 3.4: Phase change material's melting temperature (°C) measured at a heating rate of 1 (°C/min)

Supplier	Melting Temp (°C)
Group A	4.92 ± 0.02
Group B	5.43 ± 0.03
Group C	4.90 ± 0.02
Group D	4.80 ± 0.02

As illustrated by Figure 3.2, group A samples showed very good latent heat and melting temperature values. The latent heat values were consistent (221, 222, and 223 kJ/kg) at different heating/cooling rates (1 °C/min, 5 °C/min and 10 °C/min) respectively. The only concern was the fact that DSC exotherm curves have broad peaks indicating some impurities (<2%). This is acceptable to a large extent since it is very hard to get a 100% pure n-Tetradecane. Moreover, as illustrated in Figure 3.3, group A samples showed very high stability and durability after 50 cycles of heating and cooling.

In Figure 3.4, group B samples showed good and acceptable latent heat figures, within target melting temperature and the DSC exotherm curves have sharp peaks indicating low impurities. The only concern with the results is the fact that the latent heat values are inconsistent (213, 204, and 189 kJ/kg) at different heating/cooling rates (1 °C/min, 5 °C/min and 10 °C/min) respectively. The DCS exotherm curves at 1 °C/min rate for group B is showing acceptable behavior and meet the targeted range. It is worth mentioning

that, the discharging rate of actual PCC-TES is designed for much smaller than 1 °C/min. Moreover, as illustrated in Figure 3.5, group B samples showed acceptable stability and durability after 50 cycles of heating and cooling.

Group C samples as illustrated by in Figure 3.6 showed very good latent heat and melting temperature values. The latent heat values were consistent (213, 215, and 217 kJ/kg) at different heating/cooling rates (1 °C/min, 5 °C/min and 10 °C/min) respectively. The only concern was the fact that DSC exotherm curves have broad peaks (similar to group A) and an indication of some impurities. Again, this is acceptable to a certain extent since it is very hard to get a 100% n-Tetradecane purity. Moreover, as illustrated in (Figure 3.7), group C samples showed very high stability and durability after 50 cycles of heating and cooling.

Very good latent heat figures by group D samples as shown in (Figure 3.8) samples showed very good latent heat and melting temperature values. The latent heat values were consistent (226, 227, and 228 kJ/kg) at different heating/cooling rates (1 °C/min, 5 °C/min and 10 °C/min) respectively. The only concern was the fact that DSC exotherm curves have broad peaks indicating some impurities, which was the same observation for all n-Tetradecane. Again, this is acceptable to a certain extent since it is very hard to get a 100% pure n-Tetradecane. Moreover, as illustrated in Figure 3.9, group D samples showed very high stability and durability after 50 cycles of heating and cooling.

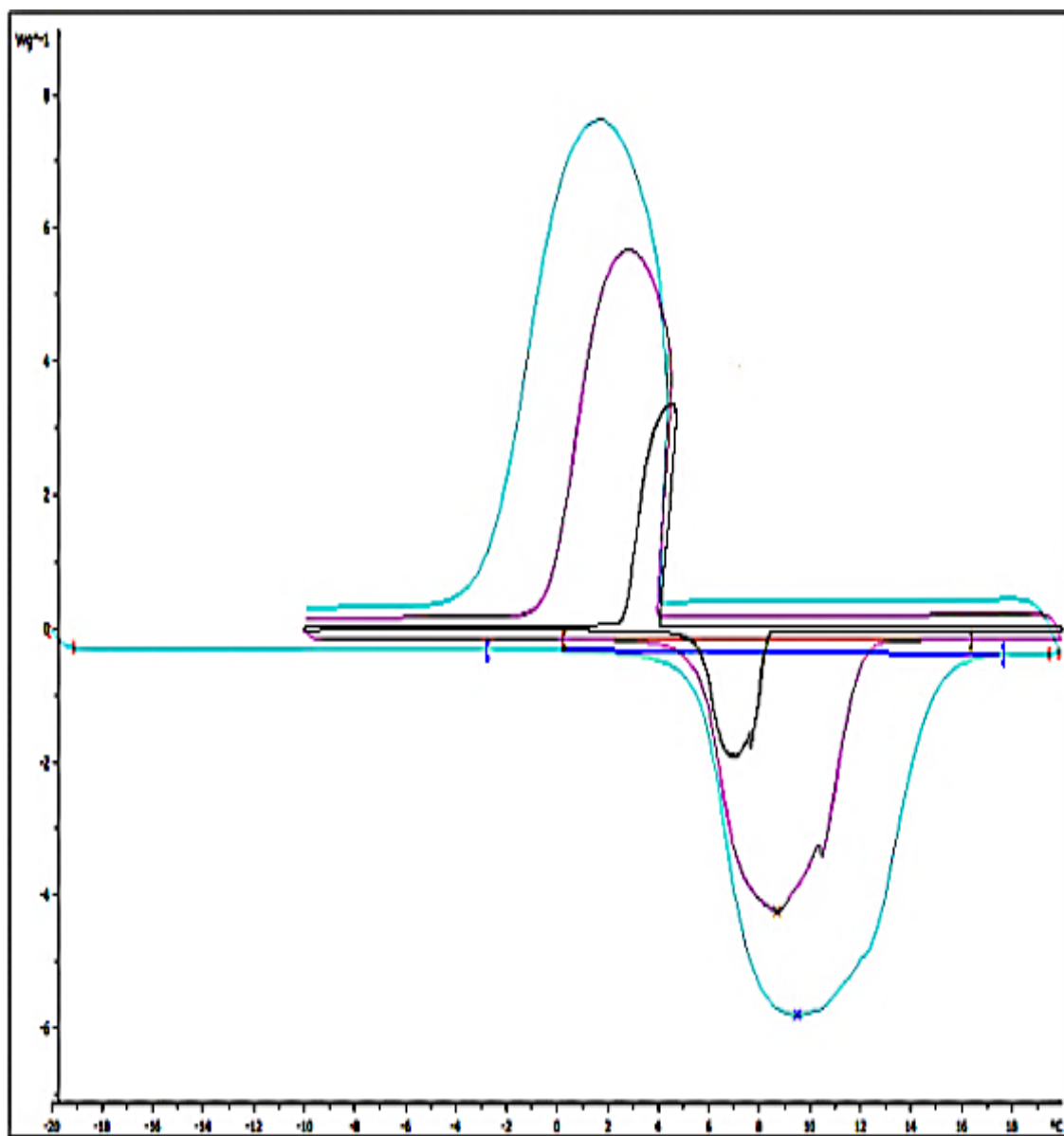


Figure 3.2: DSC exotherm curves of samples (Group A)

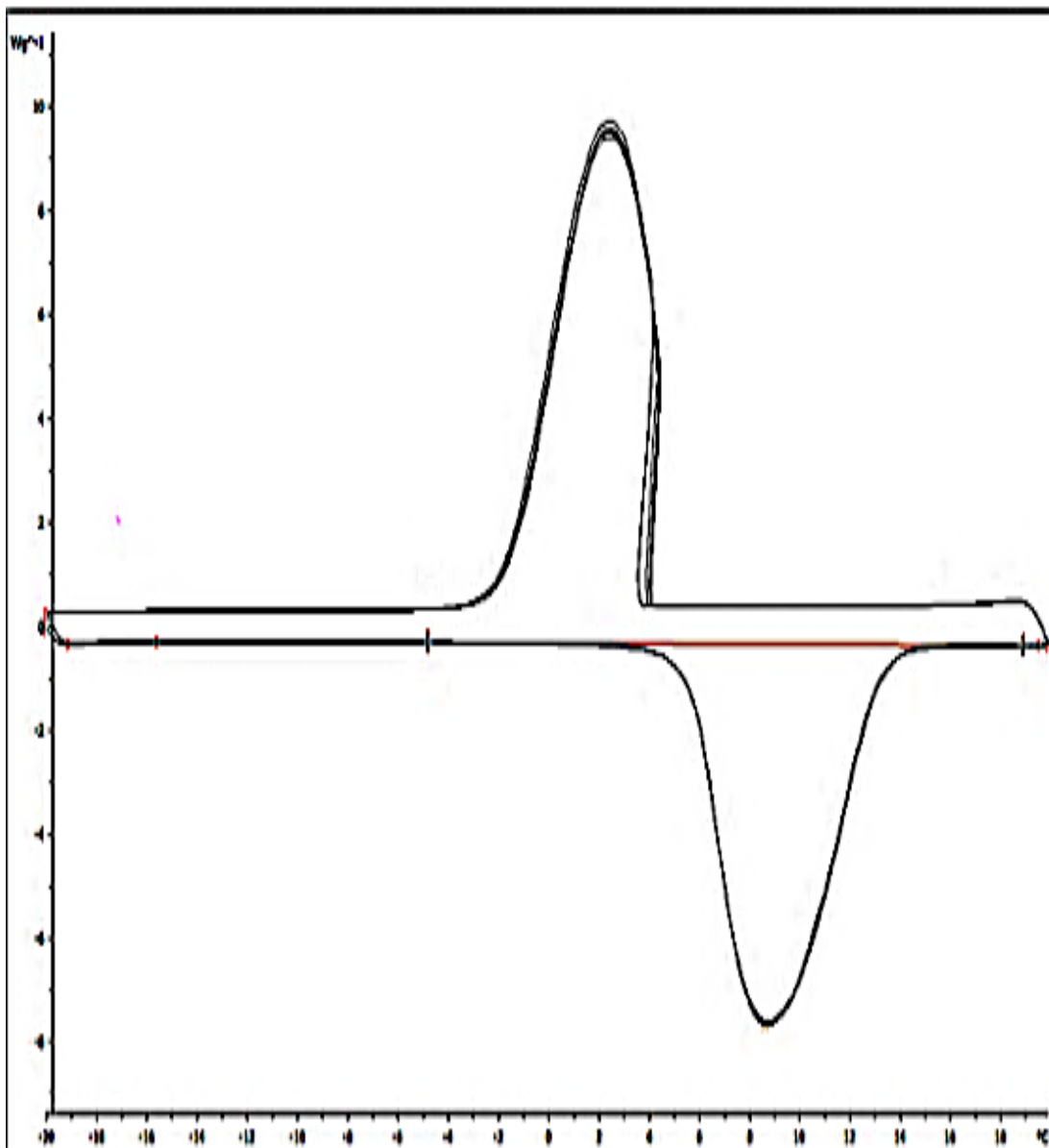


Figure 3.3: DSC exotherm curves of Group A after 50 cycles of heating and cooling

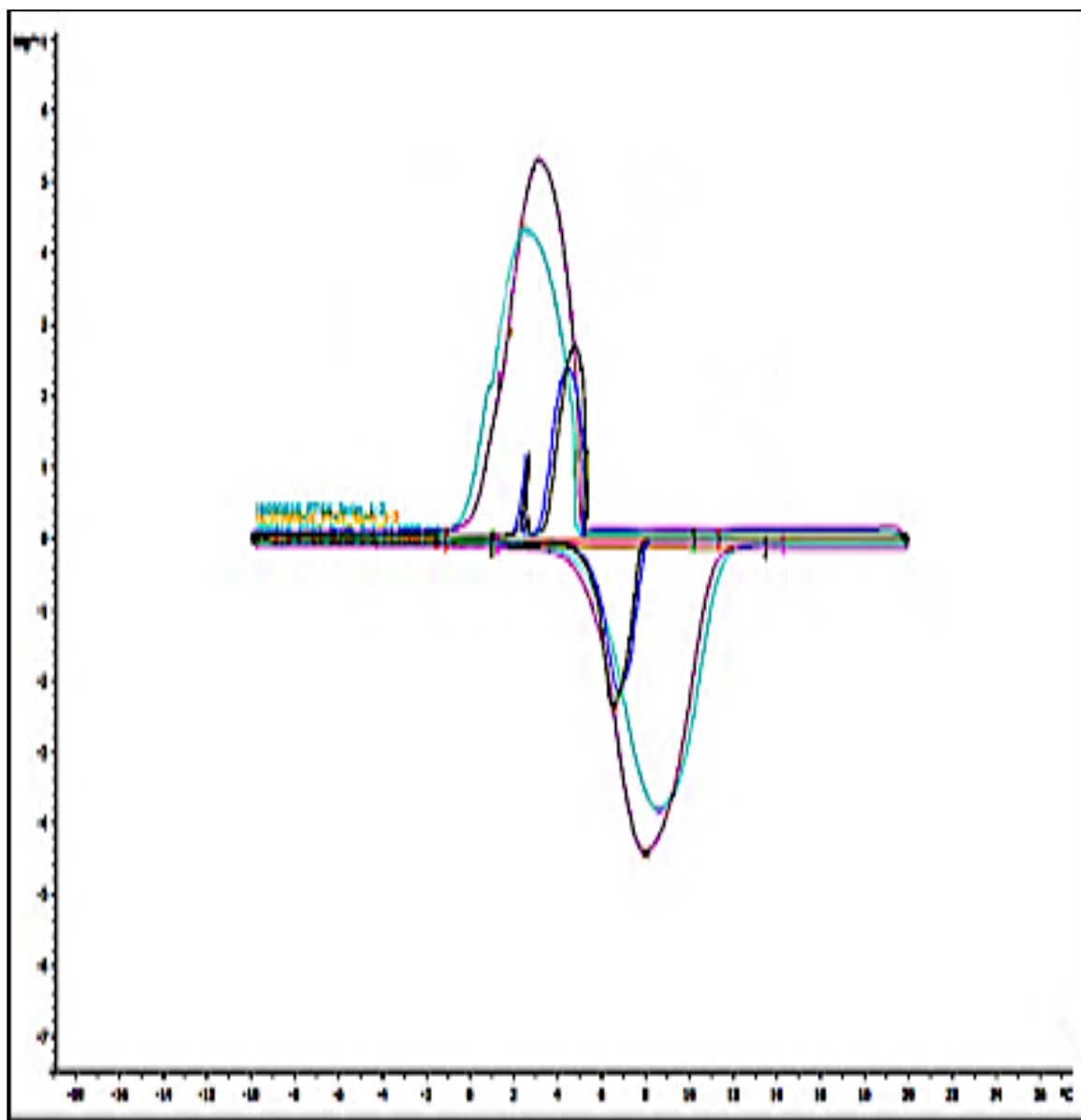


Figure 3.4: DSC exotherm curves of samples (Group B)

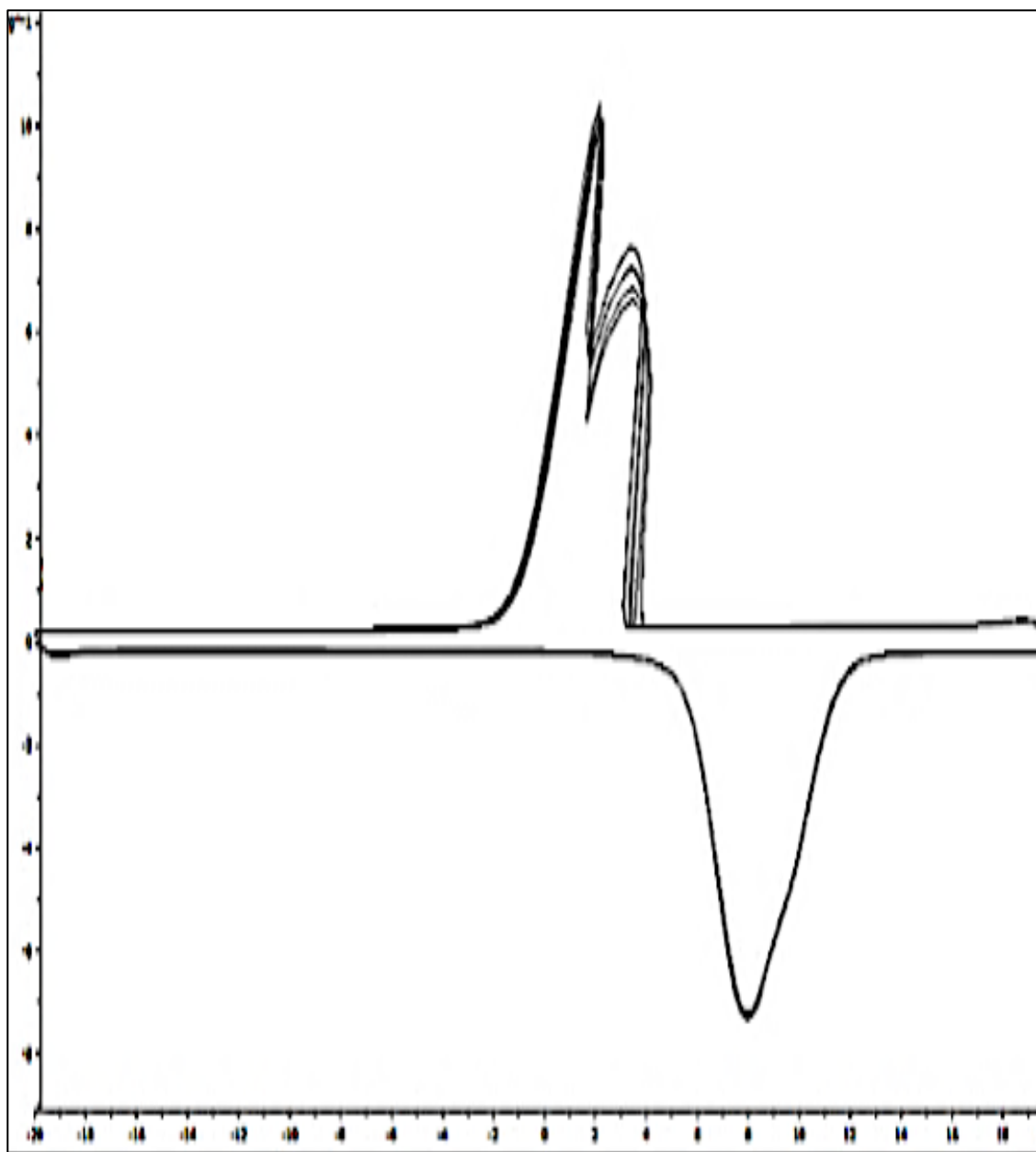


Figure 3.5: DSC exotherm curves of Group B after 50 cycles of heating and cooling

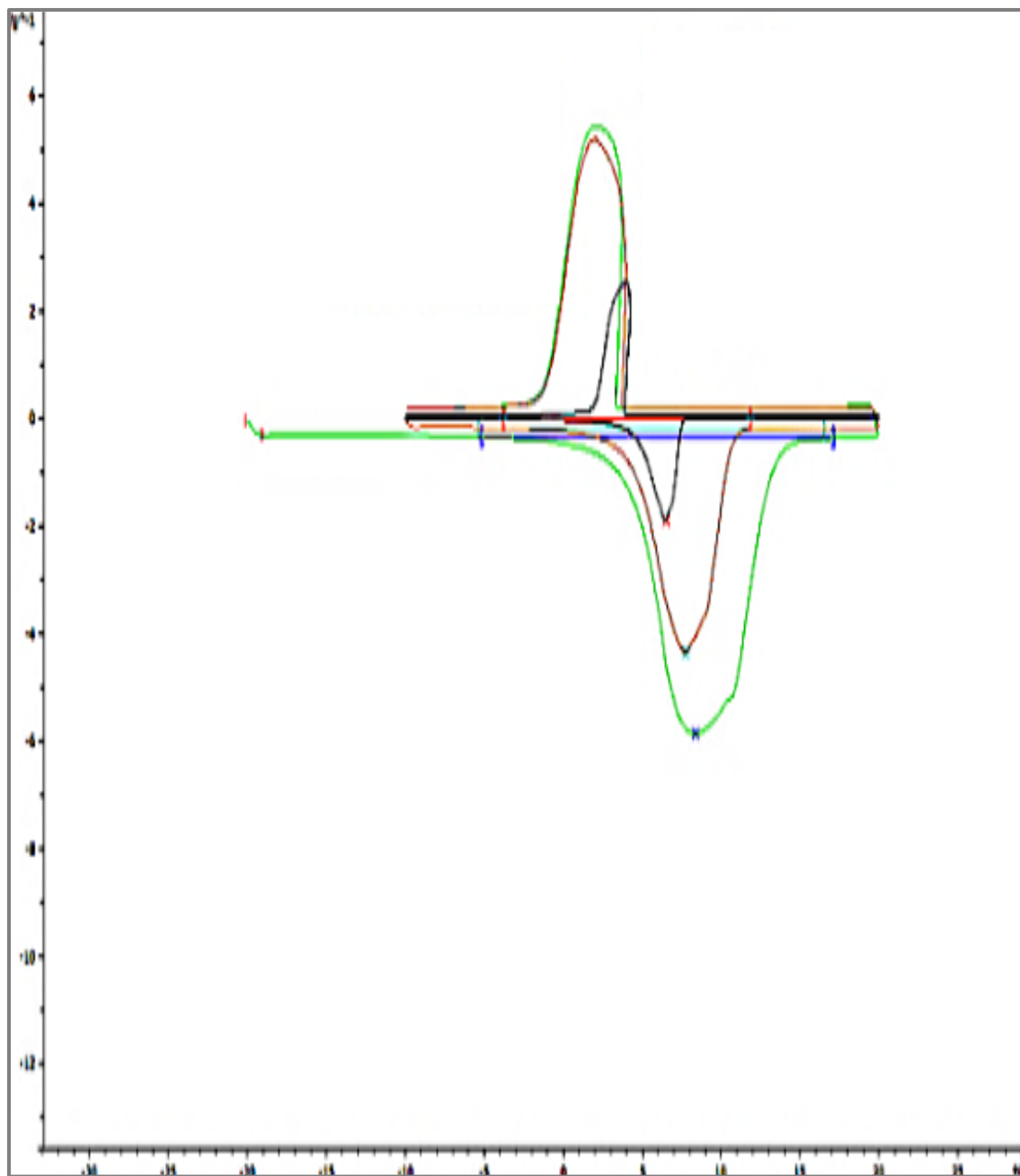


Figure 3.6: DSC exotherm curves of samples (Group C)

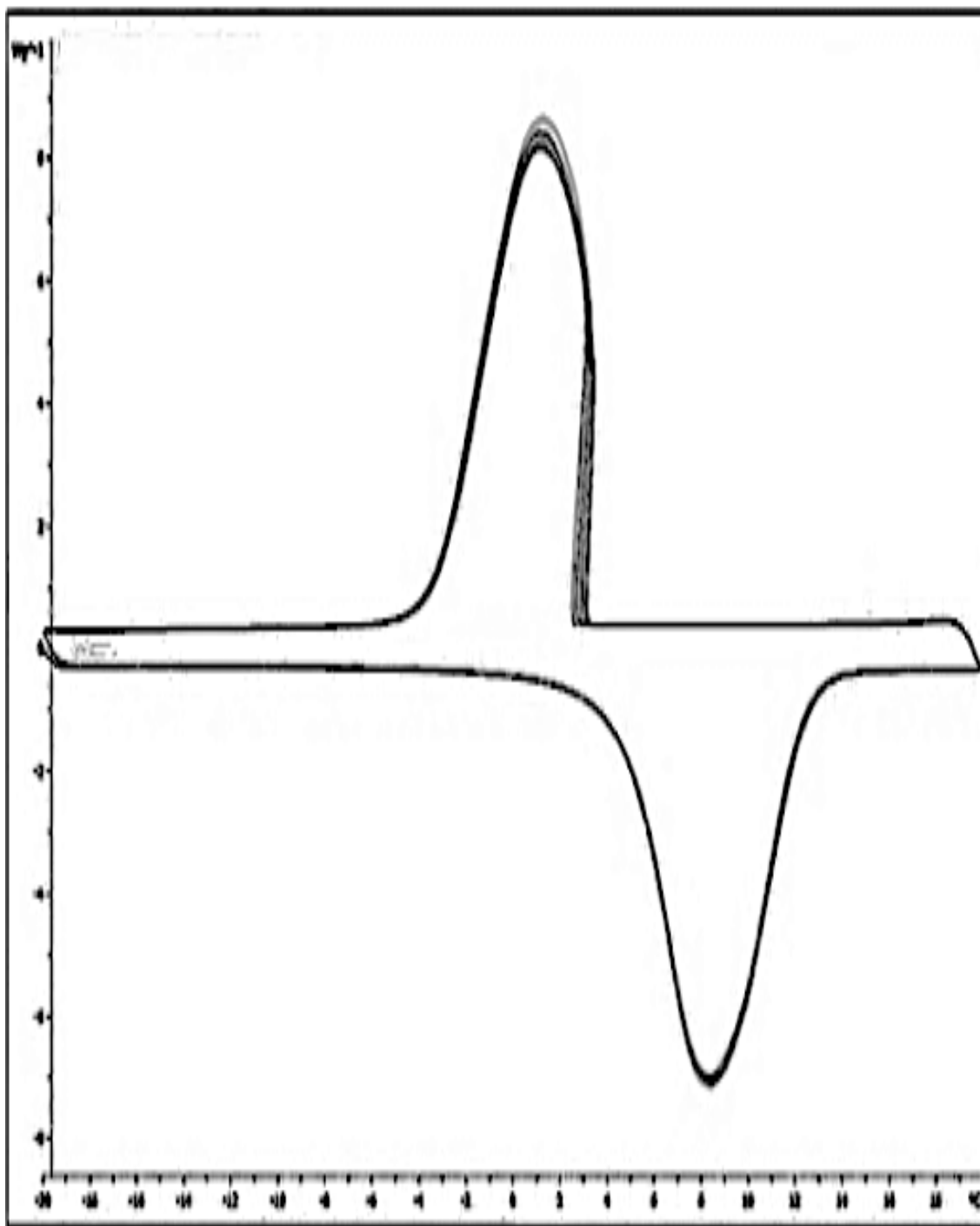


Figure 3.7: DSC exotherm curves of Group C after 50 cycles of heating and cooling

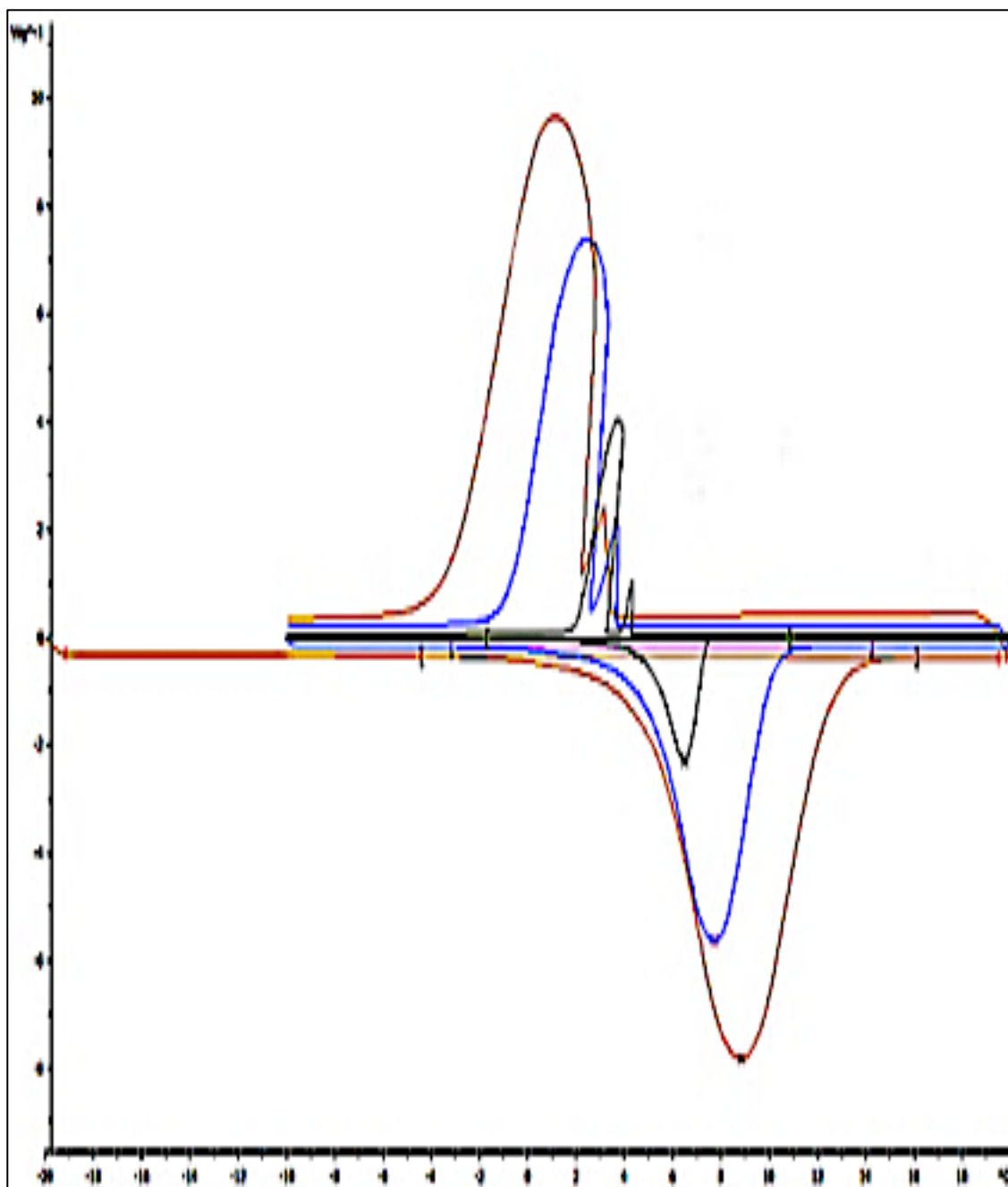


Figure 3.8: DSC exotherm curves of samples (Group D)

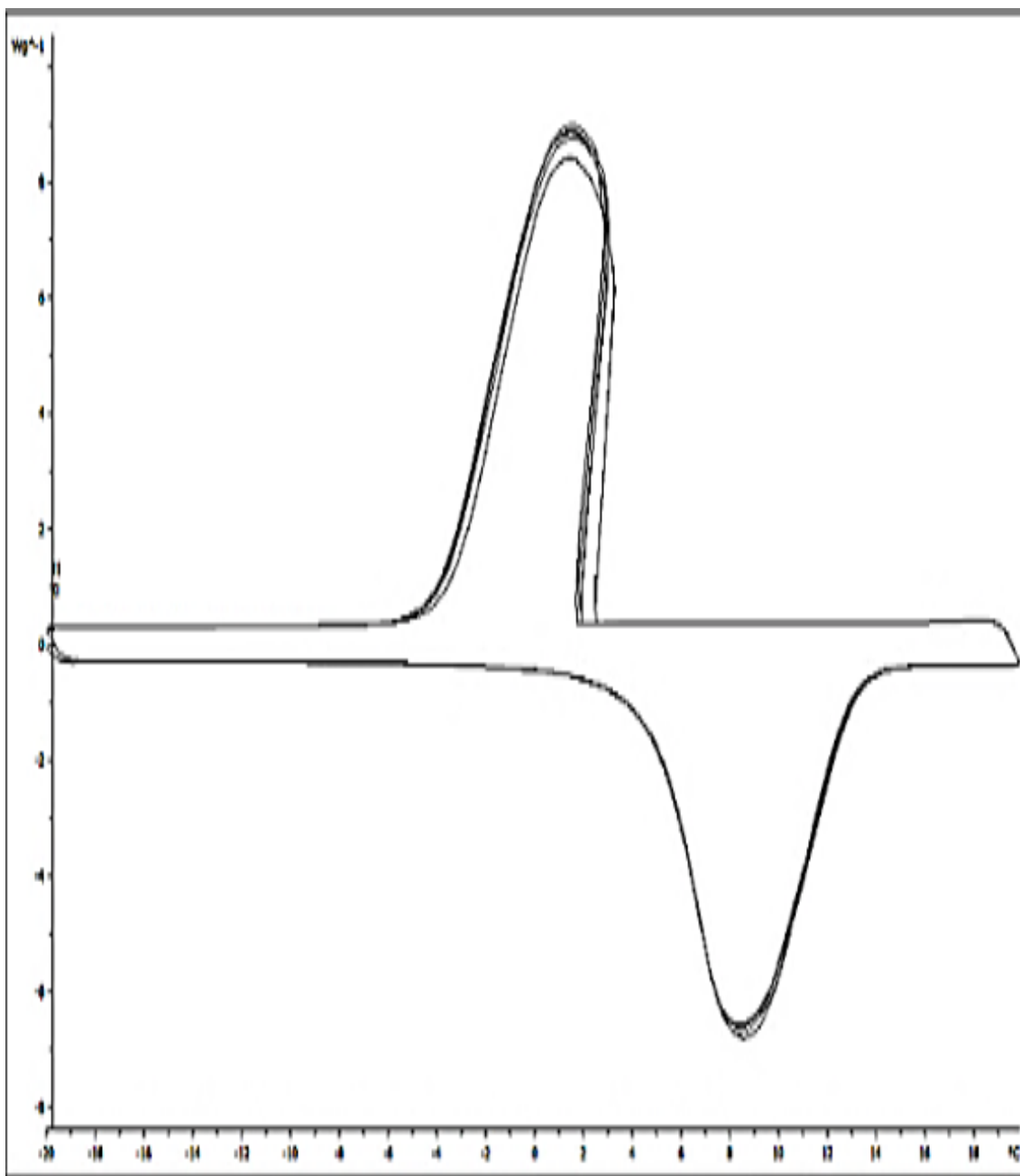


Figure 3.9: DSC exotherm curves of Group D after 50 cycles of heating and cooling

Table 3.5 below highlights the summary of observations revealed by the DSC curves and latent heat measurements. All samples from all groups behaved similarly to a large extent. Cost, delivery cost and availability would significantly contribute to final judgment and selection of the source of a bulk order of PCM.

Table 3.5: Summary of observations

	Pros	Cons
Group A	<ul style="list-style-type: none"> • Very good latent heat • Consistent latent heat at different heating/cooling rates 	<ul style="list-style-type: none"> • High price • The DSC curves have broad peaks indicating some impurities
Group B	<ul style="list-style-type: none"> • Good latent heat • The DSC exotherm curves have sharp peak indicating low impurities 	<ul style="list-style-type: none"> • Not very consistent latent heat at different heating/cooling rates. Slightly different melting temperature in comparison with other groups, still within acceptable range. • Availability/abundance of bio-based are of high concerns
Group C	<ul style="list-style-type: none"> • Good latent heat • Very consistent latent heat at different heating/cooling rates 	<ul style="list-style-type: none"> • The DSC curves have broad peaks indicating some impurities • Overseas supplier
Group D	<ul style="list-style-type: none"> • Very good latent heat • Consistent latent heat at different heating/cooling rates 	<ul style="list-style-type: none"> • The DSC curves have broad peaks indicating some impurities (98% C₁₄H₃₀, 1% C₁₃H₂₈, 1% C₁₅H₃₂) • Overseas supplier

3.2.1.3 Graphite impregnation

Compressed expanded graphite (CEG) serves as the porous structure that holds the PCMs and boosts thermal conductivity. Eight identical expanded graphite blocks were prepared to test how much PCM can be impregnated into the pores of the prepared blocks of compressed expanded graphite. All blocks are in equal dimensions of (1” width, 4” length, 1” height). All blocks were soaked into containers filled with PCMs for 24 hours. The ratio of the weight of PCM in the impregnated (soaked) compressed expanded graphite to original weight of un-soaked graphite blocks was calculated by equation (1) as follow:

$$\frac{\text{new weight of soaked graphite} - \text{original weight of unsoaked graphite}}{\text{original weight of unsoaked graphite}} \times 100\% \quad (3.1)$$

Table 3.6: PCM weight % of impregnated graphite blocks

Weight % of PCM in impregnated graphite blocks		
Supplier	Sample 1	Sample 2
Group A	76.64 %	75.99 %
Group B	76.56 %	75.85 %
Group C	76.47 %	76.60 %
Group D	75.80 %	75.83 %

All graphite blocks were in placed into a bath filled with the phase change material (PCM), namely n-Tetradecane for group A, C and D samples and bio-based for group B, causing identical weight gain effect on all blocks (as shown in Table 3.6 and Figure 3.10). In particular, after soaking (impregnation) experiment, PCM presented nearly 77% (by weight) of the original weight of each graphite block.

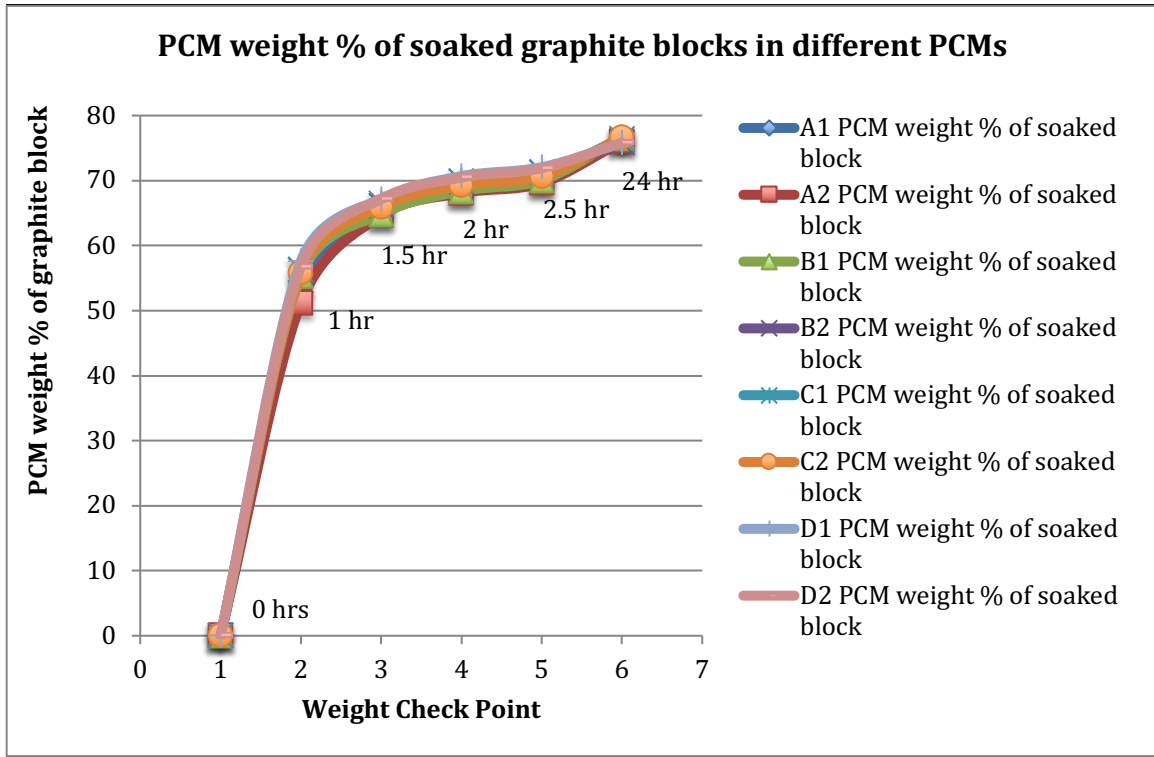


Figure 3.10: Nearly identical weight % of impregnated graphite blocks along the duration of graphite impregnation experiment

3.2.1.4 Evaporation rate of the PCMs

After being soaked in PCMs, all expanded graphite blocks were left on the lab bench for 2-month period exposed to the atmosphere pressure at room temperature. This experiment was conducted to experimentally calculate evaporation rates of PCMs from impregnated graphite blocks if not adequately contained and sealed. As illustrated by Table 3.7, all PCMs have shown evaporation rate figures within the range of 116.75 to 131.31 $\mu\text{g.m}^{-2} \cdot \text{s}^{-1}$. That is calculated to be approximately 15% loss of total mass of impregnated graphite over a 2-month period due to PCM evaporation if not adequately contained and sealed. The next section of this chapter will compare these experimental results to general theory prediction correlations.

Table 3.7: Experimental PCM evaporation rates from impregnated graphite blocks

	Sample 1 $\mu\text{g.m}^{-2}.\text{s}^{-1}$	Sample 2 $\mu\text{g.m}^{-2}.\text{s}^{-1}$
Group A experimental	131.31	124.48
Group B experimental	124.02	121.05
Group C experimental	120.98	116.75
Group D experimental	126.33	120.33

Evaporation rate of PCM is one of the main challenges that need to be addressed for TES applications due to the fact that exposing a PCC-TES system to hot ambient conditions will drastically affect its function if the overall PCC-TES structure is not adequately contained and sealed. Thus, good engineering measures need to be taken to prevent PCM loss from the actual PCC-TES system. Experimental evaporation rates were compared with theoretical predictions.

Donald Mackay and Ian van Wessenbeck presented a general theoretical correlation in their scientific paper (Mackay and Wessenbeck 2014) titled “Correlation of Chemical Evaporation Rate with Vapor Pressure”. The correlation developed by (Mackay and Wessenbeck 2014) relates evaporation rate to molar mass and vapor pressure as follow by equation (3.2):

$$ER (\mu\text{g m}^{-2} \text{h}^{-1}) = 1464 \times P (\text{Pa}) \times M (\text{g mol}^{-1}) \quad (3.2)$$

The correlation interrelates evaporation rate to vapor pressure and molar mass as a general correlation for chemicals and not specifically for n-Tetradecane. Accordingly, the evaporation rate of n-Tetradecane was theoretically calculated based on the technical data of n-Tetradecane and equation (3.2). The calculated theoretical evaporation rate of n-

Tetradecane was found to be 125.05 ($\mu\text{g.m}^{-2}.\text{s}^{-1}$). On the other hand, the experimental evaporation rate figures of n-Tetradecane in ($\mu\text{g.m}^{-2}.\text{s}^{-1}$) are illustrated in Table 3.8.

Table 8: Theoretical vs. experimental of n-Tetradecane evaporation rate in $\mu\text{g.m}^{-2}.\text{s}^{-1}$

	n-Tetradecane evaporation rate ($\mu\text{g.m}^{-2}.\text{s}^{-1}$) from impregnated graphite blocks	
	Sample 1	Sample 2
Group A	131.33	124.48
Group C	120.98	116.75
Group D	126.33	120.33
Theoretical Predictions	125.05	125.05

The experimental evaporation rate figures of n-Tetradecane showed very good agreements with theoretical predictions. 1.347% is the averaged error of experimental evaporation rates compared to theoretical predictions. That illustrates the correlation by (Mackay and Wesenbeeck 2014) can provide a reliable scientific approach to quantify evaporation rate from graphite blocks if n-Tetradecane is not adequately contained and sealing. It is worth mentioning, an adequately contained and sealed PCC-TES would not experience n-Tetradecane loss as was also tested in our lab. This section was intended to quantify the evaporation rate of n-Tetradecane if neither adequately contained nor sealed.

3.2.1.5 Latent heat of the PCC

Approximately 10 experiments were performed for each sample to determine averaged latent heat in (kJ/kg) for each sampled group using a Differential Scanning Calorimetry (DSC), Mettler-Toledo Model No-DSC823e/700. Ten specimens (8-12 mg each) were

placed in 40 μL (microliters) aluminum pans, which were then hermetically sealed. The experiments were performed at a scan rate of 1 $^{\circ}\text{C}/\text{min}$ and the results for the heating cycle are shown in Table 3.9.

Table 3.9: Latent heat (kJ/kg) of the proposed PCC

Supplier	Property Measured at a heating rate of 1 $^{\circ}\text{C}/\text{min}$
	Averaged Latent heat (kJ/kg)
Group A	180 ± 0.9
Group B	175 ± 0.9
Group C	175 ± 0.9
Group D	180 ± 0.9

3.2.2 Stage two of characterization: thermal diffusivity

3.2.2.1 Thermal diffusivity and thermal conductivity of the proposed PCC

The ability of phase change material (PCM) to rapidly transfer heat is equally important to the capability of the PCM material to store a large amount of heat within a small volume. The thermal diffusivity was measured using a TA Instruments DXF-200 laser flash instrument (actual photo of the device is illustrated in Figure 3.11).



Figure 3.11: DXF-200 laser flash instrument at AllCell Technologies lab

On the other hand, thermal conductivity is calculated in terms of lab measured thermal diffusivity (α), specific heat (C_p) and weighted average density (ρ) as illustrated by equation (3.3):

$$k = \rho \alpha C_p \quad (3.3)$$

To measure thermal diffusivity, samples were prepared with a diameter of 12.7 mm and a thickness of 2.5-3.5 mm. One side of the sample was covered with a thin layer of silver paint which was placed to improve temperature measurement by the sensor. Each sample was tested by three consecutive laser pulses, each pulse is separated by 5-minute equilibration periods. Due to the anisotropic behavior of graphite material in the PCC composite, thermal properties change depending on the direction within the structure. Therefore, thermal diffusivities were measured for both in-plane and through-plane samples. Measurements of the three samples were averaged to obtain a mean thermal

diffusivity of the measured samples for both in-plane and through-plane samples as illustrated by Table 3.10. In-plan samples are samples cut parallel to compacted layers of graphite. Through-plane are samples cut perpendicular to compacted layers.

Table 3.10: Averaged measured thermal diffusivity and calculated thermal conductivity of graphite and PCC

Material	Property	Unit	Value
Graphite	Averaged Measured (in-plane) Thermal diffusivity (α)	m ² /s	0.012
Graphite	Averaged Measured (Through-plane) Thermal diffusivity (α)	m ² /s	0.004
Graphite	Averaged Calculated Thermal Conductivity (in-plane)	W/m. K	20.25
Graphite	Averaged Calculated Thermal Conductivity (through-plane)	W/m. K	6.04
Paraffin	Thermal conductivity	W/m. K	0.24
PCC	Averaged Measured (in-plane) Thermal diffusivity (α)	m ² /s	0.016
PCC	Averaged Measured (Through-plane) Thermal diffusivity (α)	m ² /s	0.008
PCC	Averaged Calculated Thermal Conductivity (in-plane)	W/m. K	22
PCC	Averaged Calculated Thermal Conductivity (through-plane)	W/m. K	6.5

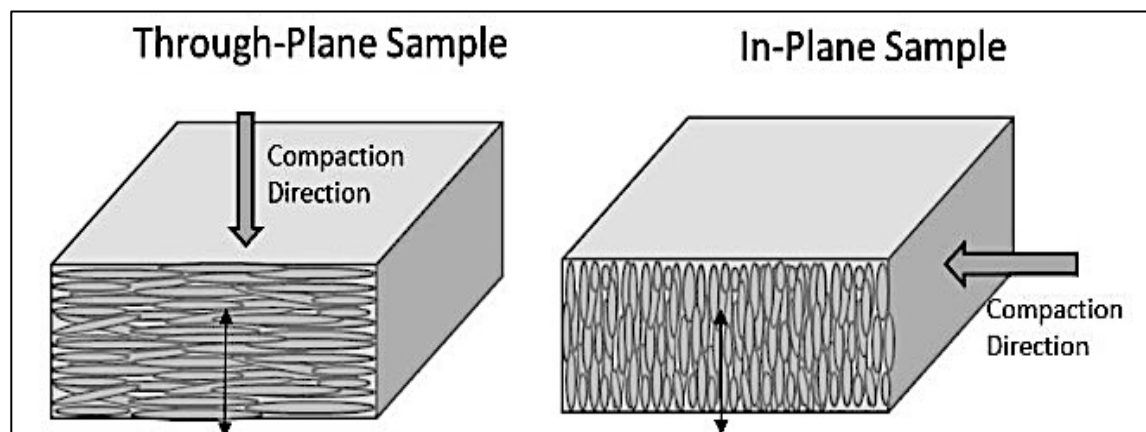


Figure 3.12: Schematic of in-plane and through-plane samples with respect to compaction (compressing) direction.

3.2.2.2 Effect of density and compression on thermal conductivity of the PCC

To study the effect of varying density (by compressing expanded graphite blocks) on thermal conductivity, four (4) samples of expanded graphite blocks were prepared. Each block was separately compressed to reach a specific desired density. The densities of the compressed blocks were as follow:

- Block 1: Compressed Expanded Graphite (CEG) at a density of 670 g/l
- Block 2: Compressed Expanded Graphite (CEG) at a density of 490 g/l
- Block 3: Compressed Expanded Graphite (CEG) at a density of 380 g/l
- Block 4: Compressed Expanded Graphite (CEG) at a density of 150 g/l

Each of four (4) blocks was divided by half. One half of each block was impregnated with the low-temperature paraffin, namely n-Tetradecane, while the other half left as it is (unsoaked/unfilled compressed expanded graphite matrix). The reason for that, the surface morphologies of the blocks shall be examined before and after the impregnation with n-Tetradecane. Therefore, there is now 2 sets of samples to be examined.

- Set-1 of samples:
 - Sample 1: CEG (no paraffin impregnation) at a density of 670 g/l. This sample will be called (CEG- Sample 1).
 - Sample 2: CEG (no paraffin impregnation) at a density of 490 g/l. This sample will be called (CEG- Sample 2).

- Sample 3: CEG (no paraffin impregnation) at a density of 380 g/l. This sample will be called (CEG- Sample 3).
- Sample 4: CEG (no paraffin impregnation) at a density of 150 g/l. This sample will be called (CEG- Sample 4).
- Set-2 of samples:
 - Sample 1: is the same as sample 1 from set 1 but impregnated with paraffin. This sample will be called (PCC- Sample 1).
 - Sample 2: is the same as sample 2 from set 1 but impregnated with paraffin. This sample will be called (PCC- Sample-2).
 - Sample 3: is the same as sample 3 from set 1 but impregnated with paraffin. This sample will be called (PCC- Sample 3).
 - Sample 4 is the same as sample 4 from set 1 but impregnated with paraffin. This sample will be called (PCC- Sample 4).

The thermal conductivity of the PCC-samples (1/2/3/4) were measured to determine the effect of varying density on thermal conductivity. The results are illustrated in Table 11. The thermal conductivity increases for in-plane samples in proportion to density increase. On the other hand, thermal conductivities of the samples were almost constant for through-plane samples even though density was varied. It is worth mentioning that, a trade-off between thermal conductivity and ability to impregnate paraffin is observed. In particular, as the density of the compressed expanded graphite increases the ability of the compressed

expanded graphite block to impregnate paraffin decreases and consequently adversely affect the latent heat capacity of the PCC.

Table 3.11: Averaged calculated thermal conductivity based on thermal diffusivity measurements PCC- Samples 1/2/3/4

Sample	Thermal Conductivity (in-plane) (W/m.K)	Thermal Conductivity (Through-plane) (W/m.K)	Ability to impregnate Paraffin (%)
PCC- Sample 1	63 ± 0.31	6.50 ± 0.03	40
PCC- Sample 2	44 ± 0.22	6.46 ± 0.03	48
PCC- Sample 3	34 ± 0.17	6.20 ± 0.03	60
PCC- Sample 4	22 ± 0.11	6.01 ± 0.03	78

3.2.3 Stage three of PCC characterization: SEM (Scanning Electron Microscope)

In this stage of the PCC characterization experiments, SEM (Scanning Electron Microscope) device at the Argonne Lab Facility was utilized to provide surface morphologies images of the porous graphite matrix before and after impregnation with the paraffin.

Similar SEM imaging experiments for a comparable (porous graphite matrix impregnated with high-temperature paraffin) were conducted by (Mills et al. 2006) as illustrated by (Figures 3.13 & 3.14). Figure 3.13 illustrates SEM images of compressed expanded graphite matrix alone (no paraffin impregnation yet) illustrated at x200 magnification by (Mills et al. 2006). Figure 3.14 illustrates SEM images of the graphite matrix (filled with

paraffin) illustrated at x200 and x5000 magnifications. As illustrated by Figure 3.14 the void spaces are now filled with high-temperature paraffin by (Mills et al. 2006).

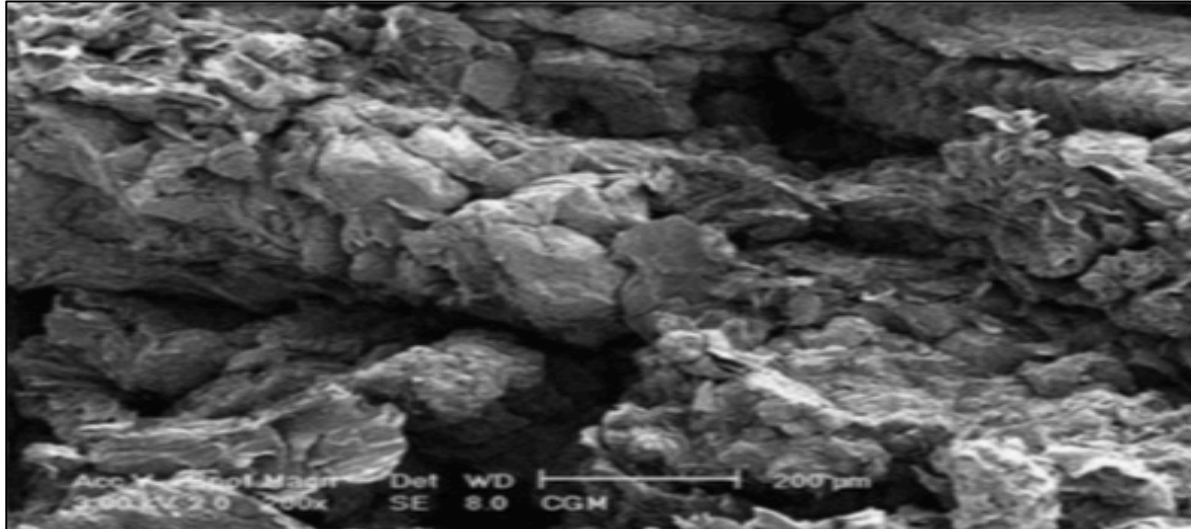


Figure 3.13: SEM images of graphite matrix (**no paraffin impregnation**) showing at x200 magnification (Mills et al. 2006).

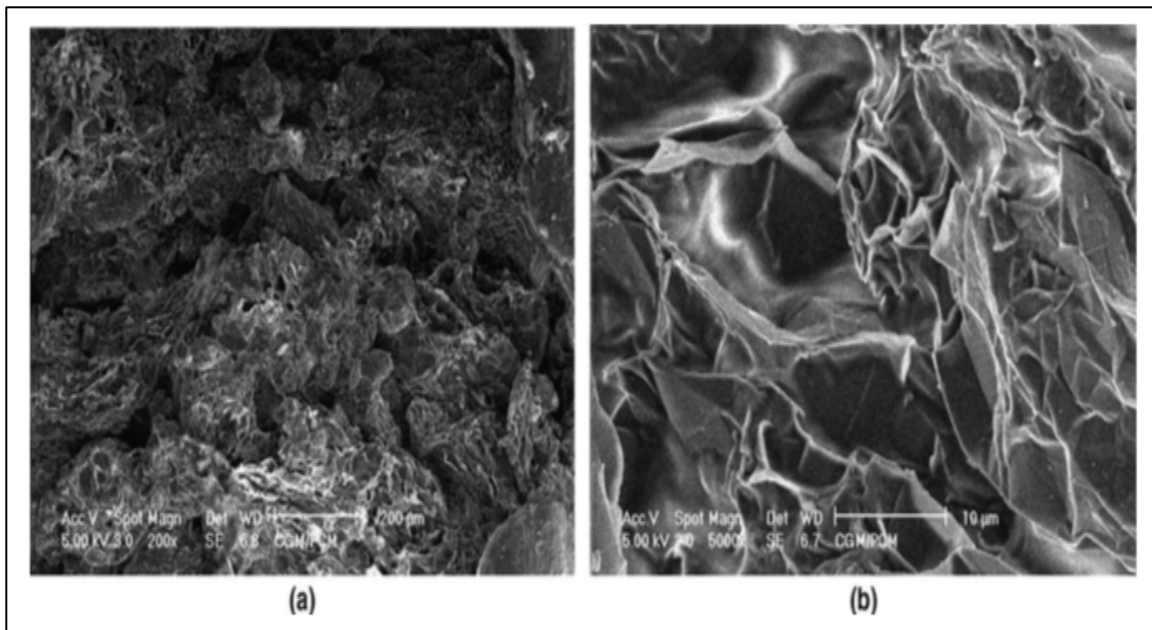


Figure 3.14: SEM images of graphite matrix (**paraffin impregnated**) showing (a) at x200 magnification and (b) at x5000 magnification (Mills et al. 2006).

The work by (Mills et al. 2006) used a (high) temperature paraffin (which starts melting at 55 °C) as a safety precaution to protect Lithium-ion batteries from thermal runaway.

In this present study, the (low) temperature paraffin (which starts melting at 4 °C) was selected to serve as a storage medium for air conditioning applications.

Just like stage 2, four (4) samples of expanded graphite blocks were prepared. Each sample was separately compressed (compacted) to reach a specific desired density. The densities of the samples were as follow:

- Sample 1: Compressed Expanded Graphite (CEG) at a density of 670 g/l
- Sample 2: Compressed Expanded Graphite (CEG) at a density of 490 g/l
- Sample 3: Compressed Expanded Graphite (CEG) at a density of 380 g/l
- Sample 4: Compressed Expanded Graphite (CEG) at a density of 150 g/l

Each of these four (4) samples were divided by half. Half of the samples were impregnated with paraffin while the other half left as it is (un-soaked/unfilled compressed expanded graphite matrix). The reason for that, the surface morphologies of the samples before and after the low-temperature paraffin impregnation shall be examined. Therefore, there is now 2 sets of samples as follows:

- Set-1 of samples:
 - Sample 1: CEG (no paraffin impregnation) at a density of 670 g/l. We will call this sample in this study CEG- Sample 1.

- Sample 2: CEG (no paraffin impregnation) at a density of 490 g/l. We will call this sample in this study CEG- Sample 2.
 - Sample 3: CEG (no paraffin impregnation) at a density of 380 g/l. We will call this sample in this study CEG- Sample 3.
 - Sample 4: CEG (no paraffin impregnation) at a density of 150 g/l. We will call this sample in this study CEG- Sample 4.
-
- Set-2 of samples:
 - Sample 1: is the same as sample 1 from set 1 but impregnated with paraffin. We will call this sample in this study (PCC- Sample 1).
 - Sample 2: is the same as sample 2 from set 1 but impregnated with paraffin. We will call this sample in this study (PCC- Sample-2).
 - Sample 3: is the same as sample 3 from set 1 but impregnated with paraffin. We will call this sample in this study (PCC- Sample 3).
 - Sample 4 is the same as sample 4 from set 1 but impregnated with paraffin. We will call this sample in this study (PCC- Sample 4).

An actual photo (at Argonne National lab facility) of the SEM device, which was utilized to provide surface morphology images of the four samples from each group, is illustrated by (Figure 3.15).

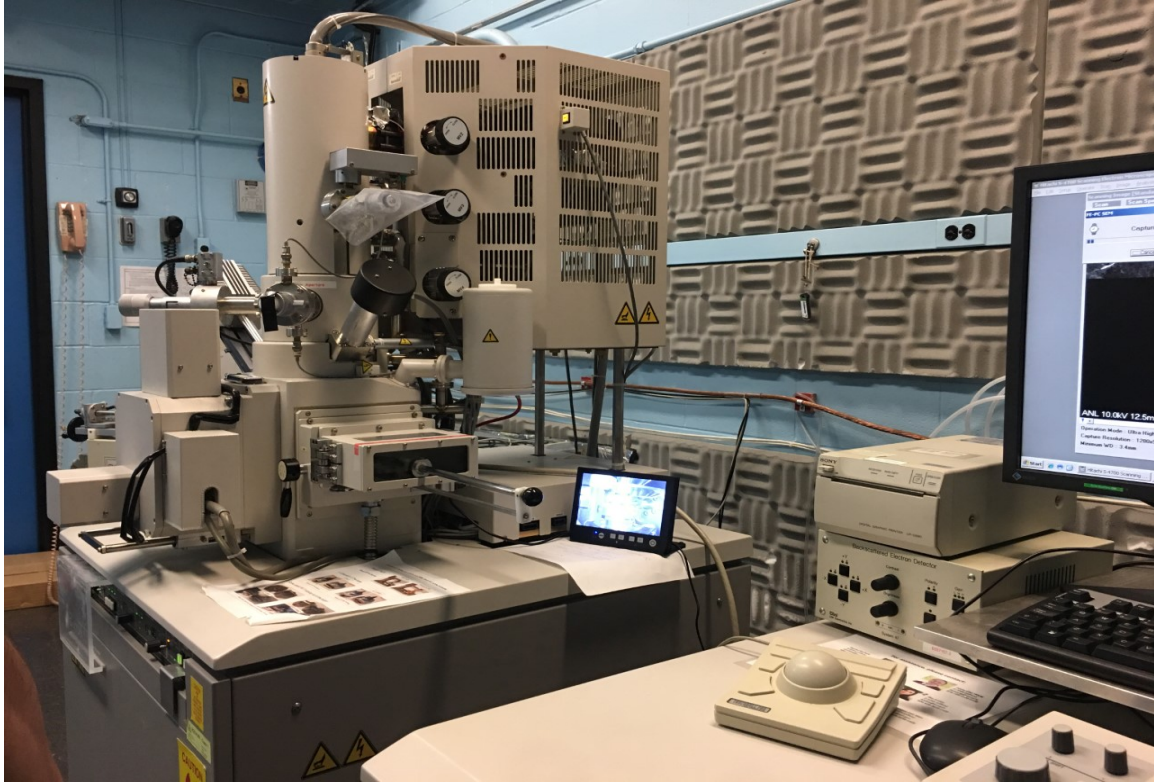


Figure 3.15: SEM device at Argonne National Lab (ANL) Facility.

Figure 3.16 illustrates four SEM images at (x50 magnification) of graphite samples-- CEG-Sample 1, CEG-Sample 2, CEG-Sample 3 and CEG-Sample 4—(no paraffin impregnation for each of these samples) at four various densities of (670 g/l) , (490 g/l), (380 g/l) and (150 g/l.). We can observe that lower density samples have more void spaces than higher density samples.

Figure 3.17 illustrates four SEM images at (x100 magnification) of graphite samples-- CEG-Sample 1, CEG-Sample 2, CEG-Sample 3 and CEG-Sample 4—(no paraffin impregnation for each of these samples) at four various densities of (670 g/l) , (490 g/l), (380 g/l) and (150 g/l.). Here also, we can observe that lower density samples have more void spaces than higher density samples.

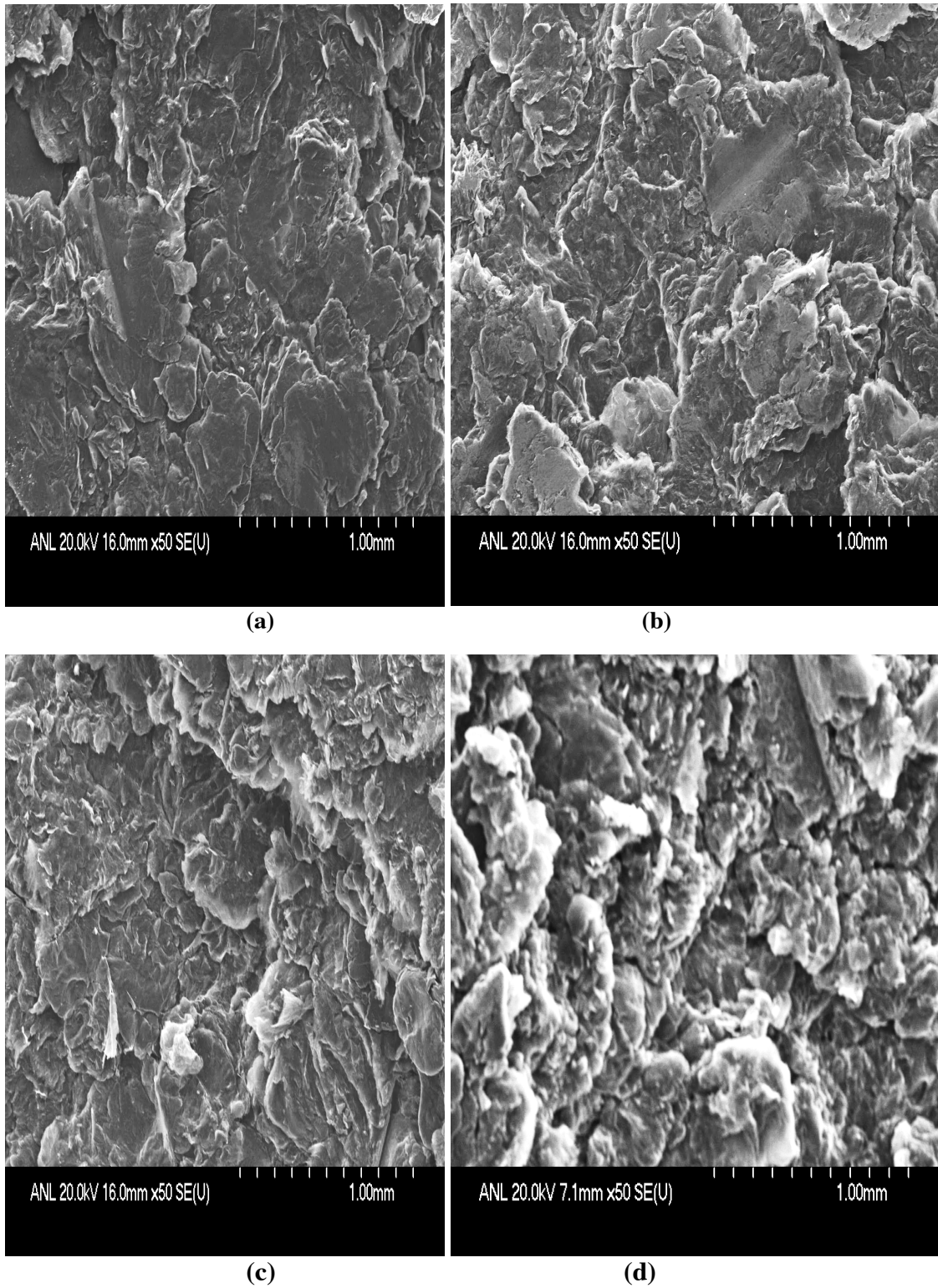


Figure 3.16: SEM images at (x50 magnification) of graphite samples-- CEG-Sample 1, CEG-Sample 2, CEG-Sample 3 and CEG-Sample 4—(**no paraffin impregnation**) at four various densities of (670 g/l) , (490 g/l), (380 g/l) and (150 g/l).

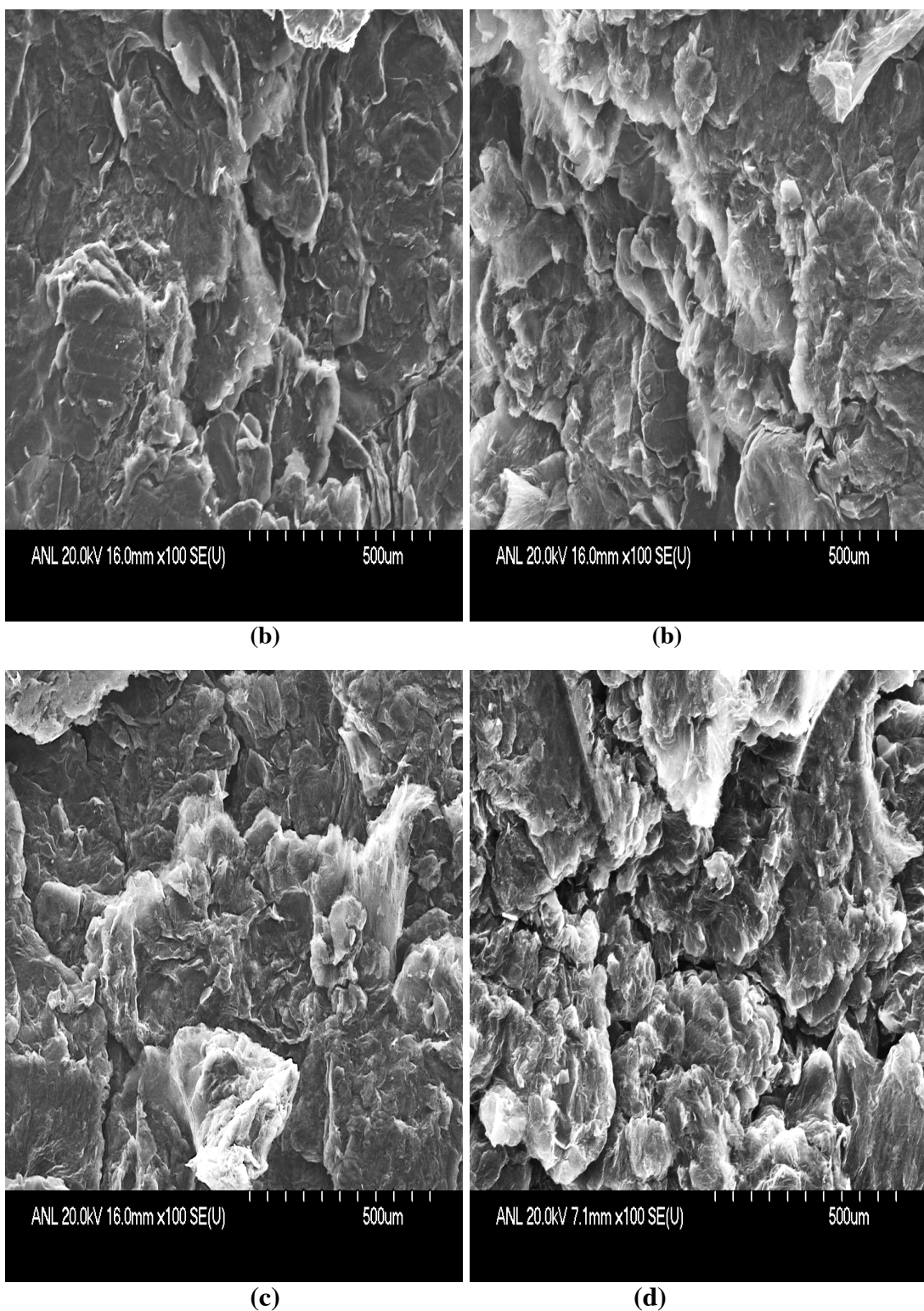
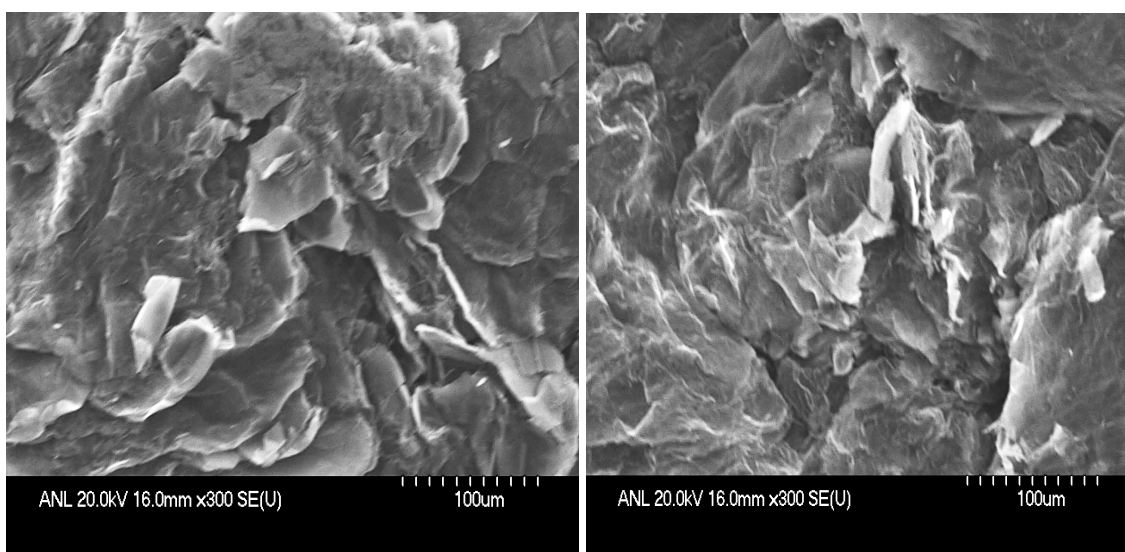
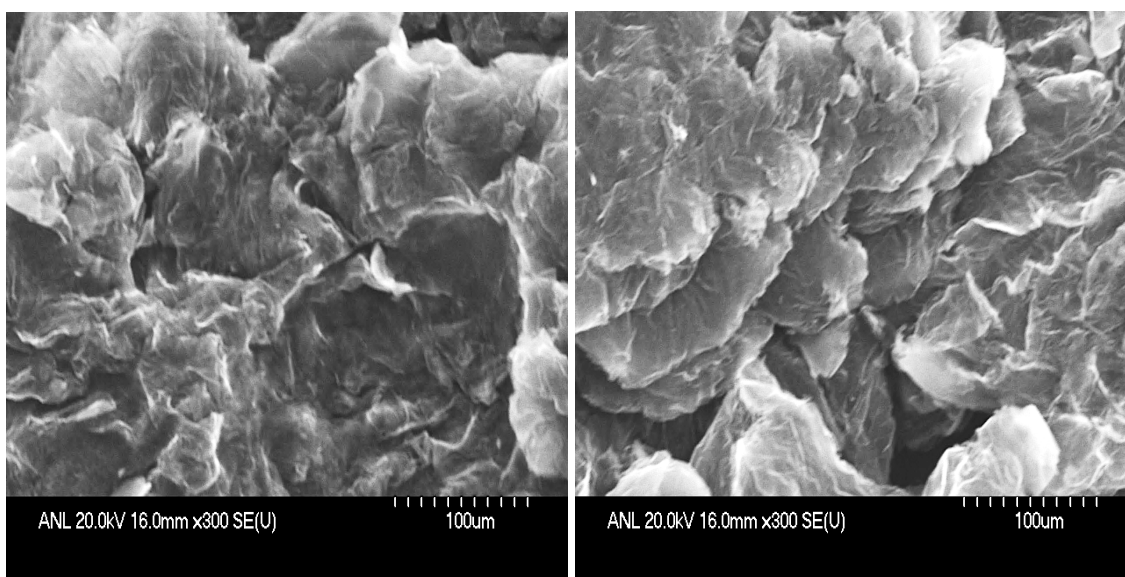


Figure 3.17: SEM images at (x100 magnification) of graphite samples-- CEG-Sample 1, CEG-Sample 2, CEG-Sample 3 and CEG-Sample 4—(**no paraffin impregnation**) at four various densities (a) 670 g/l , (b) 490 g/l , (c) 380 g/l (d) 150 g/l.



(a)

(b)



(c)

(d)

Figure 3.18: SEM images at (x300 magnification) of graphite samples-- CEG-Sample 1, CEG-Sample 2, CEG-Sample 3 and CEG-Sample 4—(**no paraffin impregnation**) at four various densities (a) 670 g/l , (b) 490 g/l , (c) 380 g/l (d) 150 g/l.

Figures (3.19- 3.26) illustrate SEM images of graphite matrix (**paraffin impregnated**) showing at x30, x150, x300, x500, x2.5k and x5.0k magnifications for PCC-sample 1, PCC-sample 2, PCC-sample 3, and PCC-sample 4. In Figures (3.19- 3.26), we can observe that void spaces are now filled with paraffin.

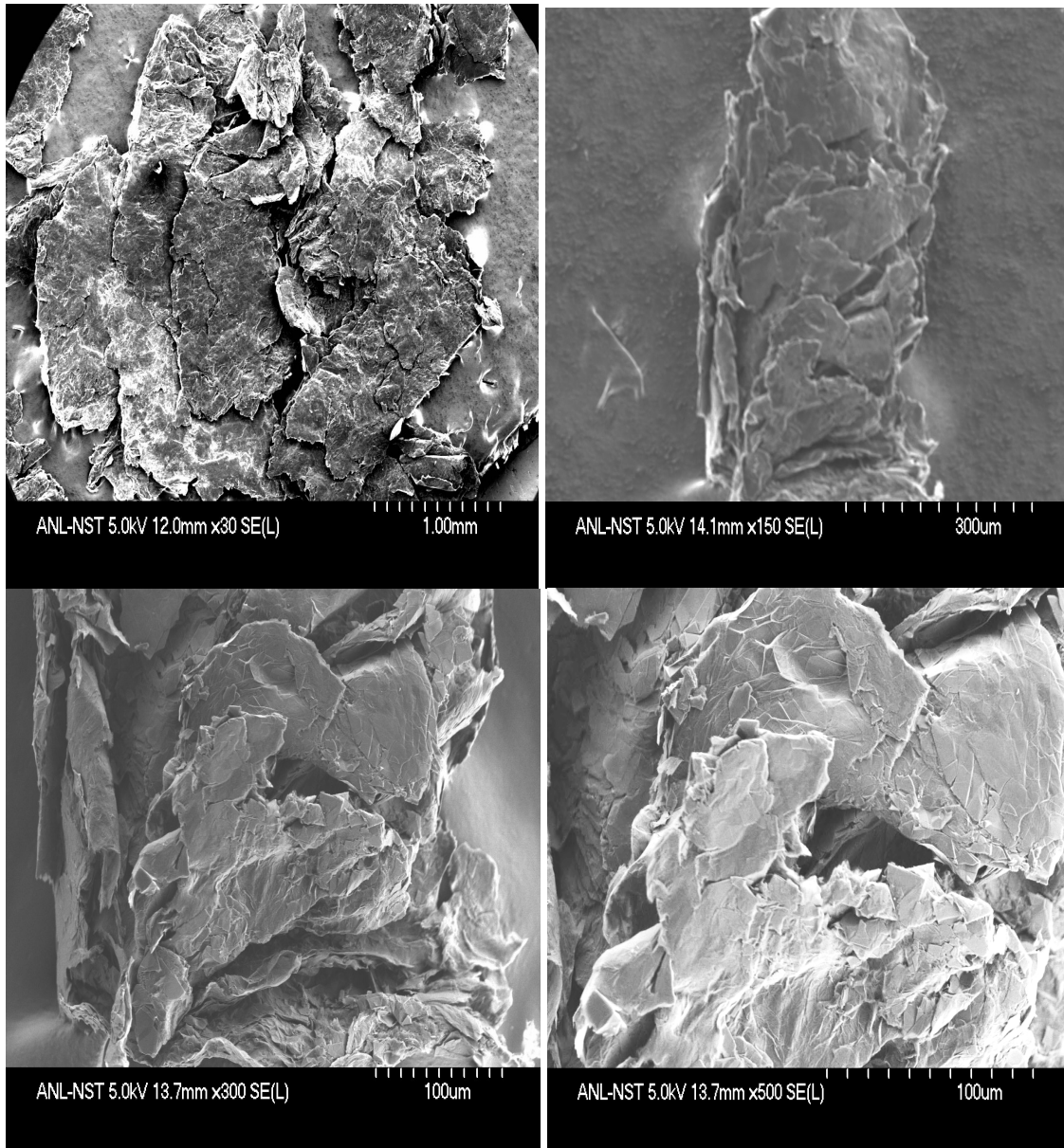


Figure 3.19: SEM images of graphite matrix (**paraffin impregnated**) showing at x30, x150, x300 and x 500 magnifications for PCC-sample 1

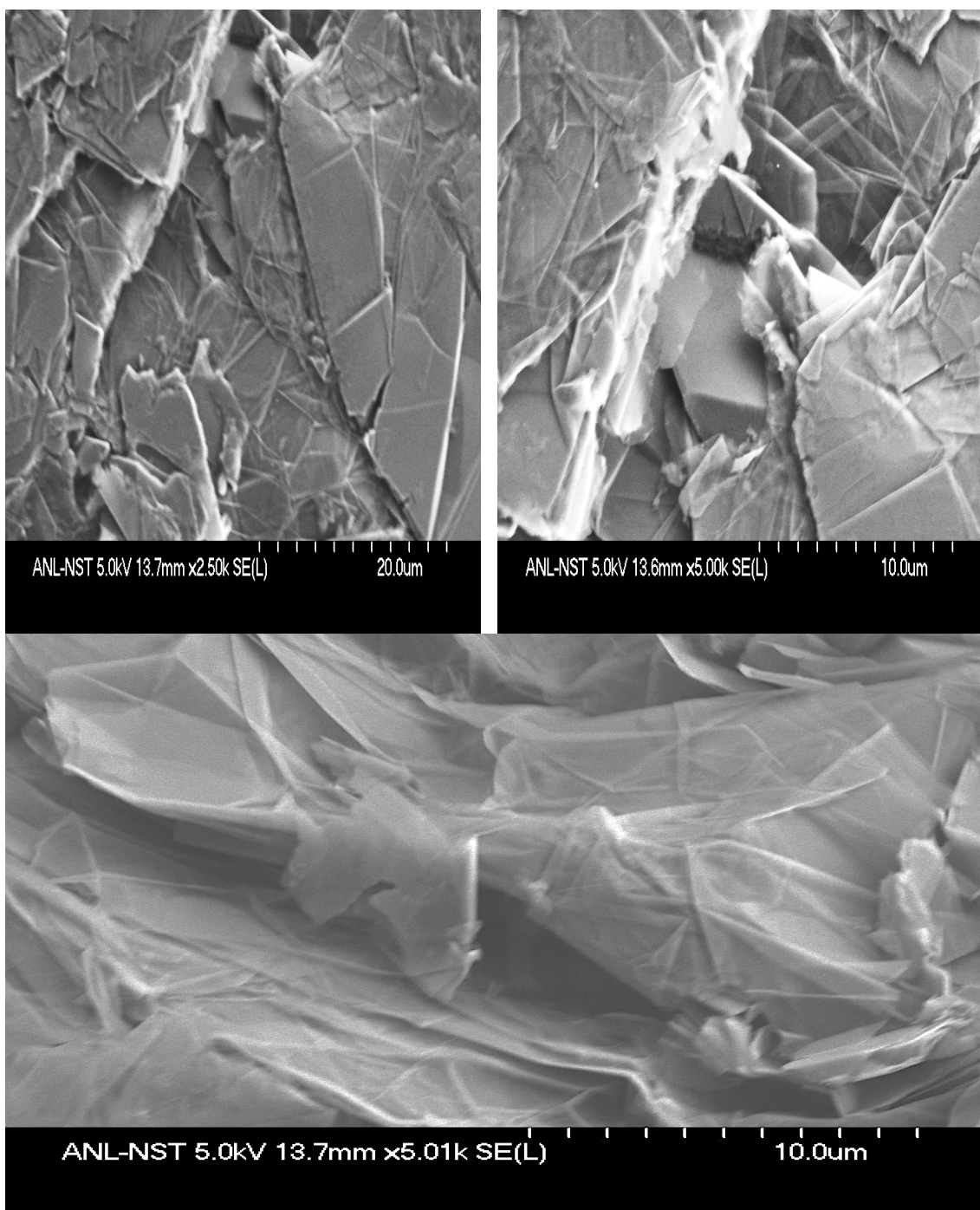


Figure 3.20: SEM images of graphite matrix (**paraffin impregnated**) showing at x2.50k, x5.0K and x5.01k magnifications for PCC-sample 1

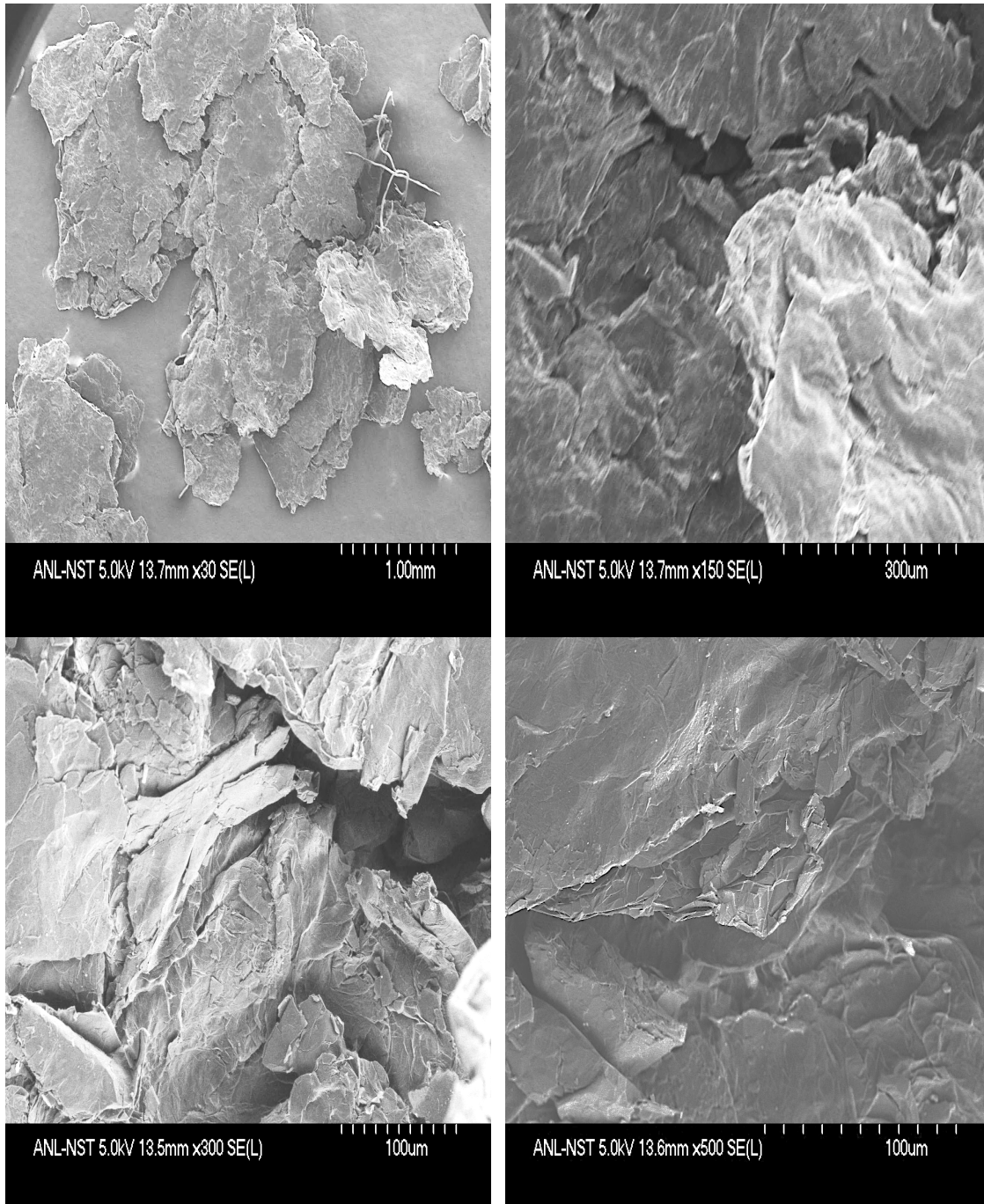


Figure 3.21: SEM images of graphite matrix (**paraffin impregnated**) showing at x30, x150, x300 and x 500 magnifications for PCC-sample 2

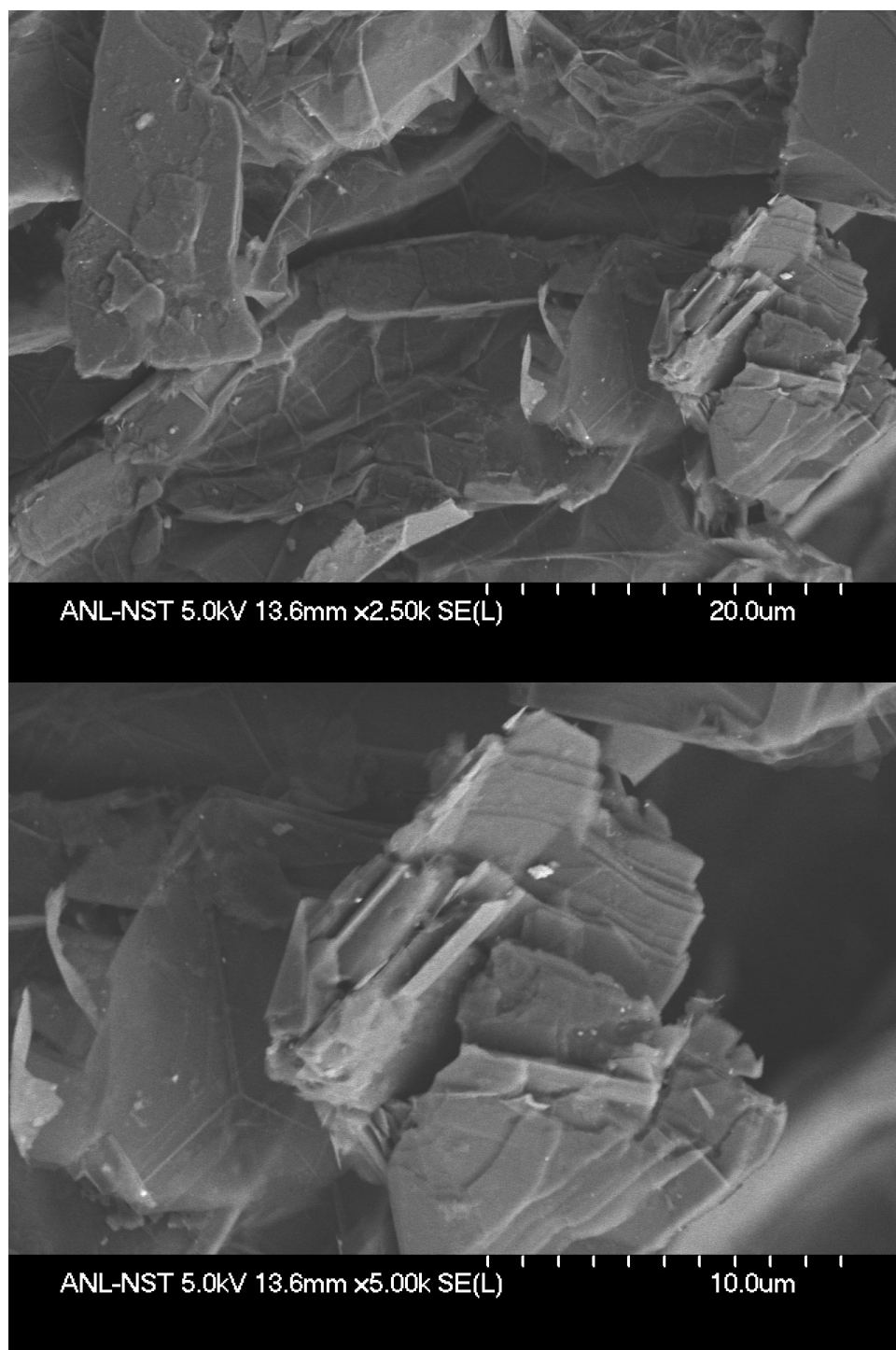


Figure 3.22: SEM images of graphite matrix (paraffin impregnated) showing at x2.5k and x5.0K magnification for PCC-sample 2

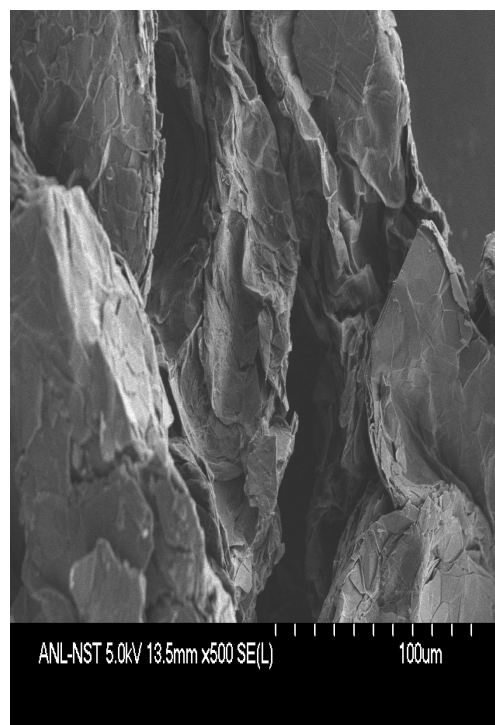
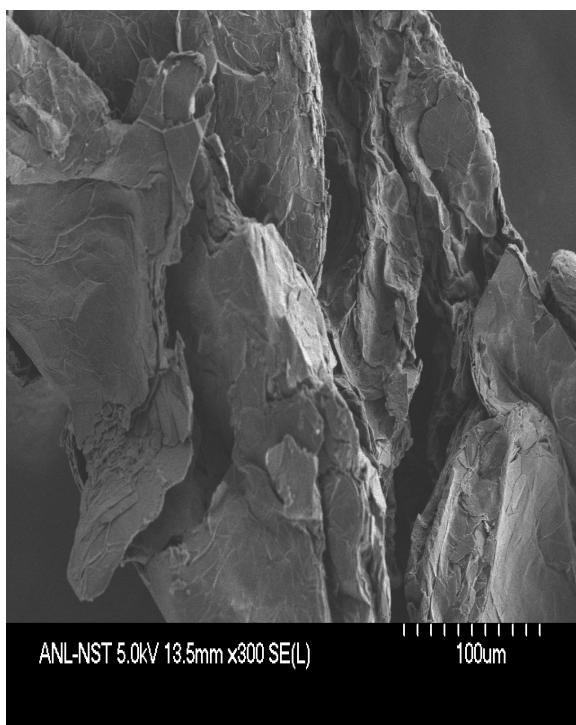
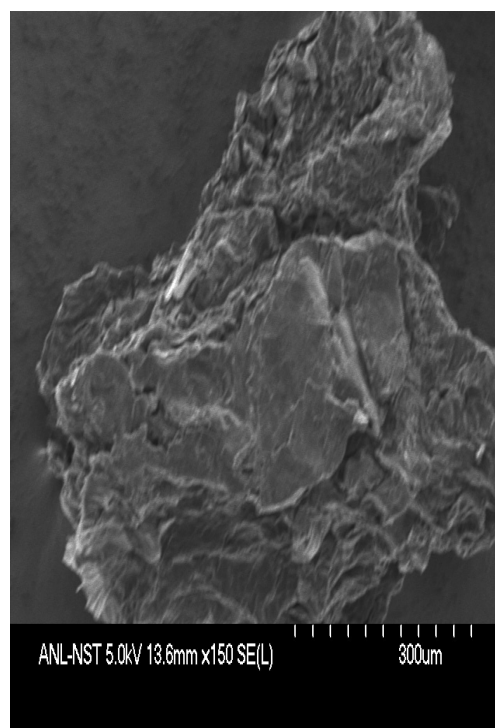
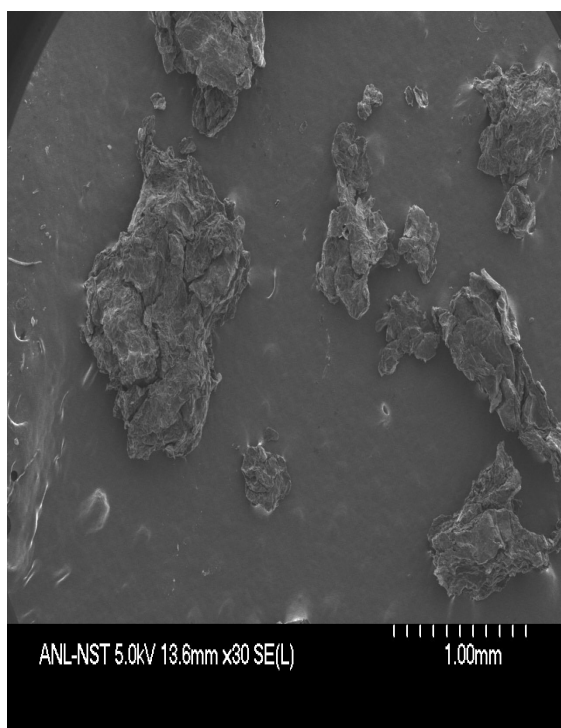


Figure 3.23: SEM images of graphite matrix (**paraffin impregnated**) showing at x30, x150, x300 and x 500 magnifications for PCC-sample 3

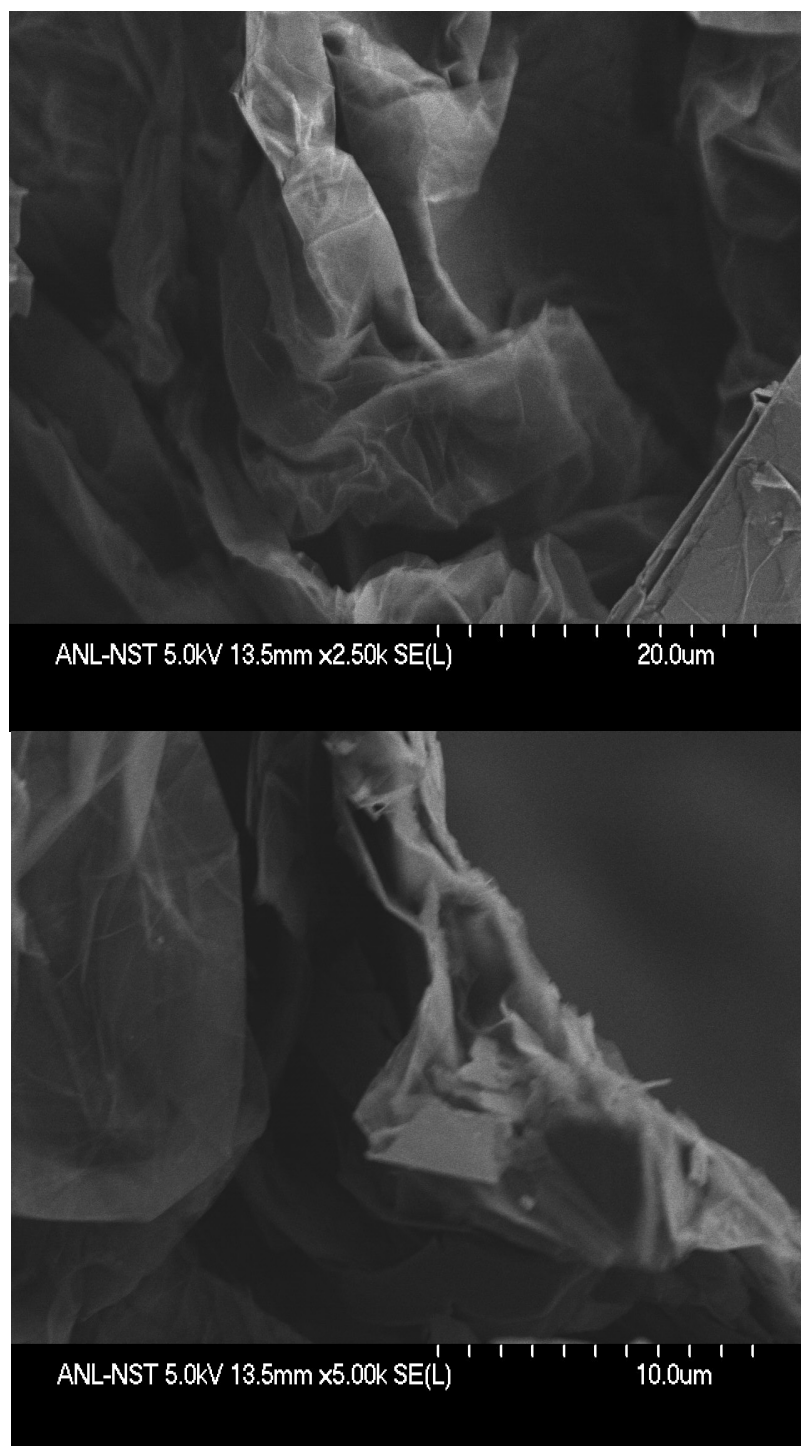


Figure 3.24: SEM images of graphite matrix (paraffin impregnated) showing at x2.5k and x5.0K magnification for PCC-sample 3

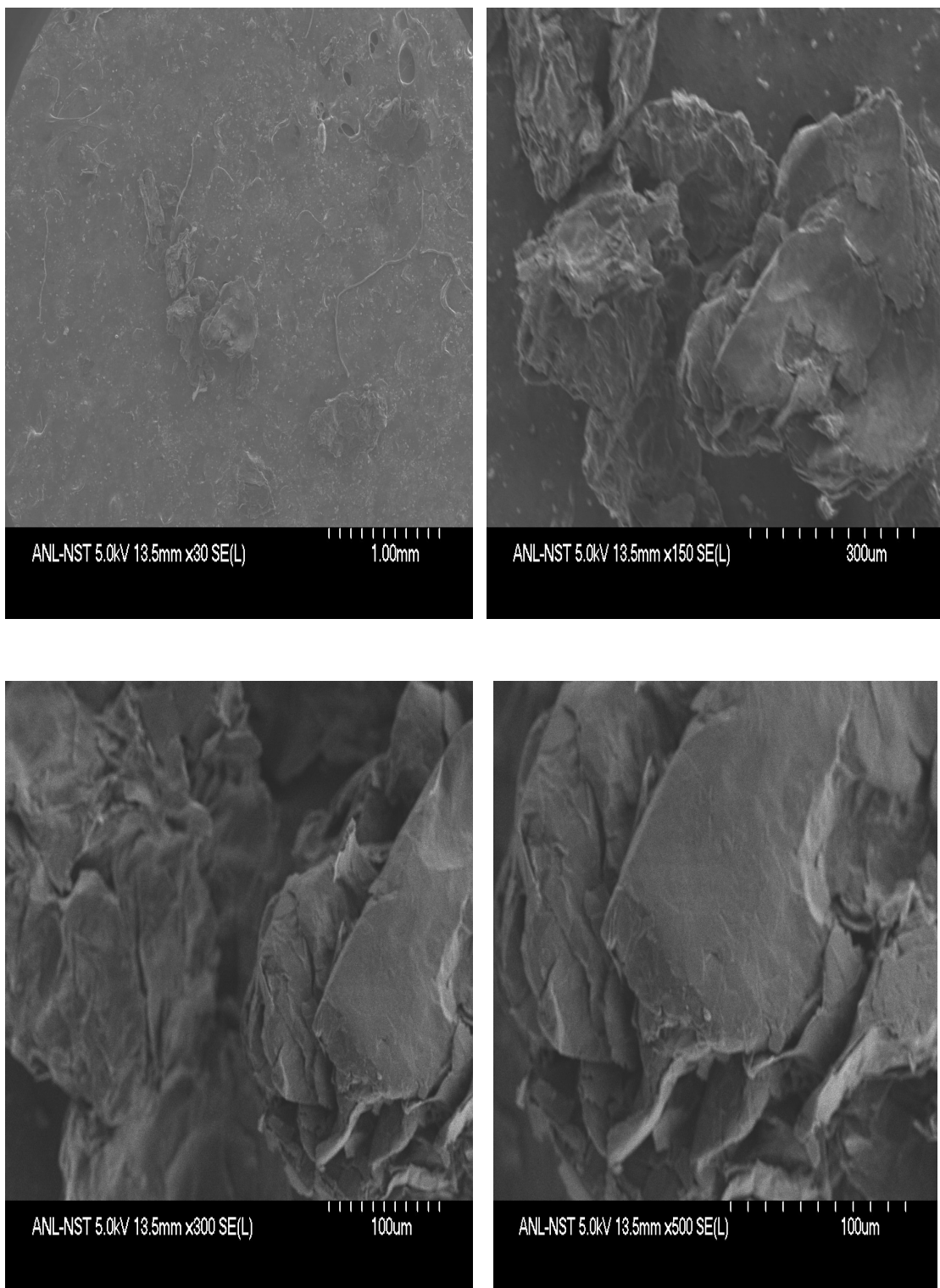


Figure 3.25: SEM images of graphite matrix (**paraffin impregnated**) showing at x30, x150, x300 and x 500 magnifications for PCC-sample 4

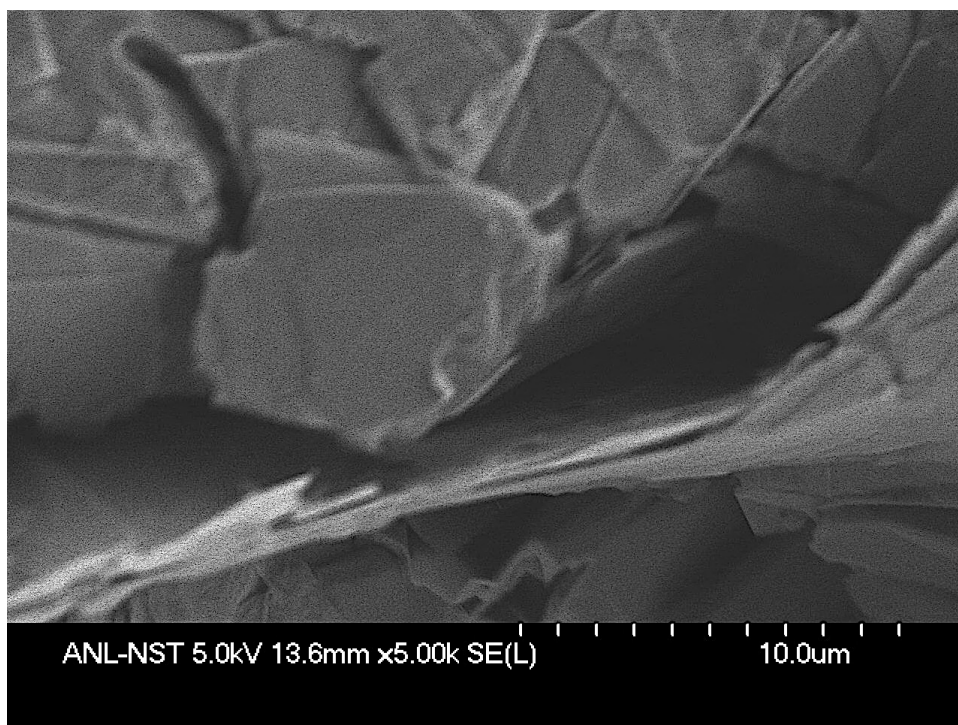
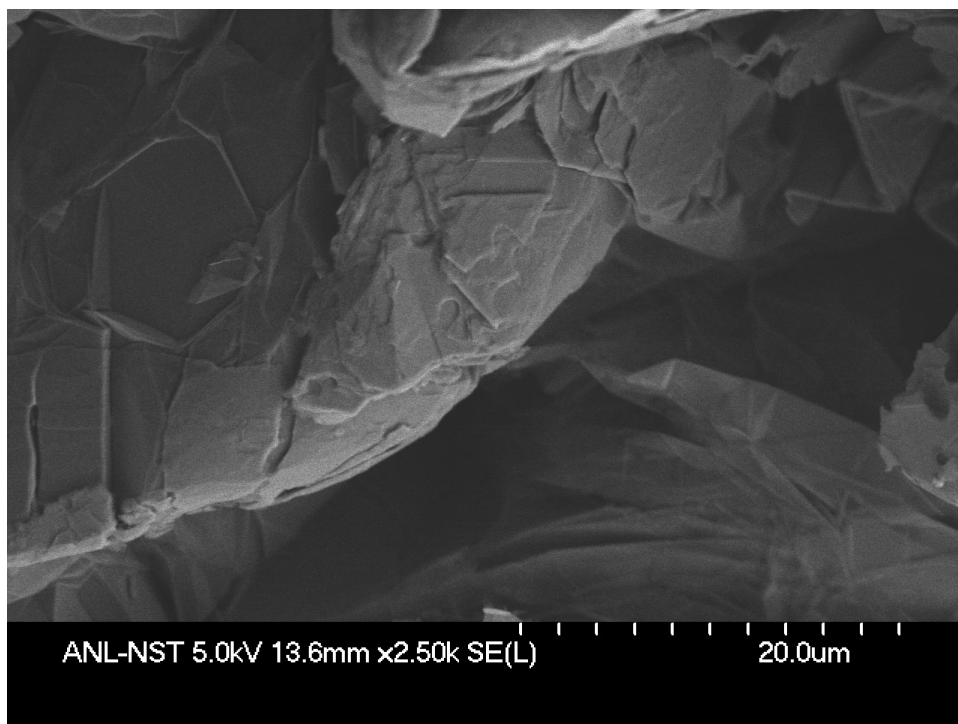


Figure 3.26: SEM images of graphite matrix (paraffin impregnated) showing at x2.5k and x5.0K magnification for PCC-sample 4

3.2.4 Stage four of PCC characterization: Crystalline structure analysis

XRD (X-ray diffraction) is widely used to study the structural characteristics of materials. The actual photo of the device used is illustrated by (Figure 3.27). In principle, X-ray is directed into the specimens. Then, X-ray scatters in response to the structure at a diffraction angle forming strong and/or weak intensity peaks indicating a predetermined structure as discussed by (Gogoi, Bhattacharyya, and James Raju 2011; Tao, Wei, and Yulan 2015) for similar expanded graphite materials. Many papers in the literature agreed and indicated that expanded graphite exhibits a strong peak at $2\theta = 26.52^\circ$ and a weak peak at $2\theta = 54.85^\circ$ as highlighted by (Gogoi, Bhattacharyya, and James Raju 2011) and many others like (Peng et al. 2018; Qu et al. 2017).

In this stage of characterization, specimens from the 2 sets of samples that were used for the SEM imaging are also used in this characterization stage. In this study, we want to examine if the compaction of the expanded graphite into different densities would change the crystal structure. We also want to examine if the impregnation with paraffin would change the crystal structure.

- Set-1 of samples:
 - CEG- Sample 1 (at a density of 670 g/l) with no paraffin impregnation.
 - CEG- Sample 2 (at a density of 490 g/l) with no paraffin impregnation.
 - CEG- Sample 3 (at a density of 380 g/l) with no paraffin impregnation.
 - CEG- Sample 4 (at a density of 150 g/l) with no paraffin impregnation.

- Set-2 of samples:
 - PCC- Sample 1: (the same as CEG- Sample 1), impregnated with paraffin.
 - PCC- Sample 2: (the same as CEG- Sample 2), impregnated with paraffin.
 - PCC- Sample 3: (the same as CEG- Sample 3), impregnated with paraffin.
 - PCC- Sample 4: (the same as CEG- Sample 4), impregnated with paraffin.



Figure 3.27: XRD device at Argonne Lab Facility.

3.2.4.1 CEG (Graphite only) Samples XRD patterns

XRD patterns for (4) samples of the same compressed expanded graphite (at various densities) are illustrated by (Figure 3.28) below.

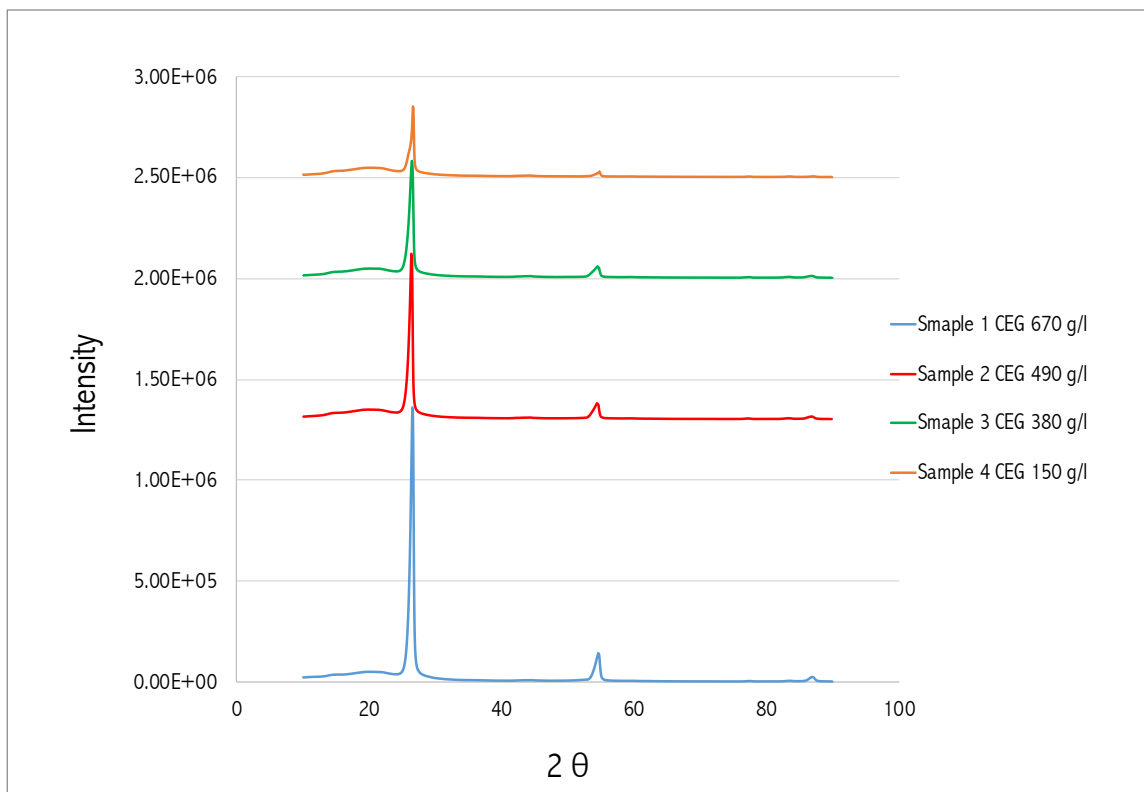


Figure 3.28: XRD patterns for (4) samples of the same compressed expanded graphite at various densities. (Please note: the patterns are actually on top of each other and they start from the same 0.0 intensity baseline. They were shifted vertically so that they can be clearly visualized). Identical locations of peaks clearly indicate no change in crystal structure.

The strong and weak peaks at all XRD patterns in (Figure 3.28) appear at the same locations that were discussed by many papers in the literature, indicating that compressing expanded graphite into different densities did not change the crystal structure of the expanded graphite. Higher density corresponds to the highest intensity and vice versa. The explanation for that is, the higher density samples have more organized structure which lead to more diffractions and accordingly higher intensity. Please note that XRD patterns

illustrated by Figure 3.28 are actually on top of each other and they all start from the same 0.0 intensity baseline. They were only shifted vertically so that they can be clearly visualized. Identical locations of peaks clearly indicate no change in the crystal structure.

3.2.4.2 PCC samples XRD patterns

XRD patterns for (4) samples of the PCC as showing in Figure 3.29 below.

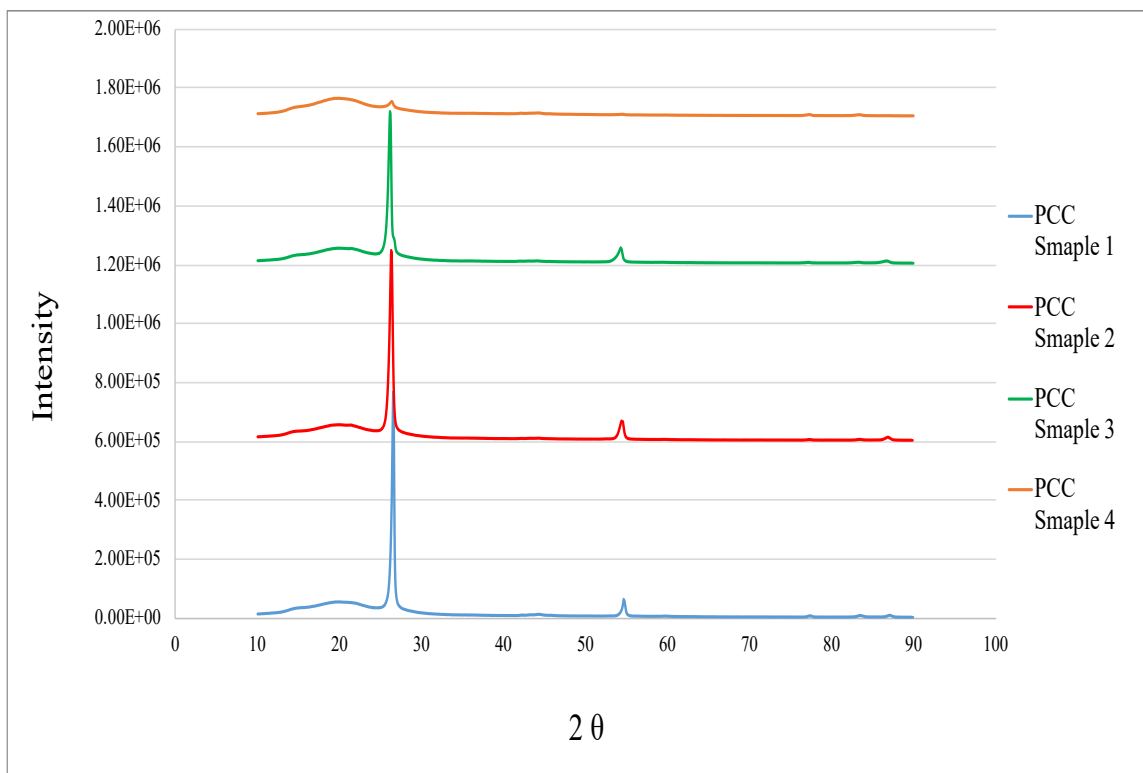


Figure 3.29: XRD patterns for (4) samples of PCC at various densities. (Please note: the patterns are actually on top of each other and they start from the same 0.0 intensity baseline. They were shifted vertically so that they can be clearly visualized. Identical locations of peaks clearly indicate no change in the crystal structure.

The strong and weak peaks at all XRD patterns in (Figure 3.29) appear at the same location as they appeared in (Figure 3.28) indicating that graphite impregnated samples (PCC) did not undergo any structure changes after the impregnation. Please note that XRD patterns illustrated by Figure 3.29 are actually on top of each other and they all start from the same

0.0 intensity baseline. They were only shifted vertically so that they can be clearly visualized. Identical locations of peaks clearly indicate no change in the crystal structure.

3.2.4.3 PCC Samples vs. Graphite Samples

XRD patterns from (Figures 3.28 and 3.29) are combined for each sample separately in (Figures 3.30 to 3.33).

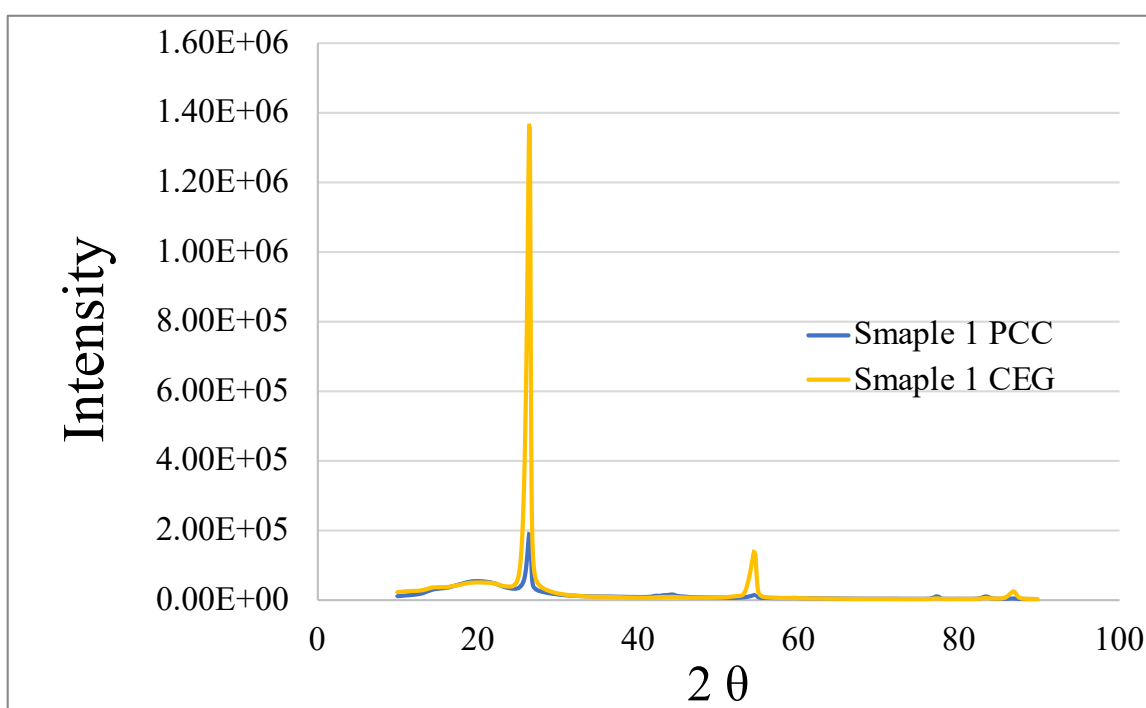


Figure 3.30: XRD patterns for Sample 1 of CEG and PCC.

Figure 3.30 illustrates the XRD patterns of CEG vs. PCC for sample 1. The peaks are in the same locations, but they were reduced so sharply (comparing PCC versus CEG for sample 1). The reason for the reduction in the intensity is the fact that the paraffin impregnated to the PCC reduced the diffraction of the x-ray and leads to a lower intensity.

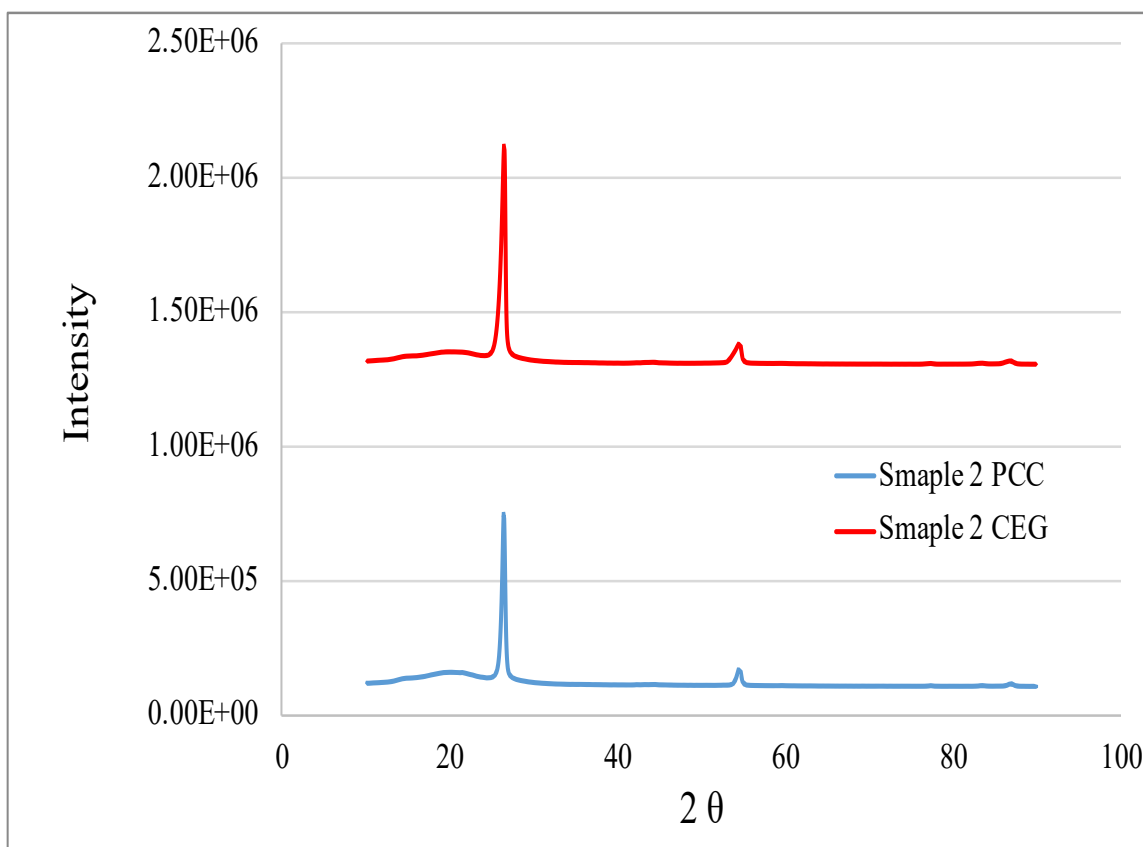


Figure 3.31: XRD patterns for CEG and PCC of sample 2. (Please note: the patterns are actually on top of each other and they start from the same 0.0 intensity baseline. They were shifted vertically so that they can be clearly visualized). Identical locations of peaks clearly indicate no change in crystal structure.

Figure 3.31 illustrates the XRD patterns of CEG vs. PCC for sample 2. The peaks are in the same locations indicating no change in crystal structure. The paraffin impregnated to the PCC reduces the diffraction and leads to a lower intensity. Please note that XRD patterns illustrated by Figure 3.31 are actually on top of each other and they all start from the same 0.0 intensity baseline. They were only shifted vertically so that they can be clearly visualized. Identical locations of peaks clearly indicate no change in crystal structure.

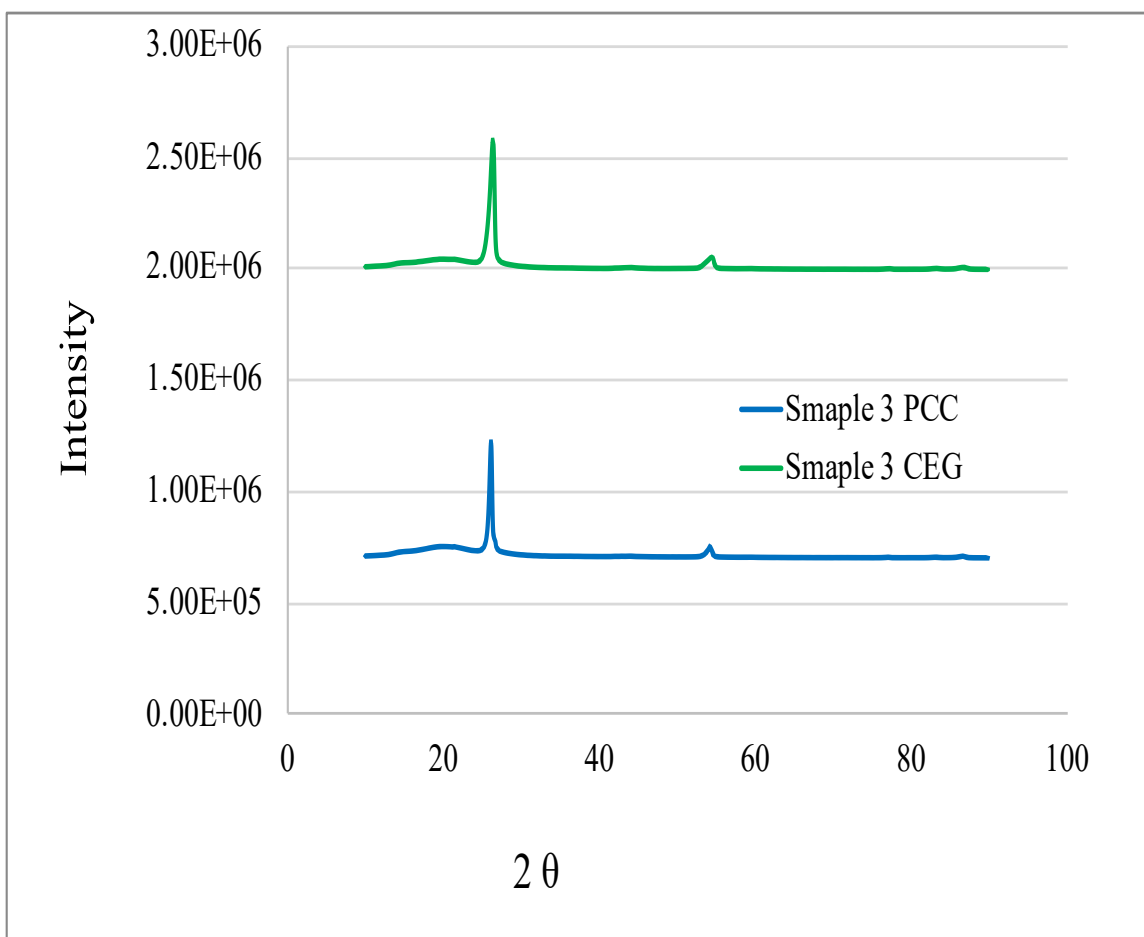


Figure 3.32: XRD patterns for CEG and PCC of sample 3. (Please note: the patterns are actually on top of each other and they start from the same 0.0 intensity baseline. They were shifted vertically so that they can be clearly visualized). Identical locations of peaks clearly indicate no change in crystal structure.

Figure 3.32 illustrates the XRD patterns of CEG vs. PCC for sample 3. The peaks are in the same locations. The paraffin impregnated to the PCC reduces the diffraction and leads to a lower intensity. Please note that XRD patterns illustrated by Figure 3.28 are actually on top of each other and they all start from the same 0.0 intensity baseline. They were only shifted vertically so that they can be clearly visualized. Identical locations of peaks clearly indicate no change in crystal structure.

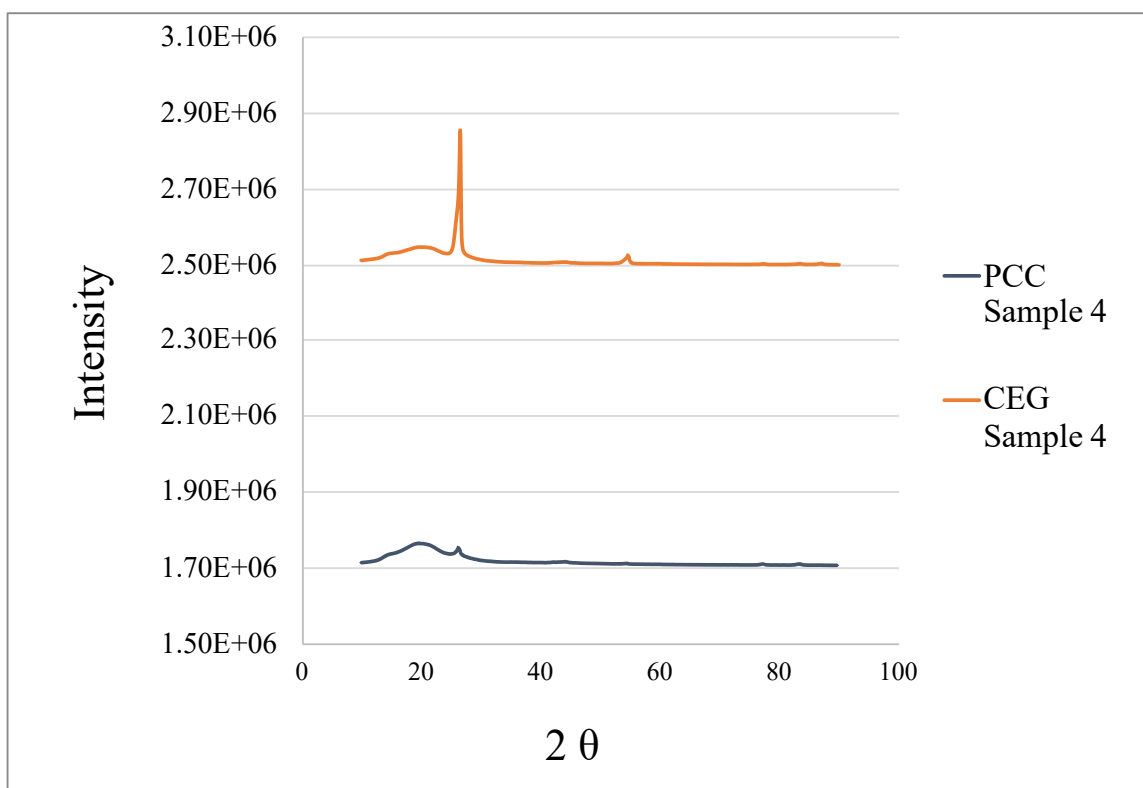


Figure 3.33: XRD patterns of CEG and PCC for Sample 4. (Please note: the patterns are actually on top of each other and they start from the same 0.0 intensity baseline. They were shifted vertically so that they can be clearly visualized). Identical locations of peaks clearly indicate no change in crystal structure.

Figure 3.33 illustrates the XRD patterns of CEG vs. PCC for sample 4. The peaks are in the same locations, but they were reduced so sharply. Sample 4 as introduced earlier has the lowest density. The PCC sample was impregnated with the highest percentage of paraffin among the other PCC samples. The paraffin impregnated to the PCC sharply reduces the diffraction and leads to a lower intensity. Please note that XRD patterns illustrated by Figure 3.33 are actually on top of each other and they all start from the same 0.0 intensity baseline. They were only shifted vertically so that they can be clearly visualized. Identical locations of peaks clearly indicate no change in crystal structure.

3.2.5 Stage five of PCC characterization: Mechanical Compression Testing

The physical property (stiffness) is widely evaluated using Universal Testing Machine (UTM) for mechanical compression testing device. Stiffness is described by Young's module. In particular, Young's module defines how materials deform under compression. Young's module defines the relationship between stress and strain. Stress is equal to the force per surface area (Units: N/m²). The strain, which is a dimensionless property, describes the proportional deformation in the material in response to the applied force. In other words, Young's module determines how stiff the material is. The higher the young's module the stiffer the material. The higher the young module the more elastic the material, hence, the smaller the deformation would be for a given applied load. Selecting a high stiffness material would ensure low elastic deformation at high load. Young's module is defined as the slope of stress vs. strain curve for the linear (reversible region) of the stress vs. strain curve. Young's module has the same units as stress (Pascal or Mega Pascal—Pa or MPa). On the other hand, yield strength is the point at which the material starts to experience an irreversible deformation. The maximum compressive strength is the maximum force applied per unit area before irreversibly deform the sample.

In this study, the mechanical compression experiment is conducted using the widely known Instron 3300R Floor Model Universal Testing System (an actual device used at AllCell Technologies lab is illustrated by Figure 3.34). Load accuracy $\pm 0.5\%$ of reading, extension rate accuracy $\pm 0.2\%$ of set speed. Data was collected using Instron Bluehill software. Five specimens (dimensions: 0.5-inch x 0.5-inch x 1-inch) were prepared for each of the four different densities of compressed expanded graphite impregnated with paraffin.

The specimens were collected from the samples used in the previous stages of this characterization chapter:

- PCC- Sample 1: (the same as CEG- Sample 1), but impregnated with paraffin.
- PCC- Sample 2: (the same as CEG- Sample 2), but impregnated with paraffin.
- PCC- Sample 3: (the same as CEG- Sample 3), but impregnated with paraffin.
- PCC- Sample 4: (the same as CEG- Sample 4), but impregnated with paraffin.



Figure 3.34: Mechanical testing device at AllCell Technologies Lab Facility.

As described earlier, Young's module defines the relationship between stress and strain in the linear of the stress vs. strain curve (which is the reversible region before prior to permeant deformation).

Yield strength is the point at which the material starts to experience an irreversible deformation. Maximum compressive strength is the maximum force applied per unit area to irreversibly deform the sample. As illustrated by Table 3.12 and (Figures 3.35 – 3.39), the higher the density of the sample the higher the stiffness, maximum compressive strength and yield strength of the sample.

Table 3.12: Mechanical compression testing for all four densities of compressed expanded graphite impregnated with paraffin evaluated for this study

Property	Young's Module (MPa)	Maximum Compressive Strength (MPa)	Yield Strength (MPa)
PCC- Sample 1	96.16	1.10	0.90
PCC- Sample 2	53.72	0.88	0.70
PCC- Sample 3	28.33	0.67	0.42
PCC- Sample 4	11.19	0.30	0.14

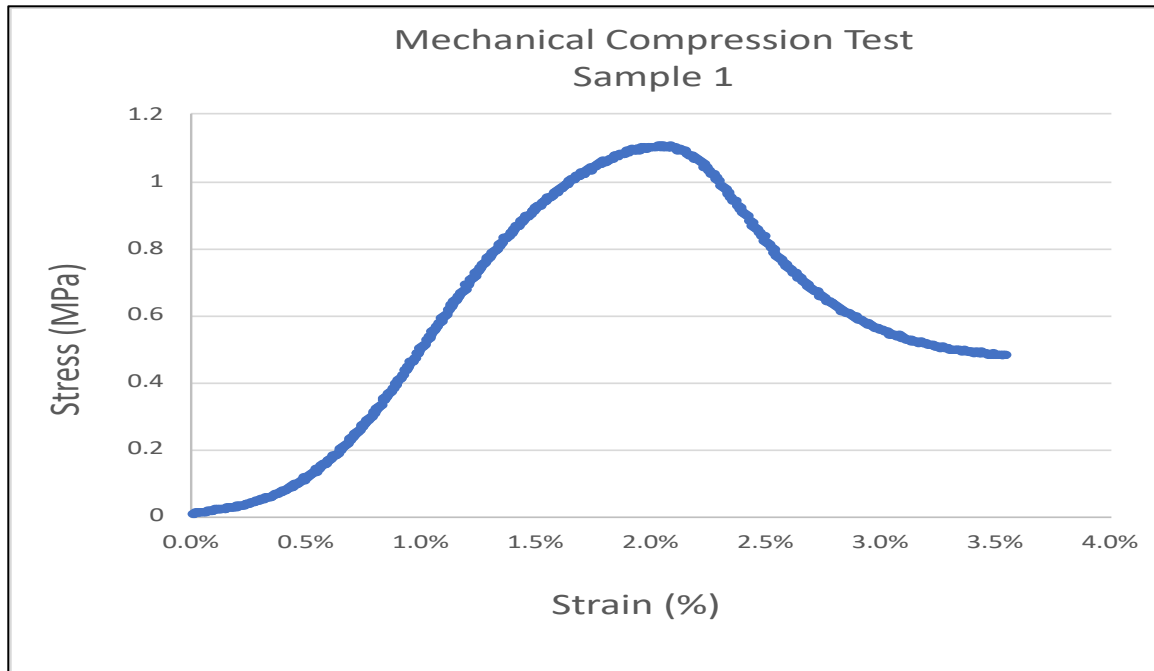


Figure 3.35: Mechanical compression test for PCC-Sample 1

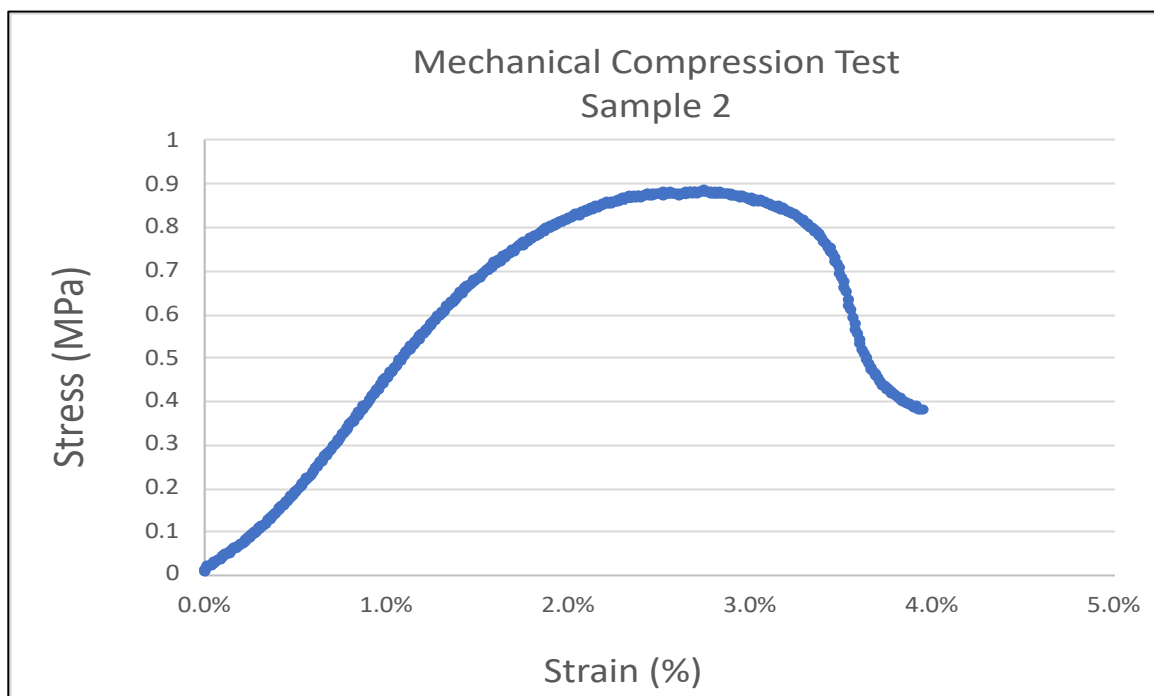


Figure 3.36: Mechanical compression test for PCC-Sample 2

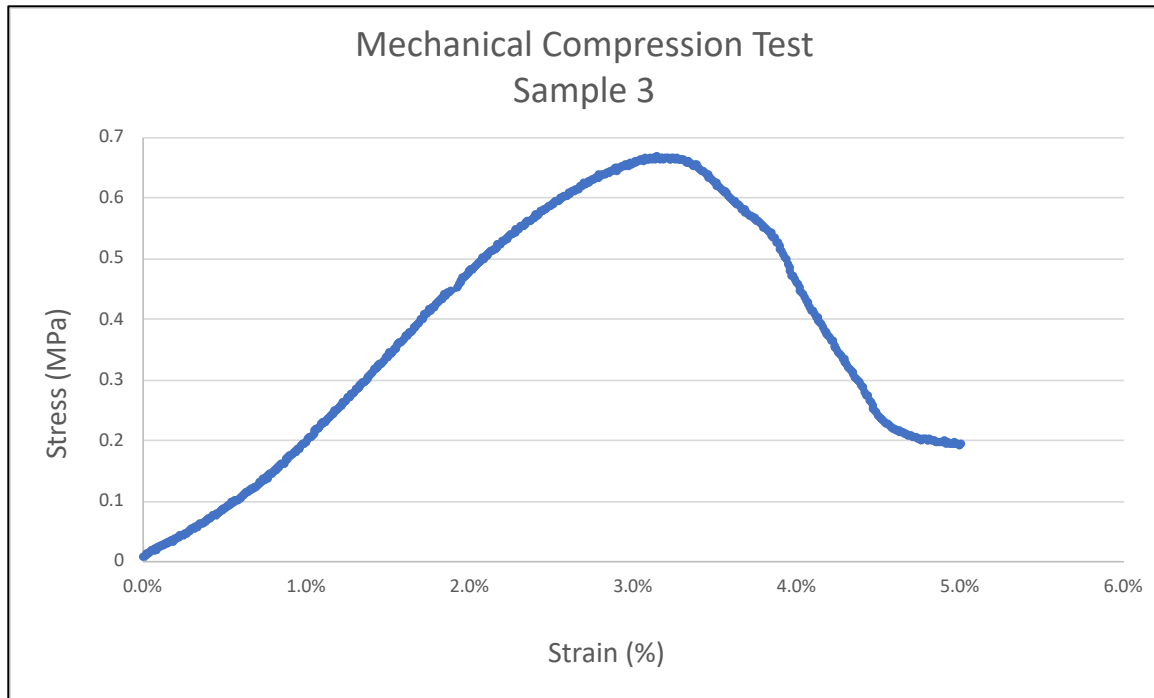


Figure 3.37: Mechanical compression test for PCC-Sample 3

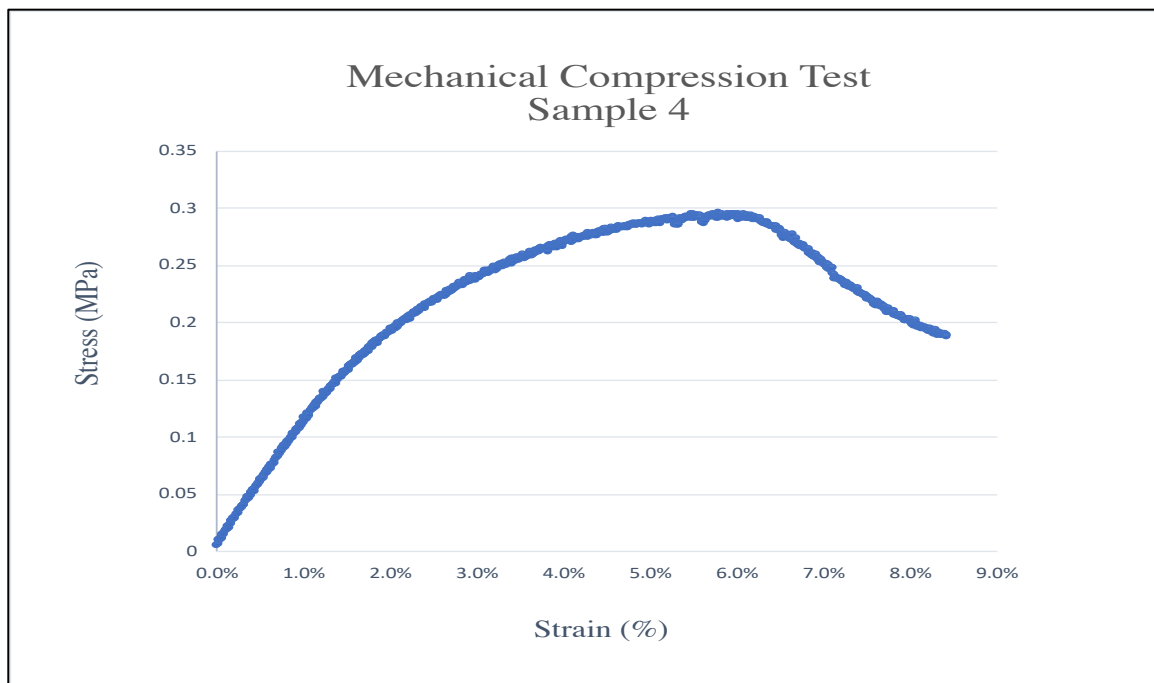


Figure 3.38: Mechanical compression test for PCC-Sample 4

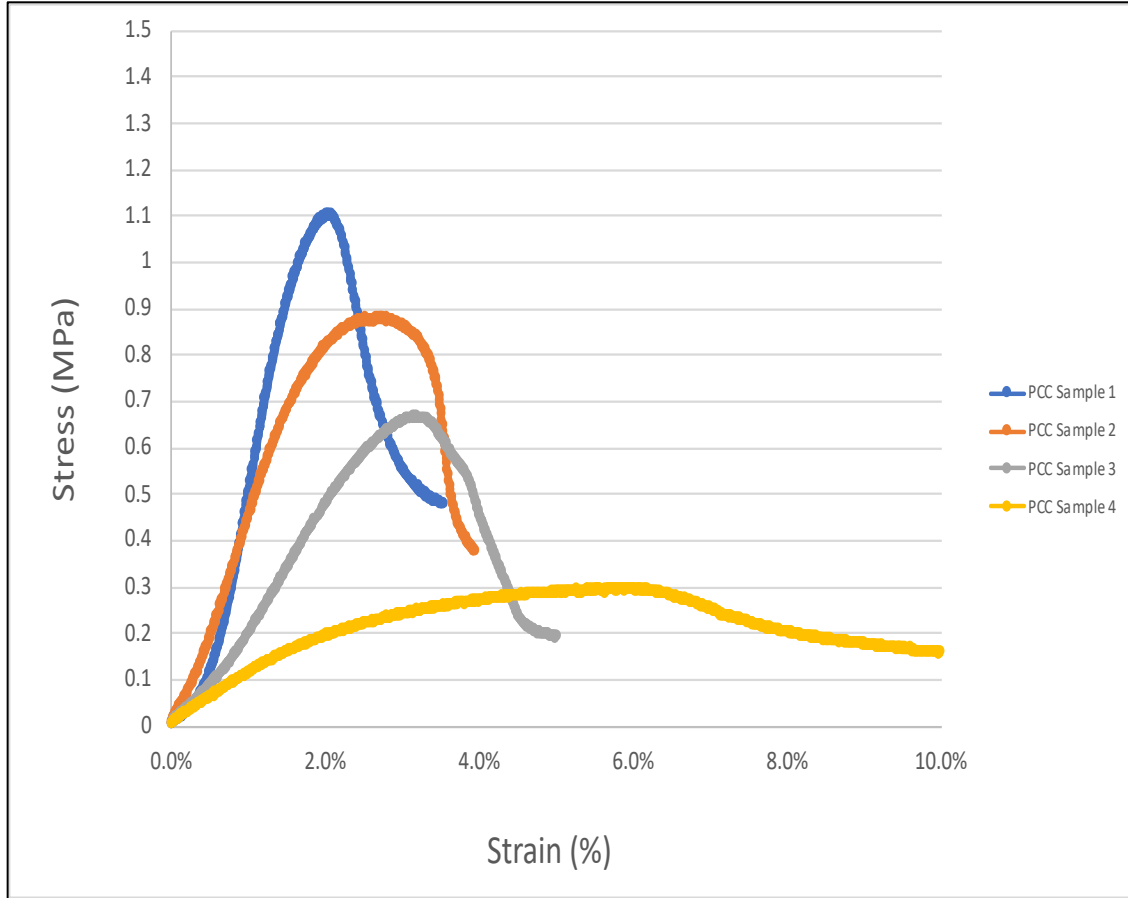


Figure 3.39: Mechanical compression test for PCC-Samples 1/2/3/4

3.3 Summary of observations from material characterization chapter

This chapter highlighted the characterization work performed by this study on the proposed phase change composite (PCC) material to serve as the energy storage medium in a thermal energy storage (TES) for air conditioning applications. Such characterization work for the proposed phase change composite, PCC, (consisting of 78% n-Tetradecane and 22% compressed expanded graphite) has not been reported in the literature. Both components of the proposed PCC are commercially available from local US suppliers and international suppliers. The PCC characterization was conducted in five stages. On stage one, identical

testing procedures were performed on multiple n-Tetradecane samples obtained from multiple local and international suppliers. All n-Tetradecane samples were analyzed with respect to a set of properties of interest such as latent heat in (kJ/kg), melting temperature in (degree Celsius), graphite impregnation ratio and finally evaporation rates from impregnated graphite samples in (microgram/m².s) at ambient conditions. Then, on stages two through five, samples of compressed expanded graphite impregnated with n-Tetradecane (C₁₄H₃₀), were examined and analyzed using DSC (Differential Scanning Calorimetry) for latent heat and melting range analysis, DXF-200 laser flash analyzer for thermal diffusivity analysis, SEM (Scanning Electron Microscope) for surface morphologies analysis, XRD (X-ray diffraction) for crystal structure analysis and UTM (Universal Testing Machine) for mechanical compression testing.

Table 3.13: Summary of observations from characterization experiments of proposed PCC, effects of varying density by compression on properties of interest

Relationship between density and material properties of interest	Density and ability to impregnate paraffin relationship	Density and thermal conductivity relationship	Density and crystal structure relationship	Density and mechanical strength relationship
Density of compressed Graphite	As density increases, the ability to impregnate paraffin decreases and consequently latent heat capacity decreases and vice versa	As density increases, thermal conductivity (in-plane direction) increases and vice versa	XRD patterns reveals no change on the crystal structure and vice versa	As density increases, mechanical strength increases and vice versa

As highlighted by (Table 3.13), the chapter also demonstrated that there is a trade-off between some of the properties tested. For example, as the density of the compressed expanded graphite matrix increases (by compression), porosity and ability to impregnate the phase change material and consequently heat capacity decrease while properties such as thermal conductivity and mechanical strength increase. No effect is recorded on the crystal structure as the graphite is compressed and density increases as shown by XRD analysis before and after the expanded graphite samples are compressed. On the other hand, as the density of the graphite structure decreases, porosity and ability to impregnate a phase change material and consequently latent heat capacity increase while thermal conductivity and mechanical strength decrease. No effect on the crystal structure of compressed expanded graphite is recorded if impregnated with the low-temperature paraffin (namely, n-Tetradecane) as shown by XRD analysis before and after impregnation of compressed expanded graphite samples.

CHAPTER 4: PCC-TES EXPERIMENTAL TESTING

The work illustrated in this chapter of the dissertation is published in the Journal of energy and conversion management:

A. Aljehani, S. A. K. Razack, L. Nitsche, S. Al-Hallaj, *Design and optimization of a hybrid air conditioning system with thermal energy storage using phase change composite*, Energy Convers. Manage. 169 (2018) 404–418. doi: 10.1016/j.enconman.2018.05.040.

4.1 PCC-TES structural overview

The PCC-TES system (Figures 4.1 and 4.2) consists of a stack of 28 slabs of PCC material that is composed of graphite and low-temperature phase change material (PCM). Compressed expanded graphite (CEG) is the structure that holds the phase change material PCM and boosts the overall thermal conductivity of the composite. The straight-chain paraffin, n-Tetradecane ($C_{14}H_{30}$), serves as the PCM that is capable of storing or releasing a large amount of heat during phase transition from solid to liquid or from liquid to solid. The whole PCC-TES structure is thermally insulated with building insulation materials. Each slab is a graphite structure that has been pressed and then soaked into a bath of n-Tetradecane for at least 24 hours until impregnated with n-Tetradecane. The slabs are numbered from top to bottom; top being number 1. As illustrated by (Figures 4.1 and 4.2), copper tubes pass back and forth in between the 28 slabs. A stream of Ethylene Glycol (EG) runs through the copper tubes. EG enters the PCC-TES structure from inlet provision at the top and exits from the bottom of the structure at outlet provision. EG mediates heat exchange between incoming hot air and the (thawing) PCC during discharging mode.

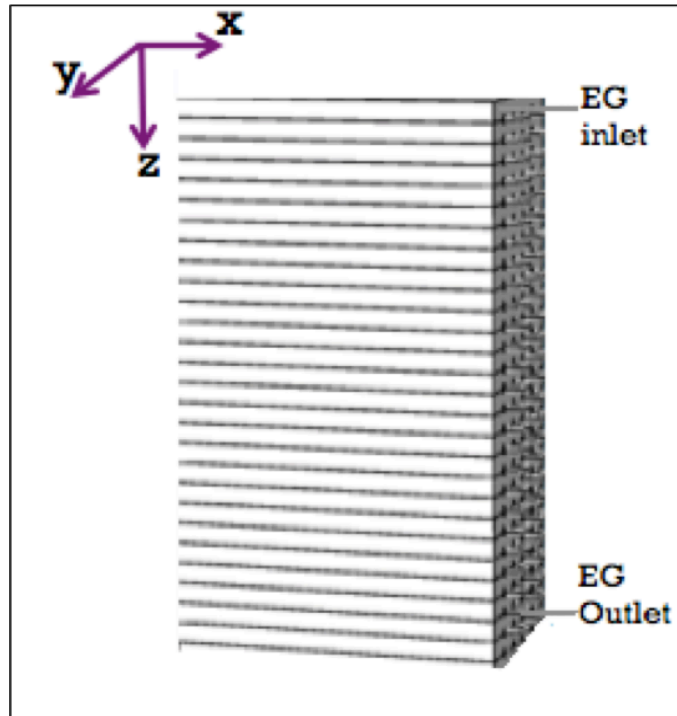


Figure 4.1: PCC-TES conceptual design; PCC-TES exchanging heat with EG stream [reference: (A. Aljehani et al. 2018)]

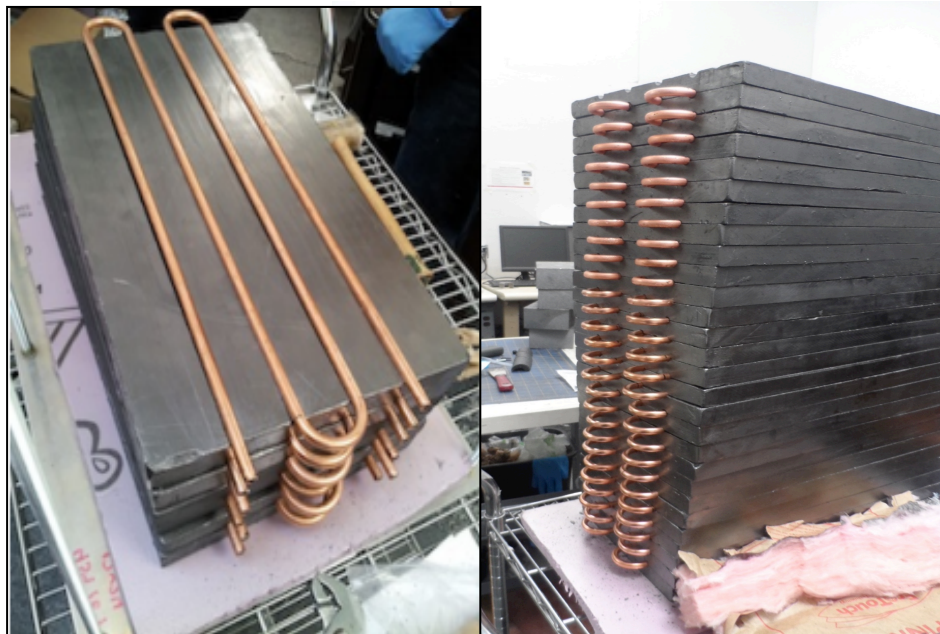


Figure 4.2: Actual representation of the proposed PCC-TES system [reference: (A. Aljehani et al. 2018)]

4.2 Materials and initial preparations of the PCC-TES structure

The overall 4 kWh PCC-TES benchtop system is designed for experimental testing and proof of concept purposes. The whole PCC-TES stack is thermally insulated (as illustrated by Figure 4.3) from outside boundaries with building's insulation materials. The PCC-TES system consists of a stack of 28 slabs of PCC material. Each slab of the PCC-TES is initially prepared by compressing the expanded graphite using a press machine targeting a density of $(150-200) \text{ kg/m}^3$. This targeted density has been determined to maintain the right balance between thermal conductivity and availability of latent heat capacity as discussed in the characterization chapter of this dissertation.



Figure 4.3: Inside view of the actual 4kWh PCC-TES structure (28 slabs stack)

After that, the compressed expanded graphite structure is cut to desired shape and dimension using a special pressing machine (CNC) and special molds.

Then, the compressed expanded graphite (CEG) structure is soaked into a liquid bath of a phase change material, namely n-Tetradecane, for at least 24 hours until the (CEG) structure is impregnated (or fully saturated) with n-Tetradecane. The slabs are stacked on top of each other forming the PCC-TES structure. The slabs are numbered from top to bottom; top being number 1 and bottom being number 28.

Thermocouples, T-type, were connected to preselected slabs to measure the temperature of the specific slabs during the experiment. Thermocouples for measuring the temperature of the inlet and outlet ethylene glycol stream were also connected at the inlet and outlet piping of EG. The temperature readings are recorded by the digital data logger (DAC) throughout the experiment. The digital data logger, SMARTDAC GP/20, is manufactured by Yokogawa Electric (Sugar Land, TX).

The copper tubes are sandwiched in between each two neighboring slabs. A special engraving made for the copper tubes at the surface of each slab.

Table 4.1 provides detailed information about the PCC-TES structure and the copper tubes.

Table 4.1: Detailed information about the PCC-TES structure and copper tubes for the experimental testing

Materials	
PCC Latent Heat (kJ/kg)	180
one slab Dimension: length, Width and thickness (m)	(0.46, 0.26 and 0.0254)
Number of Slabs (#)	28
Total Mass of PCC slabs (kg)	78
weight (%) of PCC/Graphite in each slab	(78% PCC) / (22% Graphite)
Total Copper tube's length (m)	5.724
Copper tube Outer diameter (in)	0.38
Copper tube Outer diameter (in)	0.32
Ethylene Glycol volumetric flow rate (l/min)	2.3
Ethylene Glycol inlet Temperature (C)	14
Solidified (cold) PCC initial temperature	-2

4.3 Experimental setup: design

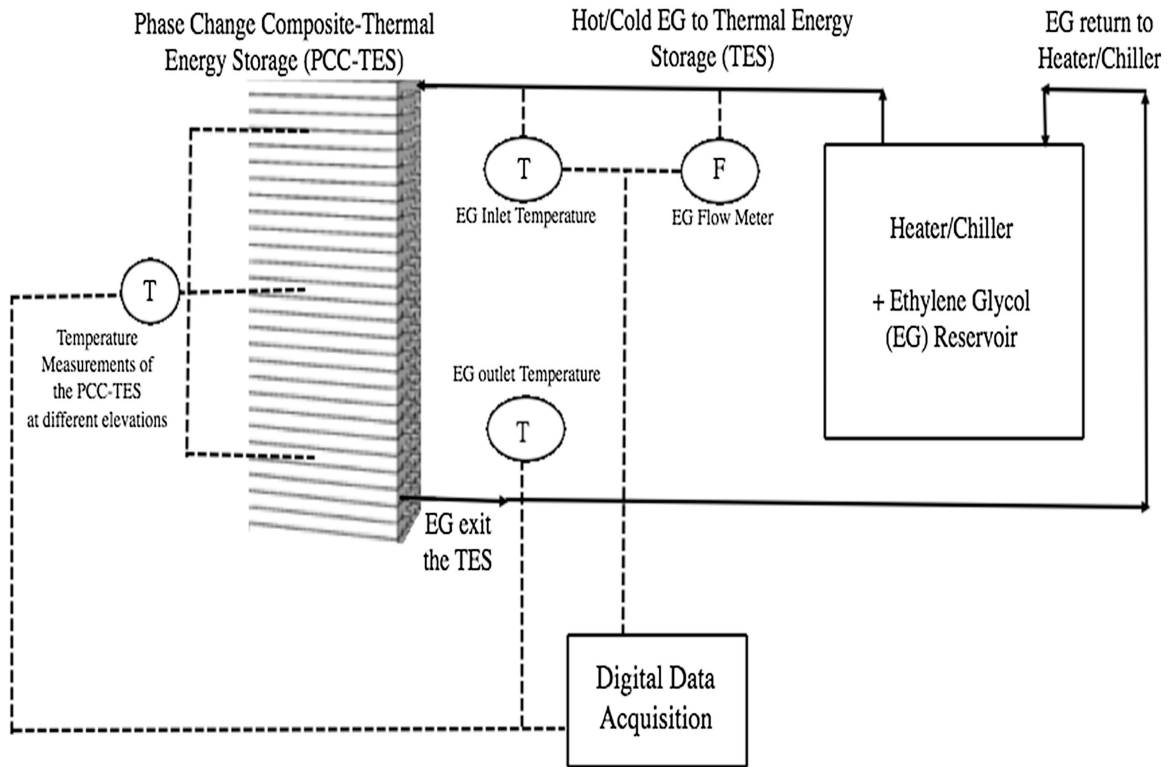


Figure 4.4: Schematic of the PCC-TES system's main components [reference: (A. Aljehani et al. 2018)]

As it is illustrated by (Figures 4.4 & 4.5), the experimental setup is divided into three main components: the actual 4 kWh PCC-TES structure, the copper tubes, and the electric heat exchanger.

The first component is the actual 4 kWh PCC-TES consisting of compressed expanded graphite (CEG) and n-Tetradecane, which serves as the phase change material PCM. CEG is the structure that holds the PCM and boosts thermal conductivity. The PCM or

specifically n-Tetradecane is the phase change material that is capable of storing or releasing heat depending on the mode of operations; whether discharging or charging.

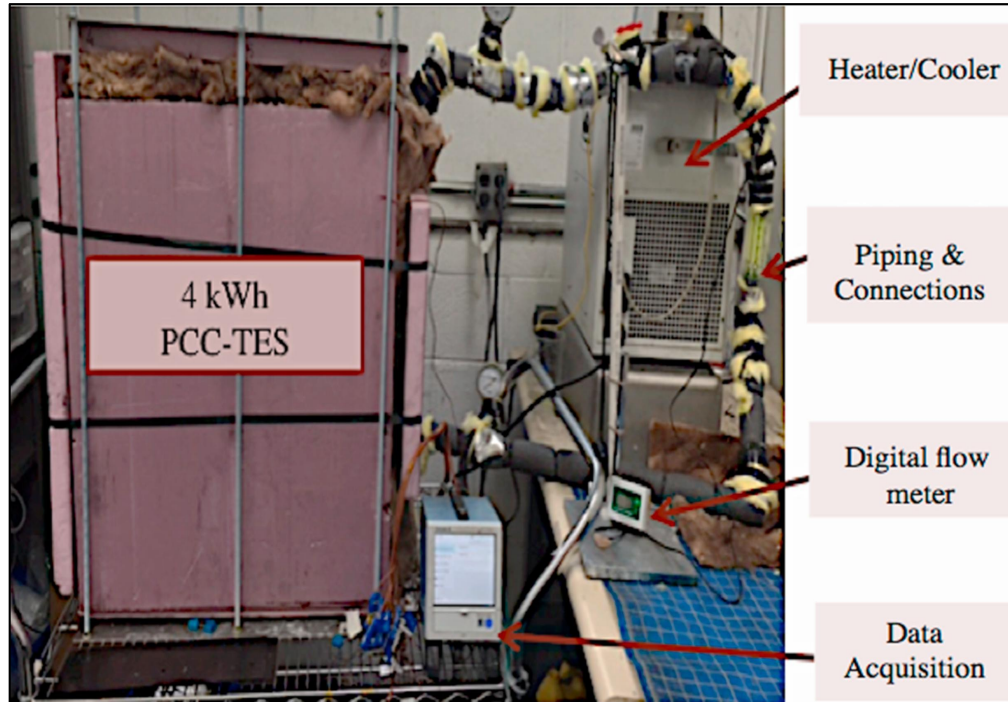


Figure 4.5: Actual 4kWh PCC-TES system's main components

The second component is the copper tube, which passes back and forth in between the 28 slabs, enters the PCC-TES structure from the top and leaves from the bottom of the structure. The copper tubes leaving the bottom of the PCC-TES structure are connected to the inlet piping of the electric heat exchanger. On the other hand, the outlet piping of the electric heat exchanger is connected to the copper tubes entering the top of the PCC-TES structure from inlet provision. The heat transfer fluid (HTF) stream, namely EG, runs through copper tubes circulating between the PCC-TES structure and the electric heat exchanger. A bypass piping is connected allowing the EG flow exiting the electric heat exchanger to circulate back to the heat exchanger without passing through the PCC-TES.

This bypass provision is used to ensure that EG flow reached a certain predetermined temperature and pressure before being introduced to the PCC-TES.

The third component is the electric heat exchanger that is the device that controls the temperature of the EG being pumped through the tubes to exchange heat with the PCC-TES. The electric heat exchanger serves as a reservoir for the EG. Depending on whether it is intended to be discharging or charging experiment, the electric heat exchanger set the temperature of the EG to 14 or -5 °C respectively. The electric heat exchanger has a built-in pump to boost the pressure of the EG.

4.4 Experimental setup: testing activity

There are two modes of operation for the PCC-TES which are the discharging mode and the charging mode. During the discharging mode, PCC-TES stores thermal energy and melts. In charging mode, the PCC-TES rejects the heat and solidifies. The discharging experiment was the chosen mode to be conducted, tracked, and discussed in this experimental chapter.

One of the main preparations steps for the discharging experiment is making sure the PCC-TES is actually solidified (charged) and ready to remove heat from a hot Ethylene Glycol (EG) stream. Therefore, hours before discharging experiment, the PCC-TES was completely charged (or solidified) using a cold EG stream circulating for few hours at -2 °C through the copper tubes. After that, all the thermocouples connected to the PCC slabs were reading a temperature of -2° C as a consequence of this cold circulation preparation

step. The 4 kWh PCC-TES system at -2°C marks a “completely solidified” or “completely charged” status.

The EG fluid flow rate was set to 2.3 liters per minute by adjusting the pump speed that is situated in the electric heat exchanger system. The EG will be circulating between the electric heat exchanger system and the PCC-TES structure. Now, for the discharging experiment, the initial temperature of the EG fluid was set to be pumped to the PCC-TES system inlet provision at 14°C by the electric heat exchanger controller. The official recorded starting time of the experiment was at the moment at which the 14°C EG was pumped through cold PCC-TES. Few minutes later, the temperature of the EG exiting the bottom of the PCC-TES dropped down to 6°C . This is because the hot EG stream is rejecting the heat to the 4 kWh PCC-TES system while running through the slabs. Then, the cold EG exiting the bottom of the PCC-TES at 6°C was continuously rerouted again to the electric heat exchanger to be heated again to 14°C . The EG continued to enter the top of the PCC-TES at 14°C and leaves the bottom of the PCC-TES at 6°C until the PCC-TES approached “completely melted” status. Accordingly, the temperature of the EG exiting the completely melted PCC-TES started to rise to about 8°C after a little over 3 hours of heat exchange. The discharging experiment was considered officially stopped at the moment at which the EG temperature reached 10°C approximately after 3 hours and 27 minutes.

4.5 Experimental Chapter: results and discussion

Figure 4.6 illustrates the experimental data of the discharging experiment. As introduced earlier there are T-type thermocouples that are connected to preselected slabs to measure

the temperature of the specific slabs during the experiment. Thermocouples for measuring the temperature of the inlet and outlet ethylene glycol stream were also connected at the inlet and outlet piping of EG. The temperature readings are recorded by the digital data logger (DAC) throughout the experiment. In Figure 4.6, the temperature probe labeled (slab #9) illustrating the temperature profile of the 9th slab of the actual benchtop PCC-TES, which is located at the top half of the PCC-TES. Likewise, the temperature probe labeled (slab #12) represents the temperature of the 12th slab located near the middle segment of the PCC-TES. As Figure 4.6 indicates, slab number 9 melted before slab number 12 because the hot EG enters the PCC-TES at the top and leaves out at the bottom. Likewise, slab number 18 melted before slab number 21 and after slab 12 as Figure 4.6 indicates. This illustrates a top to bottom melting profile of the slabs, which is a rational consequence of the fact that hot EG enters the PCC-TES from the top and leaves of the bottom.

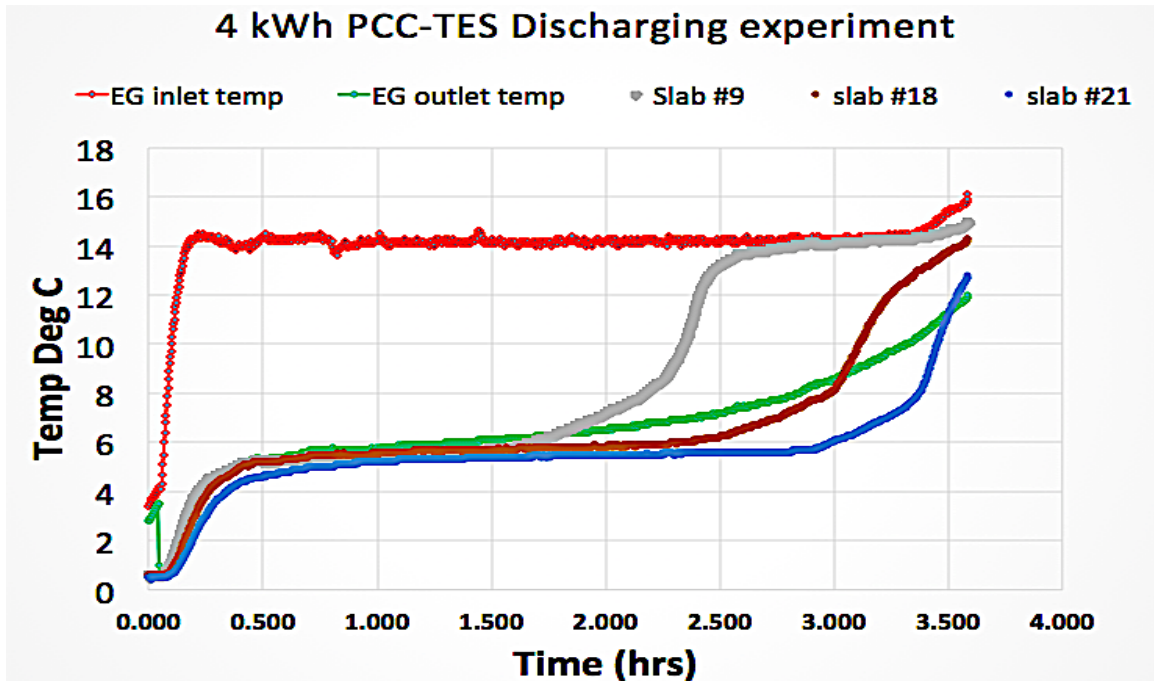


Figure 4.6: Discharging experiment of the actual 4 kWh PCC-TES [reference: (A. Aljehani et al. 2018)]

The PCC-TES discharging experiment proved the capability of the PCC-TES to operate as a heat sink absorbing approximately 14,400 kJ (or 4 kWh) from the hot EG loop during the entire discharging experiment (Table 4.2). The designed heat capacity of the PCC-TES is 4.4 kWh (4 kWh of latent heat storage + 0.4 kWh of sensible heat storage).

Therefore, based on actual experimental testing, the thermal efficiency of the PCC-TES is approximately 90%, while 10% was classified as heat losses. The experimental heat released by the EG (highlighted by Table 4.2) was calculated from the discharging experiment using the experiment volumetric flow rate of EG, density of EG, EG's specific heat and the average temperature driving force recorded during the experiment.

Table 4.2: Heat released by EG vs. PCC-TES designed heat storage

Heat Released by Ethylene Glycol (EG)		PCC-TES Designed heat Storage (Latent + Sensible)	
Volumetric flow rate of EG	2.3 liters/minute	Latent Heat	180 kJ/kg
Averaged overall duration of discharging experiment	220 minutes	Total weight of PCC	78 Kg
Specific heat (C_p)	3.3 kJ/kg. K	Specific heat (C_p)	1.6 kJ/kg. K
Experimental heat released by EG	14400 kJ	Designed heat storage (kJ) (latent+ sensible)	15840 kJ
Experimental heat released by EG	4 kWh	Designed heat storage (kWh) (latent+ sensible)	4.4 kWh

CHAPTER 5: SYSTEM LEVEL EVALUATION OF THE INTEGRATION CONCEPT USING PROCESS SIMULATION SOFTWARE (ASPEN PLUS ®)

The work illustrated in this chapter is published in the Journal of energy and conversion management:

Aljehani, S. A. K. Razack, L. Nitsche, S. Al-Hallaj, Design and optimization of a hybrid air conditioning system with thermal energy storage using phase change composite, Energy Convers. Manage. 169 (2018) 404–418. doi:10.1016/j.enconman.2018.05.040.

5.1 Proposed System

To guide formulation of the overall theoretical/computational model, and specifically of the block diagram in Aspen Plus®, we first address the [AC + PCC-TES] approach with reference to conceptual flowsheets that illustrate the complete system and its operation in charging (night) versus discharging (peak day) modes. As our point of departure, Figure 5.1 depicts a conventional AC refrigeration cycle where all of the air-cooling occurs within the evaporator. Figure 5.2 illustrates one possible integration of AC with PCC-TES. In discharging mode (Figure 5.3) during peak daytime hours, a portion of the incoming hot air stream is rerouted from the evaporator (air handling unit) to the hot air/EG exchanger where EG Loop #1 mediates cooling with the PCC material. Lifting a portion of the peak-cooling load from the AC cycle (partial shaving) means that the compressor can be reduced in size. An alternative approach would be to completely shave the cooling load during peak-hours by designing a larger PCC-TES system to entirely cool the hot air stream without operating the AC cycle at all. Figure 5.3 illustrates the charging mode, at which the PCC-TES rejects the stored heat and solidifies utilizing the vapor compression refrigeration loop of the conventional AC during inexpensive off-peak-hours.

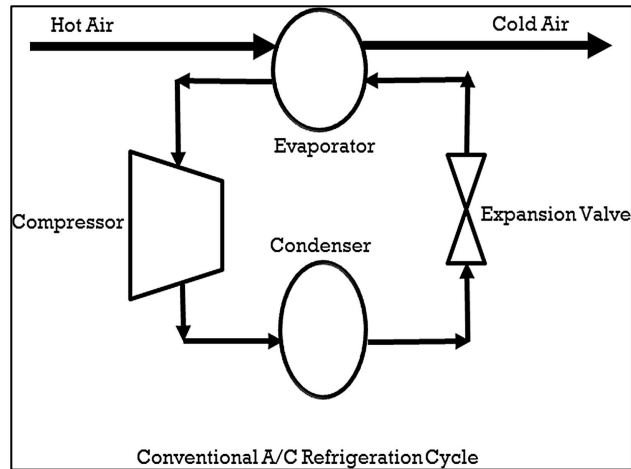


Figure 5.1: AC's conventional refrigeration cycle [reference: (A. Aljehani et al. 2018)]

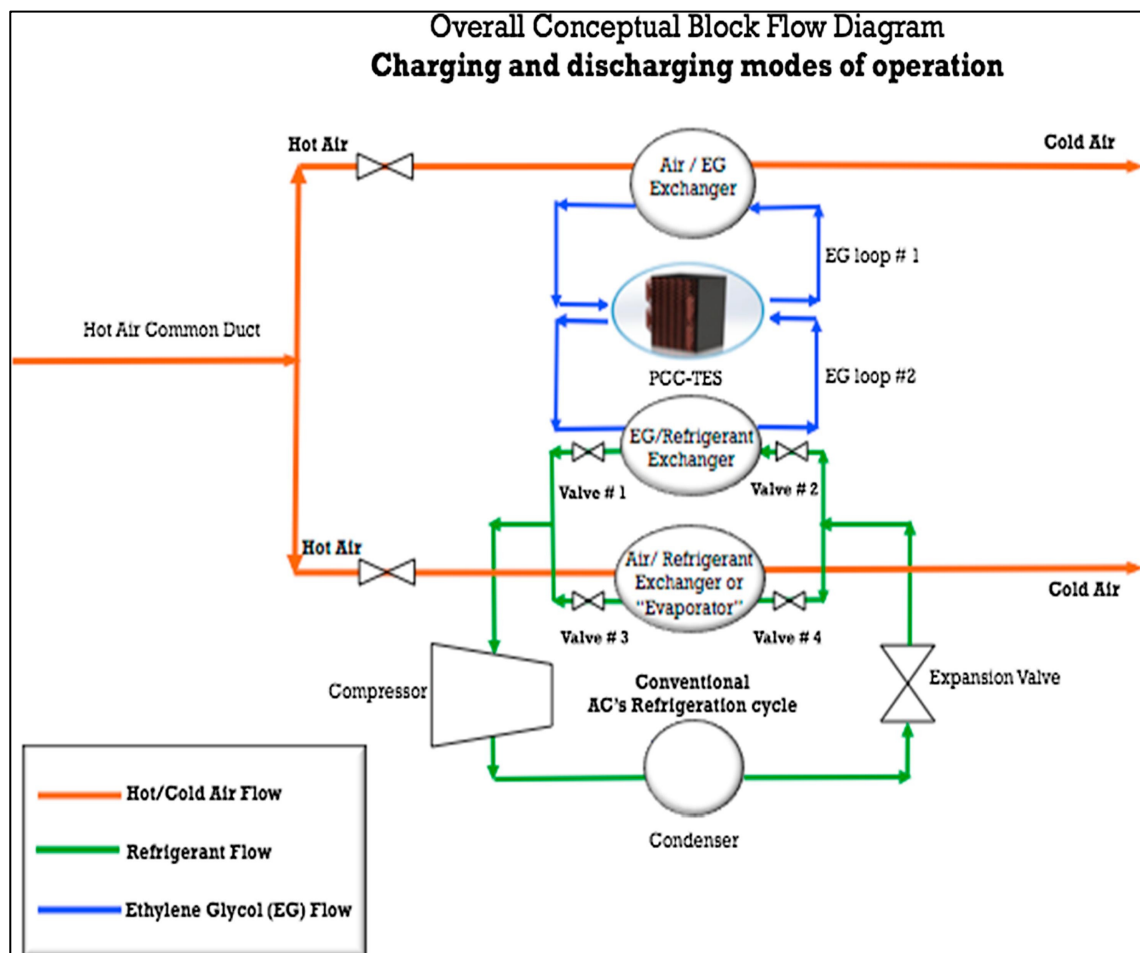


Figure 5.2: Complete system. EG Loop #1 mediates heat exchange between incoming hot air and the (thawing) PCC during discharging mode. EG Loop #2 mediates heat exchange between the refrigerant and the (freezing) PCC during charging mode. [reference: (A. Aljehani et al. 2018)]

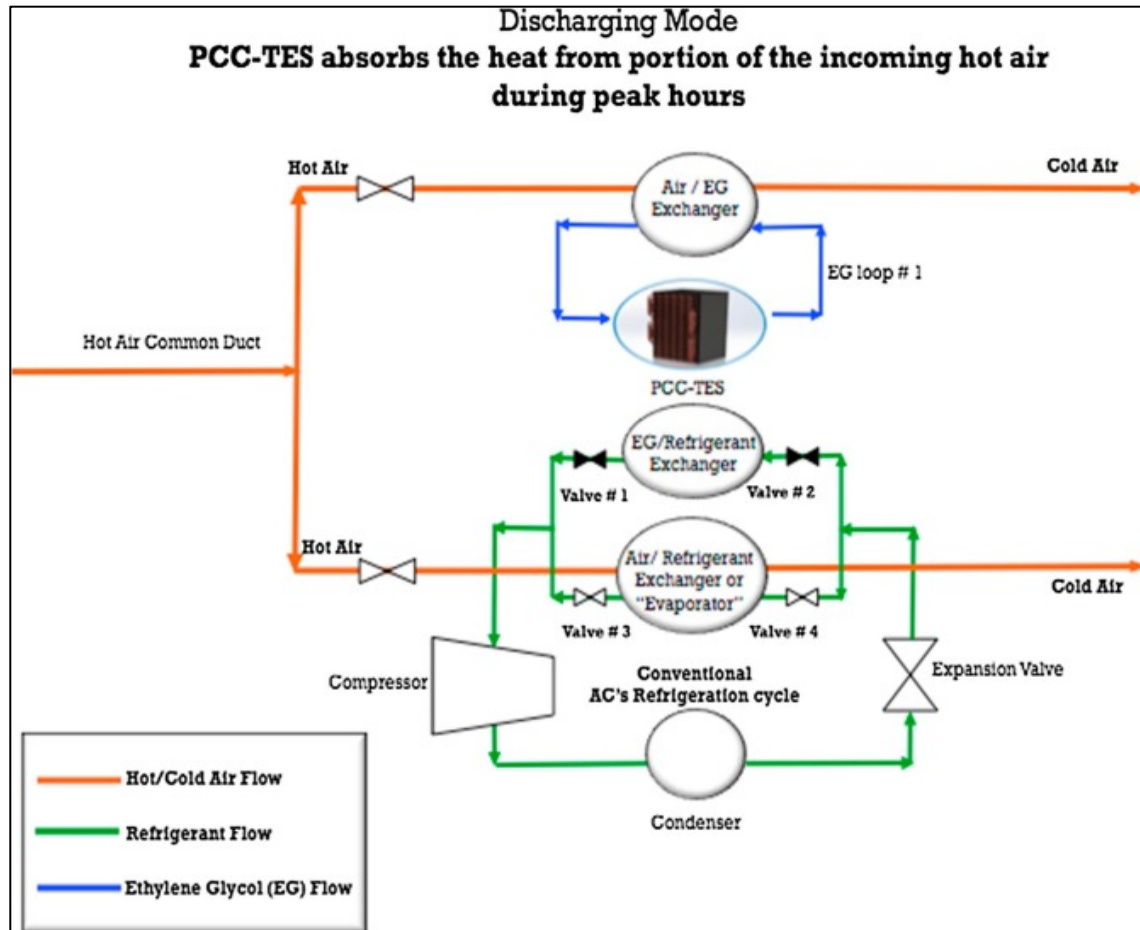


Figure 5.3: Discharging mode operates with valves 1 and 2 closed and valves 3 and 4 open. During peak day hours cooling of hot air is divided between the refrigerant loop and the melting PCC. [reference: (A. Aljehani et al. 2018)]

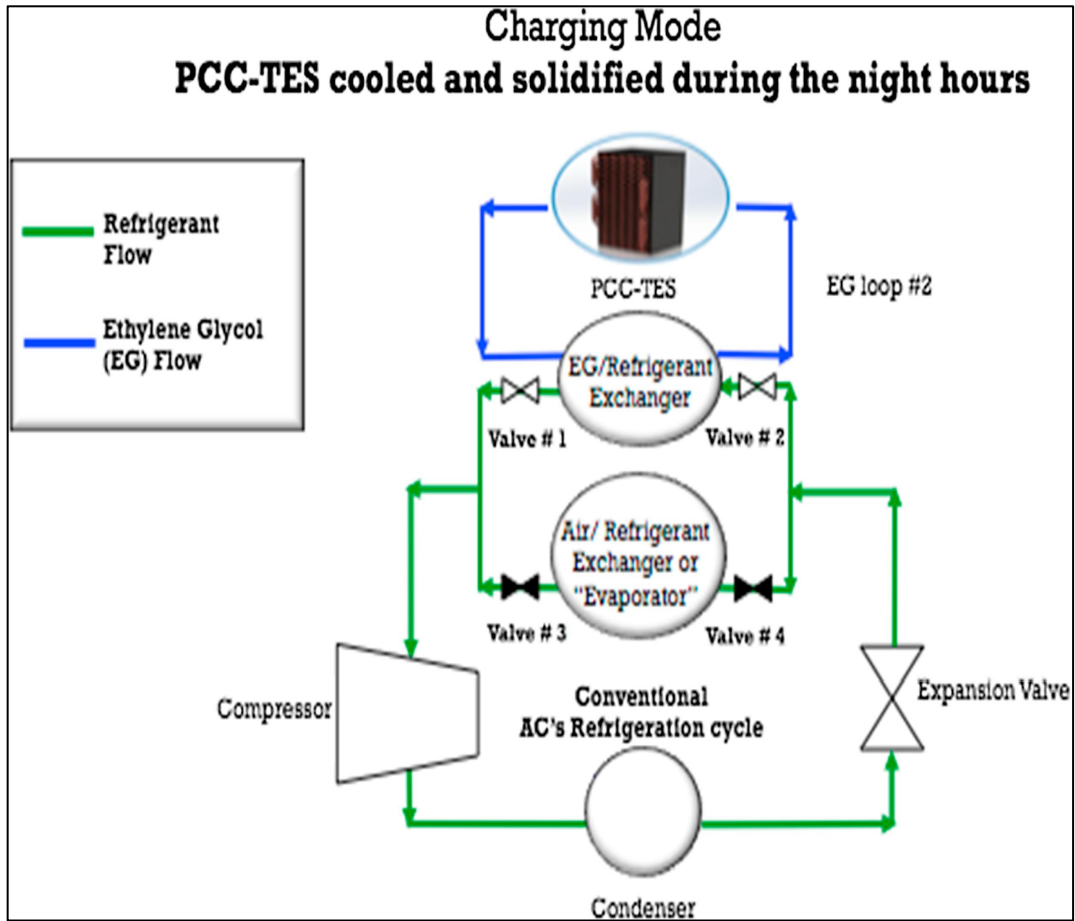


Figure 5.4: Charging mode operates with valves 1 and 2 open and valves 3 and 4 closed. During night hours the AC refrigerant loop cools and freezes the PCC. [reference: (A. Aljehani et al. 2018)]

As discussed in chapter 4, the PCC-TES system (Figures 5.5 and 5.6) consists of a stack of 28 slabs of PCC material that is composed of graphite and low-temperature phase change material (PCM). Each slab is (46 x 26 x 2.54) cm and weighs 2.79 kg (22% graphite and 78% graphite). Graphite is the structure that holds the phase change material PCM and boosts the thermal conductivity of the composite. The paraffin, n-Tetradecane ($C_{14}H_{30}$), serves as the PCM that is capable of storing or releasing a large amount of heat during the phase change (solid to liquid) or (liquid to solid). The whole PCC-TES structure is thermally insulated with building insulation materials. Each slab is a graphite structure that has been pressed and then soaked into a bath of n-Tetradecane for at least 24 hours until

impregnated with n-Tetradecane. The slabs are numbered from top to bottom; top being number 1. As illustrated by Figures 5.5 & 5.6, copper tubes pass back and forth in between the 28 slabs. A stream of Ethylene Glycol (EG) runs through the copper tubes. EG enters the PCC-TES structure from an inlet provision at the top of the structure and exits from the bottom of the structure. EG (as illustrated by Figure 5.2, loop # 1) mediates heat exchange between incoming hot air and the (thawing) PCC during discharging mode.

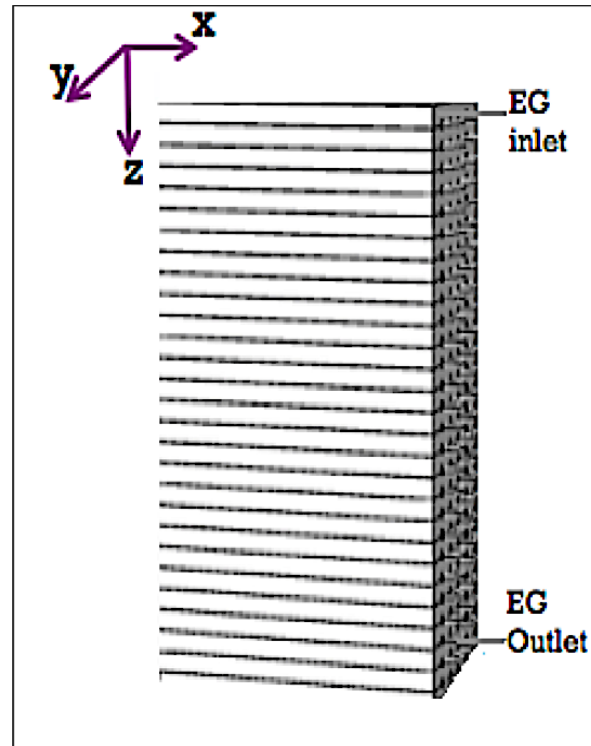


Figure 5.5: PCC-TES conceptual design; PCC-TES exchanging heat with EG stream

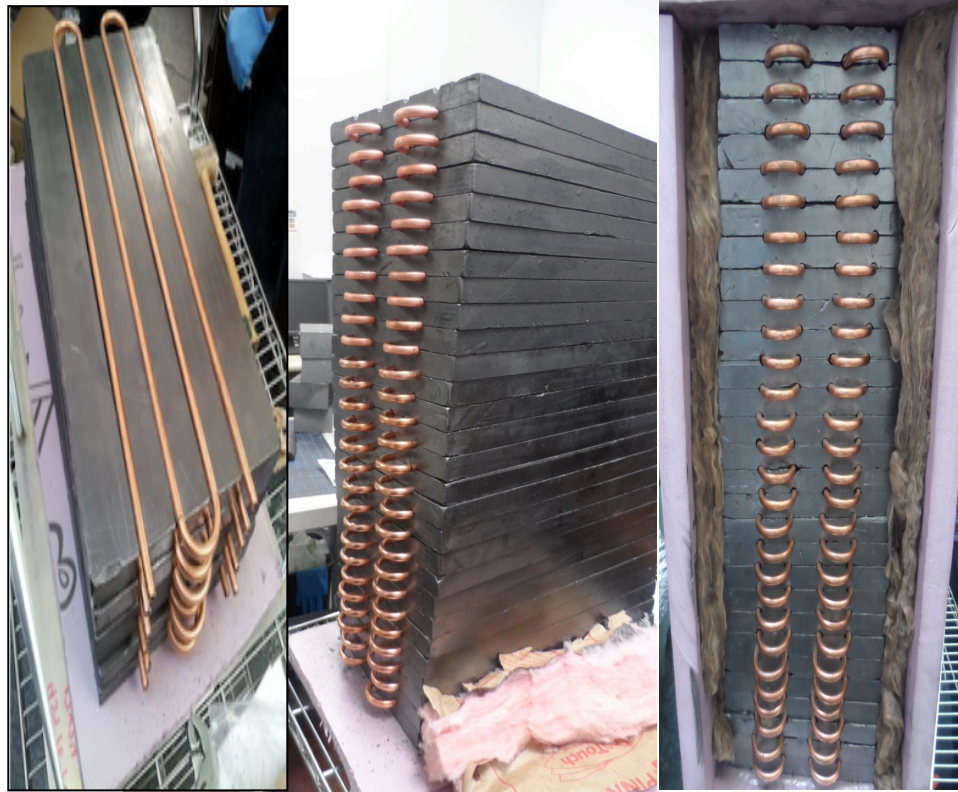


Figure 5.6: Actual representation of the proposed PCC-TES system

5.2 The Aspen Plus® model

Guided by the conceptual flowsheet, the first part of the simulation model was built using the Aspen Plus® flowsheet environment imitating the overall integration between the PCC-TES and the AC system. This portion simulates the AC's vapor compression refrigeration loop, both EG loops and the hot and cold air streams entering and exiting the air-handling units. Although Aspen Plus® can properly simulate an air conditioning refrigeration loop, it does not have a built-in library to predict melting and solidification behaviors of a PCC material. The accurate computation of melting and solidification behavior would assist in estimating the heat absorbed/released in association with any particular stage of melting or

solidification respectively. This section will shed some light on the generation of the Aspen Plus® flowsheets while the next section will address the mathematical heat transfer model that we formulated as a system of equations and programmed it into Fortran; which was eventually written within a calculation block in Aspen Plus® to communicate with the Aspen Plus® simulation environment.

Three Aspen Plus® main flowsheets were generated. The first flowsheet simulates a conventional vapor compression refrigeration loop of a conventional air conditioning system. The conventional air conditioning system in this study will be evaluated to either provides (1) the entire cooling load (the conventional base case) or (2) half of the cooling load (reduced load case), being augmented by the PCC-TES.

The second flowsheet simulates the discharging mode of the PCC-TES, by which PCC-TES meets the remaining half of the cooling demand by melting the PCC material. Even though the AC and the PCC-TES work jointly (in the proposed integration scenario) to meet the cooling demand, the two systems were simulated in two different flowsheets to avoid confusion and to show that each process is independently meeting half of the entire cooling demand on its own.

The third flowsheet simulates the charging mode of the PCC-TES; at which the conventional vapor compression refrigeration loop will cool and solidify the PCC-TES during the night.

5.2.1 The first flowsheet – conventional vapor compression cycle

The first flow sheet is comprised of conventional refrigeration loop components. The purpose of the first flowsheet is to benchmark the base case (Figure 5.7) with the reduced load case (Figure 5.8). The first flowsheet represents the base case (Figure 5.7) of a conventional vapor compression refrigeration loop to meet the entire cooling demand.

The first flowsheet (Figure 5.7) simulated the four major components of the vapor compression refrigeration loop; which are the evaporator, the compressor, the condenser and the throttle valve. The refrigerant used in the vapor compression refrigeration loop is R-410A which is composed of 50% of difluoromethane (CH_2F_2) and 50% of pentafluoroethane (CHF_2CF_3). The operating conditions of the vapor compression refrigeration loop are simulated with reference to Universal R-410A Safety Training Manual (Tomczyk, Nott, and Shaw 2002). The evaporator, represented by the equipment tagged (EVAP), was simulated to operate at approximately 4 °C (39 °F), cooling the incoming hot air while the cold liquid refrigerant (R-410A) absorbs the heat and transforms into a vapor refrigerant stream. At the evaporator, the enormous latent heat of evaporation of the refrigerant stream is utilized to cool down the incoming hot air from 40 °C to 25 °C while changing phase from liquid to vapor. The overall heat transfer value was estimated to be approximately 0.25 kW/m².K with reference to the Machinery's handbook guideline of (0.1-0.5 kW/m².K) (HOLBROOK L. HORTON, HENRY H. RYFFEL ERIK OBERG 2004). The refrigerant isentropic compressor, represented by the equipment tagged (COMP) in Figure 5.7, was simulated to rise up the pressure of the refrigerant to 418 psig (29 bar); transforming into a superheated refrigerant stream. The condenser, represented

by the equipment tagged (COND) in Figure 5.7, is simulated to operate at the same discharge pressure of the same of the isentropic compressor and produce a saturated refrigerant stream at approximately 120 °F (48 °C). Particularly designed to operate around 120 -110 °F (48-43 °C) because the condenser is intended to have the superheated refrigerant stream existing the isentropic compressor directly exchange with the outside air. The saturated refrigerant stream is then directed through the throttle valve (or expansion valve) represented by (EXP-Valve) in Figure 5.7. The outlet pressure specification for the expansion valve was simulated at 130 psig (9 bar) producing a vapor-liquid stream; which is directed to the evaporator. The operating parameters of the base case of the vapor compression refrigeration loop, were as follow: mass flowrate of refrigerant was 420 kg/hour and correspondingly size of the compressor required was 5 kW. The air stream is cooled from 40 °C to 25 °C, and the air stream mass flowrate was 4000 kg/hr. The cooling load requirement was 16 kW on every hour of the peak-hours; which is equivalent to 57,600 kJ/hour. The operating parameters of the reduce load case, were as follow: mass flowrate of refrigerant was 210 kg/hour and correspondingly the size of the compressor required was 2.5 kW. The air stream is cooled from 40 °C to 25 °C, and the air stream mass flowrate was 2000 kg/hr. The cooling load requirement was 8 kW on every hour of the peak-hours; which is equivalent 28,800 kJ/hour.

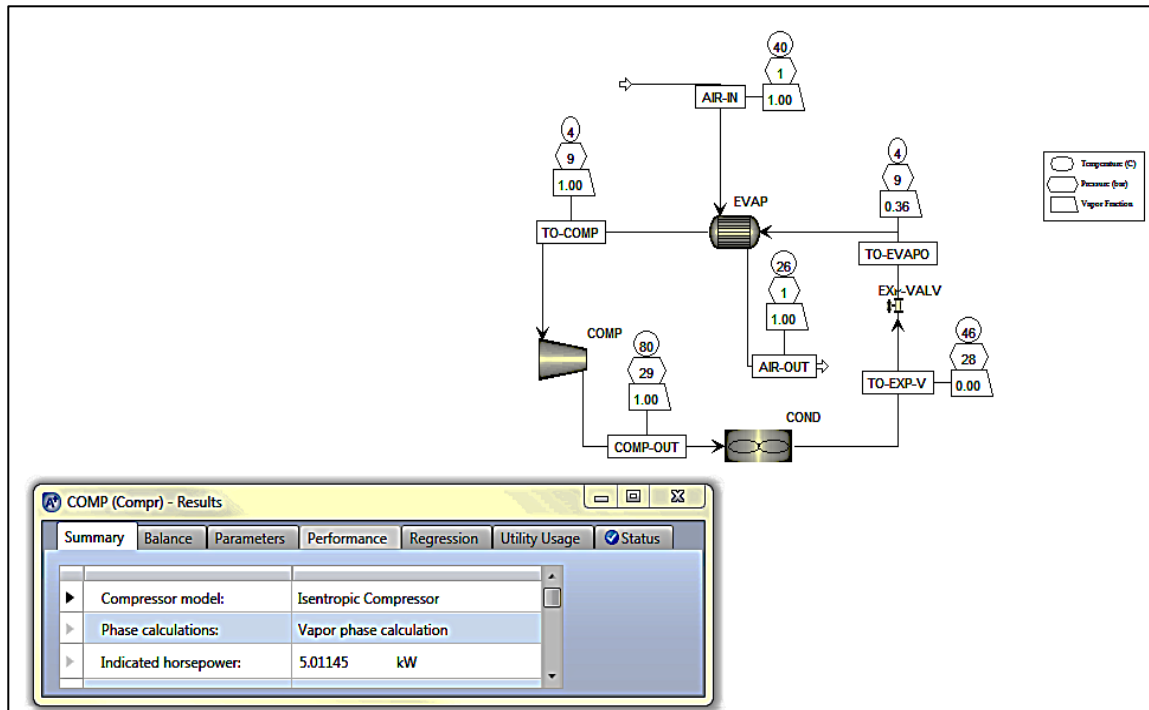


Figure 5.7: First flow sheet simulating major components of vapor compression refrigeration loop meeting the entire cooling demand (base case) of 16 kW.

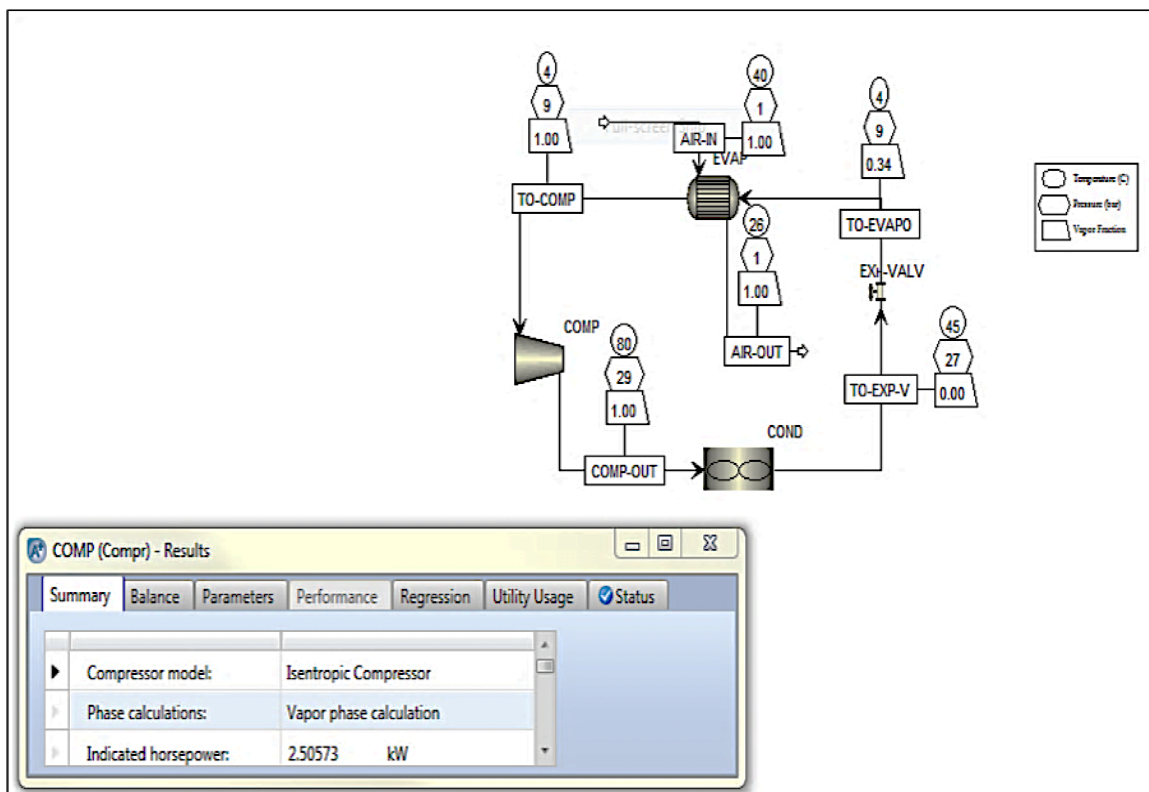


Figure 5.8: First flowsheet, this time simulating major components of vapor compression refrigeration loop meeting 50% of the cooling demand (reduce load case) of 8 kW.

5.2.2 The second flowsheet – discharging mode of the PCC-TES

The second flowsheet (Figure 5.9) models the discharging mode of the PCC-TES by which PCC-TES meets the remaining half of the cooling load in the proposed integrated system. As briefly introduced by Figures 5.5 & 5.6, the PCC-TES is capable of storing or releasing a large amount of heat during the phase change (solid to liquid) or (liquid to solid). Therefore, the second flowsheet primarily focuses on the characteristic of the phase change of the PCC material in response to exchanging heat with air. Ethylene glycol (EG) is used to mediate the heat exchange between the PCC-TES and the air stream. The EG stream is actually composed of 50% EG and 50% Water. As also illustrated earlier, copper tubes pass back and forth through the PCC-TES stack (Figures 5.5 & 5.6). The ethylene glycol (EG) stream runs through the copper tubes. EG enters the PCC-TES structure at the top and exit from the bottom outlet provisions of the structure.

The development of the second flowsheet was associated with two main challenges:

The first challenge was the fact that Aspen Plus® does not have a built-in library to predict the melting and solidification behaviors of PCC and associated thermodynamics and transport properties. Therefore, to overcome the first challenge, we formulated a suitable mathematical heat transfer model as a system of equations and programmed their solution in Fortran. The model represented phase-change behavior and associated thermodynamic and transport properties and was implemented using a Calculator Block residing within and communicating with the larger Aspen Plus® model. With that, the calculator block of Aspen Plus® is now acknowledging the fact that the PCC-TES is melting while cooling the EG stream that is cooling the air. Depending on the heat content, initial and final

temperatures of the PCC-TES and all other necessary data (such as mass flow and initial temperatures of air and EG stream, etc), Aspen Plus® can estimate the energy absorbed by the PCC-TES and the melted fraction and make necessary calculations to estimate the steady state temperatures of the EG and air streams.

The second challenge was the fact that we were interested in melting duration, while Aspen Plus® would land into the overall steady state solution of the overall system. We were not only interested in the EG steady state temperature during the PCC-TES phase change duration, the total energy absorbed by the PCC-TES and melted fraction. But also, interested in the position of the melting front in z-dimension (top to bottom) and the melting duration of each segment within the overall 28-slabs stack (treating the PCC slabs as one continuous overall block). The PCC-TES is gradually melting from top to bottom in association with the hot EG stream circulating and passing through the PCC-TES stack from the top to bottom. So, to overcome this challenge, we employed the “Sensitivity Analysis” feature within Aspen Plus® to calculate melting duration. The formulated mathematical heat transfer model was also utilized within the Sensitivity Analysis feature to describe the melting progression. The Sensitivity Analysis now provides an estimate of heat absorbed by one segment at that particular quasi steady state along with estimates of the position of the melting front in z-dimension (in length units) and the time duration that would take a particular segment to melt. The theory, scientific equations and consequently the mathematical model will be discussed in detail in later section of this chapter.

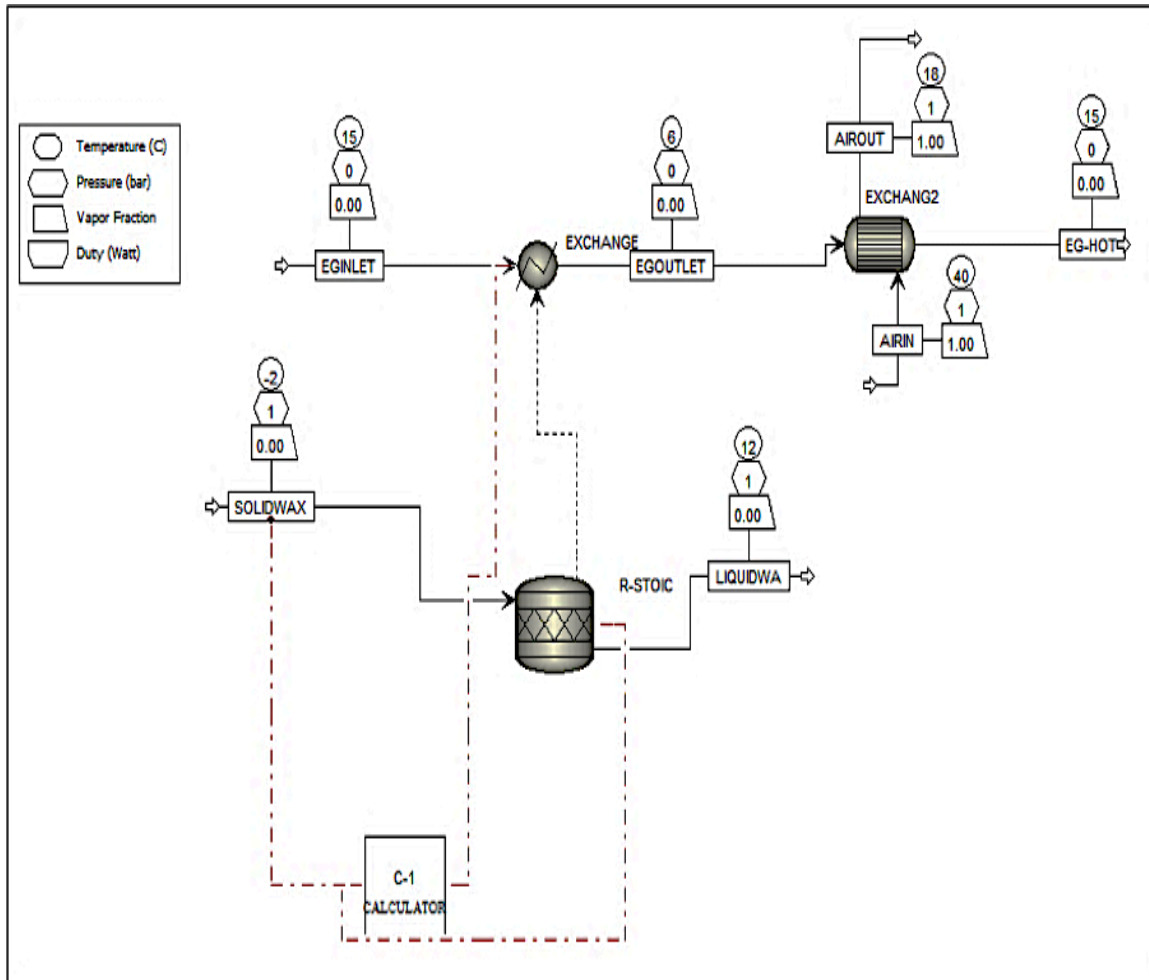


Figure 5.9: Second flowsheet simulates the discharging process and addresses phase change behavior and associated valuable information

The second flowsheet, shown by Figure 5.9, is attempting to model the heat transfer between the PCC and EG stream. The heat exchange is modeled with a heater block, represented by the equipment (EXCHANGE) in Figure 5.9. The (EXCHANGE) is simulating the effect of heat exchange on EG outlet temperature. The heat stream affecting the EG outlet temperature is constituted by the calculator block; which in turns linked with a stoichiometric calculator. The purpose of the stoichiometric calculator in this flowsheet is to artificially simulate the melting progression or the phase conversion of the PCC (from solid to liquid) governed by the calculator block. The calculator block gives the decision

based on the formulated mathematical heat transfer model that was programmed (in Fortran code) into the calculation block. To further clarify, it is worth mentioning that the stoichiometric calculator is only an artificial element in the flowsheet to fulfill two purposes. First, calculate how much latent heat is absorbed by the PCC during the melting progression or the phase conversion. Second, to communicate the heat absorbed by the PCC to the (EXCHANGE) equipment utilizing a heat steam. Moreover, the second flowsheet is imitating the actual experimental set up (as will be discussed in the model validation section of this chapter), therefore the PCC properties, slabs dimensions, EG properties and EG flowrate in the flowsheets are similar to the actual experiment. The calculator block retrieves EG flowrate and inlet temperature along with the PCC properties before calculating the output. Furthermore, the artificial inflowing solid and outflowing liquid stream which are connected to the stoichiometric reactor are simply recording and tracking the input and results of the PCC melting progression calculations and neither inflow or outflow out of the PCC stack nor interact with anything else in the flowsheet.

5.2.3 The third flowsheet- charging mode of the PCC-TES

The third flowsheet is generally very similar to the second flowsheet. However, the third sheet is addressing the charging mode at which the vapor compression refrigeration loop is cooling and solidifying the PCC-TES (Figure 5.10). Similar to the second flowsheet, intermediate ethylene glycol (EG) loop is used to mediate the heat exchange.

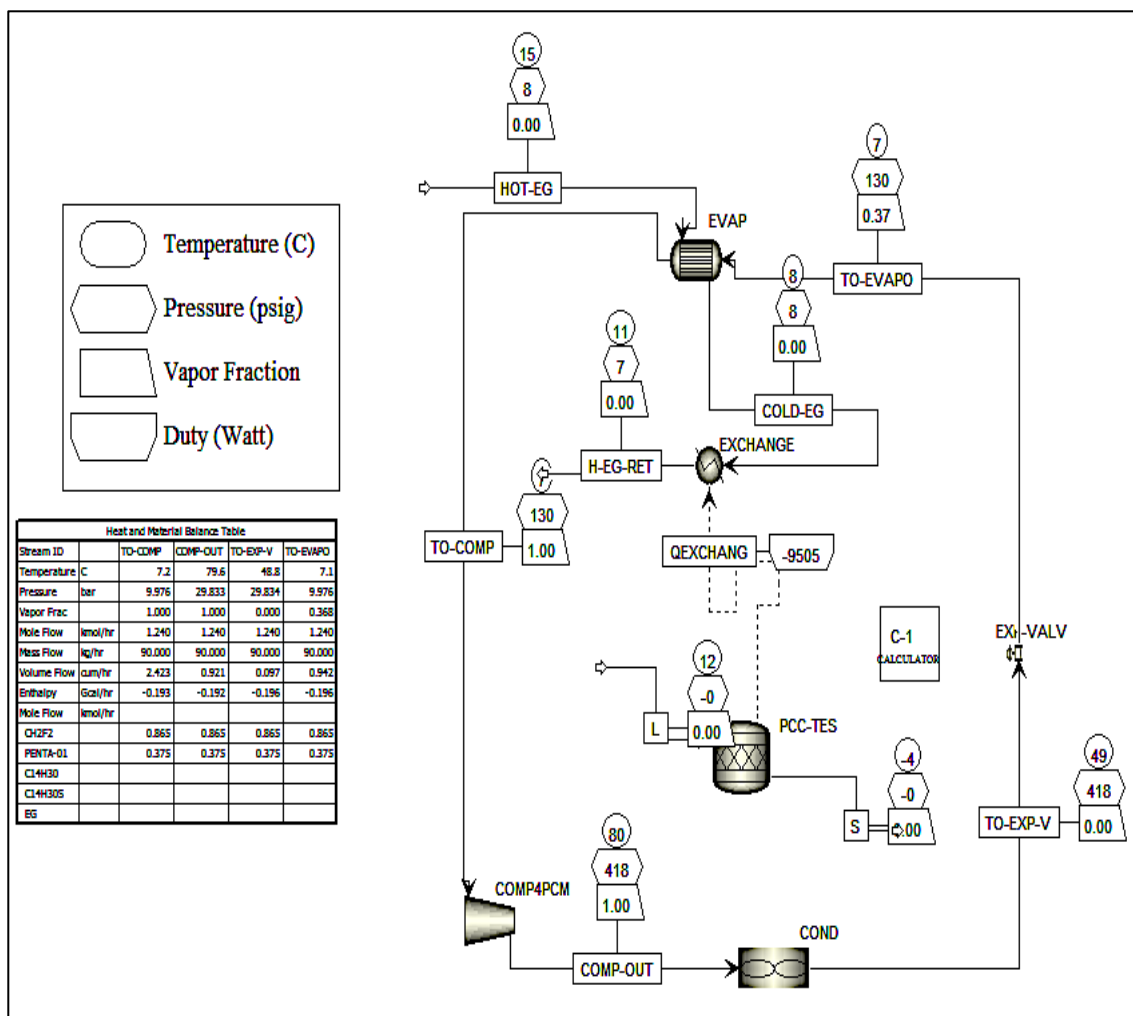


Figure 5.10: The third flowsheet simulates the charging process and addresses phase change behavior and associated valuable information

This paves the road to introduce the heat transfer model and briefly discuss theory and model development.

5.3 Theoretical background and foundations

The second part of the simulation model is the mathematical representation of melting and solidification behaviors within the PCC material. This requires modeling the position and movement of the moving phase boundary between the liquid and solid phases within the

PCC material. The resulting system of equations is implemented in a Fortran code within the calculation block of Aspen Plus®. This block exchanges data with the Aspen Plus® simulation environment.

The theoretical foundation of the heat transfer problem is presented in section 2.5 is the foundation of the work of this section. This present chapter considered the whole PCC structure as one interwoven system, the mass of PCC material has heat sinks/sources distributed within its volume from EG loop #1; see Figure 5.2. However, we can stylize each (circuitous) tube pass of EG between adjacent slabs of PCC material as a uniform planar heat sink/source. Then thermal communication between the PCC material and EG loop #1 can be modeled approximately with a “stack” of appropriately formulated problems. In particular, each slab is now regarded as being in contact with isothermal, surfaces (x - y plane) at the top and bottom supplied/depleted by a heat flux, assumed uniform in the two external heat fluxes energy sources propagating heat at the upper and lower surfaces of the slab. Upper and lower external heat sources are assumed to have a flux uniformity in the x -direction and symmetry across the centerline. In one given approach individual slabs can be considered as the finite volume for the energy balance. Accordingly, the temperature profile of the PCC material and the spatial position profile of the surface boundary between the two states of matter can be generated for each slab individually. At which the final boundary limits of a slab are the initial boundary limits of the underneath slab, which implies continuous profiles of temperature and spatial position of surface boundary across the whole structure. It was assumed that the heat transfer is a one-dimensional heat transfer in z -direction in the PCC-TES in corresponds to hot fluid temperature profile that is entering the top of the PCC-TES structure and leaves off the

bottom. The distance travelled by the EG along the copper tubes is much longer than the radius of the tube. Therefore, hot EG fluid passing through the PCC-TES assumed to have a uniform heat flux in x-direction while varying in z-direction. Also, the heat transport by convection by EG is more dominant and heat transport by conduction is negligible (Figure 5.11). Therefore, averaged EG was estimated to represent the temperature of EG passing through the horizontal tubes within the PCC-TES.

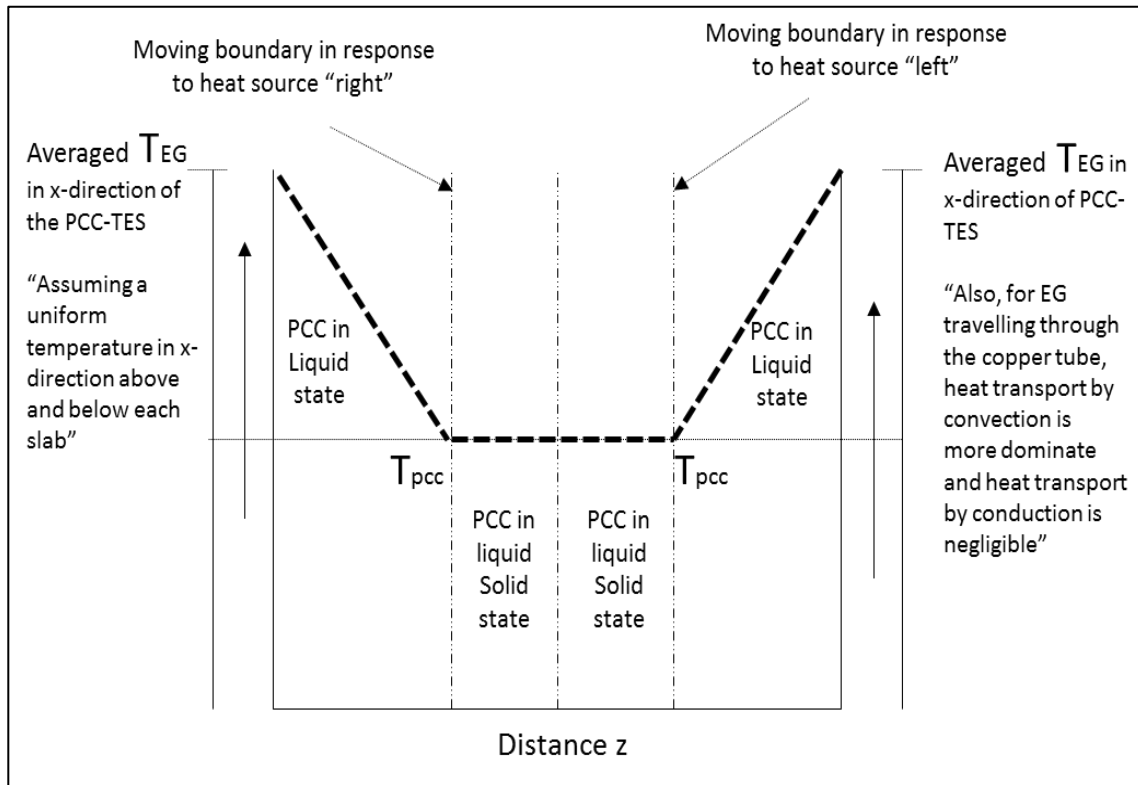


Figure 5.11: A conceptual temperature profile of a layer of finite thickness with upper and lower external energy sources illustrated by left and right heat sources

The entire PCC-TES can be considered as one finite volume for the energy balance. In this chapter, we are interested in describing the overall behavior of the entire PCC-TES system from top to bottom (Figure 5.12). The magnitude of heat released by the hot EG is proportional to the effective surface area of the copper tubes. Therefore, the effective

surface area of the copper tubes passing through the PCC-TES structure was calculated. The effective surface area is a function of the surface area of a single tube multiplied by the length of a single tube multiplied by the number of tube passes within the PCC-TES structure. Likewise, the magnitude of heat released by the hot EG is proportional to the heat transfer coefficient of EG. The heat transfer coefficient will be calculated following the calculation of Reynolds and Nusselt numbers. The spatial position (in z-direction) of the boundary surface at the upper surface of the upper-most slab of the PCC-TES structure is considered the starting point of the volumetric heat exchange emerged. The position in z-direction at the bottom surface of the bottom-most slab of the PCC-TES structure is considered the endpoint of the volumetric heat exchange emerging. As a reminder note, the PCC-TES structure is thermally insulated from all sides.

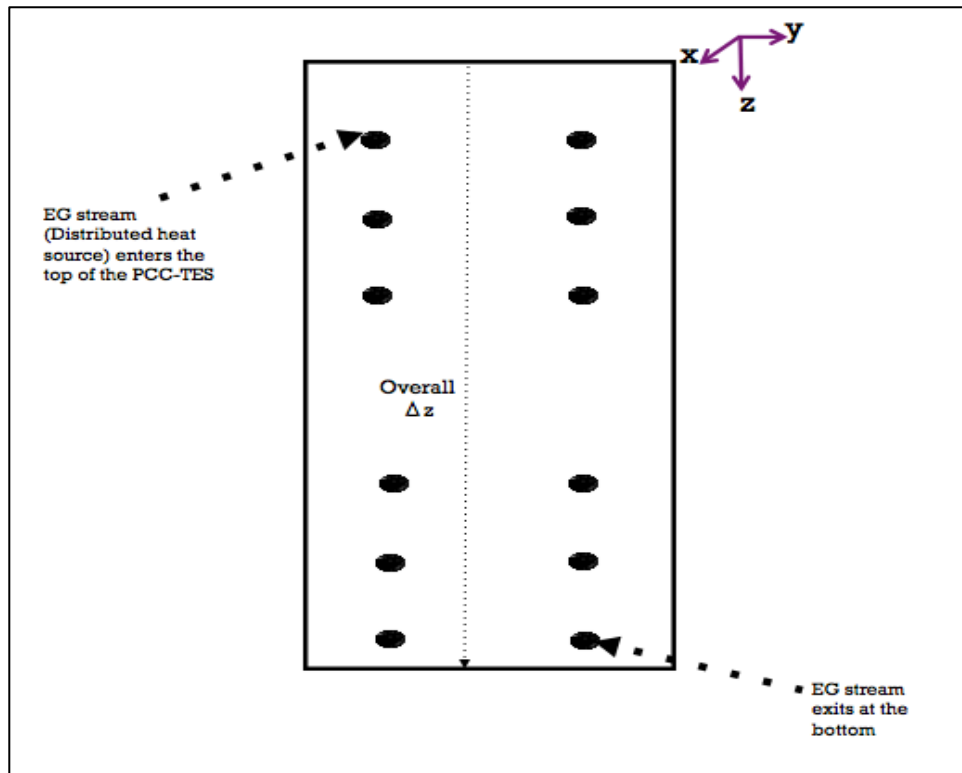


Figure 5.12: Space-time continuum theory approach to solve present heat transfer problem

Therefore, the whole system was discretize using an analytical model to calculate time duration for the melting progression of the overall homogenous structure, from top to bottom, as will be discussed in the next section.

5.4 The analytical model accounting for latent/sensible heat and time duration

The absorption and rejection of thermal energy by a phase change material involves both the latent and sensible heat:

$$Q = \int_{T_i}^{T_f} m C_{p_{eff}} dT \quad (5.10)$$

Q in equation (5.10) is equal to the cumulative heat or thermal energy (absorbed or rejected) by the phase change material, m is the mass of the phase change material (PCM), $C_{p_{eff}}$ is the effective specific heat of the phase change material; which can be defined along the temperature profile by the equations (5.6-5.9) described earlier with reference to (Khateeb et al. 2005). Moreover, T_i and T_f are the initial and final temperatures of the PCM respectively.

For a single component, such as ice, the melting temperature is a single point at which melting or solidification occurs. However, for a composite of several components, the melting temperature cannot be described by a single point melting temperature, therefore melting temperature for a composite would be represented using a melting range. Recall that the PCC melting temperature range is (4-6 °C); where 4 °C marks completely solid state of the material and 6 °C marks completely liquid state.

The melting range of a composite phase change material approximated to have a direct relationship with melted or solidified fraction in the process of absorbing or releasing heat respectively as expressed in equation (5.11) with reference to the “Liquid fraction - PCM Temperature relationship” as discussed by (Iten and Liu 2014):

$$\text{melted fraction} = \frac{(T - T_s)}{(T_l - T_s)} \quad (5.11);$$

reference (Iten and Liu 2014)

Where T is the PCM actual temperature. T_s is the temperature at which (or lower) PCM is completely solid. T_l is the temperature at which (or higher) PCM is completely liquid.

“Liquid fraction- PCM Temperature relationship” was further illustrated by (Iten and Liu 2014):

- Liquid fraction = 0, if $T < T_s$
- Liquid fraction= between 0 and 1, if $T_s < T < T_l$
- Liquid fraction = 1, if $T > T_l$

5.4.1 Characterization of melting and solidification behaviors

The heat rejected or absorbed by phase change material is associated with valuable information to researchers and designers such as charging and discharging rates, fraction melted (or solidified) of the PCM, location of the moving phase boundary between liquid and solid phases in space and melting duration. Therefore, equation (5.10) was used to

calculate the sensible/latent heat depend on the temperature and discharging/charging rates. Equation (5.11) was utilized to calculate the melting fraction. However, to predict the melting time duration an analytical model previously discussed by (Mehling and Cabeza. 2008) and (Hans Dieter Baehr and Karl Stephan 2014) was utilized in this present chapter. These models not only calculate time duration, but also are valuable to study effect of multiple variables on the overall heat transfer process such as PCM thermal conductivity, surface area of the PCM, optimum surface area of tubes and optimum heat transfer fluid characteristics...etc. The analytical model as described by (Mehling and Cabeza. 2008) assumed a couple of assumptions to simplify a complicated approach and land into analytical solution. The main assumptions presented by (Mehling and Cabeza. 2008) were as follows: 1-dimensional heat transfer and negligible volume variation between the two states of solid and liquid. Moreover, latent heat is much larger than sensible heat; hence sensible heat can be ignored (Mehling and Cabeza. 2008). The latter assumption is certainly in line with the fact that thermal energy storage systems have the ultimate goal of capturing the enormous latent heat resulting from the phase change.

Therefore, the heat transfer model major assumptions were as follow:

1. Only latent heat is considered during melting stage.
2. Only sensible heat is considered during the duration of the sensible heat exchange before and after melting.
3. The hot EG fluid passing through the PCC-TES assumed to have a uniform heat flux in x-direction. Also, the hot fluid tube length is much longer than the radius of

the tube. Therefore, the temperature of hot fluid would certainly vary from top to bottom.

4. Accordingly, assumed a one-dimensional heat transfer in z-direction in the PCC-TES in corresponds to hot fluid temperature profile that is entering the top of the PCC-TES structure and leaves off the bottom as illustrated by Figures 5.14-5.15.
5. Within the PCM, heat is transferred by conduction only. There is no heat transfer by convection since the PCM particles are stationed and trapped within the graphite porous structure.
6. Negligible volume variation between solid and liquid states.
7. Well-insulated system.
8. In discharging (melting mode), PCM is initially completely solid. While, in charging mode (solidifying mode), PCM is initially completely liquid.

Assumptions were produced with reference to (Hans Dieter Baehr and Karl Stephan 2014; Mehling and Cabeza. 2008; S. Wu, Fang, and Chen 2012). According to similar derivation to references (Mehling and Cabeza. 2008; Hans Dieter Baehr and Karl Stephan 2014), equation (5.12) describes the melting duration of the PCM (in units of time) as a function of the location of the moving phase boundary between the two phases of solid and liquid:

$$t = \frac{\Delta m * \Delta h * s^2}{2 * \lambda_{PCM} * \Delta T} \left(\frac{A_{PCM}}{A_{eff-tube}} \right) \left(1 + \frac{2 * \lambda_{PCM}}{s * k} \right) \quad (5.12)$$

In equation (5.12), t represents the melting duration of the PCM (in units of time), Δm represents the fraction melted (or solidified) of the PCM during phase transition, Δh represents the energy content per volume of PCM, while s represents the depth or (the

location of the liquid/solid moving phase boundary of the PCM). $\left(\frac{A_{PCM}}{A_{eff-tube}}\right)$ is the ratio of surface area of PCM to effective surface area of heat transfer fluid (HTF)'s tubes.

λ_{PCM} is the thermal conductivity of the PCM. T_{pcmf} , & T_{pcmi} are the final and initial temperatures of the PCM respectively, and $\frac{1}{k}$ is described by equation (5.13) as follow:

$$\frac{1}{k} = \left(\frac{d_o - d_i}{\lambda_{wall}} + \frac{1}{h_{fluid}} \right) \quad (5.13)$$

Here, h_{fluid} is the heat transfer coefficient of the HTF, d_i and d_o are the inside and outside diameters of the HTF's tube respectively, and λ_{wall} is thermal conductivity of the HTF's tube wall.

It is worth mentioning that the derivation by (Mehling and Cabeza. 2008; Hans Dieter Baehr and Karl Stephan 2014) started by first setting the heat absorbed by the PCM equal to the heat released by the heat transfer fluid (HTF) as illustrated by equation (5.14) and (5.15). This is a similar approach to equation (5.5) discussed earlier in the theoretical background and foundation section, at which heat absorbed, because of the phase transformation (latent heat of fusion) and the sensible heat stored, is equated with the heat rejected from the heat source.

$$\dot{q}_{PCC} = A_{PCM} \Delta h \frac{ds}{dt} \quad (5.14)$$

$$\dot{q}_{EG} = \frac{A_{eff-tube} * \Delta T}{\frac{s(t)}{\lambda_{PCM}} + \frac{d_o - d_i}{\lambda_{wall}} + \frac{1}{h_{fluid}}} \quad (5.15)$$

Where, equation (5.14) represent the heat absorbed by the phase change material while equation (5.15) represents the heat rejected by EG. The $s(t)$ is calculated using equation (5.16):

$$z = s = \frac{Q (kJ)}{A (m^2) * \Delta h (\frac{kJ}{m^3})} \quad (5.16)$$

Here, Q is the heat absorbed in (kJ) by each segment (calculated using equation 5.10), A is the surface area of each segment, and Δh is the energy content per volume of the segment.

Figure 5.13 describes the conceptual approach used to discretize the model and calculate time duration for the melting progression of the overall homogenous structure using equation (5.12). An approach that is similar in concept to the approach conducted by (Dolado et al. 2006) in their semi-analytical method.

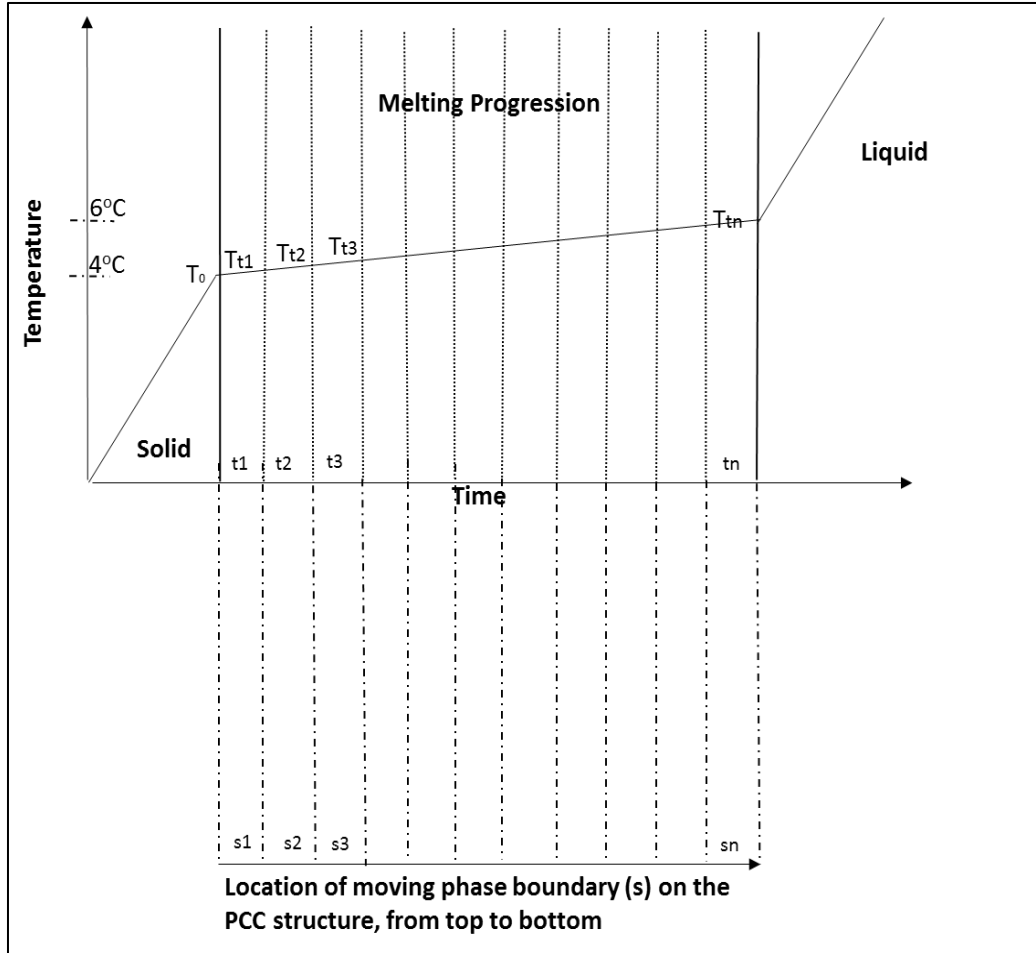


Figure 5.13: A conceptual approach to discretize PCC-TES and calculate time duration with respect to position (s) for melting progression of overall structure using equation (7) [reference: (A. Aljehani et al. 2018)].

The following are essential remarks with regards the development of the model:

1. Within the PCM, heat is transported by conduction only. There is no heat transfer by convection since the PCM particles are stationed and trapped within the graphite porous structure.
2. During conduction, enthalpy has approximately linear relation with the melting range temperatures for most composite phase change materials as described by (Iten and Liu 2014).

3. Also, during melting stage, total volumetric heat content of the system is known and predetermined in (kJ/m³) units.
4. So, if the PCC structure would be hypothetically divided into equal volumetric segments, then each segment would absorb nearly equal amount of thermal energy in order to melt. In other words, each segment would be associated with predetermined volumetric heat capacity. The heat absorbed is equivalent to the heat released by hot ethylene glycol (EG) passing through each volumetric segment. Heat from hot EG is distributed within the PCC-TES structure. Therefore, the melting of each volumetric segment is associated with the distributed hot EG passing through this segment or (predetermined volume).
5. The surface area of each predetermined volume of PCC is also known.
6. Heat absorbed by a predetermined segmental volume of the PCC is equivalent to heat released by hot EG as described by equations (5.14) and (5.15) above.
7. Therefore, the depth in *z*-direction (location of the surface phase boundary) for the predetermined volume segment can be calculated using equation (5.16).

Depth in *z*-direction for the specified volume segment of the PCC structure:

$$Depth (m) = \frac{Q (kJ)}{A (m^2) * \Delta h (\frac{kJ}{m^3})} \quad (5.16)$$

Where, *Q* is the heat absorbed in (kJ) by each segment (calculated using equation 5), *A* is the surface area of each volumetric segment, and Δh is the energy content per volume of the segment.

8. Using equation (5.12) illustrated above (derived by acknowledging point 6, setting equations (5.14) and (5.15) equal to each other, rearranging, integrating and solving for t), we analytically can calculate the time required for each segment to melt with respect to depth as a result of the distributed hot ethylene glycol passing through the segment.
9. Moreover, the temperature profile has been figured out acknowledging the linear relationship between enthalpy and temperature as addressed in point 2 above.
10. Derivation of equation (5.12), started first by setting equation (5.14) equals to equation (5.15):

$$A_{PCC} \Delta h \frac{ds}{dt} = \frac{A_{eff-tube} * \Delta T}{\frac{s(t)}{\lambda_{PCC}} + \frac{d_o - d_i}{\lambda_{wall}} + \frac{1}{h_{fluid}}} \quad (5.17)$$

Then, rearrange equation (6.17) as follow:

$$\left(\frac{s(t)}{\lambda_{PCC}} + \frac{d_o - d_i}{\lambda_{wall}} + \frac{1}{h_{fluid}} \right) ds = \frac{A_{eff-tube}}{A_{PCC} \Delta h} \Delta T dt \quad (5.18)$$

Then, use $\frac{1}{k} = \left(\frac{d_o - d_i}{\lambda_{wall}} + \frac{1}{h_{fluid}} \right)$ and plug in equation (5.18)

So equation (5.18) becomes:

$$\left(\frac{s(t)}{\lambda_{PCC}} + \frac{1}{k} \right) ds = \frac{A_{eff-tube}}{A_{PCC} \Delta h} \Delta T dt \quad (5.19)$$

Integrate both sides of equation (5.19):

$$\int_0^s \left(\frac{s}{\lambda_{PCC}} + \frac{1}{k} \right) ds = \int_0^t \frac{A_{eff-tube}}{A_{PCC} \Delta h} \Delta T dt \quad (5.20)$$

After integration,

$$\left(\frac{s^2}{2 * \lambda_{PCC}} + \frac{s}{k} \right) = \frac{A_{eff-tube}}{A_{PCC} \Delta h} \Delta T t \quad (5.21)$$

Re-arrange the expression and solve for t:

$$t = \left(\frac{\Delta h * A_{PCC}}{\Delta T * A_{eff-tube}} \right) \frac{s^2}{2 * \lambda_{PCC}} + \left(\frac{\Delta h * A_{PCC}}{\Delta T * A_{eff-tube}} \right) \frac{s}{k}$$

Take $\frac{\Delta h * s^2}{2 * \lambda_{PCM} * \Delta T} \left(\frac{A_{PCM}}{A_{eff-tube}} \right)$ as a common factor to reproduce (5.12).

Equation (5.12) as illustrated earlier would calculate the time required for each volumetric segment to melt, with respect to location in space (s) in z-direction and temperature of the PCC, as a result of the distributed hot ethylene glycol passing through the segment of the PCC-TES structure.

11. Here are examples of the discretization of the model to calculation time duration for the overall structure as illustrated by (Figure 5.15):

$$t1 = \frac{\Delta m * \Delta h * s^2}{2 * \lambda_{PCM} * (T_{t1} - T_0)} \left(\frac{A_{PCM}}{A_{eff-tube}} \right) \left(1 + \frac{2 * \lambda_{PCM}}{s * k} \right) \quad (5.22)$$

$$t2 = \frac{\Delta m * \Delta h * s^2}{2 * \lambda_{PCM} * (T_{t2} - T_0)} \left(\frac{A_{PCM}}{A_{eff-tube}} \right) \left(1 + \frac{2 * \lambda_{PCM}}{s * k} \right) \quad (5.23)$$

$$t3 = \frac{\Delta m * \Delta h * s^2}{2 * \lambda_{PCM} * (T_{t3} - T_0)} \left(\frac{A_{PCM}}{A_{eff-tube}} \right) \left(1 + \frac{2 * \lambda_{PCM}}{s * k} \right) \quad (5.24)$$

$$tn = \frac{\Delta m * \Delta h * s^2}{2 * \lambda_{PCM} * (T_{tn} - T_0)} \left(\frac{A_{PCM}}{A_{eff-tube}} \right) \left(1 + \frac{2 * \lambda_{PCM}}{s * k} \right) \quad (5.25)$$

With reference to the work of (S. Wu, Fang, and Chen 2012), four thermal resistances were evaluated when addressing the heat transfer between the PCC and the HTF, which are illustrated in equation (5.26) below:

$$R_{tot} = R_1 + R_2 + R_3 + R_4 \quad (5.26)$$

Where, R_{tot} represent the total resistances, R_1 represents the thermal resistance of the melting (or solidifying) PCC, R_2 represents the thermal resistance due to tube wall, R_3 represents the thermal resistance due to convection by HTF inside the tubes, and R_4 represents the thermal resistance due to the convection of the molten PCC. However, R_4 was considered negligible with respect to other resistances. Therefore, equation (5.27) was used in the analytical model:

$$R_{tot} = \frac{s}{\lambda_{PCM}} + \frac{d_o - d_i}{\lambda_{wall}} + \frac{1}{h_{fluid}} \quad (5.27)$$

All necessary equations used to prepare the analytical heat transfer model were written as a system of equations in Fortran code within the calculation block of Aspen Plus® simulation software.

5.5 Material Evaluation

Table 5.1 illustrates key components and properties of the PCC material that was used to build the model in Aspen Plus®.

Table 5.1: Phase change composite (PCC) material

Phase Change Composite (PCC)	
Composition	Paraffin + Graphite
Composition %	78% Paraffin + 22% Graphite
Energy Content	180 kJ/kg
Melting Range	4.0 -6.0 °C

Table 5.2 illustrates the properties of the AC's refrigerant (R-410A) and the properties of the heat transfer fluid (HTF), namely Ethylene Glycol (EG), being the intermediate loop between the hot air stream and the cold PCC-TES. Ethylene glycol (EG) also facilitates the heat exchange between the refrigeration cycle and the PCC-TES during the charging mode at night.

Tabel 5.2: AC refrigeration loop data & Ethylene Glycol (EG) data

Air Conditioning's refrigerant		Intermediate loop (Ethylene Glycol)	
Type	R-410A	Type	Ethylene Glycol (EG)
Composition %	50% CH ₂ F ₂ + 50% CHF ₂ CF ₃	Composition %	50% EG + 50% Water

Table 5.3 illustrates the properties and dimensions of the copper tubes carrying the heat transfer fluid that is passing through the PCC-TES structure.

Table 5.3: Copper tubes dimensions for the PCC-TES system

Copper tubes dimensions	
Inside diameter of copper tubes	0.32"
Outside diameter of copper tubes	0.38"
Total length of copper tube passes	51 meters

5.6 Model Validation

The simulation model developed for this research work was validated by crosschecking the simulation model's results with the results from an actual experimental system of 4 kWh PCC-TES benchtop thermal storage system. The actual 4 kWh PCC-TES benchtop system was built for actual testing and proof of concept purposes. Figure 5.14 shows a schematic of the main components of the overall PCC-TES system. Figure 5.15 illustrates the actual 4 kW PCC-TES benchtop system.

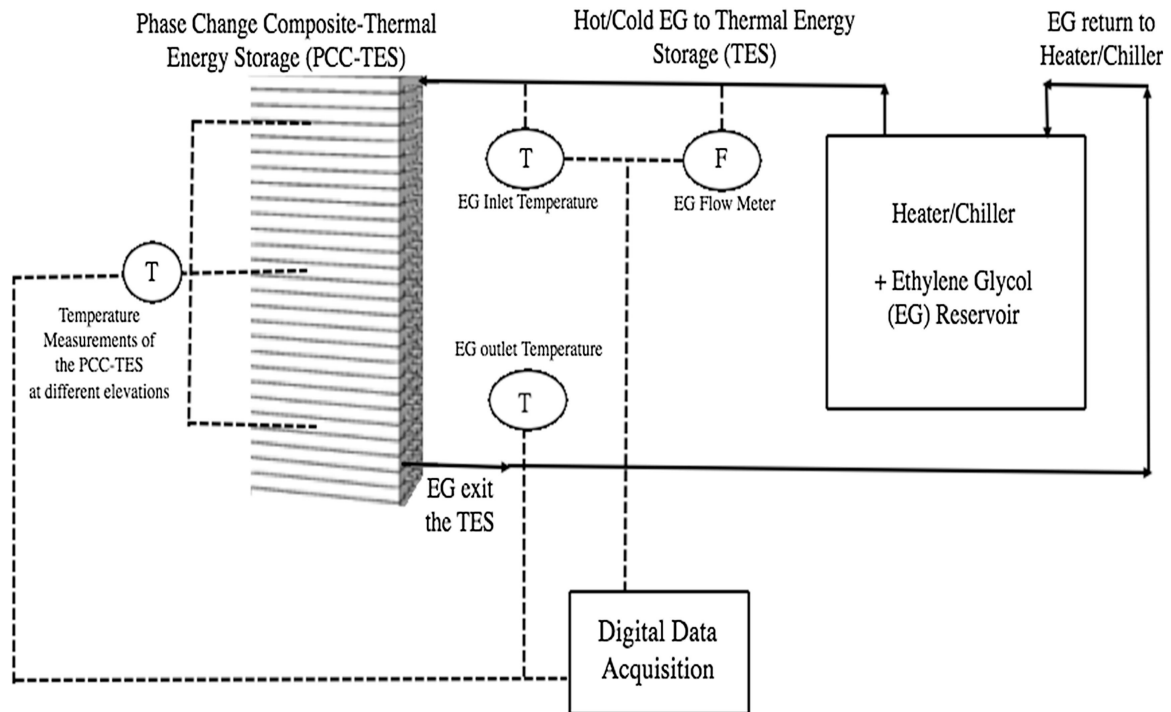


Figure 5.14: Schematic of the PCC-TES system's main components [reference: (A. Aljehani et al. 2018)]

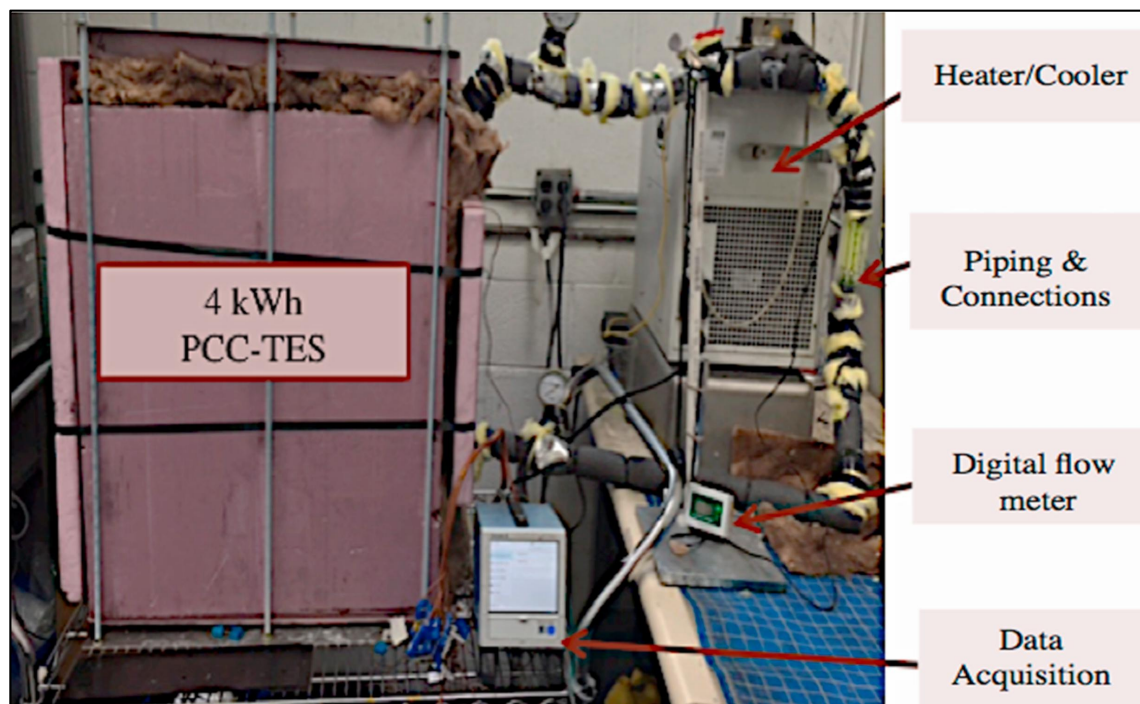


Figure 5.15: Actual 4kWh PCC-TES system's main components [reference: (A. Aljehani et al. 2018)]

The first checkpoint was to verify if the developed Aspen Plus® simulation model enhanced with the required scientific equations and the heat transfer analytical model can adequately mimic the actual 4KWh PCC TES benchtop system's performance and anticipate equivalent results.

Therefore, the evaluation model was built reflecting the exact dimensions and storage capacity of the 4 kWh PCC-TES benchtop system. The simulation model also mimicked the flow rate and composition of the heat transfer fluid (HTF), namely ethylene glycol (EG).

The specifications and dimensions of the real experimental setup and accordingly the model is illustrated in Table 5.4. As stated in the introduction section, this study evaluates the feasibility of utilizing the proposed phase change composite (PCC) material to serve as the storage medium for a TES system for cooling applications.

Therefore, it was a good starting point to check if the proposed PCC-TES can actually prove the concept and capabilities of storing and releasing thermal energy by exchanging heat with EG.

Table 5.4: Simulation model validation: (model input vs. real experiment input) for the actual 4 kWh PCC-TES benchtop [reference: (A. Aljehani et al. 2018)]

Real Experiment Data		Input to Model's equations	
PCC Latent Heat (kJ/kg)	180	PCC Latent Heat	180
Slab Dimension: length,	(0.46, 0.26	Slab Dimension: length,	(0.46, 0.26 and
Width and thickness (m)	and 0.0254)	Width and thickness (m)	0.0254)
Number of Slabs (#)	28	Number of Slabs (#)	28
Total Mass of PCC slabs	78	Total Mass of PCC	78
Weight (%) of paraffin and	(78% paraffin	Weight (%) of paraffin	(78% paraffin +
Graphite in each slab	+ 22%)	and Graphite in each	22% graphite)
	graphite)	slab	
Copper tube outer diameter	0.38	Copper tubes outer	0.38
(in)		diameter (in)	
Copper tube inner diameter	0.32	Copper tubes inner	0.32
Total length of copper tube	51 meters	Total length of copper	51 meters
Ethylene Glycol volumetric	2.3	Ethylene Glycol	2.3
flow rate (l/min)		volumetric flow rate	
Ethylene Glycol input	14	Ethylene Glycol input	14
Solidified (cold) PCC	-2	Solidified (cold) PCC	-2
PCC melting range (°C)	4-6	PCC melting range (°C)	4-6
Air inlet temperature (°C)	Not tested	Air inlet temperature	40
		(°C)	

The experimental setup is divided into three main components: the actual 4 kWh PCC-TES system, the copper tubes, and the chiller/heater as illustrated by Figures 5.14 & 5.15.

The first component is the actual 4 kWh PCC-TES consisting of graphite, which is the structure that holds the PCM and boosts thermal conductivity, and n-Tetradecane, which serves as the PCM that is capable of storing or releasing heat depending on the mode of operations; whether discharging or charging. It is worth mentioning that, the actual 4 kWh PCC-TES structure is made of 28 slabs of PCC. The whole PCC-TES structure is thermally insulated with building insulation materials. Each slab represents a graphite structure that has been soaked into n-Tetradecane for at least 24 hours until impregnated with n-Tetradecane. The slabs are numbered from top to bottom; top being number 1. The second component is the copper tubes or the copper coils, which pass back and forth in between the 28 slabs. The copper tubes enter the PCC-TES structure from the top and exits from the bottom of the structure. The EG stream runs through the copper tubes. The third component is the chiller/heater that is the device that controls the temperature of the EG being pumped through the tubes to exchange heat with the PCC-TES and also serves as the EG reservoir.

Depending on whether it is intended to be a discharging or charging experiment, the chiller/heater sets the temperature of the EG to 14 or (-2) °C respectively. As introduced earlier, the discharging mode takes place when the PCC-TES stores thermal energy and melts accordingly. On the other hand, during charging mode the PCC-TES rejects the stored heat to cold EG passing through and solidifies.

The discharging experiment was the chosen mode to be conducted and tracked first in order to start validating the simulation model. Therefore, the initial temperature of the 4 kWh PCC-TES system was set to (-2) °C marking a “completely solidified” PCC-TES status; after being charged (or solidified) using a cold EG stream in prior perpetration setups. For the discharging experiment, the EG fluid flow rate was set to 2.3 liters per minute.

The initial temperature of the EG fluid was set to 14 °C by the chiller/heater controller. The official recorded starting time of the experiment was at the moment at which the 14 °C EG was pumped through cold PCC-TES.

A few minutes later, the temperature of the EG existing the PCC-TES dropped down to 6 °C, rejecting the heat to the 4 kWh PCC-TES. The EG exiting the bottom of the PCC-TES was again rerouted through the outlet piping back to the chiller/heater to be heated again to 14 °C and back to the PCC-TES.

The EG continued to leave the bottom of the PCC-TES at 6 °C until the PCC-TES approached “completely melted” status. Then, the temperature of the EG exiting the bottom of the PCC-TES started to rise above 8 °C after a little over 3 hours of heat exchange.

The discharging experiment was considered officially stopped at the moment at which the EG temperature reached 10 °C approximately after 3 hours and a half. Output parameters of the simulate on model and actual discharging experiment are listed in Table 6.5.

Table 5.5: Simulation model validation: (model output vs. experimental results) for the actual 4 kWh PCC-TES benchtop [reference: (A. Aljehani et al. 2018)]

Real Experiment Data		Model Output	
Discharging rates (time)	3 hours and 27 minutes	Discharging rates (time)	3 hours and 37 minutes
Time frame	(Sensible heat before melting + melting duration + Sensible heat after melting)	Time frame	(Sensible heat before melting + melting duration + Sensible heat after melting)
EG outlet temperature (°C)	6	EG outlet temperature (°C)	6
PCC final temperature (°C)	10	PCC final temperature (°C)	10
Air outlet temperature (°C)	Not tested (heat exchange of EG and Air was not part of the actual testing setup, only in modeling part)	Air outlet temperature (°C)	18
Air volumetric flow rate (CFM)	Not tested (heat exchange of EG and Air was not part of the actual testing setup, only in modeling part)	Air volumetric flow rate (CFM)	370

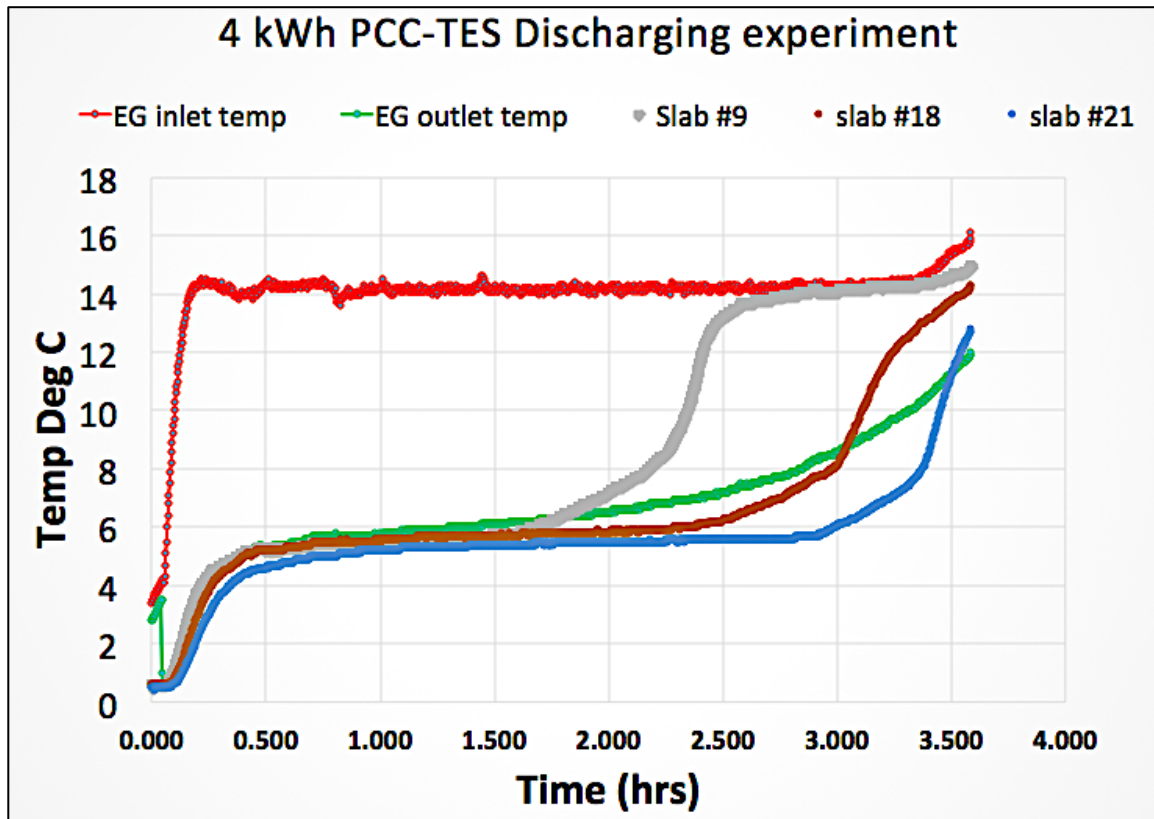


Figure 5.16: Representation of discharging experiment temperature profiles with respect to time [reference: (A. Aljehani et al. 2018)]

Figure 5.16 illustrates the temperature profiles of selected slabs during the discharging experiment. The EG inlet and outlet temperatures are indicated by the red and green curves respectively.

The temperature probe labeled (slab #9) in Figure 5.16 illustrates the temperature profile of the 9th slab of the actual benchtop PCC-TES, which is located at the top quarter of the PCC-TES structure. On the other hand, the temperature probe labeled (slab #12) represents the temperature of the 12th slab located on 2nd quarter segment of the PCC-TES. As

indicates, slab number 9 melted before slab number 18 because the hot EG enters the PCC-TES at the top and leaves out at the bottom. Likewise, slab number 18 melted before slab number 21. This illustrates a top to bottom melting profile of the slabs, which is a rational consequence to the fact that hot EG enters the PCC-TES from the top and leaves of the bottom. The inlet and exiting temperatures of ethylene glycol were also illustrated in Figure 5.16.

Figure 5.16 represents the change in temperature with respect to time. Figure 5.17 illustrates slab locations (in z-direction) plotted in terms of temperature and time respectively. As illustrated by (Figures 5.16 & 5.17) producing a top to bottom melting profile in response to heat rejected by the hot EG traveling through the PCC-TES structure from top to bottom. Table 5.6 illustrates a sample of the PCC-TES simulation model's sensitivity analysis. As illustrated by Table 5.5, the whole PCC-TES structure would fully discharge in approximately 3 hours and 37 minutes according to the simulation model. As discussed earlier, the discharging duration of the model accounted also for the useful heat, sensible heat durations before and after melting in addition to melting duration. Figure 5.18 illustrates the timing of melting profiles with respect to the position in PCC-TES.

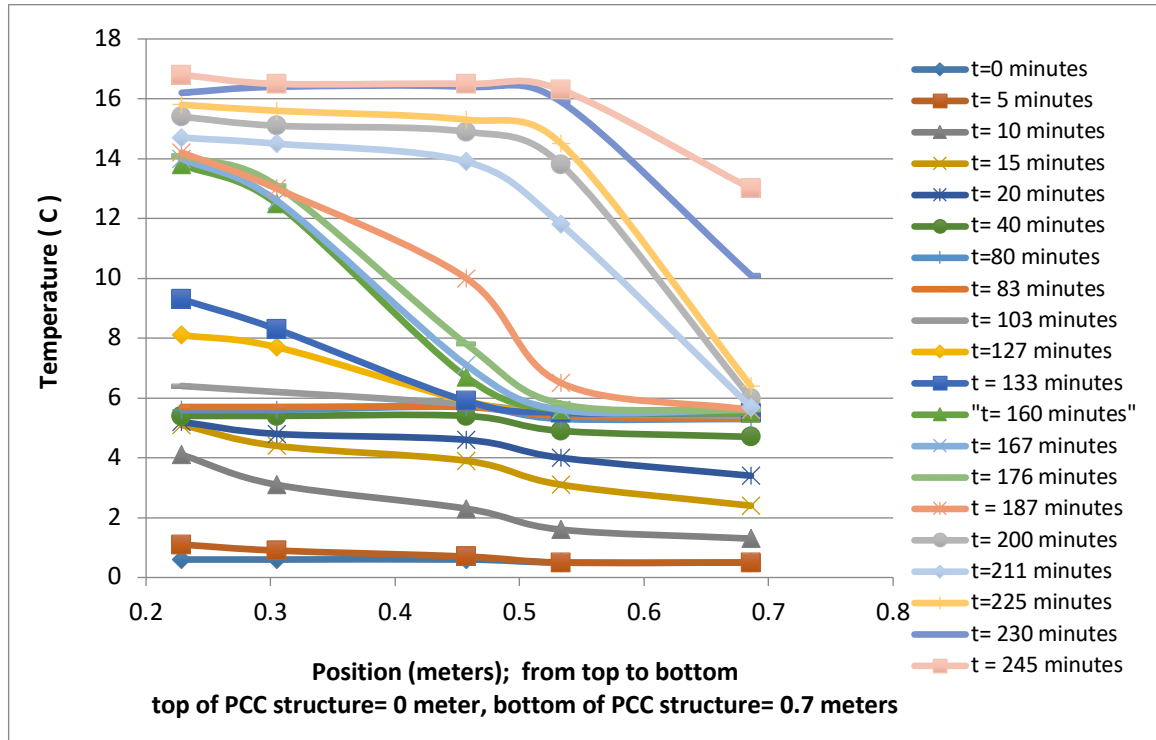


Figure 5.17: Temperature with respect to position during the melting progression [reference: (A. Aljehani et al. 2018)]

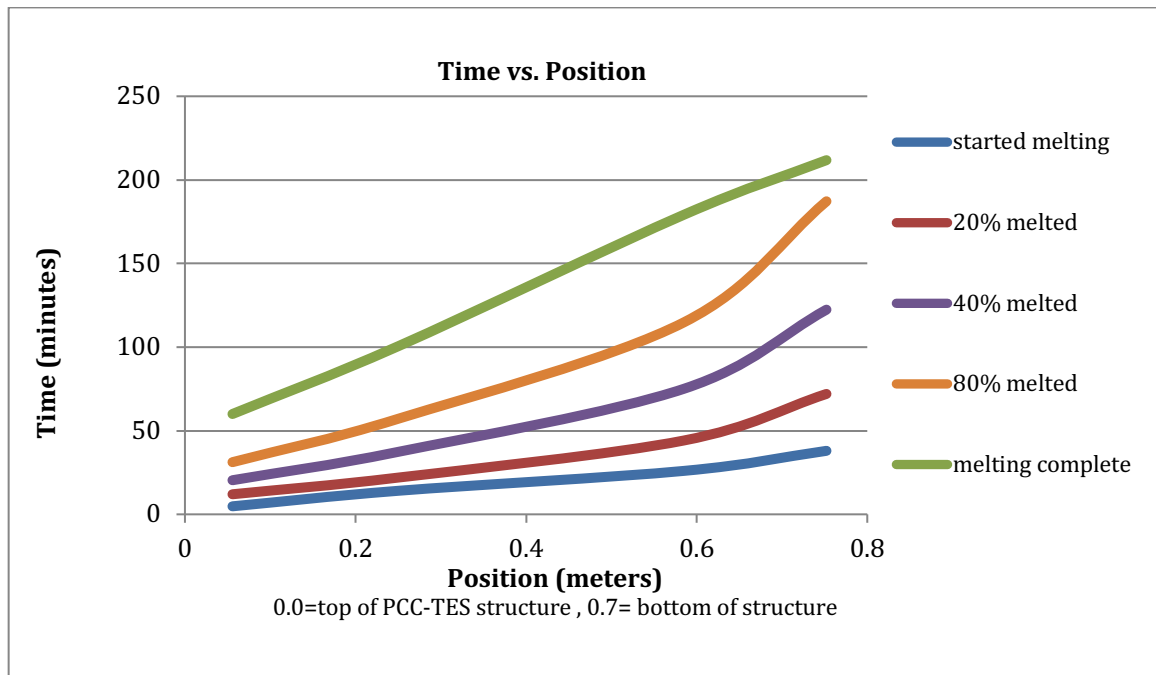


Figure 5.18: Timing of melting profiles with respect to position in PCC-TES [reference: (A. Aljehani et al. 2018)]

On the other hand, the actual experiment revealed approximately the same duration of useful heat exchange of approximately 3 hours and 27 minutes as illustrated by Figure 5.18 and discussed earlier. The actual experiment duration also accounted for sensible heat before and after melting in addition to melting duration. The small discrepancy may be attributed to possible heat loss to surroundings in the actual experiment. In light of the very good agreements between the experimental data and the evaluation model's forecast, the simulation model was considered validated and was ready to perform further analysis.

Before proceeding to perform further analysis, it is worth mentioning that one of the main advantages of simulation modeling over actual experimental testing is the capability of simulating downstream heat exchange between EG intermediate loop and the air stream while that was not a provision in the actual experimental setup. One more advantage of simulation modeling over actual testing is the capability of changing dimensions, thermal capacities and operating strategies without having to build multiple actual experimental setups.

5.7 Case studies

In previous sections, the concept of integrating a TES into an AC system was introduced. In addition to that, the evaluation model's scientific background, the simulation model developing approach and model validation were also discussed. This section will utilize the validated simulation model to evaluate and analyze the following conceptual case study.

5.7.1 Case study: AC integrated with PCC-TES vs. Conventional AC without a TES

This case study explores whether or not the concept of integrating a PCC-TES (Phase Change Composite-Thermal Energy Storage) into an AC system can have a positive impact on the overall air conditioning system performance and electricity consumption. The validated simulation model was used to address the performance comparison.

5.7.1.1 Comparison criteria

To conduct the case study, two air conditioning systems: a conventional AC without a TES versus a conventional AC integrated with a PCC-TES were simulated, analyzed and compared. The comparison analysis was performed with respect to the following comparison criteria: refrigeration compressor size (kW), electricity consumed (kWh) by the compressor, cost of electricity consumed by the compressor (\$), compressor efficiency during cooler hours/days of the year and CO₂ emissions (lbs. of CO₂).

5.7.1.2 Testing basis

As far as the price of electricity consumed by the compressor, this present work applied Southern California Edison Electric utility company (ToU) rate plan on year 2016 (Southern California Edison 2016). That is 0.235 \$/kWh from 12 pm to 6 pm plus a demand charge of \$9.5/MAX kW for each billing cycle. The company applies \$0.191/kWh and \$0.064/kWh electricity ToU charges for mid-peak and off-peak-hours respectively. As far as cooling load requirement, Table 5.6 illustrates the thermal cooling load requirements to be met by both systems. Both systems were required to meet the same thermal cooling loads of 24 kW and 12 kW during peak-hours and off-peak-hours respectively. No cooling

loads were required to be met during off-peak-hours assuming a small shop space or a restaurant. To better understand the relation between the required thermal cooling load and compressor rating, it is very useful to recall, from thermodynamics principles, that the coefficient of performance (COP) of a refrigeration loop is equal to the useful heat (Q) provided by a given system divided by the electricity consumed (E) by the same system as illustrated by equation (5.28).

$$(COP) = \frac{Q}{E} \quad (5.28)$$

Table 5.6: Cooling load demand required to be met by both systems

Cooling Load Required to be met by both systems	
Peak-hours (noon- 6 pm)	16 kW
Mid-peak-hours during: (9 am- Noon) & (6 pm -11pm)	8 kW
Off-Peak-hours (11pm-9am)	No Requirement

5.7.1.3 **Results and discussion**

Following the preliminary design stage for the refrigeration cycle for each of the two systems using the developed and validated Aspen Plus® simulation model, the following facts were revealed:

- 1) 5 kW Compressor is required for the “conventional AC with no TES” to meet the 16 kW per hour of thermal cooling load during each of the six peak-hours. However, it is oversized for the 8 kW per hour thermal cooling demand during each of the mid-peak-hours.

- 2) 2.5 kW compressor is required for the new proposed system (AC + PCC-TES) to meet 50% of the 8 kW thermal cooling load requirement during each hour of the six peak-hours while the PCC-TES meets the other half of cooling load requirement. During mid-peak-hours, the 2.5 kW compressor has just the precise size needed to meet the cooling demand.
- 3) The other half of the thermal cooling load during each of the six peak-hours will be met by PCC-TES. Accordingly, a total of 960 kg of PCC is required to meet the cooling load demand of 8 kW that is equivalent to 28800 kJ on each of the six peak-hours, a total of 172800 kJ during the whole 6 hours peak period. On each peak hour approximately 160 kg of PCC will be melted; recall that PCC has latent heat of 180 kJ/kg.

Table 5.7 summarized the overall results of the case study's performance comparison. As illustrated by Table 5.7, integrating a conventional AC with a PCC-TES would result in designing for a smaller refrigerant loop and accordingly a smaller compressor size. The smaller compressor is also just the right size for mid/off-peak-hours. It is neither oversized for cooler mid/off-peak-hours nor oversized for the other cooler seasons of the year.

The Aspen Plus® simulation model showed that the proposed system (AC + PCC-TES) would have the advantage of 50% approximate reduction in refrigerant compressor size. Running a 50% smaller compressor during cooler hours/days of the year, instead of an oversized compressor, will reduce electricity consumed. Due to smaller refrigerant compressor, proposed system would result in 45% reduction in electricity bill. Similarly, proposed integration of (AC + PCC-TES) would result in approximately 30% reduction in CO₂ emissions during a summer season in comparison to conventional AC's CO₂ emissions. Moreover, proposed integration would result in doubling the COP during mid

and off-peak-hours in comparison to the COP of an oversized conventional AC during those hours. The COP is doubled during mid/off-peak-hours because of the fact that the new AC (integrated with the PCC-TES) is not oversized anymore to meet the peak-hours of a summer season, it is now just the right size for mid/off-peak-hours demand. A conventional AC without a TES is usually designed to be large enough to handle summer seasons, yet oversized for other seasons. Therefore, this case study concluded that integrating a conventional AC with a PCC-TES would certainly have great positive impacts on the overall system performance and electricity consumption as demonstrated by Table 5.7.

Table 5.7: Modeling Comparison: Conventional AC vs. an integrated unit (AC+ PCC-TES). reference: (A. Aljehani et al. 2018)

Details	Conventional AC	Integrated unit (AC + PCC-TES)	Quantified Benefits of integrated system (AC + PCC-TES)
Compressor Size + Storage Size	5 kW + no storage	2.5 kW + 960 KG of PCC thermal storage	50% reduction in compressor size
COP (During Mid/off-peak)	1.6	3.2	Double COP during Mid/Off-peak-hours
Electricity consumed by the refrigeration compressor (kWh/Summer)	4,200 kWh	3,000 kWh	Approximately 30% reduction in electricity consumption during a summer season
Cost of Electricity Consumption (\$)	\$ 929	\$ 522	45% reduction in electricity bill during a summer season
CO ₂ Emission (lb. CO ₂ /Summer Season)	2,200 lbs. CO ₂	1,572 lbs. CO ₂	Approximately 30% reduction in CO ₂ emissions during a summer season

Accordingly, Table 5.8 was generated to provide a detailed breakdown of the electricity consumed by the refrigeration compressor in each case and the associated reduction in CO₂ emissions

Table 5.8: Breakdown of electricity consumed by each refrigeration compressor and associated reduction in CO₂ emissions [reference: (A. Aljehani et al. 2018)]

Breakdown of compressor's electricity consumption durations	Conventional AC	Integrated air conditioning unit (AC + PCC-TES)	Remarks
AC's compressor consumption (kWh) during peak-hours (12PM- 6 PM) = (6 hours) for weekdays only assuming flat rate in weekend (6 hours)	(5 kW compressor rating) X (6 hours) X (5 days) X (4 weeks) X (3 Months) = 1800 kWh	(2.5 kW compressor rating) X (6 hours) X (5 days) X (4 weeks) X (3 Months) = 900 kWh	New proposed system would require smaller compressor since the PCC-TES would meet half of the cooling load demand during peak-hours
AC compressor consumption (kWh) during mid-peak-hours (9am-12noon) + (6 pm -11 pm) = (8 hours)	(5 kW compressor rating) X (8 hours) X (5 days) X (4 weeks) X (3 Months) = 2400 kWh	(2.5 kW compressor rating) X (8 hours) X (5 days) X (4 weeks) X (3 Months) = 1200 kWh	Conventional AC wastes energy during mid and off-peak-hours due to oversized compressor to meet peak-hours demand while the (AC+ PCC-TES) will have just the right size compressor.
AC compressor consumption (kWh) during off-peak-hours (6 hours)	The conventional AC compressor is not operated due to no cooling demand at night = 0 kWh	(2.5 KW compressor rating) X (6 hours) X (5 days) X (4 weeks) X (3 Months) = 900 kWh	The PCC-TES needs to be charged again during the nighttime. That's why the refrigeration compressor is running while no cooling load demand is required from a conventional AC during off-peak-hours
Cumulative kWh consumed during a summer season	4200 kWh	3000 kWh	Approximately 30% reduction in electricity consumed during a summer season
Total CO ₂ emissions during a summer season Emission rate= (electricity consumed kWh)* (0.524 lbs. of CO ₂ /kWh) ¹ ¹ Reference: (California Public Utilities Commission)	(4200 kWh) * (0.524 CO ₂ /kWh) = 2200 lbs. of CO ₂	(3000 kWh) * (0.524 CO ₂ /kWh) = 1572 lbs. of CO ₂	Approximately 30% reduction in total CO ₂ emissions during a summer season

Likewise, Table 5.9 was generated to provide a breakdown of the electricity cost of electricity consumed.

Table 5.9: Breakdown of electricity's cost per compressor consumption [reference: (A. Aljehani et al. 2018)]

Breakdown of electricity costs per compressor	Conventional AC	Integrated air conditioning unit (AC + PCC-TES)	Benefits of proposed system and remarks
<p>Peak-hours compressor consumption (\$/summer season) Time: (12 - 6 pm), weekdays Electricity Price: \$0.235 /kWh</p> <p>Demand charge = (9.51\$/MAX KW a Month)</p>	<p>Cost of electricity consumed by the compressor= 1800 kWh * 0.235 (\$/kWh) = \$ 423</p> <p>Demand charges =5 KW * \$ 9.5 = \$47.5</p> <p>Total charges = \$423 + \$47.5 = \$ 470.5</p>	<p>Cost of electricity consumed by the compressor = 900 kWh * 0.235 (\$/kWh) = \$ 211.5</p> <p>Demand charges= 2.5 KW * \$ 9.5 = \$23.75</p> <p>Total charges =\$211.5 + \$23.75 = \$ 235.25</p>	<p>50% reduction in electricity's bill during peak-hours of a summer season</p>
<p>Mid-peak-hours consumption (\$/summer season) (9 am-12 pm) and (6 pm -11 pm)</p> <p>Electricity Price: \$0.191 /kWh</p>	<p>Electricity cost per compressor consumption</p> <p>2400 kWh * 0.191 \$/kWh = 458.4 (\$/summer season)</p> <p>No Demand charges associated with mid or off-peak-hours</p>	<p>Electricity cost per compressor consumption</p> <p>1200 kWh * 0.191 \$/kWh = 229.2 (\$/summer season)</p> <p>No Demand charges associated with mid or off-peak-hours</p>	<p>50% reduction in electricity's bill during mid-peak-hours of a summer season</p>
<p>Off-peak-hours consumption (\$/summer season)</p> <p>Electricity Price: \$0.064 /kWh</p>	<p>No electricity consumed since the compressor is not running at this time of the day</p>	<p>Electricity cost per compressor consumption 900 kWh * 0.064 \$/kWh = \$ 57.6</p> <p>No Demand charges associated with off-peak-hours</p>	<p>The TES needs to be charged again during the nighttime. The compressor is running in the new proposed case</p>
<p>Cumulative electricity cost during a summer season</p>	<p>\$ 929*</p>	<p>\$ 522*</p>	<p>45% reduction in total electricity's bill during a</p>

Table 5.9 calculations illustrate a nearly 1.5 refrigerant-ton AC system to meet a low thermal cooling load of 16 kW per hour; higher benefits would be seen if larger cooling loads were considered.

5.7.1.4 Case Study 1 Conclusions

The analysis in this chapter revealed that integrating a conventional AC with a PCC-TES would certainly have a positive impacts on the overall conditioning system performance and electricity consumption. The proposed PCC-TES integration with AC would result in 50% smaller AC's compressor design requirement, 30% lower electricity consumption, 45% lower electricity bill and 30% lower CO₂ emissions during expensive peak-hours of a summer season.

The work of this chapter successfully tested and verified the proposed hypothesis, which suggests that integrating a conventional AC with a PCC-TES, would result in great benefits concerning compressor size, compressor efficiency during cooler hours/days of the year, electricity consumed and CO₂ emissions. The subject integration would contribute to completely or partially shift electricity demand from peak-hours to off-peak-hours; contributing to reduce the worldwide ever-increasing electricity demand during peak-hours. This would contribute to reduce necessity for building additional expensive new power plants and distribution lines. To test the hypothesis, a simulation model in Aspen Plus® software was prepared. However, Aspen Plus® did not have an in-built library to predict PCC's melting and solidification behaviors. Therefore, an analytical heat transfer model was written as a system of equations in Fortran into Aspen Plus® calculation block to simulate the phase change behavior and associated valuable information. The simulation of the proposed integration between the AC and the PCC-TES revealed that the proposed integration would result in downsizing compressor design by 50%, lowering electricity consumption by 30%, doubling the efficiency during mid and off-peak-hours, and lowering

CO₂ emissions by 30%. The simulation model was validated by crosschecking the simulation model results with actual experimental data from an actual 4 kWh PCC-TES benchtop thermal storage system. A very good agreement between the simulation model results and the actual experimental data was observed.

5.7.2 Case study 2: PCC-based TES (PCC-TES) vs. ICE-based TES (ICE-TES)

5.7.2.1 Introduction to case study 2

As mentioned in the literature review of this study, ice has been popularly used for commercial cold (TES) applications integrated into a conventional air conditioning system. However, ice thermal energy storages are not very ideal candidate for building cooling applications due to supercooling issues, low thermal conductivity and low melting temperature. The melting temperature of ice is much lower than the required optimum operating temperature for a conventional AC and therefore reduces operating efficiency by 30% - 40%. Therefore, ice-based thermal energy storage (ice-TES) needs to be oversized to compensate for the low thermal conductivity and low operating efficiency. Many efforts in the literature also studied alternating control strategy of air conditioning system to ensure faster response to cooling load (Xue Xue et al. 2015; S. Wang and Tang 2017; Kui Shan, Shengwei Wang, Chengchu Yan 2016; Cui et al. 2015). However, such alternation in control strategy may lead to discomfort and chiller operation instability.

In light of aforementioned, study case 2 is addressing the performance comparison between the PCC-TES and the ice-TES by quantifying discharging characteristics of both systems. This part of the chapter compares PCC-TES, with an equivalent in thermal capacity ice-

thermal energy storage (ice-TES). The work developed in this study proposed, tested and verified a hypothesis, which suggests that a PCC-TES system would have a quicker response to cooling demand than a comparable, in thermal capacity, ice-TES system due to the presence of highly conductive graphite in the PCC.

Hypothesis. The proposed phase change composite-thermal energy storage (PCC-TES) system would have a quicker response to cooling demand than a comparable, in thermal capacity, ice-TES system due to the presence of highly conductive graphite in the phase change composite (PCC).

To test the hypothesis, this current research work used the same conceptual analytical simulation model developed and experimentally validated in the previous. How fast a given air conditioning system would respond to cooling demand? Many efforts in the literature studied alternating control strategy of air conditioning system to ensure faster response to cooling load (Cui et al. 2015; S. Wang and Tang 2017; Kui Shan, Shengwei Wang, Chengchu Yan 2016; Xue Xue et al. 2015). However, such alternation in control strategy may lead to discomfort and chiller operation instability. With the concentration on speed of response, this study compares the use of a phase change composite (PCC) material, consisting of paraffin wax (n-Tetradecane) and expanded graphite, as a potential storage medium for cold TES system with the use of ice as the current and dominant phase change material for air cooling applications. The comparison of discharging characteristics or the speed of response of the two equivalent systems (PCC-TES and ice-TES) was not yet addressed in the literature.

5.7.2.2 Case study 2: comparison criteria

Case study 2 explores whether a PCC-based TES (PCC-TES) can be a better alternative for an ice-based TES (ice-TES). Therefore, both systems, PCC-TES and ice-TES, were analyzed and benchmarked with respect to how fast they can respond to thermal cooling load. In particular, the discharging rate of each system was calculated and benchmarked using the same evaluation model specially designed and developed for this present work.

5.7.2.3 Case study 2: testing basis

For identical testing basis, both systems, PCC-TES and ice-TES, were required to provide the same thermal cooling load and be the sink for 4 kW of thermal cooling load. Table 5.10 illustrates the cooling load required from each system and attributes of each of the two systems evaluated.

Table 5.10: Cooling load demand required to be met by both systems + systems attributes

Cooling load requirement for PCC-TES and system attributes		Cooling load requirement for ice-TES and system attributes	
Cooling load requirement	4 kW	Cooling load	4 kW
PCC Latent heat	180 kJ/kg	Ice Latent heat	334 kJ/kg
PCC weight Required	80 kg	Ice weight Required	44 kg
Total length of copper tube passes	51 meters	Total length of copper tube passes	51 meters
Density, ρ	850 (kg/m ³)	Density, ρ	1000 (kg/m ³)
Specific heat, C_p	1.6 (kJ/kg.°C)	Specific heat, C_p	3.3 (kJ/kg.°C)

5.7.2.4 Case study 2: results and discussion

As highlighted by Table 5.12, the simulation model results revealed PCC-TES will melt within approximately 3 hours and 37 minutes. The ice-TES simulation model output illustrates that the whole ice-TES will melt within approximately 14 hours and 12 minutes. Therefore, current work case study investigation revealed that a PCC-TES has faster discharging rate than an ice-TES system. The PCC-TES system discharges approximately 11 hours faster than ice-TES; that's means a faster response to cooling demand. The slow response of ice-TES is attributed to low thermal conductivity of ice in comparison to PCC as highlighted by Table 5.12. Furthermore, the thermal diffusivity for PCC material, expressed in units of (m^2/s), is much higher than the thermal diffusivity of ice as highlighted by Table 5.11.

Table 5.11: Comparing the discharging rates of PCC-TES vs. PCC-ice in addition to the comparison of most important system attributes effecting discharging rates

PCC-TES discharging duration and most important system attributes		ICE-TES discharging duration and most important system attributes	
Discharging duration of a 4 kWh PCC-TES	3 hours and 37 minutes	Discharging duration of a 4 kWh ice-TES	14 hours and 12 minutes
Thermal Conductivity (W/m. K)	22	Thermal Conductivity (W/m. K)	2.2
Thermal Diffusivity (m^2/s)	0.016	Thermal Diffusivity (m^2/s)	0.00066

To achieve a better response, the ice-TES system should have approximately 10 times the existing copper tubes length as revealed by the trial and error approach using the simulation

model. Figure 5.19 of an ice-TES illustrates the high number of copper tubes needed to compensate for the low thermal conductivity of ice.

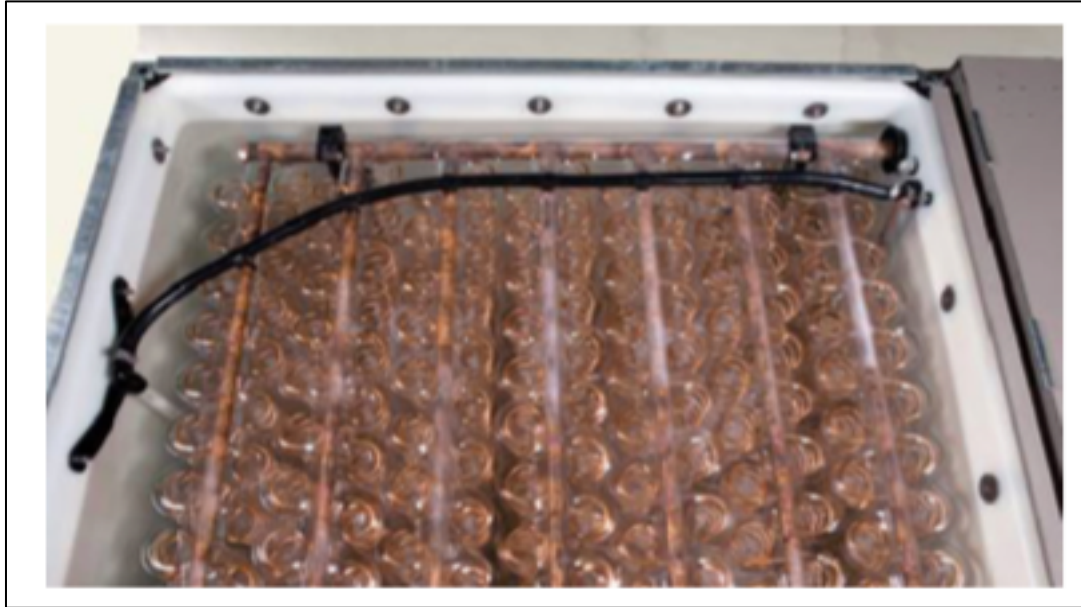


Figure 5.19: high number of copper tubes is required for ice-TES to compensate for the low thermal conductivity of ice (source: (Yau and Rismanchi 2012))

Accordingly, oversizing the ice storage volume, to accommodate the significant increase in the number of copper tubes. This will negatively affect the overall system's latent heat per volume ratio. This will also require enlarging the size of the vapor compression refrigeration loop to speed up the solidification process of the ice-TES during charging mode within the limited night hours. Enlarging the size of the refrigeration loop and accordingly the refrigerant compressor will certainly result in additional electricity consumption and consequently lower the overall efficiency of the ice-TES.

It is worth mentioning that, a 4 kW thermal cooling load is a very small requirement, a larger thermal cooling load requirement would oblige a larger surface area of copper tubes to meet the same discharge rate of an equivalent in size PCC-TES system. The higher

the number of copper tubes, the higher the size of the ice-TES system and the associated vapor compression refrigeration loop and the higher initial cost. Furthermore, the significant increase in the number of tubes and total length would decrease the overall volumetric energy density of the ice-TES, which in turns reduce the latent heat capacity of the system in ratio to overall volume.

On the other hand, the PCC-TES will consume less electricity during “charging mode” than an oversized ice-TES for the same cooling load requirement due to smaller system size, higher thermal conductivity and higher solidifying temperature. Recall that, the melting temperature of ice is zero, which is much lower than the melting range temperature of PCC, which is 4.0 - 6.0 °C. The optimum melting temperature for the intended purpose of air conditioning applications should be in the range of 5-10 °C as illustrated in the literature review section. It is useful at this point to recall from heat transfer principles that thermal diffusivity is the thermal conductivity of the material divided by its volumetric heat capacity as described by equation (3.29):

$$\alpha = \frac{k}{\rho C_p} \quad (5.29)$$

5.7.2.5 Case study 2 conclusion

Case study 2 analysis revealed that a 4 kWh PCC-TES would fully discharge in 3 hours and 37 minutes while the equivalent in size 4 kWh Ice-TES was fully discharged in 14 hours and 12 minutes. The faster discharge rate of PCC-TES system is attributed to high bulk thermal conductivity of the PCC material, which is 10 times higher than ice.

CHAPTER 6: NUMERICAL MODELING OF TRANSIENT HEAT TRANSFER IN A PHASE CHANGE COMPOSITE THERMAL ENERGY STORAGE (PCC-TES) SYSTEM FOR AIR CONDITIONING APPLICATIONS

The research work illustrated by this chapter is published in the Journal of Applied Thermal Engineering:

Ahmed Aljehani, Ludwig C. Nitsche, Said Al-Hallaj, *Numerical Modeling of Transient Heat Transfer in a Phase Change Composite Thermal Energy Storage (PCC-TES) System for Air Conditioning Applications*, Applied Thermal Engineering, 2019, <https://doi.org/10.1016/j.applthermaleng.2019.114522>.

6.1 Introduction, motivation and hypothesis

The work in chapter 5 utilized a mathematical heat transfer model coupled with Aspen Plus® simulation model to (i) study the feasibility of integrating a PCC-TES into the air conditioning system and (ii) describe the melting duration of the PCC-TES and the position of the moving phase boundary. The simplified analytical model was developed with reference to the work of (Mehling and Cabeza. 2008) and (Hans Dieter Baehr and Karl Stephan 2014).

In this chapter, the goal is to generate a more detailed and realistic numerical heat transfer model and consequently provide a more accurate representation of the transient heat transfer problem. The mathematical modeling of the PCC-TES involves formulating two PDEs that represent conduction within the PCC (phase 1) and advection within the heat transfer fluid (EG), which is denoted by phase 2, with interphase heat transfer terms in each equation. The two coupled PDEs were solved with a finite difference method, including unwinding of the advective derivative. The numerics were implemented using Fortran. The

results were validated using experimental data and demonstrated an acceptable agreement and an accurate representation of the transient heat transfer problem.

6.1.1 The hybrid [AC + PCC-TES] at a glance with reference to (Chapter 5) and (A. Aljehani et al. 2018)

Figure 6.1, as illustrated in (Chapter 5) and (A. Aljehani et al. 2018), is a simple diagram of the vapor compression refrigeration loop of a conventional roof-top air conditioner. A conventional vapor compression refrigeration system is composed of a compressor, condenser and expansion valve and an evaporator.

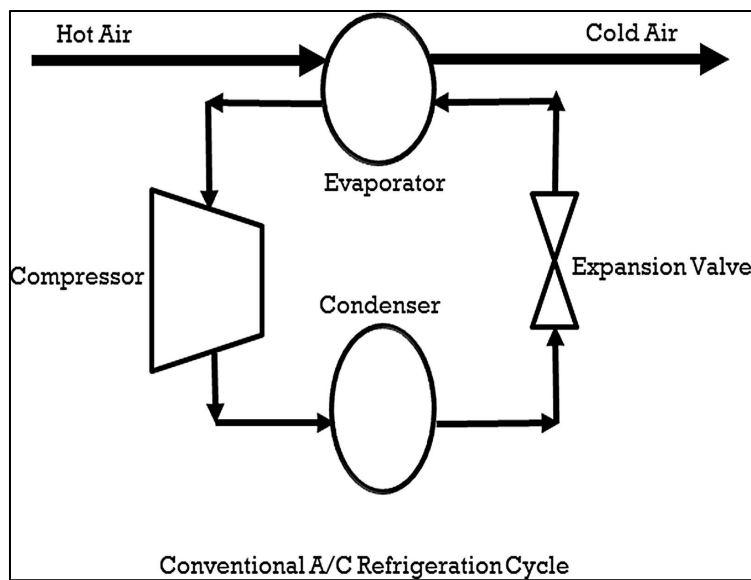


Figure 6.1: AC's conventional refrigeration cycle [reference: (A. Aljehani et al. 2018)]

On the other hand, Figure 6.2 illustrates the concept of the hybrid design [AC + PCC-TES]. As discussed by (Chapter 5) and illustrated here by Figure 6.2 Ethylene Glycol (EG) Loop #1 mediates heat exchange between incoming hot air and the (thawing) PCC during discharging mode. Ethylene Glycol (2) EG Loop #2 mediates heat exchange between the refrigerant and the (freezing) PCC during charging mode.

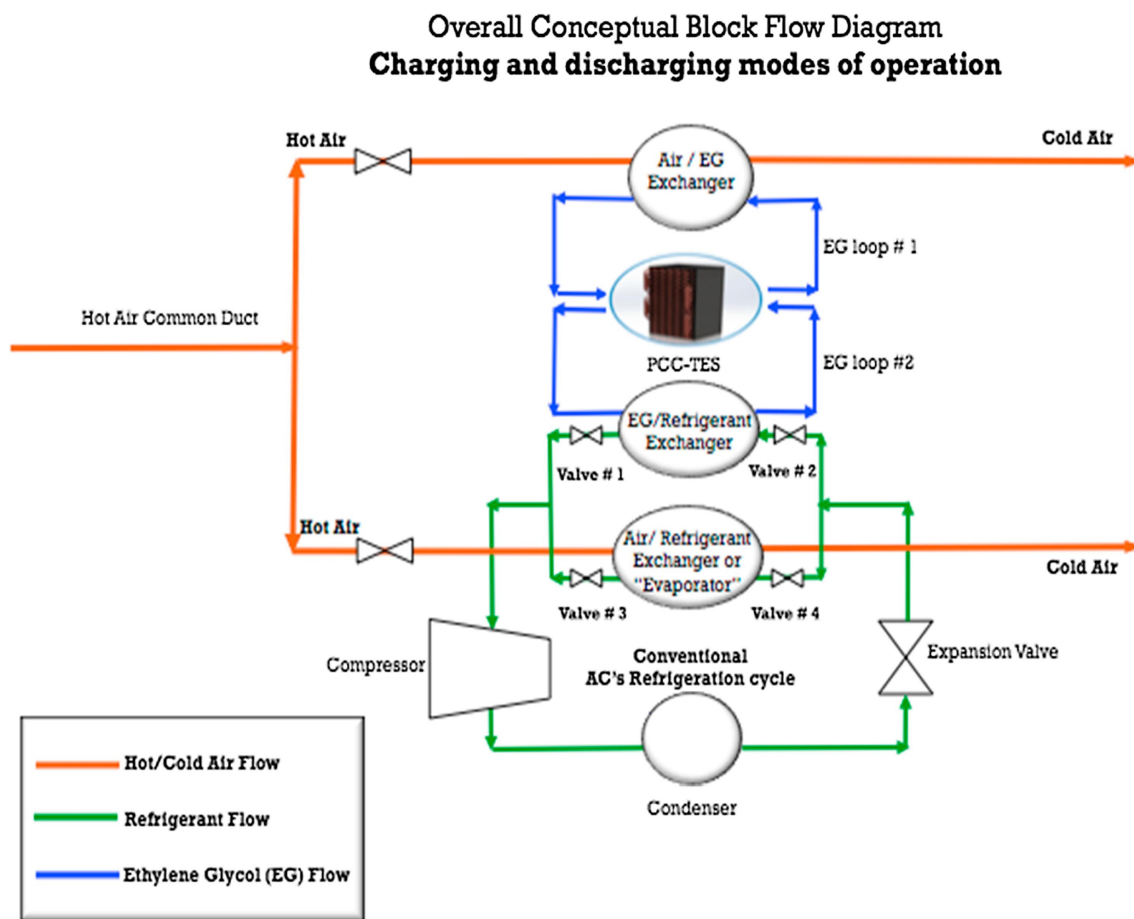


Figure 6.2: Complete system. EG Loop #1 mediates heat exchange between incoming hot air and the (thawing) PCC during discharging mode. EG Loop #2 mediates heat exchange between the refrigerant and the (freezing) PCC during charging mode (reference: [(A. Aljehani et al. 2018)]).

Figure 6.3 depicts the “charging mode” of the PCC-TES during night hours. The PCC-TES rejects heat to the AC’s refrigeration loop and consequently solidifies. As discussed by [(A. Aljehani et al. 2018)] “utilizing the vapor compression refrigeration loop of the conventional AC during inexpensive off-peak-hours”.

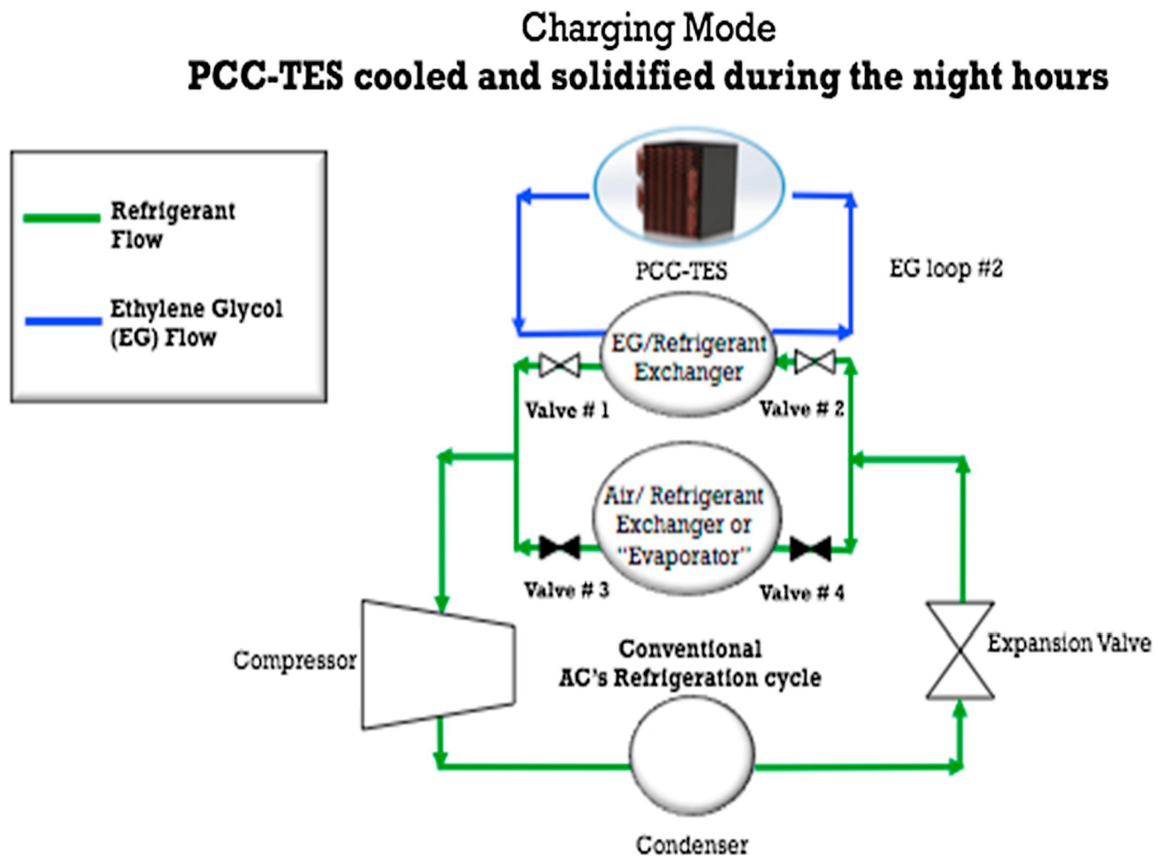


Figure 6.3: Charging mode operates with valves 1 and 2 open and valves 3 and 4 closed. During night hours the AC refrigerant loop cools and freezes the PCC (reference: (A. Aljehani et al. 2018)).

In the “discharging mode” during peak-hours, Figure 6.4, the PCC-TES absorbs the heat from incoming air and melts as it provides supplemental cooling.

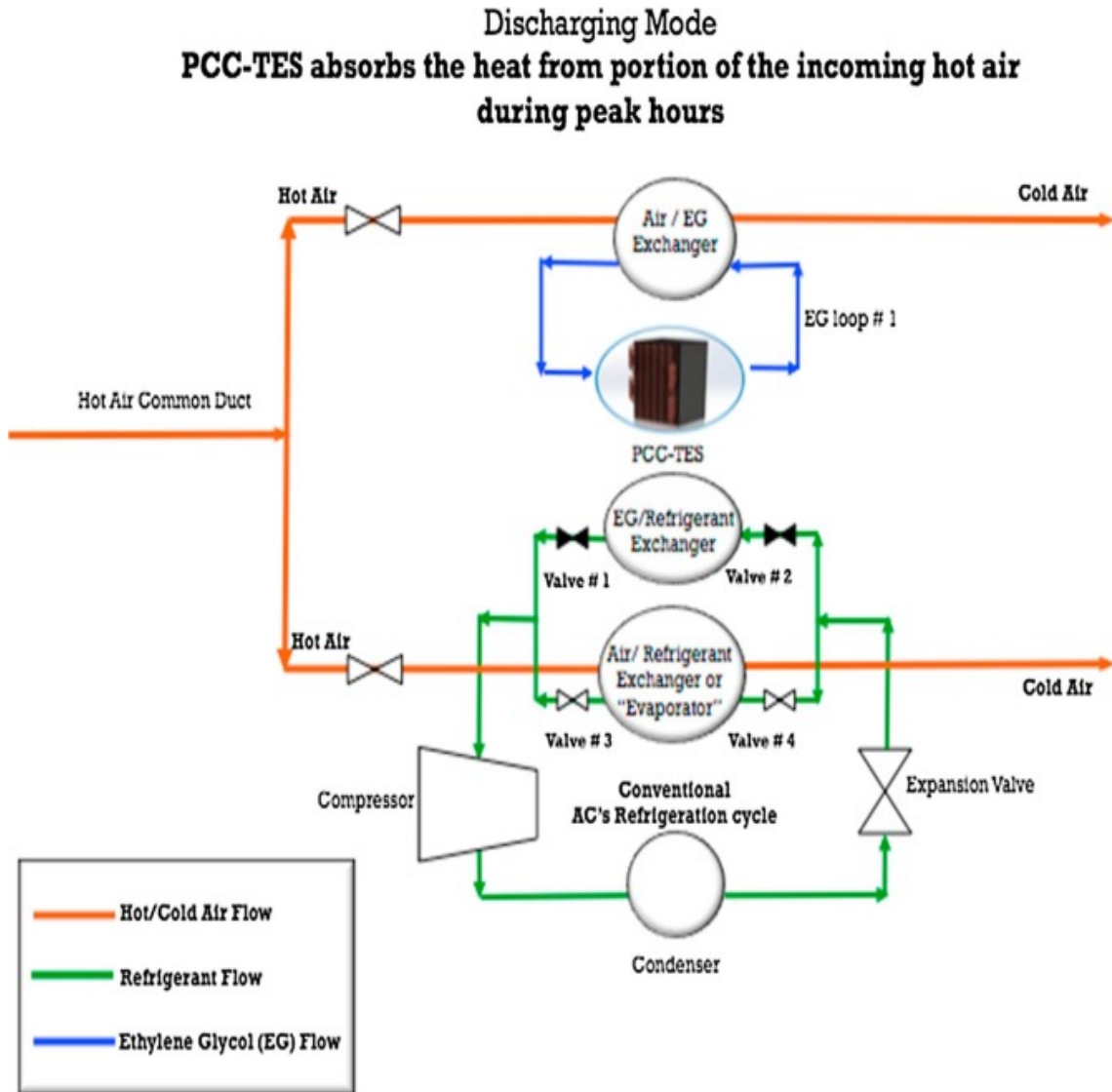


Figure 6.4: Discharging mode operates with valves 1 and 2 closed and valves 3 and 4 open. During peak day hours cooling of hot air is divided between the refrigerant loop and the melting PCC (reference: [(A. Aljehani et al. 2018)]).

6.1.3 Theoretical foundation about the heat transfer problem formulation in previous work

In Chapter 5 (A. Aljehani et al. 2018), the heat transfer problem was addressed experimentally (as shown by Figures (6.5 and 6.6) and also theoretically — the latter by

adapting an available analytical solution of the Stefan problem [(Mehling and Cabeza. 2008; Hans Dieter Baehr and Karl Stephan 2014; Kostenko, Pribis, and Puzynin 2003)].

The goal of Chapter 6 is to generate a more detailed and realistic numerical heat transfer model and consequently provide a more accurate representation of the transient heat transfer problem.

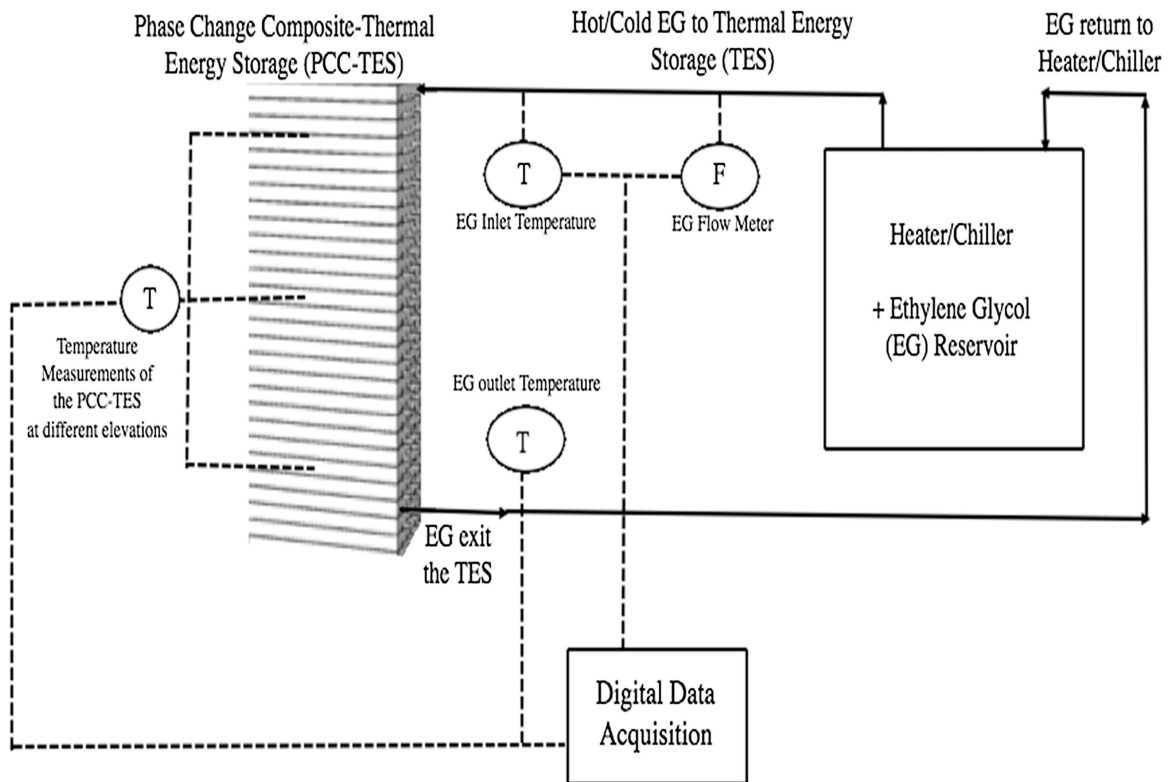


Figure 6.5: Schematic of the PCC-TES system (reference: (A. Aljehani et al. 2018)).

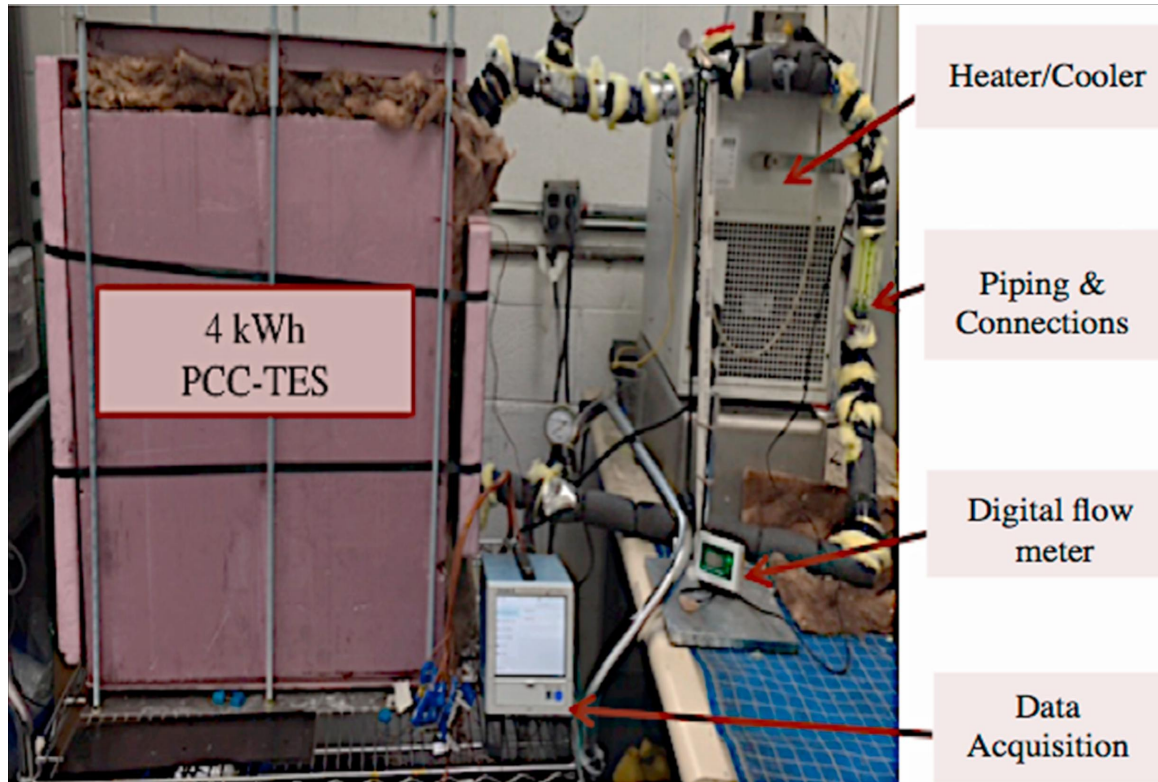


Figure 6.6: Actual experimental set up of the PCC-TES system (reference: (A. Aljehani et al. 2018))

The work by Chapter 5 (A. Aljehani et al. 2018) highlighted two differences between the classical Stefan problem and our case of the PCC-TES system:

(1) The heat source (EG flowing through copper tubing among slabs of PCC) is distributed throughout the volume and not only exposed to the outside surface. We referenced an article by (Kostenko, Pribis, and Puzynin 2003) that successfully articulated an applicable heat balance for this case.

(2) The PCC contains a mixture of paraffins and therefore has a melting range instead of one melting point. Chapter 5 (A. Aljehani et al. 2018)], discussed how to use the effective

specific heat method as introduced by (Farid, M. M., Hamad, F. A., & Abu-Arabi et al. 1998; Khateeb et al. 2005).

6.2 PDE model with one space dimension

The mathematical modeling of heat uptake by the PCC-TES involves formulating two PDEs that represent conduction within the PCC (phase 1) and advection within the EG (phase 2), with interphase heat transfer terms in each equation.

We then solved the two coupled PDEs with a finite difference method, including unwinding of the advective derivative. The numerics were implemented using Fortran. Figures 6.7 and 6.8 illustrate how the Cartesian coordinate system is oriented with respect to the stack of PCC slabs.

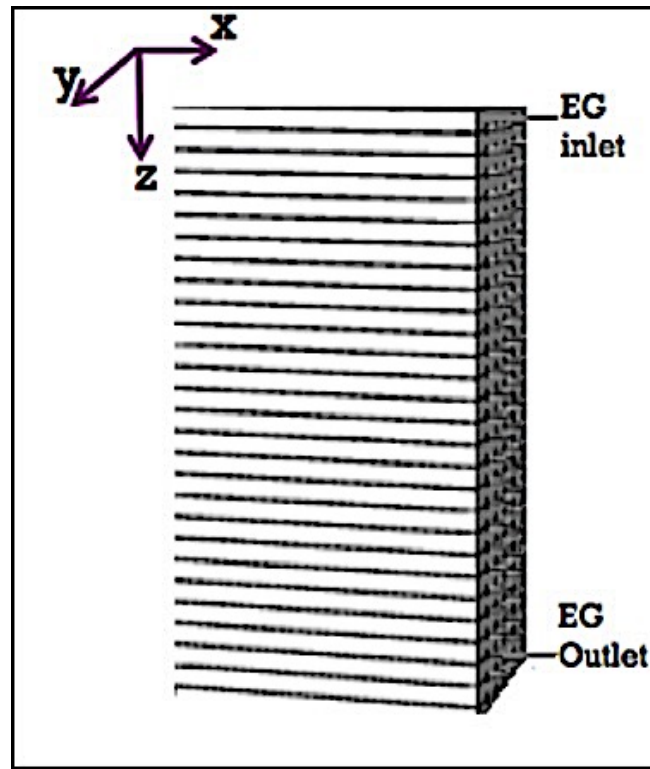


Figure 6.7: PCC-TES conceptual design; PCC-TES exchanging heat with EG stream (reference: [(Chapter 6) and (A. Aljehani et al. 2018)]).

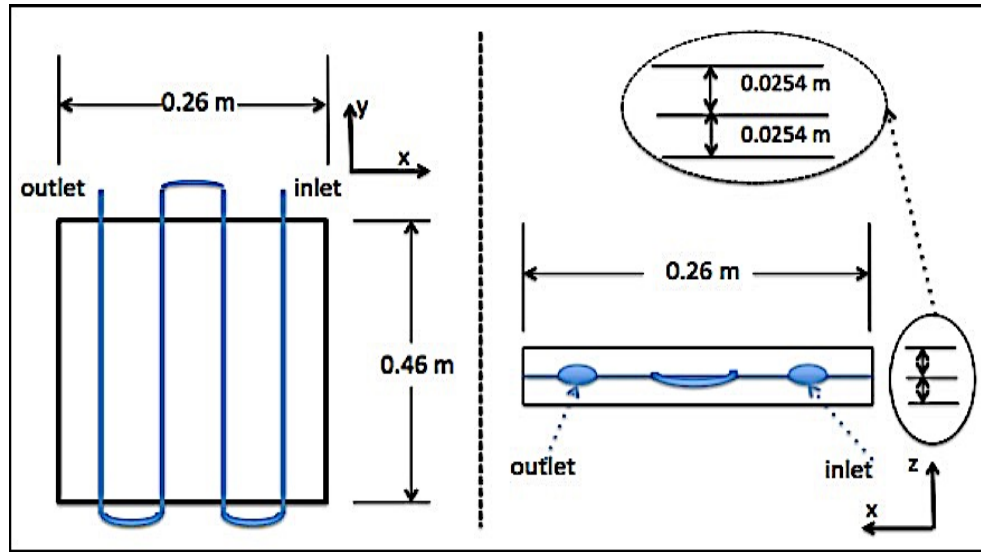


Figure 6.8: Internal details/Dimensions of one slab of the PCC-TES
(reference: (A. Aljehani et al. 2018))

6.3 Numerical model equations

As was noted in chapter 6, one dimensional heat transfer in z-direction appears sufficient to capture the important effects in the transient advection- conduction process. The one-dimensional heat transfer is assumed because the length of the tube is much larger than the radius of the tube and this corresponds to hot fluid top to bottom temperature profile. EG is entering the PCC-TES structure from top inlet provision and leaves off the bottom as illustrated by Figures (6.5 and 6.7). As opposed to the temperature drop from top to bottom, EG flowing within any slab barely varies by 0.3°C between the tortuous tube's inlet and outlet of that x-y plane. This assumption is supported by consideration of the experimental setup, Ethylene Glycol (EG) enters the top of the PCC-TES structure at $T_2 = 14^{\circ}\text{C}$ and exits at the bottom at a colder temperature that — early in the experiment — is close to the initial, uniformly frozen temperature of the PCC, $T_1 = 0^{\circ}\text{C}$. Uniformity of temperature in

the x-y plane is therefore imposed by the circuitous nature of the tube path within the cross section rather than being motivated by a small value of the relevant Biot number (which would be too large to justify the one-dimensional model considered in isolation from the tubing spread across the cross section). Conservation of energy in the PCC (phase 1) is expressed by the dimensionless PDE (6.1).

$$\frac{\partial \theta_1}{\partial \tau} = \frac{1}{\gamma(\theta_1)} \left[\frac{\partial^2 \theta_1}{\partial \zeta^2} + \mathcal{A}(\theta_2 - \theta_1) \right] \quad \text{PDE-1, (6.1)}$$

in which the position coordinate (z) is scaled to the height (L) of the entire stack of PCC slabs, the time coordinate (t) is reduced by the characteristic conduction time associated with the thermal diffusivity (α_1) in the solid phase, and temperature is expressed as a fractional rise from the coldest (T_1) to the hottest temperature (T_2) in the problem.

$$\zeta = \frac{z}{L}, \quad \tau = \frac{t\alpha_1}{L^2}, \quad \theta = \frac{T - T_1}{T_2 - T_1} \quad (6.2)$$

The dimensionless temperature-dependent effective heat capacity $\gamma(\theta_1)$ is scaled to the solid-phase heat capacity (C_p^{solid}) of the paraffin and includes latent heat over the melting range as addressed in (Chapter 3) and with reference to published effective heat capacity method discussed by (Farid, M. M., Hamad, F. A., & Abu-Arabi et al. 1998; Khateeb et al. 2005).

$$\begin{aligned}
\mathcal{A} &= \frac{Bi}{1 - \phi} \\
Bi &= \frac{hL_{\text{eff}}}{k_1} \\
L_{\text{eff}} &= \frac{\pi D \mathcal{F} L^2}{A_c} \\
\phi &= \frac{\mathcal{F} \pi D^2}{4A_c}
\end{aligned}
\tag{6.3}$$

The constant (\mathcal{A}) describing interphase heat transfer is given in terms of the Biot Number (Bi) and the volume fraction (ϕ) of the tubes passing through the PCC structure. The Biot number involves the heat transfer coefficient (h), thermal conductivity (k_I) of the PCC material, and an effective length (L_{eff}) that factors in total perimeter of the tubes, having diameter (D), and the cross-sectional area (A_c) of the PCC slab in the x-y plane. The tubes are substantially longer than (L), being folded back and forth throughout the PCC stack. The associated tortuosity (i.e., excess-length) factor is called (\mathcal{F}).

PDE (6.1) governs the temperature profile along PCC and represents the local accumulation of energy being balanced by conduction and communication of heat to/from the EG across the tube walls. For consistency with PDE (6.1) for the PCC, the energy balance equation for the flowing EG is phrased in terms of the same dimensionless position and time variables. The tortuosity factor (\mathcal{F}) converts axial position along the circuitous tube path to an equivalent dimensionless position (ζ) along the PCC.

$$\frac{\partial \theta_2}{\partial \tau} = -\mathcal{B} \frac{\partial \theta_2}{\partial \zeta} - \mathcal{C}(\theta_2 - \theta_1) + \mathcal{D} \frac{\partial^2 \theta_2}{\partial \zeta^2} \quad \text{PDE-2, (6.4)}$$

PDE-2 (6.4) equation represents accumulation of thermal energy being balanced by advection, interphase transfer and conduction. The coefficient (\mathcal{B}) is a Peclet number involving flow velocity (U) in the EG but thermal diffusivity (α_1) within the PCC:

$$\mathcal{B} = \frac{UL}{\alpha_1 \mathcal{F}}, \quad \text{with} \quad \alpha_1 = \frac{k_1}{\rho_1 C_{p,1}^{\text{solid}}} \quad (6.5)$$

The constant (\mathcal{C}) in the interphase heat transfer term:

$$\mathcal{C} = \frac{\psi}{\phi} Bi, \quad \text{with} \quad \psi = \frac{\rho_1 C_{p,1}^{\text{solid}}}{\rho_2 C_{p,2}^{\text{liq}}}. \quad (6.6)$$

The factor (ψ) represents the ratio of thermal capacities between the PCC and EG.

Finally, the dimensionless thermal conductivity is:

$$\mathcal{D} = \frac{1}{\mathcal{F}} \frac{\alpha_2}{\alpha_1}. \quad (6.7)$$

For the PCC-TES system studied in the laboratory, representative values of the dimensionless coefficients are as follows:

$$\mathcal{A} \approx 80, \quad \mathcal{B} \approx 450, \quad \mathcal{C} \approx 1400, \quad \mathcal{D} \approx 0.000083$$

Comparison of the last three coefficients shows why we would expect conduction within the EG to be relatively unimportant.

6.3.1 Initial and boundary conditions

Before the hot EG is pumped through the system, the entire stack of PCC slabs and the EG fluid filling the tubes begin uniformly at the temperature of the frozen PCC material.

$$\theta_1(\zeta, 0) = 0, \quad \theta_2(\zeta, 0) = 0 \quad (6.8)$$

The PCC stack is thermally insulated on both ends:

$$\left. \frac{\partial \theta_1}{\partial \zeta} \right|_{\zeta=0} = 0, \quad \left. \frac{\partial \theta_1}{\partial \zeta} \right|_{\zeta=1} = 0 \quad (\tau > 0) \quad (6.9)$$

If we neglect conduction in the flowing EG (the limit of $D \rightarrow 0$ in equation 6.4), then only an inflow boundary condition applies to a PDE that is now first-order in the space variable:

$$\theta_2(0, \tau) = 1 \quad (\tau > 0) \quad (6.10)$$

Otherwise we have two boundary conditions of the Danckwerts type by analogy with advection-diffusion in one-dimensional models of plug flow reactors with dispersion as discussed by (De Wilde and Froment 2012; Danckwerts 1979; Folger 2006; Mott and Green 2015).

$$\left. \frac{\partial \theta_2}{\partial \zeta} \right|_{\zeta=0^+} = \frac{\mathcal{B}}{\mathcal{D}} [\theta_2(0^+, \tau) - 1], \quad \left. \frac{\partial \theta_2}{\partial \zeta} \right|_{\zeta=1} = 0. \quad (6.11)$$

6.3.2 Numerical method

The two coupled PDEs 1 & 2 [equations (6.2) and (6.4), respectively] were solved using a finite difference method implemented with object-oriented Fortran. The space coordinates $0 \leq \zeta \leq 1$ was discretized with a regular grid of $N = 40$ intervals.

To compute the conduction terms $\partial^2 \theta / \partial \zeta^2$ we used a (second order) three-point central-difference stencil:

$$\left. \frac{\partial^2 \theta}{\partial \zeta^2} \right|_n = \frac{\theta_{n+1} - 2\theta_n + \theta_{n-1}}{(\Delta \zeta)^2} \quad (n = 0, \dots, N) \quad (6.12)$$

Applied at the end nodes ($n = 0, N$), central-difference versions of the boundary conditions (6.9) furnished function values at fictitious node points ($n = -1, N + 1$) extending beyond the domain.

$$\frac{\theta_1 - \theta_{-1}}{2\Delta\zeta} = 0 \Rightarrow \left. \frac{\partial^2 \theta}{\partial \zeta^2} \right|_0 = \frac{2(\theta_1 - \theta_0)}{(\Delta\zeta)^2} \quad (6.13)$$

$$\frac{\theta_{N+1} - \theta_{N-1}}{2\Delta\zeta} = 0 \Rightarrow \left. \frac{\partial^2 \theta}{\partial \zeta^2} \right|_N = \frac{2(\theta_{N-1} - \theta_N)}{(\Delta\zeta)^2} \quad (6.14)$$

The advective derivative in equation (PDE-2 (6.4)) is up-winded with backward stencils having either three points (second order) or two points (first order).

$$\left. \frac{\partial \theta}{\partial \zeta} \right|_n = \frac{3\theta_n - 4\theta_{n-1} + \theta_{n-2}}{2\Delta\zeta} \quad \text{or} \quad \frac{\theta_n - \theta_{n-1}}{\Delta\zeta} \quad (6.15)$$

In the former case, the node farthest upstream had to be treated with a two-point difference. The boundary condition(s) described by equations (6.10 or 6.11) was/were used to calculate the rates at the boundaries depending on whether or not conduction in flowing EG is neglected.

To satisfy Courant, Friedrichs and Lewy (CFL) stability condition: the step size in ζ and τ are 0.02 and 0.00001 respectively, while the flowing EG's velocity is 0.76 m/s.

6.3.3 Numerical model- physical parameters details

Table 6.1 summarizes the major parameters of the mathematical numerical model.

Table 6.1: Major parameters of the mathematical model (Ahmed Aljehani, Nitsche, and Al-Hallaj 2020).

Parameter	Value	Unit
Initial uniform temperature of PCC slabs (T_1)	0.0	Degree Celsius
Inflow temperature of EG (T_2)	14.0	Degrees Celsius
Tortuosity factor (F)	73.6	Dimensionless number
Heat transfer coefficient (h)	0.22	$\text{kJ/s m}^2 \text{ K}$
EG's Tube Diameter (D)	0.008	Meters
Thermal conductivity of PCC material (K_{pcc})	0.022	kJ/s m K
Density of PCC material (ρ_1)	850.0	kg/m^3
Cross sectional area of the PCC slab (A_C)	0.1196	m^2
Overall height of the PCC structure (L)	0.71	Meters
PCC material-solid phase's specific heat (C_{p_s})	1.6	$\text{kJ/kg } ^\circ\text{C}$
PCC material-liquid phase's specific heat (C_{p_l})	1.7	$\text{kJ/kg } ^\circ\text{C}$
EG specific heat ($C_{p_{eg}}$)	2.325	kJ/kg K
Density of EG (ρ_{eg})	1088.0	kg/m^3
Thermal conductivity of EG (k_{eg})	0.000251	kJ/(s m K)
Velocity of the EG flow	0.76	m/s

6.4 ODE model based on lumped capacitance

For rough, order-of-magnitude estimates of the thermal transient in the PCC-TES, one might consider a lumped-capacitance model (Košťál et al. 2015; Ranmode, Singh, and Bhattacharya 2019; B. Xu, Li, and Chan 2012; Li et al. 2014) in which the entire stack of PCC slabs is assumed to be reside at a spatially uniform temperature.

Treating heat transfer from the EG tubing to the PCC as quaisteady operation of a heat exchanger, one can derive an ODE governing time dependence of the PCC temperature.

$$\frac{d\theta_1}{d\tau} = \frac{\mathcal{A}(1 - \theta_1)}{\gamma(\theta_1)} \left(\frac{1 - e^{-NTU}}{NTU} \right), \quad NTU = \frac{4hL\mathcal{F}}{UD\rho_2 C_{p,2}^{\text{liq}}} \quad (6.16)$$

Here the number of transfer units accounts for cooling of the EG from inlet to outlet. This equation can readily be solved numerically with the Runge-Kutta method.

6.5 Results and Discussion

The model results were crosschecked with experimental data and demonstrated an acceptable agreement and accurate representation of the transient heat transfer problem. (Figure 6.9 is a three-dimensional dimensionless graph representing the temperature within the PCC-TES structure as a function of position and time. In the experiments each slab is of height is 0.0254 meter and the overall height of the 28-slab PCC-TES structure is approximately 0.71 meters. In the dimensionless representation, the top (bottom) surface of the PCC-TES is at position $\zeta = 0$ ($\zeta = 1$). (Ahmed Aljehani, Nitsche, and Al-Hallaj 2020).

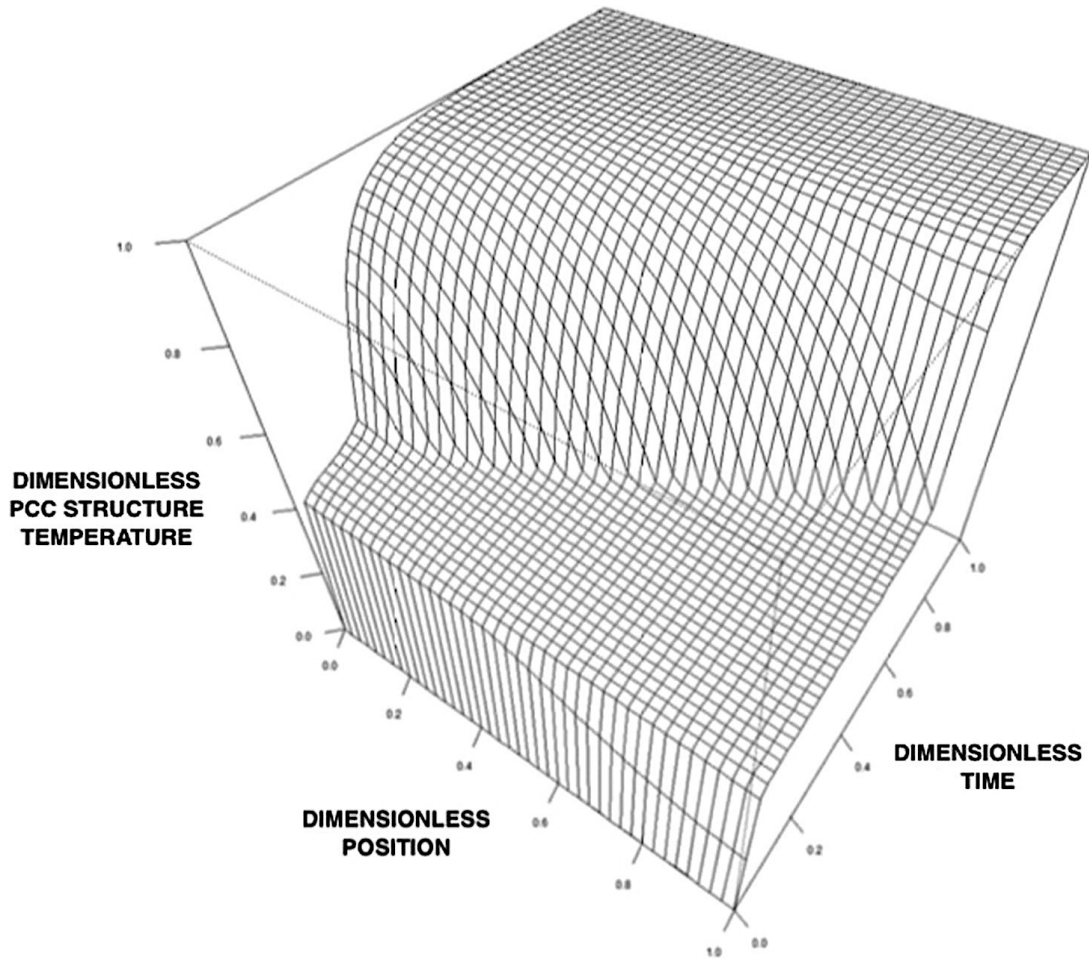


Figure 6.9: Three-dimensional representation of the change in dimensionless temperature of the PCC structure with respect to dimensionless time and position, as calculated numerically.

The whole PCC-TES structure was initially at $\theta_1 = 0$ as illustrated by (Figure 6.9) and (Figure 6.10). Then, as the hot Ethylene Glycol (EG) is introduced to the top of the structure at inlet provision (Schematic of the PCC-TES system is shown in Figure 6.5), the slabs start to absorb the heat from the EG stream. Accordingly, the temperatures of the slabs rise.

At first, the heat absorbed by the phase change material (namely n-Tetradecane, $(C_{14}H_{30})$) is actually in the form of 'sensible heat' and that explains the rise in the temperature of the slabs as soon as the experiments commenced and EG introduced to the PCC-TES structure. The slabs continue to undergo a rise in temperature until the melting temperature of the phase change material is reached as illustrated by (Figure 6.9) and (Figure 6.10). Then, the temperature of the slabs become nearly constant while the phase change material in each slab undergoes the change from solid state to liquid state. The heat absorbed by the phase change material is now in the form of 'latent heat'.

The upper sections of the PCC-TES structure melted first followed by the lower sections in corresponds to the hot EG inflow stream entering the PCC-TES structure from the inlet provision at the top and exiting from the bottom. Following complete melting of each slab, it undergoes a rise in the temperature toward $\theta_1 = 1$ as illustrated by (Figure 6.9) and (Figure 6.10), which is the temperature of the EG entering the PCC-TES structure. (Ahmed Aljehani, Nitsche, and Al-Hallaj 2020).

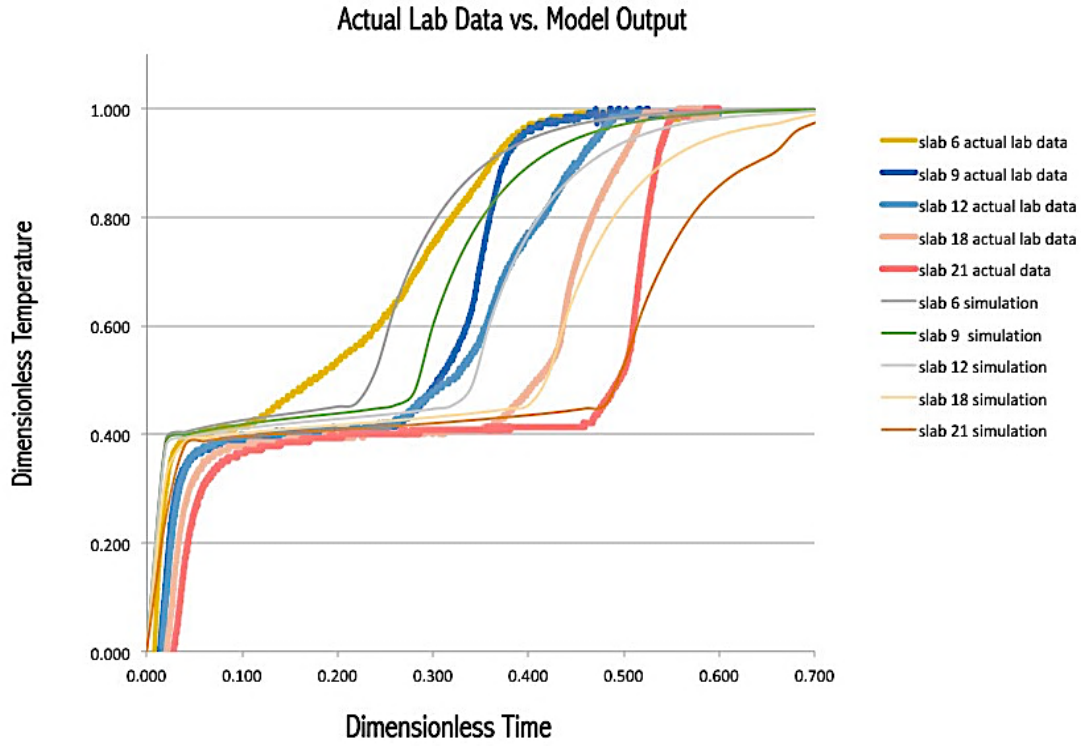


Figure 6.10: Experimental time traces of temperature measured with prefixed thermocouples plotted against numerical counterpart. The PCC temperature traces (θ_1) for various positions ζ that correspond to the placement of thermocouples. Slabs (6, 9, 12, 18, and 21) correspond to ζ positions (0.21, 0.32, 0.42, 0.64 and 0.74) respectively. (Ahmed Aljehani, Nitsche, and Al-Hallaj 2020).

Experimental time traces of temperature measured with thermocouples are shown in (Figure 6.10), converted to the dimensionless basis of the model (θ_1 , ζ , and τ). The slabs numbered (6, 9, 12, 18, and 21) correspond to dimensionless positions ζ (0.21, 0.32, 0.42, 0.64 and 0.74) respectively. For comparison with the experimental data, the corresponding numerically calculated time traces appear in the same figure (Figure 6.10). As illustrated by (Figure 6.10), all the slabs were initially at $\theta_1 = 0$. Then, as the hot Ethylene Glycol (EG) is introduced to the top of the structure at inlet provision (Schematic of the PCC-TES system is shown in (Figure 6.5), the slabs start to absorb the heat from the EG stream.

Accordingly, the temperature of the slabs rises. As soon the melting temperature is reached then the temperature will have minimal change indicating that the system is storing heat in the form of 'latent heat' as illustrated by (Figure 6.10). The top slabs will melt before the lower slabs and have the fastest rise in temperature because they are the first slabs to interact with the incoming hot EG fluid coming through the inlet provision. Some of the very bottom slabs will not exhibit a rise in the temperature until later time in the experiment indicating that the melting progression is slowly moving from top to bottom in correspondence to the top to bottom temperature profile of EG heat transfer fluid. The heat absorbed by the phase change material during the phase change in the form of latent heat. Following complete melting of each slab, it undergoes a rise in the temperature toward $\theta_1 = 1$, which is the temperature of the EG entering the PCC-TES structure from the inlet at the top. The numerically calculated time traces appear to provide an acceptable agreement to experimental time traces of temperature measured with thermocouples.

The averaged error (%) between experimental data and numerically calculated for each curve in (Figure 6.10) is illustrated by (Table 6.2). The variations between experimental time traces of temperature and numerically calculated data are attributed to the heat loss in the actual experiment. Accordingly, the slabs in the actual experiment needed a longer time to reach the final temperature of $\theta_1 = 1$, which is equivalent to the temperature of the EG entering the PCC-TES structure from the inlet at the top.

Table 6.2: Averaged error between experimental & simulation curves in Figure 6.10

Curve	Slab 6	Slab 9	Slab 12	Slab 18	Slab 21
Averaged Error	4%	6%	4%	7%	9%

Similarly, as revealed from collected experimental data, temperature measured with thermocouples as time elapsed at various predetermined positions on the PCC structure are shown on (Figure 6.11), converted to the dimensionless basis of the model (θ_1 , ζ , and τ). For comparison with the experimental data, the corresponding numerically calculated temperature versus position traces appear in the same figure (Figure 6.11). All the slabs were initially at $\theta_1 = 0$. As discussed earlier, hot EG is introduced to the top of the structure at inlet provision, the slabs start to absorb the heat from the EG stream. Accordingly, the temperatures of the slabs rise. The slabs continue to undergo a rise in temperature until the melting temperature of the phase change material is reached which corresponds to $\theta_1 = 0.4$. Then, the temperature of the slabs become nearly constant while the phase change material in each slab undergoes the change from solid state to liquid state. Following complete melting of each slab, it undergoes a rise in the temperature toward $\theta_1 = 1$, which is the temperature of the EG entering the PCC-TES structure from the inlet at the top.

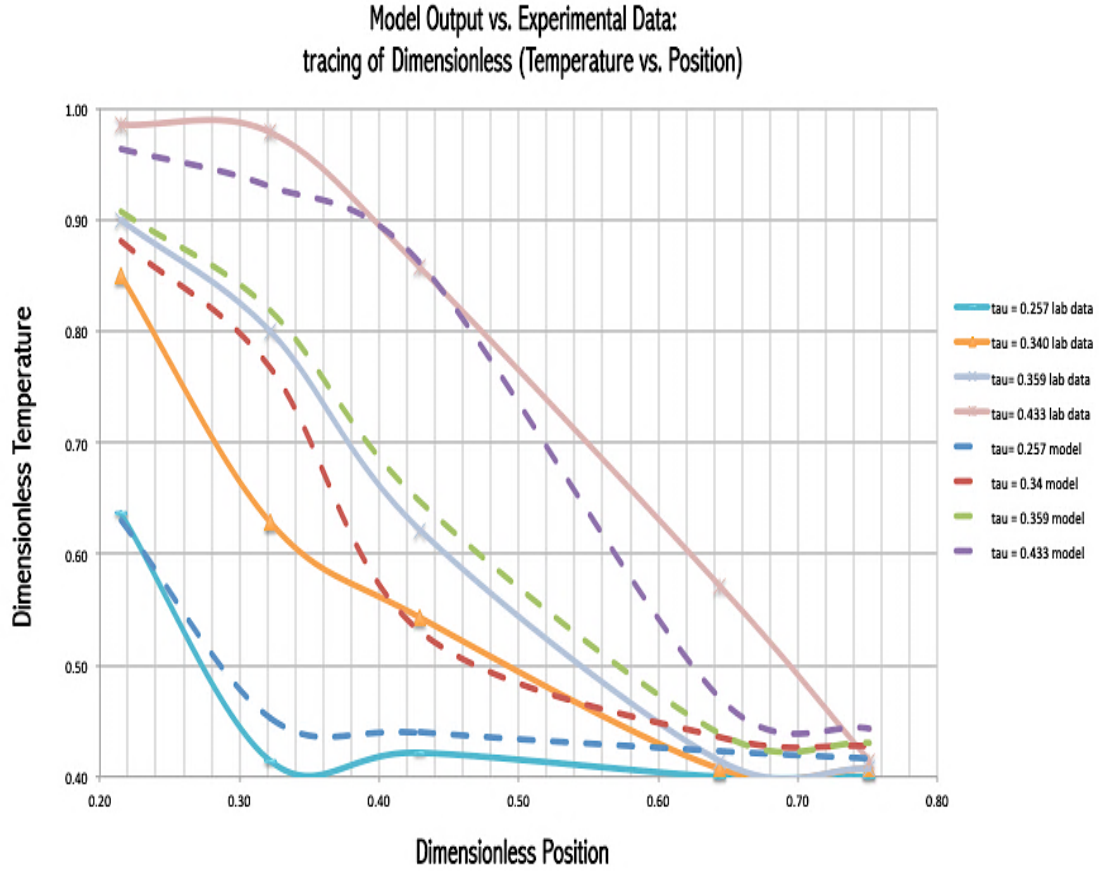


Figure 6.11: The PCC temperature traces (θ_1) for various positions (ζ) as time elapsed plotted against numerical counterpart for comparison. (Ahmed Aljehani, Nitsche, and Al-Hallaj 2020).

As illustrated by (Figure 6.11), the model output showed acceptable predictions in comparison with actual experimental data. Although, the model did not seem to accurately capture early transient compared to actual lab experiment. The reason for the mismatch during early transient could be attributed to the fact that the model assumes EG flows into the PCC-TES structure at precisely 14 deg C ($\theta_2 = 1.0$) from the first moment while in actual experiment setup EG at first flows in at much lower temperature than 14 deg C and takes few minutes to reach and stabilize at 14 deg C ($\theta_2 = 1.0$). The averaged error (%) between experimental data and numerically calculated data for each curve in (Figure 6.11)

is illustrated by (Table 6.3). The heat loss in the actual experiment is a major factor leading to the slight discrepancy between actual experiment data and numerical simulation output.

Table 6.3: Averaged error between experimental & simulation curves in Figure 6.11

Curve	Averaged error
Tau = 0.257	5 %
Tau = 0.34	7 %
Tau = 0.359	4 %
Tau = 0.433	7 %

Actual experimental temperature profiles of inflow and outflow Ethylene Glycol (EG) stream are shown in (Figure 6.12). As discussed earlier, EG is the heat transfer fluid which runs through the copper tubes and in between the slabs. EG inflow stream is introduced to the PCC-TES structure from inlet provision at the top as shown in the experiment schematic in (Figure 6.5). EG exits the PCC TES from outlet provision at the bottom. (Figure 6.13) is a dimensionless, 3D graph representing the dependence of temperature within the EG tube phase upon position and time, as calculated numerically. The inflowing temperature of the EG is always steady at $\theta_2 = 1$ (as also shown actual experimental in (Figure 6.12)) after being (re)heated to the preset temperature during re-circulation. At the beginning, at all positions there is a very rapid rise in EG temperature as illustrated in (Figure 6.13). Then, during the phase change of slabs, the temperature of EG existing the PCC structure from the bottom starts to steadily matches the bulk temperature of the PCC-TES structure during the phase change process of the slabs throughout the experiment (as also illustrated by actual experimental data shown in (Figure 6.12)). As the experiment approaches the end, the temperature of the EG exiting the PCC-TES structure from the

bottom provision starts to rise as illustrated by (Figure 6.13) and (Figure 6.12) due to the complete melting of slabs (i.e. the latent heat capacities of the slabs have been exhausted).

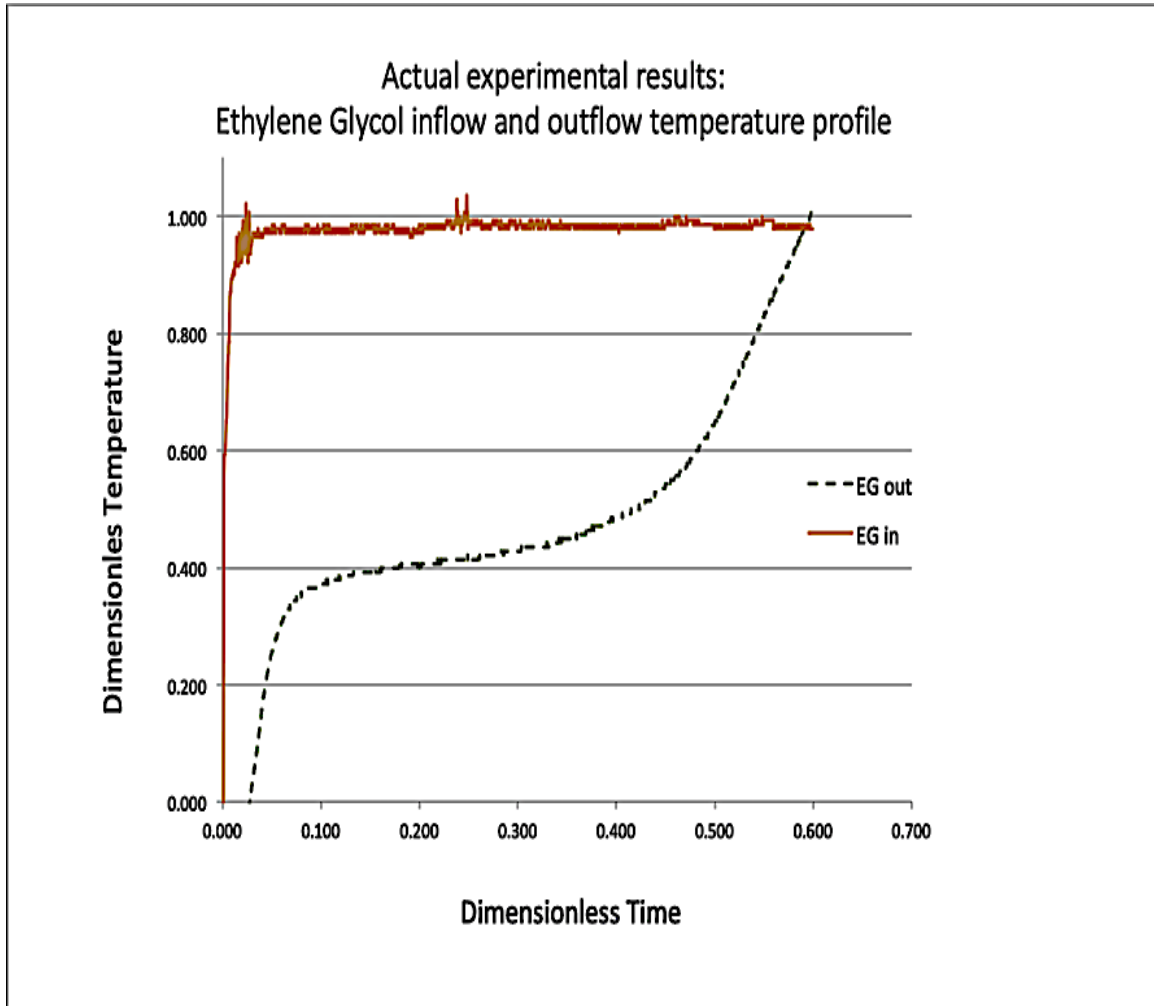


Figure 6.12: Actual experimental results: EG inflow and outflow temperature profiles (Ahmed Aljehani, Nitsche, and Al-Hallaj 2020).

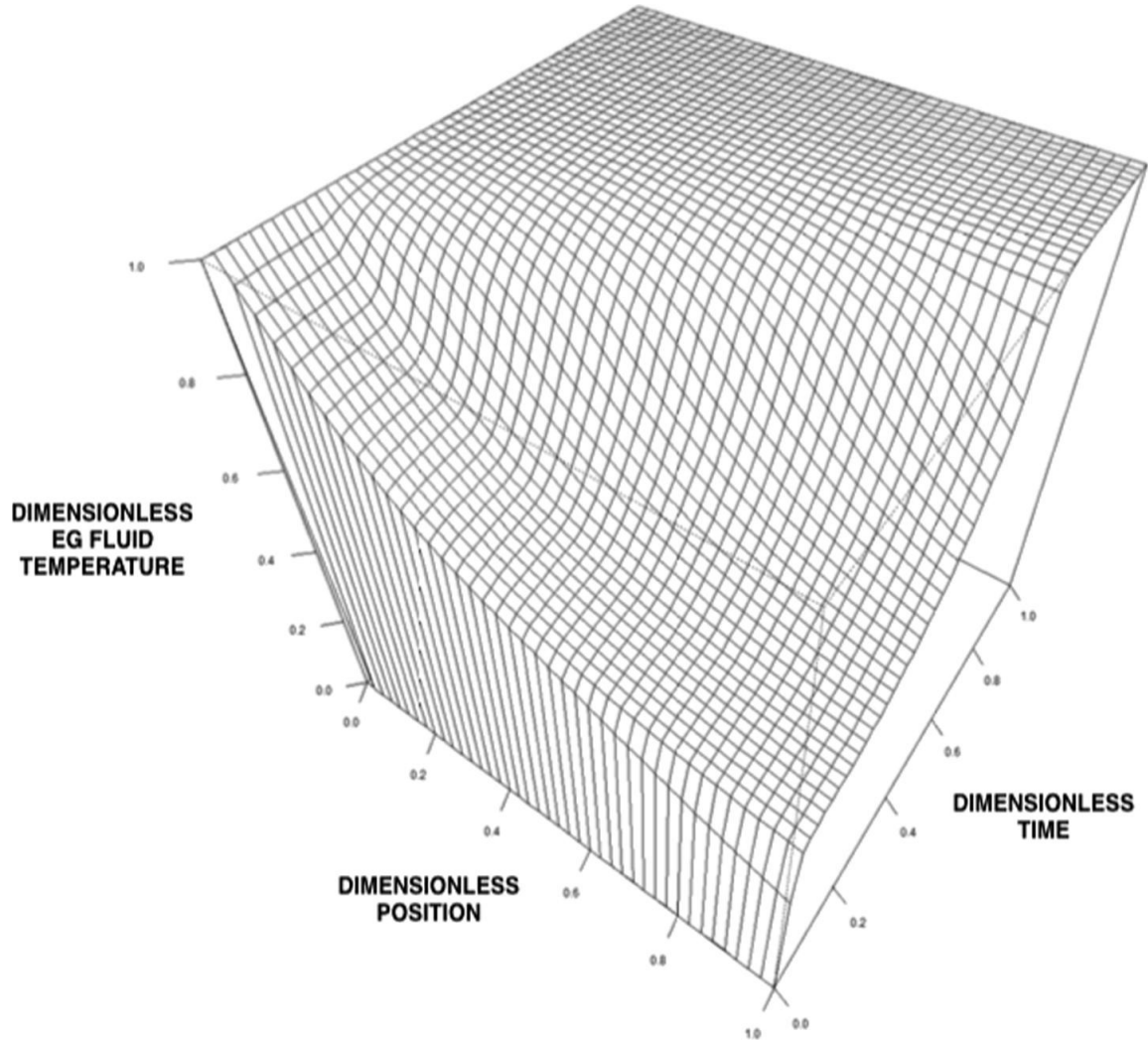


Figure 6.13: Three-dimensional representation of the change in dimensionless temperature of EG fluid with respect to dimensionless time and position (Ahmed Aljehani, Nitsche, and Al-Hallaj 2020).

(Figure 6.14) illustrates a two-dimensional representation of the change in dimensionless temperature of PCC θ_1 with respect to position at early stages of the experiment. Initially the PCC-TES structure and EG fluid within the copper tubes passing through the PCC structure were uniformly at initial dimensionless temperatures of $\theta_1 = 0$ and $\theta_2 = 0$. As soon as the hot EG fluid is introduced to the top of the PCC structure through inlet

provision, the temperature of each slab will gradually rise indicating that the system is storing thermal energy in the form of sensible heat.

Early Stages: Theta-1 vs. Zeta

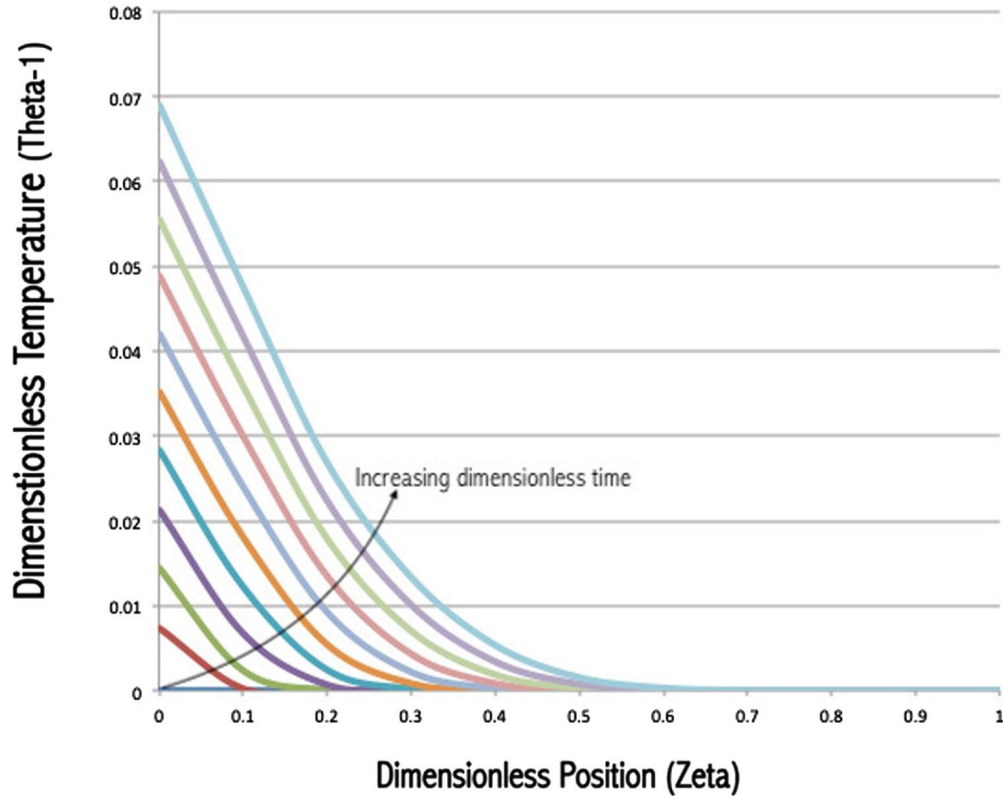


Figure 6.14: Two-dimensional representation of the change in dimensionless temperature of PCC- θ_1 with respect to position (ζ) at early stages of the experiment (Ahmed Aljehani, Nitsche, and Al-Hallaj 2020).

(Figure 6.15) illustrates a two-dimensional representation of the change in dimensionless temperature of EG fluid θ_2 with respect to position at early stages of the experiment. As represented by (Figure 6.15) EG fluid enters the PCC structure at $\theta_2 = 1$. The EG passing through the copper tubes exchanges heat with the melting PCC structure over the duration of the experiment. At this early stage, the outlet temperature of the EG matches the bulk temperature of the PCC structure (which is initially at $\theta_1 = 0$) and exits at $\theta_2 = 0$. Later on, the

outlet temperature of the EG will also match the bulk temperature of the PCC-TES during phase change and exits at a temperature nearly equal to $\theta_2 = 0.4$ as illustrated earlier by (Figure 6.13). The precise behavior was observed on the actual experiment illustrating a great representation of the numerical model of the actual experiment.

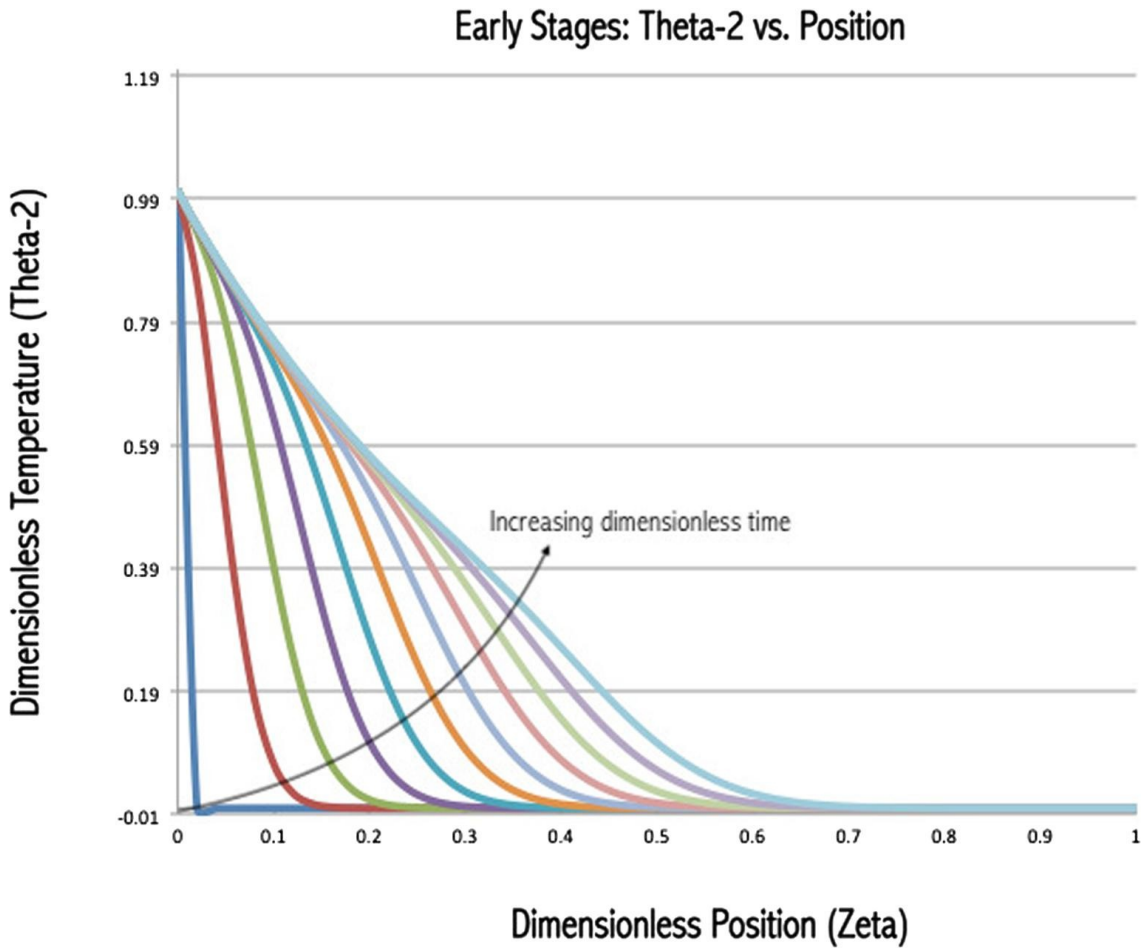


Figure 6.15: Two-dimensional representation of the change in dimensionless temperature of EG fluid θ_2 with respect to position ζ at early stages of the experiment (Ahmed Aljehani, Nitsche, and Al-Hallaj 2020).

(Figure 6.16) illustrates the temperature history of the PCC, as calculated with the lumped-capacitance (ODE) model, resembles the local time trace at an intermediate position for the full PDE model. As shown in (Figure 6.16), the temperature at the intermediate position

initially at $\theta_1 = 0$. Then, as the hot Ethylene Glycol (EG) is introduced to the top of the structure at inlet provision, the temperature at the intermediate position starts to rise. At first, the heat absorbed by the phase change material at the intermediate position is in the form of 'sensible heat' explained by the rise in temperature as illustrated in (Figure 6.16). The temperature at the intermediate position continues to rise until the melting temperature of the phase change material is reached. Then, the temperature at the intermediate position becomes nearly constant while the phase change material undergoes the change from solid state to liquid state. The heat absorbed by the phase change material is now in the form of 'latent heat'. Following the complete melting of at the intermediate position, it undergoes a rise in the temperature toward $\theta_1 = 1$, which is equivalent to the temperature of the EG entering the PCC-TES structure from the inlet at the top. The calculated time traces by the lumped-capacitance (ODE) model appear to provide an acceptable behavior due to the high conductivity of the graphite. With regard to the cumulative, total enthalpy uptake by the PCC structure (Figure 6.17), the lumped parameter (ODE) model yields very good results, despite significant temperature variations in the PCC structure attending a Biot number that is not small. One might expect this upon integrating the PDE-1 (6.1) against reduced heat capacity $\gamma(\theta_1)$ and applying the boundary conditions (6.9) to eliminate the conduction term.

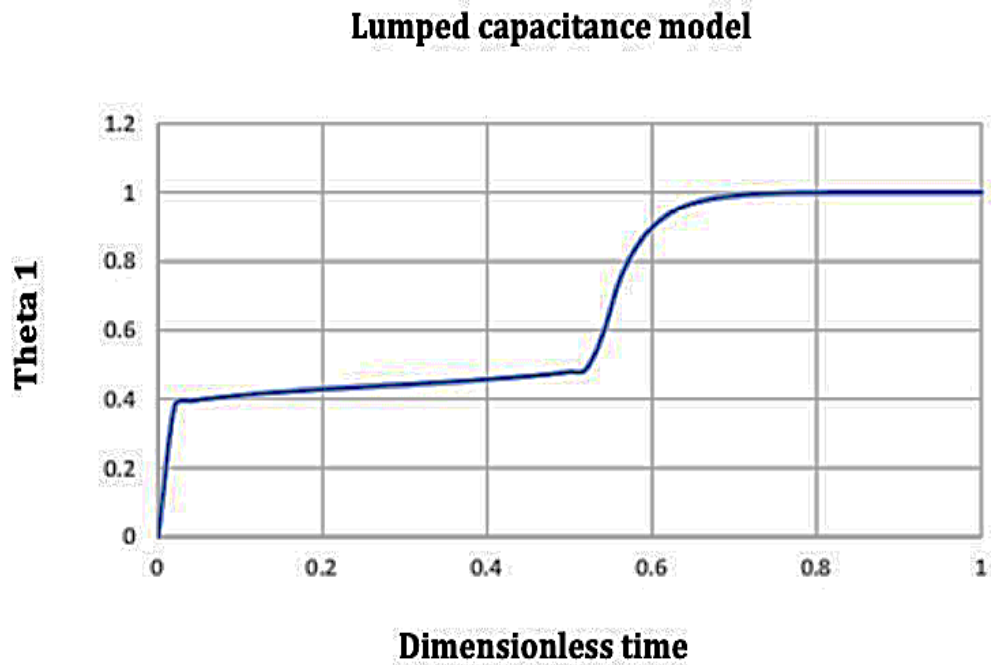


Figure 6.16: Lumped capacitance model (Ahmed Aljehani, Nitsche, and Al-Hallaj 2020).

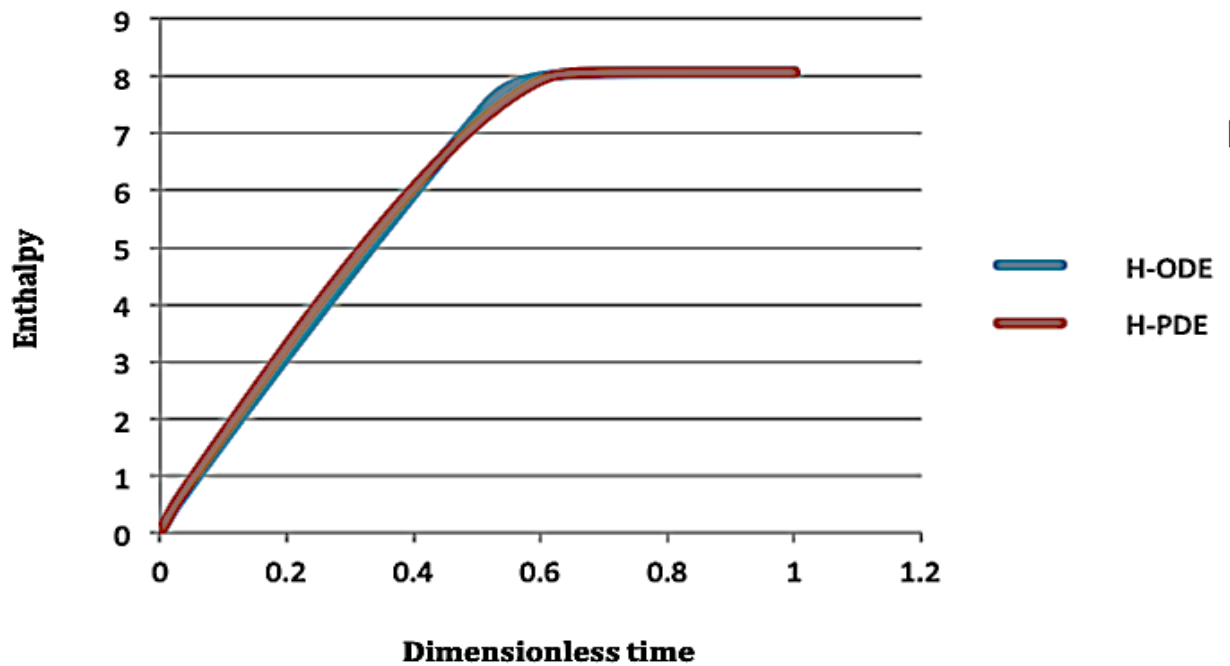


Figure 6.17: Enthalpy intake comparison (PDE vs. ODE) (Ahmed Aljehani, Nitsche, and Al-Hallaj 2020).

6.6 Chapter 6 Summary

The detailed numerical approach presented in this chapter successfully described the heat exchange between this specifically proposed phase change composite thermal energy storage (PCC-TES) and the heat transfer fluid has not been yet addressed in the literature. The mathematical modeling of the PCC-TES involved formulating two PDEs that represent conduction within the PCC and advection within the heat transfer fluid. The two coupled PDEs were solved with a finite difference method. Numerics were implemented using Fortran. Results were validated using experimental data and demonstrated acceptable agreement and an accurate representation of this specific transient heat transfer problem. The variations between experimental time traces of temperature and numerically calculated data are estimated at approximately (4 - 9 %) and attributed to the heat loss in the actual experiment. Accordingly, the slabs in the actual experiment needed a longer time to reach $\theta_1 = 1$, which is the temperature of the EG entering the PCC-TES structure from the inlet at the top. This chapter also demonstrated that the lumped- parameter ODE model can perform an incredibly good job of predicting the enthalpy uptake of the PCC precisely matching the PDE results due to the high thermal conductivity of the graphite.

CHAPTER 7: TECHNO ECONOMIC EVALUATION

(CASE STUDY: AIR CONDITIONING, A MAJOR ELECTRICITY CONSUMER IN SAUDI ARABIA. WOULD A PCC-TES HELP?)

7.1 Backgrounds and Introduction

World population is rapidly growing, and energy demand is unquestionably increasing in accordance. The future is even more challenging when the world population double or triple and when the earth resources continue to become more and more scarce. Energy ever-increasing demand in Saudi Arabia is a common concern around the world, not only in Saudi Arabia.

A severe depletion of earth fossil fuel reserves over the last century even made it worse. Previous oil-exporting countries (like Indonesia) are not in the oil-exporting business anymore due to the rapid depletion of their oil reserves. Indonesia had to withdraw from OPEC years ago as they could not sustain being a net exporter of the commodity effective January 2009.

The Indonesian business case being transformed from a net exporter to a net importer most likely will be seen in other exporting countries as well. It is the point where reserves are depleting and finding more reserves is quite a struggle or when the country local demand of the oil exceeds its production capabilities.

Oil-exporting countries are experiencing a rapid population growth and development. If this continues to happen, the kingdom would reduce their oil share to the international

market which could lead to an adverse impact on oil supply to the rest of the world and accordingly prices.

Saudi Arabia is one of the main largest oil exporters in the world (U.S. Energy Information Administration 2017). Saudi Arabia would certainly play a major role in market stability when the world's energy availability becomes a serious challenge. Saudi Arabia has their own new challenges of meeting the exponential growth of its local electricity demand, which consequently may one day limit the exporting capabilities and the world energy availability since the majority of the electricity production mix in Saudi Arabia depend on oil & gas. Strategic investments for producing clean electricity, managing demand-side, avoiding inefficient consumptions and improving people behavior towards energy consumption would lead to positive consequences on the local and global energy availability and protect environment.

To help address the new challenging situation that the kingdom of Saudi Arabia is facing; encountering the ever-increasing local energy's demand, this chapter came into light. The Saudi Arabian's challenging situation may impose future limitations on the Saudi's exporting capabilities and hence the world energy availability. This chapter started by examining current production and exporting capability figures versus the country local's energy demand obligations. The kingdom's current local demand is approximately one quarter or more of the total production in accordance with the rapid population growth and development. Possible scenarios of energy local demand growth (based on the current annual increase in local demand) were studied by many researchers and analyzed whether or not the local demand could grow and limit or reduce future exports (Organization of

Petroleum Exporting Countries 2016; Yamani 2012) . If no changes are made today, electricity availability in Saudi Arabia can be a challenging task. If no actions are taken, as illustrated by (Lahn and Stevens 2011), at some point the local demand could nearly consume the total oil production of the country adversely affecting the oil-exporting capability and the oil supply to the world as illustrated by Figure 7.1.

Saudi Arabia estimated that the local oil demand to at least double by year 2028 while a diverse mix of electricity production and great energy programs are being adopted by the kingdom (Yamani 2012).

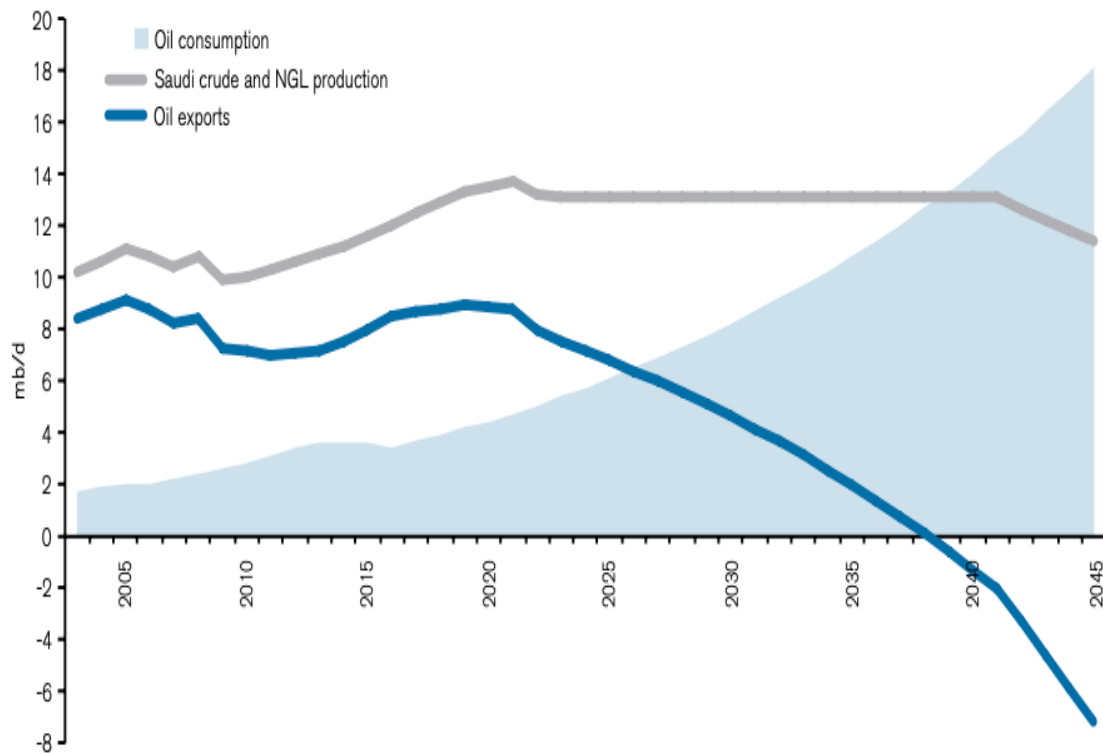


Figure 7.1 : Saudi Arabia's energy consumption/production/export forecast (source : (Lahn and Stevens 2011))

73-75% of the oil produced by Saudi Arabia is exported and 25-27% is locally consumed (Lahn and Stevens 2011; Organization of Petroleum Exporting Countries 2016; Yamani 2012). Zooming into the local share, 40-50% of the oil produced by the kingdom is utilized for direct burn in electricity generation for residential, government, and commercial buildings. Air conditioners in Saudi Arabia are accountable for 50-80% of the electricity demand in buildings and houses during peak-hours (Regulatory 2018).

Table 7.1: Oil consumers of the 25% local share (source: (Lahn and Stevens 2011; Organization of Petroleum Exporting Countries 2016; Yamani 2012))

Major oil consumers of the 25% local share in Saudi Arabia	Barrels/Day	Percentage with respect to total oil production
40-50% for electricity generation	1.0-1.1 Million	10 %
20-30% as either feedstock to other Saudi industries (i.e. Petrochemicals or goods manufacturing) or energy supply to support the industrial production and facilities	750-825 Thousand	7.5 %
20-30% for water desalination and Transportation fuel	750-825 Thousand	7.5 %
5-10% others utilized for agriculture lands & sectors, charity organizations, streets lighting, construction fuel and road paving	250-275 Thousand	2.5 %

Exploring the kingdom of Saudi Arabia electricity generation mix currently revealed mainly fully dependence on oil & gas firing. Consequently, the response to such alerting percentages and figures by governmental and local energy agencies accordingly was

promising in the last few several years. Remarkably, things have been changing rapidly especially in the electricity production perspective. Several ambitious projects in the field of renewable energy (especially solar), are gaining momentum in an attempt to diversifying the energy production mix by 2030 and free up oil for export (CNN Money 2011).

Several local and international energy analysis groups had various valuable insights. The ambitious plan of diversify the electricity generation mix over the next decade may result in liberating a good percentage of oil for export, while the local demand would be consuming around half of the total production.

Saudi Arabia is endorsing a strategic energy transformation plan towered energy efficiency and conservations (Focus, Functional, and Program, n.d.). New energy policies and techniques, if carefully addressed and acted upon, could make the difference and slow down the current energy consumption trend. Multiple low hanging fruits, opportunities and even challenges are out there. Society's cultural and behavior change (driven by evidence, logic and religion) is also equally important and people could be educated, and they could make the change happen. A PCC-TES could effectively contribute as a demand-side management solution to shave/shift electricity consumption. The proposed system will assist utilities companies in avoid building new power plants/distribution lines, boost AC's coefficient of performance (COP), and reduce electricity bills for consumers.

7.1.1 Population growth in Saudi Arabia and energy use per capita

According to the General Authority for Statistics - Kingdom of Saudi Arabia and based on 2017 statistics "the total current population is 32 million people" and the growth rate of the

total population is 2.9% (General Authority for Statistics - Kingdom of Saudi Arabia 2014). To accommodate such rapid population growth, energy consumption strategies, targets and policies shall be more creative and efficient to ensure the optimum utilization of the fading resources.

According to the Chatham report (Lahn and Stevens 2011) referencing sources from (BP 2011 and UN Population Division Data) highlighting the Saudi energy use per capita figure of four (4) million barrels of oil equivalent per day “Saudi Arabia consumes a little more than the united states and around twice as much as Japan” and inquired later on “The question is whether the value generated is commensurate with the volume of natural resources being burned...using more energy maybe considered a good thing. However, using more energy resources than is necessary to produce certain outcomes over time result in wasted resources” (Lahn and Stevens 2011).

7.2 Geographic location and climate

The kingdom of Saudi Arabia is a Middle Eastern country located in the southwestern compass's direction of the continent of Asia. This southwestern part of Asia is historically called the “Arabian Peninsula” and it is where the three continents of Asia, Africa and Europe meet. Saudi Arabia is bordered by the Red Sea on the west side, Yemen and Oman on the Southside, Bahrain, United Arab Emirates and Qatar to the East side, and finally, Jordan, Iraq and Kuwait on the Northern side of the kingdom. Riyadh city is the capital and houses the government ministries and agencies headquarters and most of the kingdom royal family members. Jeddah is the second largest city located on the west coast of Saudi Arabia and it is the commercial capital of the kingdom. The Eastern Province of Saudi

Arabia houses headquarter of the national Saudi Arabian oil company (Saudi Aramco), majority of the refineries & gas plants and nearly all of the petroleum exploration and production activities.

Saudi Arabia has a desert climate and mostly hot throughout the year (Summary, High, and Temperature, n.d.). Figure 7.2 illustrates the weather in Riyadh, the capital of Saudi Arabia. The average temperatures between 80-110 °F for nearly nine months of the year. The temperatures during the 3-month winter season are between 50-70 °F.

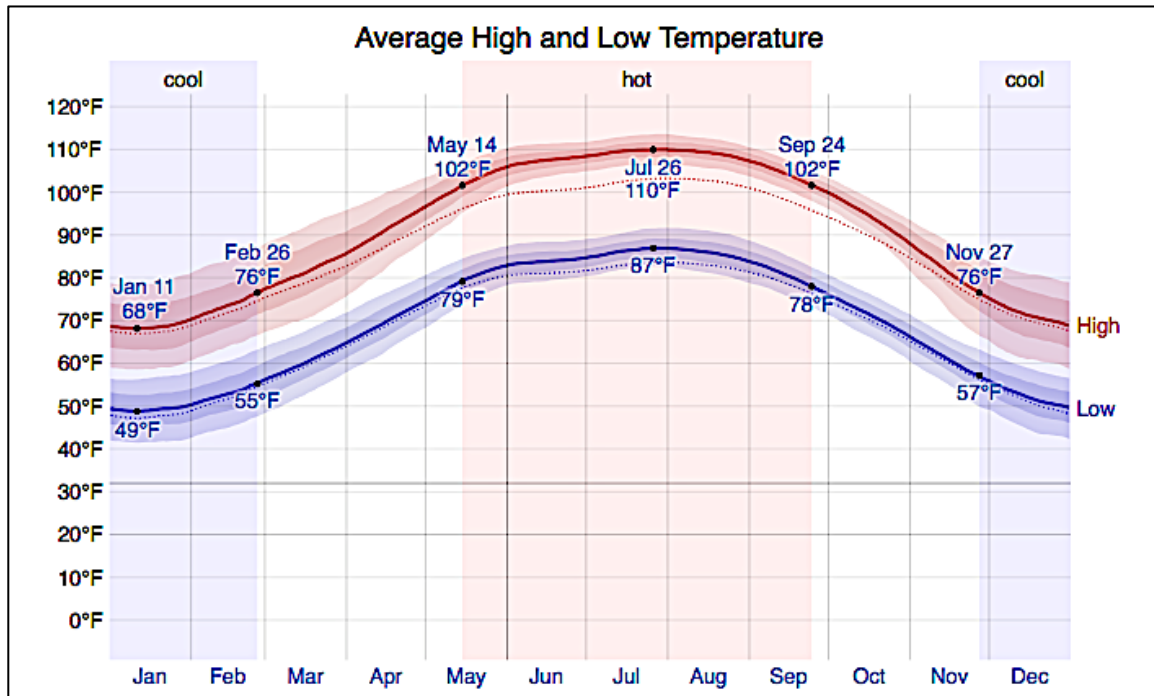


Figure 7.2 : Weather in Riyadh, Saudi Arabia (source: (Summary, High, and Temperature, n.d.))

7.3 Data Collection and Evaluation

As presented earlier, electricity production accounts for 40% of the local share of oil. Therefore, it is quite suitable at the moment to start exploring the kingdom energy production mix. It is worth mentioning that, the Saudi Electricity Company (SEC) is the

major electricity provider in the kingdom. All the electricity produced by the company, at various locations in the kingdom, is being transmitted through the nearly fully integrated electricity grid supplying the four main sectors of the kingdom, which are the western, central, eastern and southern sectors. According to the Saudi Electricity and Cogeneration Regulatory Authority (ECRA) annual report, SEC owns 75% of the generation capacity, in the kingdom, 9% owned by the Saline Water Conversion Corporation (SWCC), and the rest of the generation capacity is owned by multiple several licensed entities.

As far as transmission, at present SEC has a monopoly on transmission of electrical power in the country with the only exception of Yanbu Industrial city where it is Marafiq's responsibility. SEC also is the sole distributor of electricity to consumers in the kingdom of Saudi Arabia with the exception of Yanbu and Jubail industrial cities; where Marafiq is responsible for distribution. As being presented by Table 7.2 below, according to the Saudi Electricity Company (SEC) annual report data, the western region has the highest percentage of capacity installed and that is quite rational considering the fact that western region has high population and it host the commercial capital of the kingdom (the city of Jeddah). The western region is as well hosting the two holy cities of (Mecca and Medina). Approximately 2.5-3.0 Million Muslims, from all over the world, visit the two holy mosques in the two holy cities in the Hajj (Pilgrimage) season and throughout the whole year. On the other hand, the southern region sector has the lowest capacity installed in accordance with the size of the cities, development and population in that region. The Central and Eastern regions of the kingdom have gone through rapid business and industrial developments and the installed capacity in those regions are almost identical.

Table 7.2: Distribution of the total installed capacity by region (source: (Regulatory 2018; Authority Cogeneration Regulatory 2015))

Sector	Quantity	Unit
Western Region	32.5	%
Eastern Region	29.8	%
Central Region	29	%
Southern Region	8.7	%

Analogously, the Saudi Electricity Company (SEC) identified the distribution of consumption by category of consumers. Table 7.3 (below) illustrates that the residential area consumes an enormous portion of the electricity generated, which is once again in logical accordance with the rapid population growth and cities development that the kingdom is going through.

Table 7.3: Electricity consumption by category (Regulatory 2018; Authority Cogeneration Regulatory 2015)

Category	Quantity	Unit
Residential	73	%
Commercial	15	%
Industrial	5.4	%
Governmental	4.6	%
Agricultural	2	%

7.3.1 Air conditioners contribution to ever-increasing electricity demand

Air conditioners in Saudi Arabia are accountable for 50-80% of the electricity demand in buildings and houses during peak-hours as per the Saudi Arabia energy efficiency program website (Regulatory 2018). According to Electricity & Cogeneration Regulatory Authority

(ECRA) there is 8% annual increase in the kingdom's electricity consumption(Authority Cogeneration Regulatory 2015). The electricity consumed currently to run air conditioning systems mainly comes from burning oil and gas power plants as highlighted by Table 8.4.

Table 7.4: Saudi Arabia electricity production matrix ¹(Regulatory 2018; Authority Cogeneration Regulatory 2015)

Electricity Power Plant Category	Quantity	Unit
Thermal (Oil and Gas)	99.99	%
Renewable	0.01	%

7.3.2 Rapid increase in peak demand in Saudi Arabia

The Electricity & Cogeneration Regulatory Authority (ECRA) observed a rapid increase in peak demand in Saudi Arabia between 2004 and 2014 (Authority Cogeneration Regulatory 2015). In about 9 years peak demand climbed from 29 GW in 2005 to 56 GW in 2014.

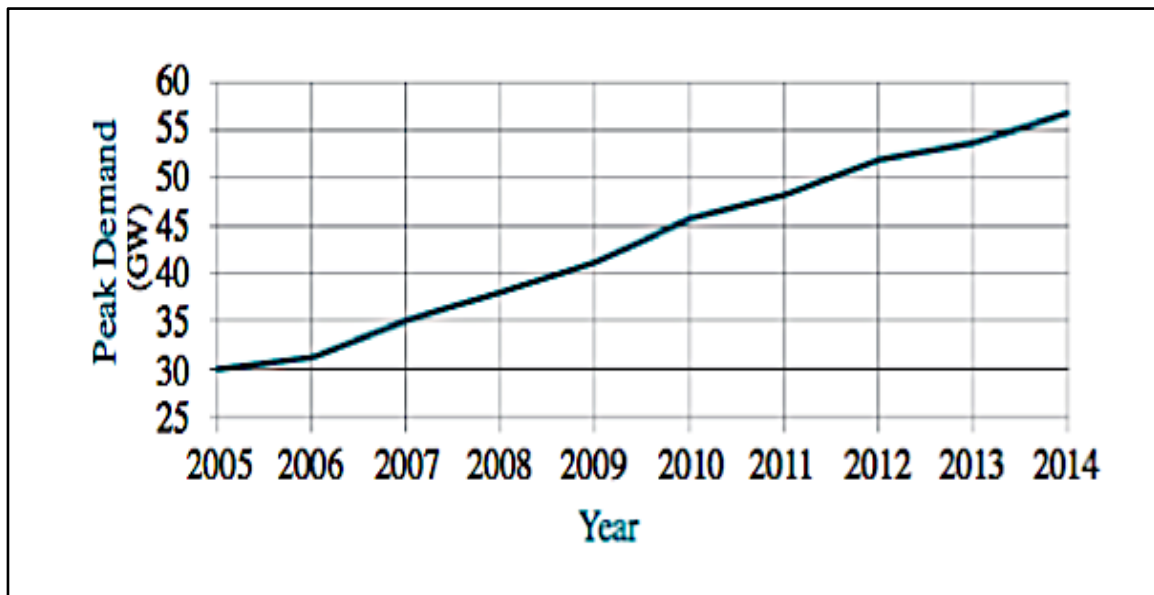


Figure 7.3 : Rapid increase in peak demand in Saudi Arabia between 2005-2014 ((Authority Cogeneration Regulatory 2015))

7.3.3 Planned Projects to install additional capacity

According the 2017 Saudi focus report (Shoaibi and Al-Yaquob 2017), Saudi Arabia plans is targeting to install 2.7 GW of renewable energy capacity by 2030 with reference to Saudi National Renewable Energy Program (NREP). This will be about 5% of the current generation capacity of 56 GW. Table 7.5 highlights the planned additional power generation projects and expected capacity increase. Saudi Arabia is planning to expand generation capacity to 140 GW to meet the ever-increasing electricity demand.

Table 7.5: Saudi Arabia upcoming project to expand electricity production matrix (Shoaibi and Al-Yaquob 2017)

Project Description	Budget	Projected Capacity to be added	Target Year
Power Expansion Project Aiming to raise generation capacity by 20.4 GW. (In the direction of firing more gas and mainly less oil)	US \$ 80 Billion	20.4 GW	2020
Renewable Energy Investment to create a solar industry in the kingdom incrementally resulting in a additional 54 GW capacity by 2030	US \$ 109 Billion	54 GW	2030

7.4 Case Study Approach (Can PCC-TES help?)

In light of the following facts:

- A rapid increase in peak demand in Saudi Arabia over the recent years.
- Vast investments in projects to install additional electricity generation capacity.
- Air conditioners are being the largest consumer of electricity in Saudi Arabia.
- As discussed in Chapter 5, the proven capability of PCC-TES to reduce electricity consumed by allowing for the design of a smaller air compressor and leveling demand between day and night.

PCC-TES can certainly have a positive contribution to the electricity balance equation in Saudi Arabia. So, the approach was as follows:

1. From the data collected in section 7.4, estimate the kWh consumed by (residential, commercial and governmental) buildings.
2. Assume that PCC-TES can be installed to offset 50% of the peak demand as the main scenario and propose an alternative scenario of 25% offset.
3. Calculate the cost of implementation and benefit added.
4. Analyze results and summarize scenarios
5. Provide feedback on the analysis outcome.

7.5 Case study results

7.5.1 Case study 1: PCC-TES installed to offset 50% of peak demand during peak-hours from residential, commercial and government buildings

Table 7.6: Case Study 1- PCC-TES installed to offset 50% of peak demand

Approach Stage	Facts & Considerations	Stage's findings
Stage 1: From the data collected in section 7.4, estimate the kWh consumed by buildings (residential, commercial and government buildings)	Electricity consumed by air conditioners during peak-hours = 70% peak demand Peak demand on 2018= 76 GW	Air conditioners are responsible for 53 GW of the total peak demand during peak-hours
Stage 2: Assume that PCC-TES can be installed to offset 50% of the peak demand during peak-hours from residential, commercial and government buildings	Cost of implementation is approximately \$150 per kWh.	Required kWh to shave 50% of peak demand by air conditioners = $0.5 * (53 \text{ GW peak demand}) * 6 \text{ hours} = 159 \text{ GWh} = 159 * 10^6 \text{ kWh}$ Cost = $(159 * 10^6 \text{ kWh}) * (150 \text{ $/kWh}) = \$ 23.85 \text{ Billion}$
Stage 3: Benefits	PCC-TES can offset at least 50% of oil consumption that is being used for electricity generation which estimated to be at least 600,000 barrels.	Assuming the price of \$60/Barrel. Saudi Arabia can save (36 million dollars/ day) as a result of freeing 600,000 barrels of oil for export.

7.5.2 Case study 2- PCC-TES installed to offset 25% of peak demand during peak-hours from residential, commercial and government buildings

The last case was repeated but now assumed the PCC-TES will offset 25% of peak demand during peak-hours.

Table 7.7: Case Study 7.2: PCC-TES installed to offset 25% of peak demand

Approach Stage	Finding	Remarks
Stage 1: From the data collected in section 7.4, estimate the kWh consumed by buildings (residential, commercial and government buildings)	Electricity consumed by air conditioners during peak-hours = 70% peak demand Peak demand on 2018= 76 GW	Air conditioners are responsible for 53 GW of the total peak demand during peak-hours
Stage 2: Assume that PCC-TES can be installed to offset 100% of the peak demand during peak-hours from residential, commercial and government buildings	Cost of implementation is approximately \$150 per kWh.	Required kWh to shave 25% of peak demand by air conditioners = $0.25 * (53 \text{ GW peak demand}) * 6 \text{ hours} = 79.5 \text{ GWh} = 79.5 * 10^6 \text{ kWh}$ Cost = $(79.5 * 10^6 \text{ kWh}) * (500 \text{ $/kWh}) =$ \$ 11.93 Billion
Stage 3: Benefits	PCC-TES can offset at least 25% of oil consumption that is being used for electricity generation which estimated to be at least 300,000 barrels.	Assuming the price of \$60/Barrel. Saudi Arabia can save (18 million dollars/ day) as a result of freeing 300,000 barrels of oil for export.

7.6 Summary

To help address the new challenging situation that the kingdom of Saudi Arabia is facing; encountering the ever-increasing local energy's demand, this chapter and study had come to light. Due to the hot Saudi climate, air conditioners are the largest consumers of electricity produced in Saudi Arabia which is primarily oil and gas driven. This chapter studied whether or not the PCC-TES can have positive contribution to the electricity balance equation in Saudi Arabia and consequently increase the oil share by Saudi Arabia to the international market. The study in this chapter revealed, assuming the price of \$60/Barrel, if the PCC-TES concept is introduced and implemented to shave 50% of oil consumed to produce electricity for air conditioning, Saudi Arabia can save 600,000 barrels/day. Similarly, if the PCC-TES systems concepts are introduced and implemented to shave 25% of oil consumed to produce electricity for air conditioning, Saudi Arabia can save 300,000 barrels/day.

CHAPTER 8: CONCLUSIONS

8.1 Summary of Contributions

This thesis is the first detailed study to thoroughly address the hybrid integration between the PCC-TES and the air conditioning system. Such multi layers study has not yet been addressed in the literature. This study evaluated the use of a phase change composite (PCC) material, consisting of paraffin wax (n-Tetradecane) and expanded graphite, as a potential storage medium for cold thermal energy storage (TES) systems to support air conditioning (AC) applications. The PCC-TES system is to be integrated with the vapor compression refrigeration cycle of an AC system. The use of this proposed solid PCC material is novel. The PCC has excellent material and thermal characteristics as compared to ice or chilled water that are predominantly used in commercial TES systems for air cooling applications. This study proposed and tested a hypothesis, which suggests that integrating a conventional AC with a PCC-TES would result in significant benefits concerning compressor size, compressor efficiency, electricity consumed and CO₂ emissions. A multi-layer research was thoroughly conducted involving: (1) literature review (2) material characterization (3) experimental work (4) proof of concept simulation (5) numerical modeling (6) real-life implementation evaluation. The study examined several key thermo-physical properties of PCC material. Actual experimental benchtop system has been built and tested. A simulation model using Aspen Plus® was successfully generated to perform overall system -level evaluation. The simulation model also compared the use of PCC materials as the energy storage medium versus the use of ice. The simulation of the proposed integration between the AC and the PCC-TES revealed that the proposed integration would result in

downsizing compressor design by 50%, lowering electricity consumption by 30%, doubling the efficiency during mid and off-peak-hours, and lowering CO₂ emissions by 30%. Furthermore, a detailed numerical model was also successfully built to describe in detail the transient heat transfer problem of a PCC-TES system exchanging heat with a heat transfer fluid (namely Ethylene Glycol). The actual experimental benchtop validated the analytical/numerical simulation models. The study was wrapped up by addressing real - life implementation of proposed integration between the AC and PCC-TES for hot and humid climate region with high electricity demand (Saudi Arabia was selected as a case study). The study revealed that, assuming the price of \$60/Barrel, if the PCC-TES concept is introduced and implemented to shave 50% of oil consumed to produce electricity for air conditioning, Saudi Arabia can save 600,000 barrels/day or 36 million dollars a day. Similarly, if the PCC-TES concept is introduced and implemented to shave 25% of oil consumed to produce electricity for air conditioning, Saudi Arabia can save 300,000 barrels/day or 18 million dollars a day.


8.2 Recommendations for future work

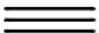


Thoroughly study the possibility of concurring charging and discharging on the PCC-TES as opposed to the independent charging and discharging cycles studied in this thesis. Study ways and means to improve mechanical strength and stiffness without jeopardizing heat capacity of the PCC-TES. Moreover, search for feasible ways to find lower cost materials and lower production cost to ultimately lower the cost of the PCC-TES. Finally, thoroughly quantify the expected life cycle of PCC-TES.

APPENDIX

Elsevier grants permission to include published papers in dissertation as long as the dissertation is not fully or partially commercially published and as long as the papers are embedded within the dissertation.

(reference <https://www.elsevier.com/about/policies/copyright/permissions>)

 ELSEVIER



Permission guidelines ScienceDirect content

Can I use material from my Elsevier journal article within my thesis/dissertation? –

As an Elsevier journal author, you have the right to Include the article in a thesis or dissertation (provided that this is not to be published commercially) whether in full or in part, subject to proper acknowledgment; see [the Copyright page](#) for more information. No written permission from Elsevier is necessary.

This right extends to the posting of your thesis to your university's repository provided that if you include the published journal article, it is embedded in your thesis and not separately downloadable.

CITED LITERATURE

- Ababneh, Amer Khalil, Amjad S. Hijazin, and Ali M. Jawarneh. 2018. "A Novelty for Thermal Energy Storage Utilizing the Principle of Solid to Solid Phase Change in a Lithium Sulfate at Elevated Temperatures." *Solar Energy* 163 (January): 45–53. <https://doi.org/10.1016/j.solener.2018.01.060>.
- Akgu, Mithat, and Kamil Kaygusuz. 2008. "Thermal Energy Storage Performance of Paraffin in a Novel Tube-in-Shell System" 28: 405–13. <https://doi.org/10.1016/j.applthermaleng.2007.05.013>.
- Akif, Mehmet, Muhammet Ozdogan, Huseyin Gunerhan, and Arif Hepbasli. 2010. "Energetic and Exergetic Analysis and Assessment of a Thermal Energy Storage (TES) Unit for Building Applications" 42: 1896–1901. <https://doi.org/10.1016/j.enbuild.2010.05.025>.
- Al-abidi, Abduljalil A, Sohif Bin Mat, K Sopian, M Y Sulaiman, C H Lim, and Abdulrahman Th. 2012. "Review of Thermal Energy Storage for Air Conditioning Systems." *Renewable and Sustainable Energy Reviews* 16 (8): 5802–19. <https://doi.org/10.1016/j.rser.2012.05.030>.
- Al-Hallaj, S., S. Khateeb, A. Aljehani, and M. Pinar. 2018. "Thermal Energy Storage for Smart Grid Applications." In *AIP Conference Proceedings*. Vol. 1924. <https://doi.org/10.1063/1.5020287>.
- Al-Hallaj, Said, Siddique Khateeb, Ahmed Aljehani, and Mike Pinar. 2018. "Thermal Energy Storage for Smart Grid Applications." In *AIP Conference Proceedings*. 1924 (AIP Publishing, 2018): 020007.
- Aljehani, A., S.A.K. Razack, L. Nitsche, and S. Al-Hallaj. 2018. "Design and Optimization of a Hybrid Air Conditioning System with Thermal Energy Storage Using Phase Change Composite." *Energy Conversion and Management* 169. <https://doi.org/10.1016/j.enconman.2018.05.040>.
- Aljehani, Ahmed, Ludwig C. Nitsche, and Said Al-Hallaj. 2020. "Numerical Modeling of Transient Heat Transfer in a Phase Change Composite Thermal Energy Storage (PCC-TES) System for Air Conditioning Applications." *Applied Thermal Engineering* 164 (January). <https://doi.org/10.1016/j.applthermaleng.2019.114522>.
- Aljehani, Ahmed, Siddique Ali K. Razack, Ludwig Nitsche, and Said Al-Hallaj. 2018. "Design and Optimization of a Hybrid Air Conditioning System with Thermal Energy Storage Using Phase Change Composite." *Energy Conversion and Management* 169 (March): 404–18. <https://doi.org/10.1016/j.enconman.2018.05.040>.
- Arai, Yuta, Yuji Yamauchi, Hiroki Tokutomi, Fuyuki Endo, Atsushi Hotta, Saman Alavi, and Ryo Ohmura. 2018. "Thermophysical Property Measurements of Tetrabutylphosphonium Acetate (TBPAc) Ionic Semiclathrate Hydrate as Thermal Energy Storage Medium for General Air Conditioning Systems." *International Journal of Refrigeration* 88: 102–7. <https://doi.org/10.1016/j.ijrefrig.2017.12.020>.
- Arasu, Amirtham valan, Agus P. Sasmito, and Arun S. Mujumdar. 2013. "Numerical Performance Study of Paraffin Wax Dispersed with Alumina in a Concentric Pipe Latent Heat Storage System." *Thermal Science* 17 (2): 419–30. <https://doi.org/10.2298/TSCI110417004A>.

- Arteconi, A., N. J. Hewitt, and F. Polonara. 2012. "State of the Art of Thermal Storage for Demand-Side Management." *Applied Energy* 93: 371–89. <https://doi.org/10.1016/j.apenergy.2011.12.045>.
- Authority Cogeneration Regulatory, Saudi Arabia. 2015. "ACTIVITIES AND ACHIEVEMENTS OF THE AUTHORITY IN 2014." <http://www.ecra.gov.sa/en-us/MediaCenter/doclib2/Pages/SubCategoryList.aspx?categoryID=4>.
- Bai, Tao, Gang Yan, and Jianlin Yu. 2018. "Experimental Investigation of an Ejector-Enhanced Auto-Cascade Refrigeration System." *Applied Thermal Engineering* 129: 792–801. <https://doi.org/10.1016/j.applthermaleng.2017.10.053>.
- Basturk, E, and M V Kahraman. 2016. "Photocrosslinked Biobased Phase Change Material for Thermal Energy Storage." *Journal of Applied Polymer Science*. <https://doi.org/ARTN 43757/r10.1002/app.43757>.
- Bayon, Alicia, Roman Bader, Mehdi Jafarian, Larissa Fedunik-Hofman, Yanping Sun, Jim Hinkley, Sarah Miller, et al. 2018. "Techno-Economic Assessment of Solid–Gas Thermochemical Energy Storage Systems for Solar Thermal Power Applications." *Energy* 149: 155–73. <https://doi.org/10.1016/j.energy.2017.11.084>.
- Beghi, Alessandro, Luca Cecchinato, Mirco Rampazzo, and Francesco Simmini. 2014. "Energy Efficient Control of HVAC Systems with Ice Cold Thermal Energy Storage" 24: 773–81.
- Bo, He, E.Mari Gustafsson, and Fredrik Setterwall. 1999. "Tetradecane and Hexadecane Binary Mixtures as Phase Change Materials (PCMs) for Cool Storage in District Cooling Systems." *Energy* 24 (12): 1015–28. [https://doi.org/10.1016/S0360-5442\(99\)00055-9](https://doi.org/10.1016/S0360-5442(99)00055-9).
- Boyaghchi, Fateme Ahmadi, and Sahar Asgari. 2017. "A Comparative Study on Exergetic, Exergoeconomic and Exergoenvironmental Assessments of Two Internal Auto-Cascade Refrigeration Cycles." *Applied Thermal Engineering* 122: 723–37. <https://doi.org/10.1016/j.applthermaleng.2017.05.065>.
- Cabello, R., D. Sánchez, R. Llopis, J. Catalán, L. Nebot-Andrés, and E. Torrella. 2017. "Energy Evaluation of R152a as Drop in Replacement for R134a in Cascade Refrigeration Plants." *Applied Thermal Engineering* 110 (517): 972–84. <https://doi.org/10.1016/j.applthermaleng.2016.09.010>.
- Cabeza, L.F., H. Mehling, S. Hiebler, and F. Ziegler. 2002. "Heat Transfer Enhancement in Water When Used as PCM in Thermal Energy Storage." *Applied Thermal Engineering* 22 (10): 1141–51. [https://doi.org/10.1016/S1359-4311\(02\)00035-2](https://doi.org/10.1016/S1359-4311(02)00035-2).
- Cabeza, Luisa F, Gustav Svensson, Stefan Hiebler, and Harald Mehling. 2003. "Thermal Performance of Sodium Acetate Trihydrate Thickened with Different Materials as Phase Change Energy Storage Material" 23: 1697–1704. [https://doi.org/10.1016/S1359-4311\(03\)00107-8](https://doi.org/10.1016/S1359-4311(03)00107-8).
- Caliskan, Hakan, Ibrahim Dincer, and Arif Hepbasli. 2012. "Thermodynamic Analyses and Assessments of Various Thermal Energy Storage Systems for Buildings." *Energy Conversion and Management* 62: 109–22. <https://doi.org/10.1016/j.enconman.2012.03.024>.
- Cengel, Y A, and A J Ghajar. 2011. "Heat and Mass Transfer : Heat and Mass Transfer," 1–79. <https://doi.org/10.1017/CBO9781107415324.004>.
- Chen, Changzhong, Wenmin Liu, Hongwei Wang, and Kelin Peng. 2015. "Synthesis and Performances of Novel Solid-Solid Phase Change Materials with Hexahydroxy

- Compounds for Thermal Energy Storage.” *Applied Energy* 152: 198–206.
<https://doi.org/10.1016/j.apenergy.2014.12.004>.
- Chiu, Justin NingWei. 2011. “Heat Transfer Aspects of Using Phase Change Material in Thermal Energy Storage Applications.”
- Choi, Eunsoo, Young I. Cho, and Harold G. Lorsch. 1992. “Thermal Analysis of the Mixture of Laboratory and Commercial Grades Hexadecane and Tetradecane.” *International Communications in Heat and Mass Transfer* 19 (1): 1–15.
[https://doi.org/10.1016/0735-1933\(92\)90059-Q](https://doi.org/10.1016/0735-1933(92)90059-Q).
- Cimsit, Canan, Ilhan Tekin Ozturk, and Olcay Kincay. 2015. “Thermoeconomic Optimization of LiBr/H₂O-R134a Compression-Absorption Cascade Refrigeration Cycle.” *Applied Thermal Engineering* 76: 105–15.
<https://doi.org/10.1016/j.applthermaleng.2014.10.094>.
- CNN Money. 2011. “Saudi Arabia Poised to Become Solar Powerhouse.”
http://money.cnn.com/2011/11/21/news/international/saudi_arabia_solar/index.htm.
- COMMISSION CALIFORNIA ENERGY, and Thermal Energy Storage Systems. 1996. “SOURCE ENERGY AND ENVIRONMENTAL IMPACTS OF THERMAL ENERGY STORAGE.” *CALIFORNIA ENERGY COMMISSION*, no. February.
- Cui, Borui, Shengwei Wang, Chengchu Yan, and Xue Xue. 2015. “Evaluation of a Fast Power Demand Response Strategy Using Active and Passive Building Cold Storages for Smart Grid Applications Q.” *Energy Conversion and Management* 102: 227–38.
<https://doi.org/10.1016/j.enconman.2014.12.025>.
- Danckwerts, P.V. 1979. “Commentary - P. V. Danckwerts , Continuous Flow Systems .” *Chemical Engineering Science*, no. 19: 3855.
- Dincer, Ibrahim, and Marc A Rosen. 2001. “Energetic , Environmental and Economic Aspects of Thermal Energy Storage Systems for Cooling Capacity” 21.
- Dolado, P, A. Lázaro, B Zalba, and J.M. Marín. 2006. “Numerical Simulation of the Thermal Behaviour of an Energy Storage Unit With Phase Change Materials for Air Conditioning Applications Between 17°C and 40°C.” *Proceedings of the Tenth International Conference on Thermal Energy Storage, Ecstock*.
- Donkers, P. A.J., L. C. Sögütöglü, H. P. Huinink, H. R. Fischer, and O. C.G. Adan. 2017. “A Review of Salt Hydrates for Seasonal Heat Storage in Domestic Applications.” *Applied Energy* 199: 45–68. <https://doi.org/10.1016/j.apenergy.2017.04.080>.
- Efimova, Anastasia, Sebastian Pinnau, Matthias Mischke, Cornelia Bretkopf, Michael Ruck, and Peer Schmidt. 2014a. “Development of Salt Hydrate Eutectics as Latent Heat Storage for Air Conditioning and Cooling.” *Thermochimica Acta*.
<https://doi.org/10.1016/j.tca.2013.11.011>.
- . 2014b. “Development of Salt Hydrate Eutectics as Latent Heat Storage for Air Conditioning and Cooling.” *Thermochimica Acta* 575: 276–78.
<https://doi.org/10.1016/j.tca.2013.11.011>.
- Eini, Saeed, Hamidreza Shahhosseini, Navid Delgarm, Moonyong Lee, and Alireza Bahadori. 2016. “Multi-Objective Optimization of a Cascade Refrigeration System: Exergetic, Economic, Environmental, and Inherent Safety Analysis.” *Applied Thermal Engineering* 107: 804–17.
<https://doi.org/10.1016/j.applthermaleng.2016.07.013>.
- Elsayed, Amr Owes. 2015. “Numerical Study on Performance Enhancement of Solid-Solid Phase Change Materials by Using Multi-Nanoparticles Mixtures.” *Journal of*

- Energy Storage* 4: 106–12. <https://doi.org/10.1016/j.est.2015.09.008>.
- Fang, Guiyin, Hui Li, Zhi Chen, and Xu Liu. 2010. “Preparation and Characterization of Stearic Acid/Expanded Graphite Composites as Thermal Energy Storage Materials.” *Energy* 35 (12): 4622–26. <https://doi.org/10.1016/j.energy.2010.09.046>.
- Farid, M. M., Hamad, F. A., & Abu-Arabi, M, Siddique A. Khateeb, Shabab Amiruddin, Mohammed Farid, J. Robert Selman, and Said Al-Hallaj. 1998. “Phase Change Cool Storage Using Dimethyl-Sulfoxide. ENERGY CONVERSION AND MANAGEMENT, 39(8), 819-826. Doi-10.1016:S0196-8904(97)00037-X.” *Journal of Power Sources* 142 (1–2): 819–26. [https://doi.org/10.1016:S0196-8904\(97\)00037-X](https://doi.org/10.1016:S0196-8904(97)00037-X).
- Farid, Mohammed M., Amar M. Khudhair, Siddique Ali K. Razack, and Said Al-Hallaj. 2004. “A Review on Phase Change Energy Storage: Materials and Applications.” *Energy Conversion and Management* 45 (9–10): 1597–1615. <https://doi.org/10.1016/j.enconman.2003.09.015>.
- Farid, Mohammed Mehdi, Feras Ahmad Hamad, and Mousa Abu-Arabi. 1998. “Phase Change Cool Storage Using Dimethyl-Sulfoxide.” *Energy Conversion and Management* 39 (8): 819–26.
- Flegkas, S., F. Birkelbach, F. Winter, N. Freiburger, and A. Werner. 2018. “Fluidized Bed Reactors for Solid-Gas Thermochemical Energy Storage Concepts - Modelling and Process Limitations.” *Energy* 143: 615–23. <https://doi.org/10.1016/j.energy.2017.11.065>.
- Focus, Energy Efficiency, Cross Functional, and Technology Program. n.d. “Energy Efficiency Focus Areas.”
- Folger, H Scott. 2006. “Fogler, H. Scott. 2006. Elements of Chemical Reaction Engineering. Upper Saddle River, NJ: Prentice Hall PTR.” *Prentice Hall PTR*. <http://ir.obihiro.ac.jp/dspace/handle/10322/3933>.
- Font, Francesc. 2014. *Beyond the Classical Stefan Problem*.
- Fukai, Jun, Yuichi Hamada, Yoshio Morozumi, and Osamu Miyatake. 2002. “Effect of Carbon-Fiber Brushes on Conductive Heat Transfer in Phase Change Materials.” *International Journal of Heat and Mass Transfer* 45 (24): 4781–92. [https://doi.org/10.1016/S0017-9310\(02\)00179-5](https://doi.org/10.1016/S0017-9310(02)00179-5).
- Fukai, Jun, Makoto Kanou, Yoshikazu Kodama, and Osamu Miyatake. 2000. “Thermal Conductivity Enhancement of Energy Storage Media Using Carbon Fibers.” *Energy Conversion and Management* 41 (14): 1543–56. [https://doi.org/10.1016/S0196-8904\(99\)00166-1](https://doi.org/10.1016/S0196-8904(99)00166-1).
- García-Romero, A., G. Diarce, J. Ibarretxe, A. Urresti, and J. M. Sala. 2012. “Influence of the Experimental Conditions on the Subcooling of Glauber’s Salt When Used as PCM.” *Solar Energy Materials and Solar Cells* 102: 189–95. <https://doi.org/10.1016/j.solmat.2012.03.003>.
- General Authority for Statistics - Kingdom of Saudi Arabia. 2014. “The Total Population in 2014” 2015: 226003.
- Ghorbani, Bahram, Mehdi Mehrpooya, Reza Shirmohammadi, and Mohammad Hossein Hamed. 2018. “A Comprehensive Approach toward Utilizing Mixed Refrigerant and Absorption Refrigeration Systems in an Integrated Cryogenic Refrigeration Process.” *Journal of Cleaner Production* 179: 495–514. <https://doi.org/10.1016/j.jclepro.2018.01.109>.

- Giannetti, Niccolò, Adriano Milazzo, Andrea Rocchetti, and Kiyoshi Saito. 2017. "Cascade Refrigeration System with Inverse Brayton Cycle on the Cold Side." *Applied Thermal Engineering* 127: 986–95. <https://doi.org/10.1016/j.applthermaleng.2017.08.067>.
- Gogoi, Jyoti Prasad, Nidhi S. Bhattacharyya, and K. C. James Raju. 2011. "Synthesis and Microwave Characterization of Expanded Graphite/Novolac Phenolic Resin Composite for Microwave Absorber Applications." *Composites Part B: Engineering* 42 (5): 1291–97. <https://doi.org/10.1016/j.compositesb.2011.01.026>.
- Guillot, Stéphanie, Abdessamad Faik, Aydar Rakhmatullin, Julien Lambert, Emmanuel Veron, Patrick Echegut, Catherine Bessada, Nicolas Calvet, and Xavier Py. 2012. "Corrosion Effects between Molten Salts and Thermal Storage Material for Concentrated Solar Power Plants." *Applied Energy* 94: 174–81. <https://doi.org/10.1016/j.apenergy.2011.12.057>.
- Guldentops, Gert, Giuseppe Ardito, Mingjiang Tao, Sergio Granados-Focil, and Steven Van Dessel. 2018. "A Numerical Study of Adaptive Building Enclosure Systems Using Solid–Solid Phase Change Materials with Variable Transparency." *Energy and Buildings* 167: 240–52. <https://doi.org/10.1016/j.enbuild.2018.02.054>.
- Habeebullah, B. A. 2006. "Economic Feasibility of Thermal Energy Storage Systems : Application to Al-Haram Grand Holy Mosque Air Conditioning Plant" 16 (2): 55–82.
- Hans Dieter Baehr and Karl Stephan. 2014. *Heat and Mass Transfer*. 2nd, revis ed. Berlin: Springer.
- Hasnain, S.M. 1998. "Review on Sustainable Thermal Energy Storage Technologies, Part II: Cool Thermal Storage." *Energy Conversion and Management* 39 (11): 1139–53. [https://doi.org/10.1016/S0196-8904\(98\)00024-7](https://doi.org/10.1016/S0196-8904(98)00024-7).
- Hasnain, Syed Mahmood, and Naif Mohammed Alabbadi. 2000. "Need for Thermal-Storage Air-Conditioning in Saudi Arabia" 65: 153–64.
- He, Bo, Viktoria Martin, and Fredrik Setterwall. 2003. "Liquid-Solid Phase Equilibrium Study of Tetradecane and Hexadecane Binary Mixtures as Phase Change Materials (PCMs) for Comfort Cooling Storage." *Fluid Phase Equilibria* 212 (1–2): 97–109. [https://doi.org/10.1016/S0378-3812\(03\)00270-X](https://doi.org/10.1016/S0378-3812(03)00270-X).
- He, Bo, and Fredrik Setterwall. 2002. "Technical Grade Paraffin Waxes as Phase Change Materials for Cool Thermal Storage and Cool Storage Systems Capital Cost Estimation." *Energy Conversion and Management* 43 (13): 1709–23. [https://doi.org/10.1016/S0196-8904\(01\)00005-X](https://doi.org/10.1016/S0196-8904(01)00005-X).
- Henze, Gregor P., Bernd Biffar, Dietmar Kohn, and Martin P. Becker. 2008. "Optimal Design and Operation of a Thermal Storage System for a Chilled Water Plant Serving Pharmaceutical Buildings." *Energy and Buildings* 40 (6): 1004–19. <https://doi.org/10.1016/j.enbuild.2007.08.006>.
- Himran, Syukri, Suwono Aryadi, and G Ali Mansoori. 1994. "Charaterization of Alkanes and Paraffin Waxes for Applications as Phase Change Energy Storage Medium." *Energy Sources* 16.1: 117–28.
- HOLBROOK L. HORTON, HENRY H. RYFFEL ERIK OBERG, FRANKLIN D. JONES. 2004. *Machinery 's Handbook*. Industrial Press, Inc., New York, NY.
- Hu, Peng, Pan Pan Zhao, Yi Jin, and Ze Shao Chen. 2014. "Experimental Study on Solid-Solid Phase Change Properties of Pentaerythritol (PE)/Nano-AlN Composite for

- Thermal Storage.” *Solar Energy* 102: 91–97.
<https://doi.org/10.1016/j.solener.2014.01.018>.
- Ibrahim, Nasiru I., Fahad A. Al-Sulaiman, Saidur Rahman, Bekir S. Yilbas, and Ahmet Z. Sahin. 2017. “Heat Transfer Enhancement of Phase Change Materials for Thermal Energy Storage Applications: A Critical Review.” *Renewable and Sustainable Energy Reviews* 74 (October 2015): 26–50.
<https://doi.org/10.1016/j.rser.2017.01.169>.
- Iten, M., and S. Liu. 2014. “A Work Procedure of Utilising PCMs as Thermal Storage Systems Based on Air-TES Systems.” *Energy Conversion and Management* 77: 608–27. <https://doi.org/10.1016/j.enconman.2013.10.012>.
- Izquierdo, M., A. Moreno-Rodríguez, A. González-Gil, and N. García-Hernando. 2011. “Air Conditioning in the Region of Madrid, Spain: An Approach to Electricity Consumption, Economics and CO2 Emissions.” *Energy* 36 (3): 1630–39.
<https://doi.org/10.1016/j.energy.2010.12.068>.
- Jeong, Su Gwang, Okyoung Chung, Seulgi Yu, Sughwan Kim, and Sumin Kim. 2013. “Improvement of the Thermal Properties of Bio-Based PCM Using Exfoliated Graphite Nanoplatelets.” *Solar Energy Materials and Solar Cells* 117: 87–92.
<https://doi.org/10.1016/j.solmat.2013.05.038>.
- Jeong, Su Gwang, Jeong Hun Lee, Jungki Seo, and Sumin Kim. 2014. “Thermal Performance Evaluation of Bio-Based Shape Stabilized PCM with Boron Nitride for Energy Saving.” *International Journal of Heat and Mass Transfer* 71: 245–50.
<https://doi.org/10.1016/j.ijheatmasstransfer.2013.12.017>.
- Jiang, Long, Huitong Lu, Ruzhu Wang, Liwei Wang, Lixia Gong, Yiji Lu, and Anthony Paul Roskilly. 2017. “Investigation on an Innovative Cascading Cycle for Power and Refrigeration Cogeneration.” *Energy Conversion and Management* 145: 20–29.
<https://doi.org/10.1016/j.enconman.2017.04.086>.
- Kahwaji, Samer, Michel B Johnson, Ali C Kheirabadi, Dominic Groulx, and Mary Anne. 2016. “Stable , Low-Cost Phase Change Material for Building Applications : The Eutectic Mixture of Decanoic Acid and Tetradecanoic Acid.” *Applied Energy* 168: 457–64. <https://doi.org/10.1016/j.apenergy.2016.01.115>.
- Kang, Yujin, Su Gwang Jeong, Seunghwan Wi, and Sumin Kim. 2015. “Energy Efficient Bio-Based PCM with Silica Fume Composites to Apply in Concrete for Energy Saving in Buildings.” *Solar Energy Materials and Solar Cells* 143: 430–34.
<https://doi.org/10.1016/j.solmat.2015.07.026>.
- Kenisarin, Murat, and Khamid Mahkamov. 2016. “Salt Hydrates as Latent Heat Storage Materials: Thermophysical Properties and Costs.” *Solar Energy Materials and Solar Cells* 145: 255–86. <https://doi.org/10.1016/j.solmat.2015.10.029>.
- Khateeb, Siddique A., Mohammed M. Farid, J. Robert Selman, and Said Al-Hallaj. 2004. “Design and Simulation of a Lithium-Ion Battery with a Phase Change Material Thermal Management System for an Electric Scooter.” *Journal of Power Sources* 128 (2): 292–307. <https://doi.org/10.1016/j.jpowsour.2003.09.070>.
- Khateeb, Siddique A, Shabab Amiruddin, Mohammed Farid, J Robert Selman, and Said Al-hallaj. 2005. “Thermal Management of Li-Ion Battery with Phase Change Material for Electric Scooters : Experimental Validation” 142: 345–53.
<https://doi.org/10.1016/j.jpowsour.2004.09.033>.
- Kostenko, B F, J. Pribis, and I V Puzynin. 2003. “Stefan’s Problem and Beyond.” *ArXiv*,

- 1–13. <http://arxiv.org/abs/math-ph/0302044>.
- Košťal, P., I. Špička, Z. Jančíková, J. David, J. Valíček, M. Harničárová, and V. Rusnák. 2015. “Lumped Capacitance Model in Thermal Analysis of Solid Materials.” *Journal of Physics: Conference Series* 588 (1): 0–7. <https://doi.org/10.1088/1742-6596/588/1/012006>.
- Kousksou, T., A. Jamil, T. El Rhafiki, and Y. Zeraouli. 2010. “Paraffin Wax Mixtures as Phase Change Materials.” *Solar Energy Materials and Solar Cells* 94 (12): 2158–65. <https://doi.org/10.1016/j.solmat.2010.07.005>.
- Kui Shan, Shengwei Wang, Chengchu Yan, and Fu Xiao. 2016. “Building Demand Response and Control Methods for Smart Grids: A Review.” *Science and Technology for the Built Environment*, no. (SS2016) 22, 692–704 Copyright C 2016 ASHRAE. IN: 2374-4731 print / 2374-474X online DOI: 10.1080/23744731.2016.1192878.
- Kurnia, Jundika C., Agus P. Sasmito, Sachin V. Jangam, and Arun S. Mujumdar. 2013. “Improved Design for Heat Transfer Performance of a Novel Phase Change Material (PCM) Thermal Energy Storage (TES).” *Applied Thermal Engineering* 50 (1): 896–907. <https://doi.org/10.1016/j.applthermaleng.2012.08.015>.
- Lachheb, Mohamed, Karkri Mustapha, Albouchi Fethi, Ben Nasrallah Sassi, Fois Magali, and Sobolciak Patrik. 2014. “Thermal Properties Measurement and Heat Storage Analysis of Paraffin/Graphite Composite Phase Change Material.” *Composites Part B: Engineering* 66: 518–25. <https://doi.org/10.1016/j.compositesb.2014.05.011>.
- Lahn, Glada, and Paul Stevens. 2011. “Burning Oil to Keep Cool: The Hidden Energy Crisis in Saudi Arabia.” The Royal Institute of International Affairs. 2011. [http://www.chathamhouse.org/sites/files/chathamhouse/public/Research/Energy, Environment and Development/1211pr_lahn_stevens.pdf](http://www.chathamhouse.org/sites/files/chathamhouse/public/Research/Energy,EnvironmentandDevelopment/1211pr_lahn_stevens.pdf).
- Li, Peiwen, Ben Xu, Jingxiao Han, and Yongping Yang. 2014. “Verification of a Model of Thermal Storage Incorporated with an Extended Lumped Capacitance Method for Various Solid-Fluid Structural Combinations.” *Solar Energy* 105: 71–81. <https://doi.org/10.1016/j.solener.2014.03.038>.
- Liu, Junwan, Min Xie, Ziyi Ling, Xiaoming Fang, and Zhengguo Zhang. 2018. “Novel MgCl₂-KCl/Expanded Graphite/Graphite Paper Composite Phase Change Blocks with High Thermal Conductivity and Large Latent Heat.” *Solar Energy* 159 (October 2017): 226–33. <https://doi.org/10.1016/j.solener.2017.10.083>.
- Liu, Lingkun, Di Su, Yaojie Tang, and Guiyin Fang. 2016. “Thermal Conductivity Enhancement of Phase Change Materials for Thermal Energy Storage: A Review.” *Renewable and Sustainable Energy Reviews* 62: 305–17. <https://doi.org/10.1016/j.rser.2016.04.057>.
- Liu, Yushi, and Yingzi Yang. 2017. “Preparation and Thermal Properties of Na₂CO₃·10H₂O-Na₂HPO₄·12H₂O Eutectic Hydrate Salt as a Novel Phase Change Material for Energy Storage.” *Applied Thermal Engineering* 112: 606–9. <https://doi.org/10.1016/j.applthermaleng.2016.10.146>.
- . 2018. “Form-Stable Phase Change Material Based on Na₂CO₃·10H₂O-Na₂HPO₄·12H₂O Eutectic Hydrated Salt/Expanded Graphite Oxide Composite: The Influence of Chemical Structures of Expanded Graphite Oxide.” *Renewable Energy* 115: 734–40. <https://doi.org/10.1016/j.renene.2017.08.097>.
- Lizarte, R., M. E. Palacios-Lorenzo, and J. D. Marcos. 2017. “Parametric Study of a

- Novel Organic Rankine Cycle Combined with a Cascade Refrigeration Cycle (ORC-CRS) Using Natural Refrigerants.” *Applied Thermal Engineering* 127: 378–89. <https://doi.org/10.1016/j.applthermaleng.2017.08.063>.
- Mackay, Donald, and Ian Van Wesenbeeck. 2014. “Correlation of Chemical Evaporation Rate with Vapor Pressure.” *Environmental Science & Technology* 48, No. 17 (2014): 10259–10263. <https://doi.org/10.1021/es5029074>.
- MacPhee, David, and Ibrahim Dincer. 2009. “Performance Assessment of Some Ice TES Systems.” *International Journal of Thermal Sciences* 48 (12): 2288–99. <https://doi.org/10.1016/j.ijthermalsci.2009.03.012>.
- Martinez, Francesc Font. 2014. *Beyond the Classical Stefan Problem*.
- Megdouli, K., B. M. Tashtoush, E. Nahdi, M. Elakhdar, L. Kairouani, and A. Mhimid. 2016. “Analyse Thermodynamique d’un Nouveau Cycle Frigorifique à Éjecteur- En Cascade Pour La Congélation et Le Conditionnement d’air.” *International Journal of Refrigeration* 70: 108–18. <https://doi.org/10.1016/j.ijrefrig.2016.06.029>.
- Mehling, Harald, and Luisa F. Cabeza. 2008. *Heat and Cold Storage with PCM: An up to Date Introduction into Basics and Applications*. Berlin: Springer.
- Mehling, Harald, and Luisa F. Cabeza. 2008. *Heat and Cold Storage with PCM. Hand Book, Publisher Springer, Germany*. <https://doi.org/10.1007/978-3-540-68557-9>.
- Mehling, Harald, Luisa F. Cabeza, J.M. Marín P. Dolado, A. Lázaro, B. Zalba, Amirtham valan Arasu, Agus P. Sasmito, Arun S. Mujumdar, C Vuik, et al. 2012. “A Work Procedure of Utilising PCMs as Thermal Storage Systems Based on Air-TES Systems.” *Energy Conversion and Management* 24 (12): 1–10. <https://doi.org/10.1016/j.rser.2011.09.004>.
- Mills, Andrew, Mohammed Farid, J. R. Selman, and Said Al-Hallaj. 2006. “Thermal Conductivity Enhancement of Phase Change Materials Using a Graphite Matrix.” *Applied Thermal Engineering* 26 (14–15): 1652–61. <https://doi.org/10.1016/j.applthermaleng.2005.11.022>.
- Mohamed, S.A., F.A. Al-Sulaiman, N.I. Ibrahim, M.H. Zahir, A. Al-Ahmed, R. Saidur, B.S. Yılbaş, and A.Z. Sahin. 2017. “A Review on Current Status and Challenges of Inorganic Phase Change Materials for Thermal Energy Storage Systems.” *Renewable and Sustainable Energy Reviews* 70. <https://doi.org/10.1016/j.rser.2016.12.012>.
- Mohamed, Shamseldin A., Fahad A. Al-Sulaiman, Nasiru I. Ibrahim, Md Hasan Zahir, Amir Al-Ahmed, R. Saidur, B. S. Yılbaş, and A. Z. Sahin. 2017. “A Review on Current Status and Challenges of Inorganic Phase Change Materials for Thermal Energy Storage Systems.” *Renewable and Sustainable Energy Reviews* 70 (June 2015): 1072–89. <https://doi.org/10.1016/j.rser.2016.12.012>.
- Mohammadi, S. M.Hojjat, and Mehran Ameri. 2016. “Energy and Exergy Performance Comparison of Different Configurations of an Absorption-Two-Stage Compression Cascade Refrigeration System with Carbon Dioxide Refrigerant.” *Applied Thermal Engineering* 104: 104–20. <https://doi.org/10.1016/j.applthermaleng.2016.05.051>.
- Mott, Henry V., and Zane A. Green. 2015. “On Danckwerts’ Boundary Conditions for the Plug-Flow with Dispersion/Reaction Model.” *Chemical Engineering Communications* 202 (6): 739–45. <https://doi.org/10.1080/00986445.2013.871708>.
- National Academy of Sciences, National Academy of Engineering, and National Research Council. 2010. *Real Prospects for Energy Efficiency in the United States*.

- Washington, DC: The National Academies Press. <https://doi.org/10.17226/12621>.
<https://doi.org/10.17226/12621>.
- Organization of Petroleum Exporting Countries. 2016. "Saudi Arabia Facts and Figures," 2–3.
- Oró, E, A De Gracia, A Castell, M M Farid, and L F Cabeza. 2012. "Review on Phase Change Materials (PCMs) for Cold Thermal Energy Storage Applications" 99: 513–33. <https://doi.org/10.1016/j.apenergy.2012.03.058>.
- Pacific Gas and Electric Company, PG & E. 1997. "An In-Depth Examination of an Energy Efficiency Technology, Thermal Energy Storage." *In-Depth Examination of an Energy Efficiency Technology*.
- Pan, Z. H., and C. Y. Zhao. 2017. "Gas–Solid Thermochemical Heat Storage Reactors for High-Temperature Applications." *Energy* 130: 155–73.
<https://doi.org/10.1016/j.energy.2017.04.102>.
- Peng, Tiefeng, Bin Liu, Xuechao Gao, Liquan Luo, and Hongjuan Sun. 2018. "Preparation, Quantitative Surface Analysis, Intercalation Characteristics and Industrial Implications of Low Temperature Expandable Graphite." *Applied Surface Science* 444: 800–810. <https://doi.org/10.1016/j.apsusc.2018.03.089>.
- Pielichowska, Kinga, and Krzysztof Pielichowski. 2014. "Phase Change Materials for Thermal Energy Storage." *Progress in Materials Science* 65: 67–123.
<https://doi.org/10.1016/j.pmatsci.2014.03.005>.
- Pincemin, S., R. Olives, X. Py, and M. Christ. 2008. "Highly Conductive Composites Made of Phase Change Materials and Graphite for Thermal Storage." *Solar Energy Materials and Solar Cells* 92 (6): 603–13.
<https://doi.org/10.1016/j.solmat.2007.11.010>.
- Pomianowski, Michal, Per Heiselberg, and Yinping Zhang. 2013. "Review of Thermal Energy Storage Technologies Based on PCM Application in Buildings." *Energy and Buildings* 67: 56–69. <https://doi.org/10.1016/j.enbuild.2013.08.006>.
- Py, Xavier, Régis Olives, and Sylvain Mauran. 2001. "Paraffin/Porous-Graphite-Matrix Composite as a High and Constant Power Thermal Storage Material." *International Journal of Heat and Mass Transfer* 44 (14): 2727–37.
[https://doi.org/10.1016/S0017-9310\(00\)00309-4](https://doi.org/10.1016/S0017-9310(00)00309-4).
- Qu, Renjie, Shuihua Tang, Xiaolong Qin, Jiawei Yuan, Yuxiao Deng, Lingshan Wu, Jie Li, and Zewei Wei. 2017. "Expanded Graphite Supported Ni(OH)₂ Composites for High Performance Supercapacitors." *Journal of Alloys and Compounds* 728: 222–30. <https://doi.org/10.1016/j.jallcom.2017.08.270>.
- Ranmode, Vaibhav, Manmeet Singh, and Jishnu Bhattacharya. 2019. "Analytical Formulation of Effective Heat Transfer Coefficient and Extension of Lumped Capacitance Method to Simplify the Analysis of Packed Bed Storage Systems." *Solar Energy* 183 (March): 606–18. <https://doi.org/10.1016/j.solener.2019.03.066>.
- Razack, Siddique A Khateeb, Mukund Bhaskar, Yoram Shabtay, Hal Stilman, Said Al-hallaj, and Madison Avenue. 2016. "Design and Performance of Thermal Energy Storage Module Using High Thermal Conductivity Phase Change Composite Material."
- Regulatory, Cogeneration. 2018. "Saudi Arabia Energy Efficiency Program." 2018.
- Rhodes, Joshua D., Brent Stephens, and Michael E. Webber. 2011. "Using Energy Audits to Investigate the Impacts of Common Air-Conditioning Design and Installation

- Issues on Peak Power Demand and Energy Consumption in Austin, Texas.” *Energy and Buildings* 43 (11): 3271–78. <https://doi.org/10.1016/j.enbuild.2011.08.032>.
- Roxas-dimaano, M N, and T Watanabe. 2002. “The Capric and Lauric Acid Mixture with Chemical Additives as Latent Heat Storage Materials for Cooling Application.” *Energy* 27 (2002) 869–888 27: 869–88. [https://doi.org/10.1016/S0360-5442\(02\)00024-5](https://doi.org/10.1016/S0360-5442(02)00024-5).
- Rutberg, Michael, Mildred Hastbacka, Alissa Cooperman, and Antonio Bouza. 2013. “Thermal Energy Storage.” *ASHRAE Journal* 55 (6): 62–66. <https://doi.org/10.1007/978-1-4419-1024-0>.
- Salhi, Khelifa, Mourad Korichi, and Khaled M. Ramadan. 2018. “Thermodynamic and Thermo-Economic Analysis of Compression-Absorption Cascade Refrigeration System Using Low-GWP HFO Fluids Powered by Geothermal Energy.” *International Journal of Refrigeration*. <https://doi.org/10.1016/j.ijrefrig.2018.03.017>.
- Sari, Ahmet. 2003. “Thermal Reliability Test of Some Fatty Acids as PCMs Used for Solar Thermal Latent Heat Storage Applications.” *Energy Conversion and Management* 44 (14): 2277–87. [https://doi.org/10.1016/S0196-8904\(02\)00251-0](https://doi.org/10.1016/S0196-8904(02)00251-0).
- Sari, Ahmet, Alper Biçer, and Cemil Alkan. 2017. “Thermal Energy Storage Characteristics of Poly(Styrene-Co-Maleic Anhydride)-Graft-PEG as Polymeric Solid–Solid Phase Change Materials.” *Solar Energy Materials and Solar Cells* 161 (September 2016): 219–25. <https://doi.org/10.1016/j.solmat.2016.12.001>.
- Sarler, Bolidar. 1995. “Stefan ’ s Work on Solid-Liquid Phase Changes” 7997 (95): 83–92.
- Sharma, Atul, V. V. Tyagi, C. R. Chen, and D. Buddhi. 2009. “Review on Thermal Energy Storage with Phase Change Materials and Applications.” *Renewable and Sustainable Energy Reviews* 13 (2): 318–45. <https://doi.org/10.1016/j.rser.2007.10.005>.
- Shoaibi, Abdulmohsin Mohammad Al, and Amin Al-Yaquob. 2017. “Saudi Arabia Solar Industry : Country Focus Report.” <https://www.solar-united.org/wp-content/uploads/2017/02/SASIA-CountryFocusReport-SP.pdf>.
- Silakhori, Mahyar, Hendrik Simon Cornelis Metselaar, Teuku Meurah Indra Mahlia, Hadi Fauzi, Saeid Baradaran, and Mohammad Sajad Naghavi. 2014. “Palmitic Acid/Polypyrrole Composites as Form-Stable Phase Change Materials for Thermal Energy Storage.” *Energy Conversion and Management* 80: 491–97. <https://doi.org/10.1016/j.enconman.2014.01.023>.
- Solé, Aran, Laia Miró, Camila Barreneche, Ingrid Martorell, and Luisa F. Cabeza. 2015. “Corrosion of Metals and Salt Hydrates Used for Thermochemical Energy Storage.” *Renewable Energy* 75: 519–23. <https://doi.org/10.1016/j.renene.2014.09.059>.
- Southern California Edison. 2016. “Tariffs and Programs for Small, Medium, and Large Power Customers, Plan GS-2 Time of Use (TOU) Rate ‘Option A’, 2016.” 2016. 2016.
- Southern California Edison Time-of-use Residential Rate Plans, TOU. 2018. “Time-Of-Use (TOU) Rate Plans Is TOU Right for You. Rates Glossary Ready to Change Your Rate ? Get Help With Your Bills.” 2018.
- Su, Weiguang, Jo Darkwa, and Georgios Kokogiannakis. 2015. “Review of Solid-Liquid Phase Change Materials and Their Encapsulation Technologies.” *Renewable and*

- Sustainable Energy Reviews* 48: 373–91. <https://doi.org/10.1016/j.rser.2015.04.044>. Summary, Climate, Average High, and Low Temperature. n.d. “Average Weather in Riyadh.”
- Sun, Zhili, Youcai Liang, Shengchun Liu, Weichuan Ji, Runqing Zang, Rongzhen Liang, and Zhikai Guo. 2016. “Comparative Analysis of Thermodynamic Performance of a Cascade Refrigeration System for Refrigerant Couples R41/R404A and R23/R404A.” *Applied Energy* 184: 19–25. <https://doi.org/10.1016/j.apenergy.2016.10.014>.
- Syukri, Hirman, Suwono Aryadi, and G Ali Mansoori. 1994. “Characterization of Alkanes and Paraffin Waxes for Applications as Phase Change Energy Storage Medium.Pdf” 16: 117–28.
- Tang, Yaojie, Guruprasad Alva, Xiang Huang, Di Su, Lingkun Liu, and Guiyin Fang. 2016. “Thermal Properties and Morphologies of MA-SA Eutectics/CNTs as Composite PCMs in Thermal Energy Storage.” *Energy and Buildings* 127: 603–10. <https://doi.org/10.1016/j.enbuild.2016.06.031>.
- Tao, Shi, Sun Wei, and Yang Yulan. 2015. “Characterization of Expanded Graphite Microstructure and Fabrication of Composite Phase-Change Material for Energy Storage.” *Journal of Materials in Civil Engineering*. [https://doi.org/10.1061/\(ASCE\)MT.1943-5533.0001089](https://doi.org/10.1061/(ASCE)MT.1943-5533.0001089).
- Tomczyk, John, Joe Nott, and Dick Shaw. 2002. *Universal R - 410A Safety Training*. Esco Press.
- Trausel, Fanny, Ard Jan De Jong, and Ruud Cuypers. 2014. “A Review on the Properties of Salt Hydrates for Thermochemical Storage.” *Energy Procedia* 48: 447–52. <https://doi.org/10.1016/j.egypro.2014.02.053>.
- U.S. Energy Information Administration. 2017. “Saudi Arabia’s Key Energy Statistics.” <https://www.eia.gov/beta/international/country.cfm?iso=SAU>.
- Ubay, By Jason. 2009. “Air Conditioning.” *Ocean Engineering*. 2009.
- Ukrainczyk, N, S Kurajica, and J Š. 2010. “Thermophysical Comparison of Five Commercial Paraffin Waxes as Latent Heat Storage Materials” c (2): 129–37.
- USDOE Office of Energy Efficiency & Renewable Energy, (EE), and (US) Office of Federal Energy Management Programs. 2000. “Thermal Energy Storage for Space Cooling Technology for Reducing On-Peak Electricity Demand and Cost Thermal.” Richland, WA (US). <https://doi.org/doi:10.2172/770996>. <https://www.osti.gov/servlets/purl/770996>.
- Vasu, Anusuiah, Ftwi Y. Hagos, M. M. Noor, R. Mamat, W. H. Azmi, Abdul A. Abdullah, and Thamir K. Ibrahim. 2017. “Corrosion Effect of Phase Change Materials in Solar Thermal Energy Storage Application.” *Renewable and Sustainable Energy Reviews* 76 (January): 19–33. <https://doi.org/10.1016/j.rser.2017.03.018>.
- Vuik, C. 1984. “Some Historical Notes on the Stefan Problem . The Stefan Problem . The Stefan Problem with a Linear Temperature Profile .,” 1–10.
- Wang, Feng, Ping Zhang, Yongren Mou, Ming Kang, Min Liu, Lixian Song, Ai Lu, and Jianzhong Rong. 2017. “Synthesis of the Polyethylene Glycol Solid-Solid Phase Change Materials with a Functionalized Graphene Oxide for Thermal Energy Storage.” *Polymer Testing* 63: 494–504. <https://doi.org/10.1016/j.polymertesting.2017.09.005>.

- Wang, Lin, Aihua Ma, Yingying Tan, Xiaolong Cui, and Hongli Cui. 2011. "Study on Solar-Assisted Cascade Refrigeration System." *Energy Procedia* 16 (PART C): 1503–9. <https://doi.org/10.1016/j.egypro.2012.01.236>.
- Wang, Shengwei, and Rui Tang. 2017. "Supply-Based Feedback Control Strategy of Air-Conditioning Systems for Direct Load Control of Buildings Responding to Urgent Requests of Smart Grids." *Applied Energy* 201: 419–32. <https://doi.org/10.1016/j.apenergy.2016.10.067>.
- Wilde, Juray De, and Gilbert F. Froment. 2012. "Computational Fluid Dynamics in Chemical Reactor Analysis and Design: Application to the ZoneFlow™ Reactor for Methane Steam Reforming." *Fuel* 100: 48–56. <https://doi.org/10.1016/j.fuel.2011.08.068>.
- Wu, Jianghong, Biwang Lu, Chaopeng Liu, and Jing He. 2018. "A Novel Cascade Micro-Unit Regeneration Cycle for Solid State Magnetic Refrigeration." *Applied Thermal Engineering*. <https://doi.org/10.1016/j.applthermaleng.2018.03.109>.
- Wu, Shuangmao, Guiyin Fang, and Zhi Chen. 2012. "Discharging Characteristics Modeling of Cool Thermal Energy Storage System with Coil Pipes Using N-Tetradecane as Phase Change Material." *Applied Thermal Engineering* 37: 336–43. <https://doi.org/10.1016/j.applthermaleng.2011.11.046>.
- Wu, Yuping, and Tao Wang. 2015. "Hydrated Salts/Expanded Graphite Composite with High Thermal Conductivity as a Shape-Stabilized Phase Change Material for Thermal Energy Storage." *Energy Conversion and Management* 101: 164–71. <https://doi.org/10.1016/j.enconman.2015.05.006>.
- Xu, Ben, Pei Wen Li, and Cho Lik Chan. 2012. "Extending the Validity of Lumped Capacitance Method for Large Biot Number in Thermal Storage Application." *Solar Energy* 86 (6): 1709–24. <https://doi.org/10.1016/j.solener.2012.03.016>.
- Xu, Yingjie, Fu Sheng Chen, Qin Wang, Xiaohong Han, Dahong Li, and Guangming Chen. 2015. "A Novel Low-Temperature Absorption-Compression Cascade Refrigeration System." *Applied Thermal Engineering* 75: 504–12. <https://doi.org/10.1016/j.applthermaleng.2014.10.043>.
- Xue Xue, Shengwei Wang, Chengchu Yan, and Borui Cui. 2015. "A Fast Chiller Power Demand Response Control Strategy for Buildings Connected to Smart Grid." *Applied Energy* 137: 77–87. <https://doi.org/10.1016/j.apenergy.2014.09.084>.
- Yamani, Hashim. 2012. "Energy Sustainability for Future Generations." http://www.saudicrm.com/energy.gov.sa/sites/default/files/files/Presentation_MIT_Meeting_Mar2012.pdf.
- Yan, Gang, Jiaheng Chen, and Jianlin Yu. 2015. "Energy and Exergy Analysis of a New Ejector Enhanced Auto-Cascade Refrigeration Cycle." *Energy Conversion and Management* 105: 509–17. <https://doi.org/10.1016/j.enconman.2015.07.087>.
- Yau, Y. H., and Behzad Rismanchi. 2012. "A Review on Cool Thermal Storage Technologies and Operating Strategies." *Renewable and Sustainable Energy Reviews* 16 (1): 787–97. <https://doi.org/10.1016/j.rser.2011.09.004>.
- Ye, Rongda, Wenzhu Lin, Xiaoming Fang, and Zhengguo Zhang. 2017. "A Numerical Study of Building Integrated with CaCl₂·6H₂O/Expanded Graphite Composite Phase Change Material." *Applied Thermal Engineering* 126: 480–88. <https://doi.org/10.1016/j.applthermaleng.2017.07.191>.
- Yu, Seulgi, Su Gwang Jeong, Okyoung Chung, and Sumin Kim. 2014. "Bio-Based

- PCM/Carbon Nanomaterials Composites with Enhanced Thermal Conductivity.” *Solar Energy Materials and Solar Cells* 120 (PART B): 549–54.
<https://doi.org/10.1016/j.solmat.2013.09.037>.
- Zalba, Belén, José M. Marín, Luisa F. Cabeza, and Harald Mehling. 2003. *Review on Thermal Energy Storage with Phase Change: Materials, Heat Transfer Analysis and Applications*. *Applied Thermal Engineering*. Vol. 23. [https://doi.org/10.1016/S1359-4311\(02\)00192-8](https://doi.org/10.1016/S1359-4311(02)00192-8).
- . 2004. “Free-Cooling of Buildings with Phase Change Materials.” *International Journal of Refrigeration* 27 (8): 839–49.
<https://doi.org/10.1016/j.ijrefrig.2004.03.015>.
- Zhai, X. Q., X. L. Wang, T. Wang, and R. Z. Wang. 2013. “A Review on Phase Change Cold Storage in Air-Conditioning System: Materials and Applications.” *Renewable and Sustainable Energy Reviews* 22: 108–20.
<https://doi.org/10.1016/j.rser.2013.02.013>.
- Zhang, Jian, and Qiang Xu. 2011. “Cascade Refrigeration System Synthesis Based on Exergy Analysis.” *Computers and Chemical Engineering* 35 (9): 1901–14.
<https://doi.org/10.1016/j.compchemeng.2011.02.015>.
- Zhang, Xinxing, Xiang Li, Yuan Zhou, Chunxi Hai, Yue Shen, Xiufeng Ren, and Jinbo Zeng. 2018. “Enhanced Thermal Conductivity in a Hydrated Salt PCM System with Reduced Graphene Oxide Aqueous Dispersion.” *RSC Advances* 8 (2): 1022–29.
<https://doi.org/10.1039/c7ra10632g>.
- Zhang, Zhengguo, Ni Zhang, Jing Peng, Xiaoming Fang, Xuenong Gao, and Yutang Fang. 2012. “Preparation and Thermal Energy Storage Properties of Paraffin/Expanded Graphite Composite Phase Change Material.” *Applied Energy* 91 (1): 426–31. <https://doi.org/10.1016/j.apenergy.2011.10.014>.
- Zhou, D., C. Y. Zhao, and Y. Tian. 2012. “Review on Thermal Energy Storage with Phase Change Materials (PCMs) in Building Applications.” *Applied Energy* 92: 593–605. <https://doi.org/10.1016/j.apenergy.2011.08.025>.
- Zhou, Yan, Xiangdong Liu, Dekun Sheng, Changhong Lin, Fance Ji, Li Dong, Shaobin Xu, Haohao Wu, and Yuming Yang. 2017. “Graphene Oxide/Polyurethane-Based Solid–Solid Phase Change Materials with Enhanced Mechanical Properties.” *Thermochimica Acta* 658 (October): 38–46.
<https://doi.org/10.1016/j.tca.2017.10.016>.

AHMED ALJEHANI-- CV

EDUCATION

PhD candidate, Chemical Engineering Dept. University of Illinois Chicago (UIC). Thesis Defense is planned on December 9th, 2019.

Master of Chemical Engineering, Illinois Institute of Technology, 2014

Bachelor of Science, Chemical Engineering, University of Alabama, 2002

NOTABLE

Lecturer, Engineering Design, University of Jeddah, Saudi Arabia, 2011 to 2012

Process, Project, Commissioning Engineer, Saudi Aramco Oil Company, 2002 to 2011

PROFESSIONAL EXPERIENCE

BP (British Petroleum)- Whiting Refinery (Oct. 2018- April 2019)

PROCESS SAFETY MANAGEMENT- Generate High level risk profile of the refinery complex units and communicate risk profile to share holder.

University of Jeddah, Saudi Arabia (2011 to 2012)

LECTURER, ENGINEERING DESIGN, co-teaching an engineering design course to undergraduate students in college of engineering.

Saudi Aramco, Oil and Gas Company , Saudi Arabia (2002- 2011)

SR. PROCESS ENGINEER/SUPERINTENDENT, Lubricating Oil Refinery (2009 to 2011)

Process engineering, lab and quality. Superintendent of process, lab and quality, managed a team of process and control engineers and lab technicians.

- Collaborated with Production Planning and Marketing departments to influence company production plans and strategies and leverage company profits.
- Increased company profits by maximizing yield & production, proposing and implementing several economic enhancements.

PROCESS ENGINEER, HNGL Recovery Construction Project (2007 to 2009)

Reviewed and taught the master control philosophy of HNGL. Joined specialty engineering team and supervised the operator training simulator project.

PROJECT, COMMISSIONING, PROCESS ENGINEER/ COMMISSIONING LEADER (2006 to 2007)

Stepped in for the plant commissioning Leader position. Managed a large team of engineering, operations and Maintenance for a very rewarding successful team experience.

PROCESS ENGINEER, Uthmaniah Gas Plant Department (2006 to 2007)

Received recognition for proposing several design enhancement projects resulting in cost avoidance and closing out all major HAZOP recommendations.

PROCESS ENGINEER, Shedgum Gas Plant Department (2005 to 2006)

Participated in the C3+ NGL recovery enhancement study. Accepted by Senior Saudi Aramco Executives and implemented in Shedgum Gas Plant. Increased revenue by \$24M.

SPECIAL PROJECT, Shedgum Gas Plant (2004)

Received **High-Impact Innovation Idea Award** for developing an improved Gas Turbine operations strategy based on forecast and current demands by adjacent Electricity Company.

PROCESS ENGINEER, Jeddah Refinery Department (2002 to 2003)

Operation engineering assignment in crude, vacuum, and fluid catalytic converter units. Heavily participated in total refinery shut-down T&I activities.

UNIVERSITY EXPERIENCE

University of Illinois – Chicago, Chemical Engineering Dept.

PhD CANDIDATE AND ENERGY RESEARCHER (2014 to Present)

Collaborating with AllCell Technologies and NETenergy start-up company in Chicago. AllCell designs and builds cutting-edge lithium-ion battery packs for transportation and renewable energy applications. NETenergy is a thermal energy storage company. Created a thermal battery using phase change composite materials.

- Collaboration involves prototype development & upgrade project, testing and analysis at AllCell Technologies lab facility and the review and analysis of different potential materials from local and international vendors and material characterization.
- PhD thesis work addresses the simulation and optimization of the integration concept of Thermal Energy Storage - Phase Change Composite (TES-PCC) into the vapor compression refrigeration cycle of a conventional air conditioning system. Integration is introduced as a demand-side management solution to shave/shift electricity consumption from peak-hours to off-peak-hours. The proposed system will assist utilities companies in avoid building new power plants & distribution lines, reduce electricity bills for consumers and boost AC's efficiency.

PUBLICATIONS

- Ahmed Aljehani, Ludwig C. Nitsche, Said Al-Hallaj, Numerical Modeling of Transient Heat Transfer in a Phase Change Composite Thermal Energy Storage (PCC-TES) System for Air Conditioning Applications, Applied Thermal Engineering, 2019, <https://doi.org/10.1016/j.applthermaleng.2019.114522>.
- Aljehani, Ahmed, Siddique Ali K. Razack, Ludwig Nitsche, and Said Al-Hallaj. "Design and optimization of a hybrid air conditioning system with thermal energy storage using phase change composite." *Energy Conversion and Management* 169 (2018): 404-418.
- Al-Hallaj, Said, Siddique Khateeb, Ahmed Aljehani, and Mike Pintar. "Thermal energy storage for smart grid applications." In *AIP Conference Proceedings*, vol. 1924, no. 1, p. 020007. AIP Publishing, 2018.

- [To be submitted for publications soon to the journal of *Energy Conversion and Management*] Ahmed Aljehani, Said Al-Hallaj. The title of potential paper would be "PCC Material Characterizations of Potential Phase Change Composite (PCC) for Thermal Energy Storage (TES)".

COMMUNITY SERVICE

Greeley Elementary Local School Council (2017- 2019)

Gardening Committee, Lake Shore Condominium Association (2017-2018)